

The University of Sheffield



Magnetization State Control of Hybrid Magnet Memory Machines

Yan Jia

A thesis submitted for the degree of Doctor of Philosophy

Department of Electronic and Electrical Engineering

The University of Sheffield

Mappin Street, Sheffield, S1 3JD, UK

February 2024

ABSTRACT

Compared with conventional permanent magnet synchronous machines (PMSMs), the variable magnetization state (MS) of variable flux memory machines (VFMMs) offers improved machine efficiency and more flexible control. As a core part of VFMM control, the benefits of MS control have significant potential for promoting the application of VFMM drive systems. In this thesis, several novel MS control methods, and solutions to improve the performance of VFMMs are proposed and validated on a hybrid magnet memory machine (HMMM) control system.

Firstly, since a VFMM under different MSs has different PM flux linkages and inductances, a set of torque-speed curves can be obtained. The torques are the same on the intersections of these torque-speed curves, and MS manipulation on these intersections can be smooth and steady. An optimal demagnetization strategy is proposed to determine the best instants of demagnetization from the intersections of these grids. This solution is also verified during the remagnetization process. Secondly, to mitigate the speed fluctuation caused by the injected large magnetizing current pulse during MS manipulation, a novel dual magnetizing current controller is proposed. A q -axis current pulse is compensated to reduce the torque variation caused by the injected d -axis magnetizing current pulse. Thirdly, the circumcircle of the voltage vector hexagon is utilized as the modified voltage limitation and set as the boundary for MS manipulation to achieve the target MS, and a new MS control method is proposed. A unique MS control method utilizing the amplitude of demagnetization d -axis current pulse is therefore proposed to eliminate the potential unintentional demagnetization (UD) issue. When the amplitude of the d -axis current is bigger than the amplitude of the previous demand magnetizing current pulse, the MS manipulation will be processed. Thus, the UD issue can be avoided in the whole speed range. Finally, to achieve the MS close-loop control, a novel MS control method utilizing torque deviation is proposed. A model-based torque calculation is utilized for the torque estimation. When the torque deviation between the present MS and target MS meets the preset conditions, the type and the switch signal of MS manipulation will be generated.

The feasibility of all the proposed MS control methods are experimentally validated on a HMMM control system. The transient performance improvements of the proposed methods are significant, especially the proposed dual magnetizing current controller, which can reduce the speed fluctuation by more than 80% compared to conventional methods.

ACKNOWLEDGMENTS

First and foremost, please allow me to express my sincerest and deepest gratitude to my supervisor, Prof. Zi-Qiang Zhu, not only for my PhD study but also for my life. When I felt confused and lost confidence in the past three years, he was like a standing lighthouse, pointing the way for me in the endless darkness and providing strong motivation for me to sail in the boundless ocean of research. His life creed “Investigate things and extend to the utmost knowledge to further gain conscience” has benefited me a lot and will benefit me for the rest of my life.

I would like to thank my company CRRC Zhuzhou Institute Co., Ltd. for providing me this precious opportunity to follow Prof. Zhu and study in the most excellent Electrical Machines and Drives (EMD) research team in this world. Many thanks to Chief Technology Officer Dr Jianghua Feng, Chief Technical Expert Mrs Shuying Guo and Mr Yifeng Li, and Vice President Mr Wenqing Mei for their supports, and my colleagues Mrs Shengli Huang, Mr Liangjie Liu, Mr Liang Hu, Dr Yue Wang, Mr Xingzhi Wang, Mr Xiangyu Fu, Mr Xi Tu, Mr Weichao Tang, and Mr Miao Li for their long-term care and help.

I would like to take this opportunity to sincerely thank Prof. Hui Yang at Southeast University, China, for kindly providing the prototype hybrid magnet memory machine, without which my research on magnetization state control could not be realized.

I am very grateful to Dr Dawei Liang, Dr Ximeng Wu, Dr Lei Xu, and Mr Peng Wang for their help and valuable suggestions on my tests. I also want to express thanks to my fellow colleagues in our research group for their knowledgeable discussions and warm accompany, particularly, Dr Shensheng Wang, Mr Yang Chen, Mr Jun Yan, Mr Dong Xiang, Mr Zhitong Ran, Mr Yinzhaoh Zheng, Mr Qiang Wei, Mr Tianzheng Xiao, Mr Hai Xu, and Mr Jialu He.

My eternal gratitude gives to my parents and my friend Zi Li for their endless care and encouragement during my PhD study. What is more, I must say thanks to myself for not giving up when encountered difficulties, not losing myself when confused, not being defeated by laziness, and finally making it.

At last not least, my special thanks give to my tennis friends, Dr Jinbei Tian, Mr Wenzhi Du, Mr Jiaming Gu, Mr Yue Yin, Mr Rentao Mao, and Mr Xingyu Xie for their accompany during my stay in Sheffield.

CONTENTS

ABSTRACT	I
ACKNOWLEDGMENTS	II
CONTENTS	III
NOMENCLATURES	VIII
LIST OF ABBREVIATIONS	X
CHAPTER 1 GENERAL INTRODUCTION	1
1.1 Introduction.....	1
1.2 Permanent Magnet Machines and Control Methods.....	2
1.2.1 Permanent Magnet Machines.....	2
1.2.2 Control Methods	4
1.3 Memory Machines	10
1.4 Modelling of Memory Machines	14
1.4.1 Magnetic Properties	14
1.4.2 Modelling Methods.....	16
1.5 Control of Memory Machines.....	18
1.5.1 Magnetization State Estimation	19
1.5.2 Magnetization State Manipulation.....	20
1.6 Scope and Contributions of the Thesis	33
1.6.1 Research Motivation	33
1.6.2 Research Outline.....	34
1.6.3 Contributions.....	36
CHAPTER 2 DEMAGNETIZATION TIMING CONTROL FOR HYBRID MAGNET MEMORY MACHINE	38
2.1 Introduction.....	38
2.2 Machine Topology And Mathematical Model	40
2.2.1 Machine Topology	40

2.2.2 Mathematical Model	44
2.3 Demagnetization Analysis for VFMM.....	44
2.4 Best Instant of Demagnetization	46
2.5 Experimental Validation.....	48
2.5.1 Test Rig	48
2.5.2 Performance on Demagnetization Points.....	50
2.5.3 Optimal Number of Demagnetization Instants	55
2.5.4 Verification on Remagnetization.....	63
2.6 Conclusion	73
 CHAPTER 3 DUAL MAGNETIZING CURRENT CONTROLLER TO MITIGATE SPEED FLUCTUATION DURING MAGNETIZATION STATE MANIPULATION... 74	
3.1 Introduction.....	74
3.2 Machine Properties	76
3.2.1 Magnetizing Current Properties	76
3.2.2 Magnetization State Properties	79
3.3 Dual Magnetizing Current Method.....	80
3.3.1 Mathematical Model for VFMM	80
3.3.2 Design of Proposed Dual Magnetizing Current Controller	81
3.3.3 Design of Torque Calculation and Look-up Table	82
3.3.4 Scheme of Proposed Dual Magnetizing Current Method	82
3.4 Simulation and Discussion.....	83
3.4.1 Control System.....	83
3.4.2 Simulation Analysis	84
3.5 Experiments and Analysis.....	89
3.5.1 Remagnetization Transient Performance	89
3.5.2 Demagnetization Transient Performance	94
3.6 Conclusion	98

CHAPTER 4 MAGNETIZATION STATE CONTROL CONSIDERING the effect of VOLTAGE LIMITATION.....	100
4.1 Introduction.....	100
4.2 Mathematical Model for VFMM	102
4.2.1 VFMM Model.....	102
4.2.2 Voltage and Current Constraints	102
4.3 Magnetization State Control Based on Voltage Limitation	103
4.3.1 Effect of Voltage Limitation on MS Manipulation	103
4.3.2 Modified Voltage limitation During MS Manipulation	103
4.3.3 Proposed MS Control Method Based on Modified Voltage Limitation.....	105
4.3.4 Overall Control Strategy	106
4.4 Experimental Validation.....	107
4.4.1 Remagnetization Experimental Validation	107
4.4.2 Demagnetization Experimental Validation	110
4.5 Conclusion	116
CHAPTER 5 MAGNETIZATION STATE CONTROL Utilizing <i>d</i>-axis Current TO ELIMINATE UNINTENTIONAL DEMAGNETIZATION OF LOW-COERCIVE FORCE PERMANENT MAGNET.....	117
5.1 Introduction.....	117
5.2 Control Method for VFMM	119
5.2.1 Mathematical Model of VFMM.....	119
5.2.2 Field-Oriented Control for VFMM.....	119
5.3 Proposed MS Controller Design	121
5.3.1 PM Flux Linkage Estimation.....	121
5.3.2 Initial MS Manipulation.....	122
5.3.3 Proposed MS Controller	122
5.3.4 Overall Control Strategy	124
5.4 Experiment Validation	125

5.4.1 PM Flux Linkage Estimation	125
5.4.2 Verification of UD Issue	127
5.4.3 Verification of Proposed MS Control Method	128
5.4.4 Dynamic Performance for Whole Speed Range	132
5.5 Conclusion	135
CHAPTER 6 MAGNETIZATION STATE Closed-loop CONTROL UTILIZING TORQUE DEVIATION	137
6.1 Introduction.....	137
6.2 Proposed MS Control Method	139
6.2.1 Proposed MS Control Method	139
6.2.2 Overall Control Strategy	140
6.3 Simulation and Discussion.....	141
6.3.1 Remagnetization Simulation	142
6.3.2 Demagnetization Simulation.....	145
6.4 Experimental Validation.....	149
6.4.1 Torque Calculation	149
6.4.2 Remagnetization Process	150
6.4.3 Demagnetization Process	155
6.5 Conclusion	161
CHAPTER 7 GENERAL CONCLUSION AND FUTURE WORK	162
7.1 Summary of Research Work	162
7.2 Conclusion	164
7.2.1 Performance Improvement During MS Manipulation	164
7.2.2 Novel MS Control Methods.....	165
7.3 Future Work	166
7.3.1 Accurate MS Estimation	166
7.3.2 Effect of Load Changes on MS Control.....	167

7.3.3 Oscillations in Three-phase Currents During MS Manipulation	167
7.3.4 Uncontrolled Generator Fault Prevention for VFMM	167
References.....	169
APPENDIX A Topology of Investigated HMMM	190
APPENDIX B Mathematical Model for VFMM.....	193
APPENDIX C Test Platform for Experimental Validation.....	194

NOMENCLATURES

Symbol	Meaning	Unit
f	Frequency of inverter output voltage	Hz
i	General current of machine	A
i_a	A phase current	A
i_b	B phase current	A
i_c	C phase current	A
I_c	Characteristic current	A
i_{cn}	Characteristic current ratio	/
i_d	d -axis current	A
i_{dM}	d -axis output current of MTPA control	A
i_d^*	Reference d -axis current	A
I_m	Current limitation	A
$i_{mag.}$	Magnetizing current pulse	A
i_s	dq -axis current vector summation	A
I_s	Amplitude of dq -axis current vector summation	A
i_q	q -axis current	A
i_{qM}	q -axis output current of MTPA control	A
i_q^*	Reference q -axis current	A
L_d	d -axis inductance	H
L_q	q -axis inductance	H
p	Pole pair number	/
R	Winding resistance	Ω
T_e^*	Reference electromagnetic torque	Nm
T_e	Actual electromagnetic torque	Nm
T_{e_pms}	Electromagnetic torque under present MS	Nm
T_{e_tms}	Electromagnetic torque under target MS	Nm
u	General voltage of machine	V
u_α	α -axis voltage	V
u_β	β -axis voltage	V
u_d	d -axis voltage	V

U_{dc}	DC-link voltage	V
u_q	q -axis voltage	V
V	Voltage amplitude of inverter output	V
V_m	Voltage limitation	V
V_{MS}	Available voltage for MS manipulation	V
V_S	Amplitude of dq -axis voltages vector summation	V
ω	Electrical angular speed	rad/s
ω_m^*	Reference mechanical angular velocity	rad/s
ω_m	Actual mechanical angular velocity	rad/s
θ	Electrical angle	rad
λ	Threshold of electromagnetic torque	/
Δi_d^*	Output of flux-weakening control	A
Δi_q	Compensated q -axis current pulse	A
ψ_m	Rotor PM flux linkage	Wb
$\psi_m(i_{mag.})$	PM flux linkage in VFMM	Wb
$ \psi_s^* $	Reference flux linkage	Wb
$ \psi_s $	Actual flux linkage	Wb

LIST OF ABBREVIATIONS

AC	Alternating current
AlNiCo	Aluminium nickel cobalt
BEMF	Back electromotive force
BLAC	Brushless alternating current
BLDC	Brushless direct current
DC	Direct current
DG	Demagnetization grid
DP	Demagnetization point
DTC	Direct torque control
FB	Feedback
FEM	Finite-element method
FF	Feedforward
FOC	Field-orient control
FW	Flux weakening
HCF	High coercivity force
HFI	High frequency injection
HM	Hysteresis model
HMMM	Hybrid magnet memory machine
IPM	Interior permanent magnet
LCF	Low coercive force
LPF	Low pass filter
LUT	Look-up table
MCP	Magnetizing current pulse
MEC	Magnetic equivalent circuit
MS	Magnetization state
MTPA	Maximum torque per ampere
MTPV	Maximum torque per voltage
NdFeB	Neodymium iron boron
PM	Permanent magnet
PMSM	Permanent magnet synchronous machine
PI	Proportional-integral

PID	Proportional–integral–derivative
PWM	Pulse width modulation
RMS	Root mean square
SmCo	Samarium cobalt
SPM	Surface mounted permanent magnet
SVPWM	Space vector pulse width modulation
UCGF	Uncontrolled generator fault
UD	Unintentional demagnetization
VFMM	Variable flux memory machine
V/f	Voltages per hertz

CHAPTER 1 GENERAL INTRODUCTION

1.1 Introduction

In human modern life and production processes, energy demand is indispensable everywhere. With the gradual improvement of human living standards, the demand for energy is increasing, and the issue of energy shortage will have a significant adverse impact on the development of human society nowadays. Therefore, developing clean energy and renewable energy and implementing energy-saving technologies have become more and more important. The development of new energy has increased the range of available energy sources, while the research on energy-saving technologies has improved energy utilization efficiency, reducing not only energy consumption but also environmental damage during the energy consumption process, in which the brushless permanent magnet synchronous machines (PMSMs) play a critical role due to the advantages of high efficiency, high torque and power density [ZHU07]. Traditional PMSM uses rare earth permanent magnets (PMs) with high remanence and high coercivity force (HCF) to improve machine performance, such as neodymium iron boron (NdFeB) magnets [JAH84] [HON10] [SEK13]. The magnetization state (MS) of a PMSM, that is the magnetization level of the PMs, is difficult to change, and the back electromotive force (BEMF) of PMSM is directly proportional to the speed. Considering the voltage limitation of the inverter DC bus, the speed range of PMSM is limited.

In order to achieve wide speed regulation operation of PMSM, the flux weakening (FW) control is usually adopted in high-speed region for PMSM [SNE85] [JAH86] [JAH87] [MAC91] [JAH94] [MOR94] [SON96] [KIM97a] [KIM97b] [BAE03] [KWO07] [KWO08] [ZHU00]. The FW control of PMSM refers to reducing BEMF of the machine by applying negative i_d on the d -axis armature current of the synchronous rotation coordinate system of the machine. However, this also brings shortcomings for PMSM: (1) Continuous FW current brings additional copper loss, increases machine heating, and reduces the efficiency in the high-speed region of the machine; (2) When the inverter capacity is constant, the increase of FW current leads to a decrease in q -axis current, resulting in a rapid decrease in electromagnetic torque; (3) The negative FW current will bring a risk of demagnetization of the PM; (4) There is a risk of failure in FW control. Once the BEMF suddenly increases during high-speed region, it can cause damage to the inverter.

To solve the problems above, Ostovic, a German scholar proposed the concept of variable flux

memory machine (VFMM) [OST03]. The variable air-gap flux can be achieved by injecting a current pulse to magnetize the low coercive force (LCF) PMs, and the MS can be “memorized” after the current pulse withdrawn, which allows the FW control current to be significantly reduced and the corresponding losses to be minimized. Then, the efficiency can be further improved. Therefore, more and more scholars have begun to devote themselves to the research on the related topics [YAN18b], including many VFMM topologies [YU11b] [ZHU17] [LIU23] [HUA19a] [HU20b] [HUA19b] [ZHO16] [ZHA18] [YAN20] [YAN19c] and advanced control strategies [CHE20] [YAN18] [HU21] [LYU20a] [TAK18] [YAN19b] [HUA17a] [CHE22] [ZHO22a] [ZHO22b] [LYU23] [ZHO23a] [ZHO24] [ZHO23c].

This thesis will focus on developing novel control strategies for VFMMs.

This chapter will review the achievements on VFMM including the machine topologies and control methods in the last 20 years with state-of-the-art research. Section 1.2 will present the PM machines and control methods. Section 1.3 will review the VFMM topologies. Section 1.4 will introduce the modelling methods for VFMM. Section 1.5 will review the existing control methods for VFMM. Finally, the research scope and major contributions of this thesis will be illustrated in Section 1.6.

1.2 Permanent Magnet Machines and Control Methods

1.2.1 Permanent Magnet Machines

In 1821, Faraday discovered that an energized conductor could rotate around a permanent magnet, successfully converting electrical energy to mechanical energy for the first time, and established a laboratory model of the machine, which is considered as the world's first PM machine. In the mid-20th century, with the emergence and continuous improvement of performance of aluminum nickel cobalt (AlNiCo) and ferrite permanent magnets, various new types of PM machines continued to emerge and were widely used. With the improvement of high-temperature resistance and price reduction of NdFeB materials, NdFeB PM machines have been increasingly widely used in industrial applications and daily life. The variety and application fields of PM machines are constantly expanding.

According to the position of the PMs on the rotor, PM machines can be divided into:

a) Surface mounted PM (SPM) machine: The PMs are usually in the shape of a tile and located on the outer surface of the rotor core. In the synchronous reference frame, the main inductances of the d -axis and q -axis are equal, i.e., $L_d = L_q$, where L_d and L_q are the dq -axis inductances,

respectively. SPM machine is called as non-salient pole PM machine, in which the reluctance torque that is affected by the difference between dq -axis inductances can be neglected.

b) Interior PM (IPM) machine: The PMs are located inside the rotor, and there are pole shoes made of ferromagnetic material on the outer surface of the PMs and inside the stator core, which can protect the PMs. For IPM machines, L_d is generally smaller than L_q . Therefore, IPM machine is salient pole PM machine, and the reluctance torque cannot be ignored.

The configurations of SPM and IPM machines are illustrated in Fig. 1.1.

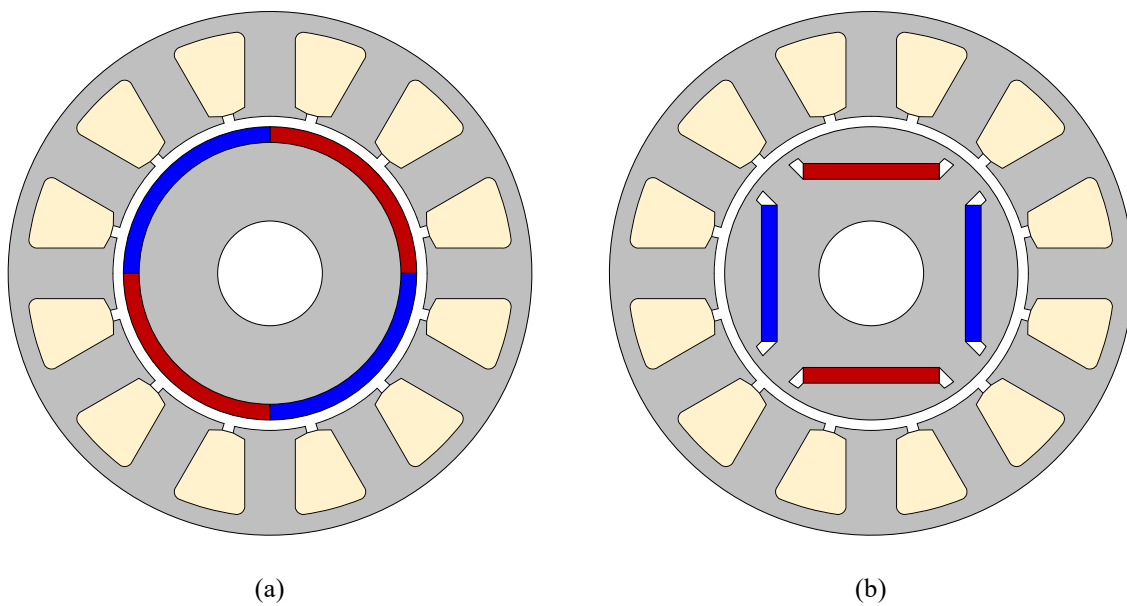


Fig. 1.1. Cross sections of PM machines. (a) SPM. (b) IPM [JAH87].

According to the relationship between the coil and tooth pitches of the stator windings, the PM machines can be classified as concentrated and distributed [ISH05] [NOG05] [HE22]. According to the driving currents, the PM machines can be divided into brushless alternating current (BLAC) and brushless direct current (BLDC) machines, where the BEMF waveforms are sinusoidal and trapezoidal, respectively [JAH84]. Generally, the BLAC drive is more popular for applications in industries and modern transportations, such as high speed train, electric vehicle, e.g. [ZHU07]. The classifications of PM machines are illustrated in Fig. 1.2. The BLAC machines with SPM and IPM rotors are also called as PMSMs, which are more popular and have attracted more researchers devoted themselves to the related topics [BIN06] [OU21] [HE21] [WU09] [LIU16] [LIU19] [FAN19].

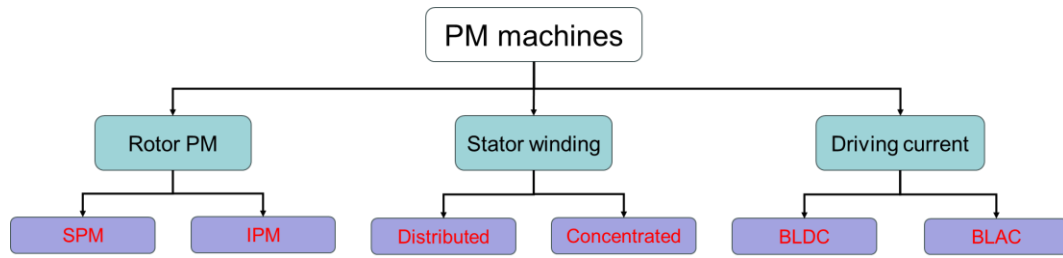


Fig. 1.2. Classifications for PM machines.

1.2.2 Control Methods

Generally, there are three basic control methods for PM machines, constant volts per hertz (V/f) control, direct torque control (DTC), and vector control (also called as field-oriented control (FOC)), as illustrated in Fig. 1.3.

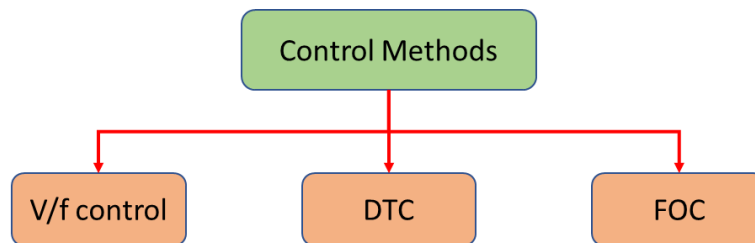


Fig. 1.3. Illustration of control methods for PM machines.

The V/f control method can be considered as an open loop control because it does not require the information of the rotor pole position [GAR98], where V refers to the voltage amplitude of the inverter output, and f refers to the frequency of the inverter output voltage. In industrial applications, the V/f control is frequently used due to its simplicity [SZA06] [ITO13] [LEE20].

DTC uses Bang-Bang control (hysteresis control) to generate drive signals to optimally control the switching state of the inverter to obtain high dynamic performance of torque. In DTC algorithm, the motor stator voltage and current are detected in real time, and the amplitudes of the torque and flux linkage are calculated and compared with the reference values of the torque and flux linkage respectively. Then, the resulting difference is used to control the amplitude of the stator flux linkage and the angle. The torque and flux linkage regulator directly outputs the required space voltage vector, thereby achieving the purpose of direct control of the flux linkage and torque. The basic principle of DTC is to directly select stator voltage vectors according to the differences between the reference and actual torque and stator flux linkage. The parameters of the machine are not used in the algorithm, except the stator resistance. Therefore, the DTC possesses advantages such as lesser parameter dependence and fast torque response when compared with the torque control via pulse width modulation (PWM) current

control [KAN95] [FRE96] [ZHO97] [TAN03] [LIU05] [ZHU06] [GUL07]. The scheme of a typical DTC drive system is illustrated in Fig. 1.4.

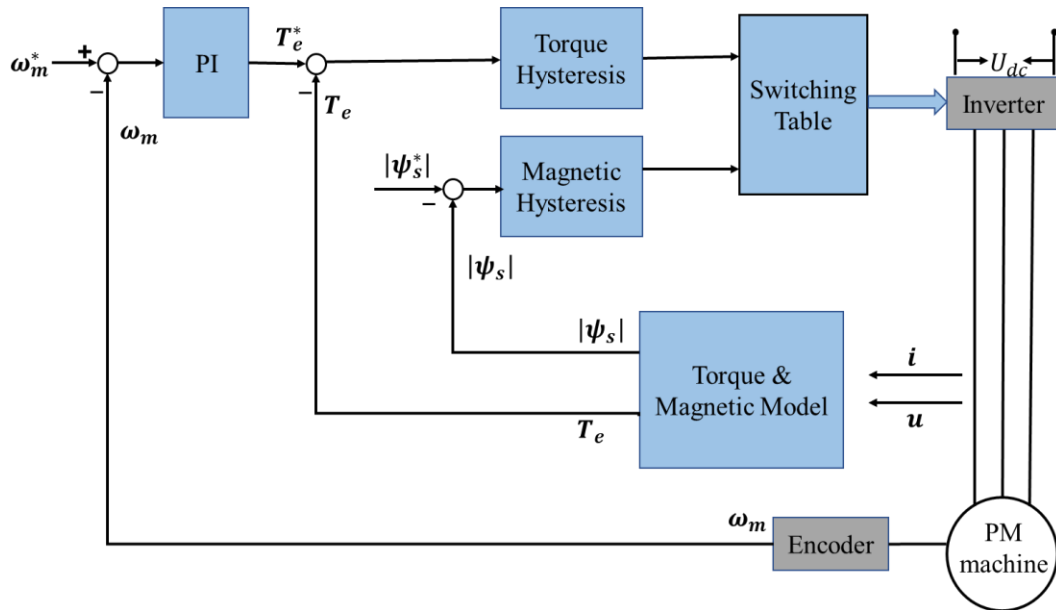


Fig. 1.4. Scheme of a typical DTC drive system [ZHO97].

where ω_m^* and ω_m are the reference and actual mechanical angular velocity, T_e^* and T_e are the reference and actual electromagnetic torque, $|\psi_s^*|$ and $|\psi_s|$ are the reference and actual flux linkage, i and u are the current and voltage from the machine, U_{dc} is the dc-link voltage.

FOC was proposed by F. Blaschke of Siemens in Germany in 1971. As a high-performance AC machine control method, the basic idea of FOC is to imitate the magnetic field orientation of DC machine. The direction of the rotor flux linkage is used as the reference direction of the rotating coordinate system. Based on this coordinate system, the stator current is decomposed into the stator current excitation component in the same direction as the rotor flux linkage and the stator current torque component orthogonal to the direction of the rotor flux linkage. These two components are orthogonal to each other and are controlled separately by controllers. FOC can obtain precise speed control, good torque response, and thus obtain operating characteristics similar to DC machines. Therefore, FOC is much more popular for PMSMs [KUM87] [PIL90] [SEN94] [SIL91] [JAH86] [JAH87] [JAH94] [LIU14d].

To better illustrate FOC, the mathematical model of PMSM is introduced first. For drive control, the conventional PMSM equations in dq -axis reference frame can usually be expressed as:

$$u_d = Ri_d + L_d \frac{di_d}{dt} - \omega L_q i_q \quad (1.1)$$

$$u_q = Ri_q + L_q \frac{di_q}{dt} + \omega L_d i_d + \omega \psi_m \quad (1.2)$$

$$T_e = 1.5p[\psi_m i_q + (L_d - L_q)i_d i_q] \quad (1.3)$$

where ψ_m , R , L_d , L_q , i_d , i_q , u_d , u_q , ω , p , and T_e are the rotor PM flux linkage, the winding resistance, the dq -axis inductances, the dq -axis currents and voltages, the electrical angular speed, the pole pair number of PMSM, and the electromagnetic torque, respectively.

The maximum voltage V_m that the inverter can supply to the machine is limited by the DC link voltage and the PWM strategy. Meanwhile, the maximum current I_m is determined by the inverter current rating and machine thermal rating. Therefore, the voltage and current of the motor have the following limits:

$$V_S^2 = u_d^2 + u_q^2 \leq V_m^2 \quad (1.4)$$

$$I_S^2 = i_d^2 + i_q^2 \leq I_m^2 \quad (1.5)$$

where I_S is the amplitude of the dq -axis current vector summation, V_S is the amplitude of the dq -axis voltage vector summation.

At steady state, neglecting the voltage drop of stator resistance, (1.1) and (1.2) can be expressed as

$$u_d = -\omega L_q i_q \quad (1.6)$$

$$u_q = \omega L_d i_d + \omega \psi_m \quad (1.7)$$

Then, the voltage constraint can be shown as:

$$(L_q i_q)^2 + (L_d i_d + \psi_m)^2 \leq \left(\frac{V_m}{\omega}\right)^2 \quad (1.8)$$

In Fig. 1.5, the maximum torque-per-current trajectory on the synchronously rotating dq -axis reference current plane is illustrated. The current trajectory is a circle centered at (0,0) and a radius of I_m . The voltage trajectory is an ellipse centered at $(-I_c, 0)$, the major axis radius is $V_m/(L_d * \omega)$, and the minor axis radius is $V_m/(L_q * \omega)$. As the speed increases, the voltage limit circle gradually shrinks.

$$I_c = \psi_m/L_d \quad (1.9)$$

where I_c is the characteristic current.

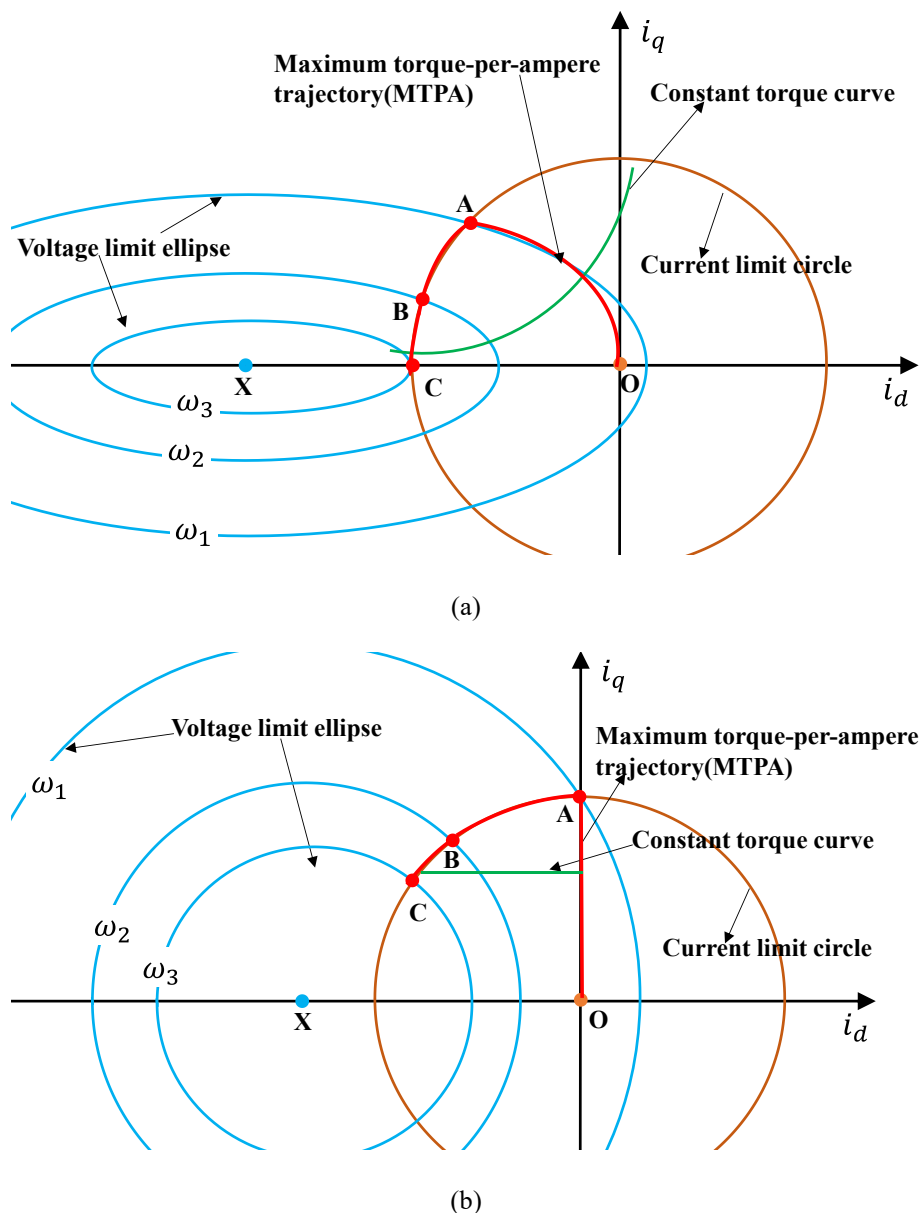


Fig. 1.5. Maximum power output current trajectory for PMSM. (a) Salient-pole PMSM ($L_d \neq L_q$). (b) Non-salient-pole PMSM ($L_d = L_q$). Speed: $\omega_1 < \omega_2 < \omega_3$.

The motor operation can be divided into three operating regions, but these three operating regions may not all exist. In [MOR90], a characteristic current ratio i_{cn} was used to distinguish the flux weakening region, which was defined as

$$i_{cn} = I_c / I_m \quad (1.10)$$

When the voltage constraint ellipses center is outside the current constraint circle, i.e., $i_{cn} > 1$, the machine has two operating regions. When the voltage constraint ellipses center is within the current constraint circle, i.e., $i_{cn} \leq 1$, the machine has three operating regions.

Operation zone 1: constant torque operation region

In this operating region, as the speed increases, the motor output torque can maintain the rated output torque. The machine operates inside the current constraint circle and the voltage constraint ellipse, i.e., $|I_S| < I_m$ and $|V_S| < V_m$. From zero speed to base speed, the maximum torque per ampere (MTPA) algorithm is usually adopted to make full use of the reluctance torque [MAC91] [MOR94]. i_d by considering the MTPA curve can be expressed as

$$\begin{cases} i_d = 0 & (L_d = L_q) \\ i_d = \frac{-\psi_m(i_d) + \sqrt{(\psi_m(i_d))^2 + 8(L_d - L_q)^2 i_s^2}}{4(L_d - L_q)} & (L_d \neq L_q) \end{cases} \quad (1.11)$$

where i_s is the input current of the MTPA control. Then, i_q can be expressed as

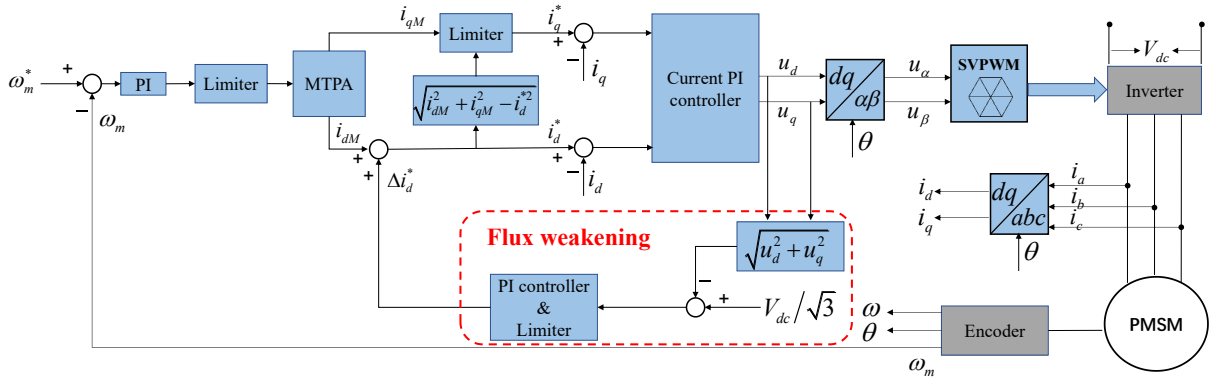
$$i_q = \sqrt{i_s^2 - i_d^2} \quad (1.12)$$

Operation zone 2: flux weakening operation region I

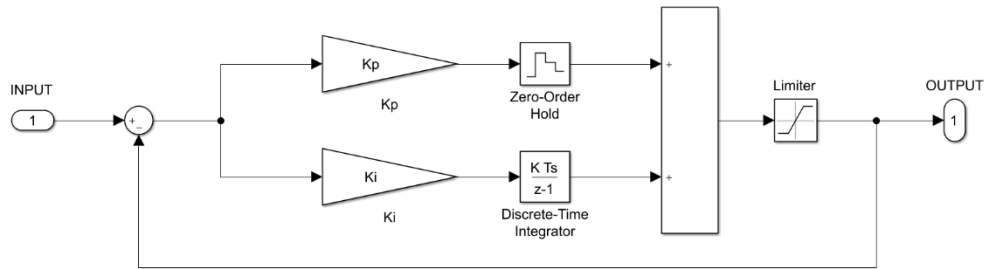
As the speed increases, when the speed reaches the base speed, the output voltage amplitude is equal to the voltage limit amplitude, i.e., $|I_S| = I_m$ and $|V_S| = V_m$, which is also called as flux weakening region I. At this time, due to the voltage limitation, the flux weakening current needs to be increased to extend the speed range. The judgment condition for switching from the operation zone 1 to the operation zone 2 is whether the inverter output voltage is saturated. Then, the machine operates on the intersection points of the current and voltage limits. The relationship between i_d and i_q on this curve by ignoring the stator resistance can be expressed as:

$$\begin{cases} i_d = \frac{-\psi_m(i_d) + \sqrt{\frac{V_m^2}{\omega^2} - (L_q i_q)^2}}{L_d} \\ i_d^2 + i_q^2 = I_m^2 \end{cases} \quad (1.13)$$

(1.13) is usually used in the feedforward flux weakening control method. The voltage magnitude feedback flux-weakening control method [KIM97b] with high robustness is illustrated in Fig. 1.6.



(a)



(b)

Fig. 1.6. Block diagram of field-orient control. (a) Feedback flux weakening control [KIM97b]. (b) PI controller.

where V_{dc} is the DC-bus voltage of the three-phase inverter, i_a , i_b , and i_c are the three-phase currents, respectively, ω_m^* is the reference mechanical angular velocity, ω_m is the real mechanical angular velocity, θ is the actual electrical angle, ω is the electrical angular speed, i_{dM} and i_{qM} are the MTPA control dq -axis currents, which can be obtained by (1.11) and (1.12), Δi_d^* is the output of the flux-weakening control, i_d^* and i_q^* are the reference dq -axis currents for the current PI control, i_d and i_q are the actual dq -axis currents, u_d and u_q are the voltages in dq -axis, u_α and u_β are the voltages in $\alpha\beta$ -axis. The “PI controller” is a conventional one, which contains the proportion part and the integration part, K_p and K_i are the corresponding parameters. This PI controller can be applied to all the control algorithm block in this thesis. The parameters differ according to the application. The “Limiter” is used to constrain the output of PI controller, which also differs by different application conditions.

Operation zone 3: flux weakening operation region II

This region exists only when $i_{cn} \leq 1$. In this region, the machine operates on the maximum torque per voltage (MTPV) region that inside the current constraint circle, i.e., $|I_S| < I_m$ and $|V_S| = V_m$, called as flux weakening region II. In this region, to maximize the torque capability

and further extend the operation speed range, the MTPV control strategy must be applied.

In [MOR90], the dq -axis currents for MTPV control can be obtained by

$$i_d = -E_0/X_d - \Delta i_d \quad (1.14)$$

$$i_q = \frac{\sqrt{(V_m/\omega)^2 - (X_d \Delta i_d)^2}}{\rho X_d} \quad (1.15)$$

where $E_0 = \omega \varphi_m / V_m$, $X_d = \omega L_d / V_m$, $\Delta i_d = \begin{cases} 0, & \dots \rho = 1 \\ \frac{-\rho E_0 + \sqrt{(\rho E_0)^2 + 8(\rho - 1)^2 (V_{max}/\omega)^2}}{4(\rho - 1)X_d}, & \dots \rho \neq 1 \end{cases}$,

$\rho = L_q / L_d$.

1.3 Memory Machines

Since the flux weakening current must be applied to extend the speed range for PMSMs as aforementioned, the efficiency of the machine will be affected. To further improve the efficiency of the drive systems, a new concept of variable flux memory machine (VFMM) was proposed by Ostovic [OST03]. As shown in Fig. 1.7, a spoke-type PM machine is converted into VFMM, which features a sandwiched rotor consisting of tangentially magnetized LCF PMs, soft irons, and non-magnetic barriers. The MS of LCF PMs can be smoothly adjusted by injecting d -axis magnetization current pulse in the stator armature windings. Thus, the variable flux property of air-gap field can be achieved. The flux barriers are designed to block the q -axis flux and thus reduce the risk of UD of LCF PMs.

The adoption of LCF PM offers a special characteristic for the machine: the magnetization level can be adjusted by a current pulse and memorized after withdrawing the current pulse, which can avoid the continuous d -axis current to extend speed range and reduce the additional losses. This can improve the efficiency of the whole machine drive system. This significant property of VFMM has attracted the attention of more and more scholars.

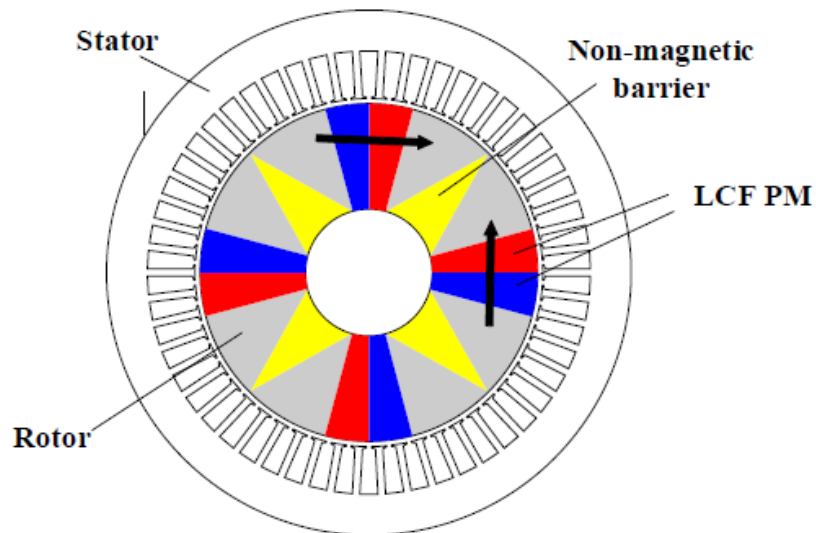


Fig. 1.7. First proposed VFMM in [OST03].

In the past two decades, VFMMs have developed rapidly, and attracted more and more attentions by scholars and manufactures worldwide. A variety of machine topologies belonging to the VFMMs were proposed and investigated, they all featured the capability of air-gap flux adjustment. In [YAN18b], the recent advance developments in VFMM were overviewed, including the diverse machine topologies and advanced control methods. Fig. 1.8 illustrates the classification of the existing VFMMs according to the PM locations and magnetic coupling between the LCF PM and the HCF PM.

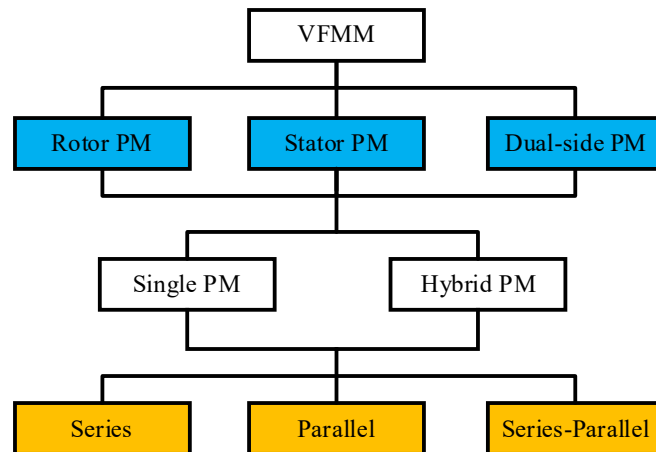
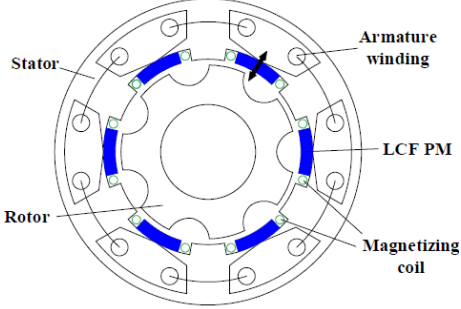
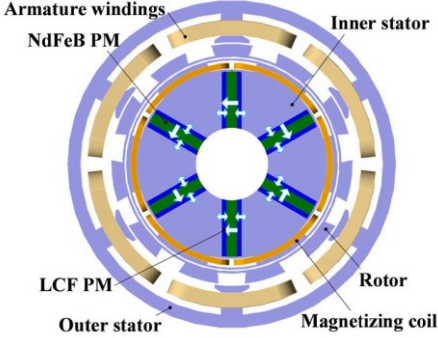
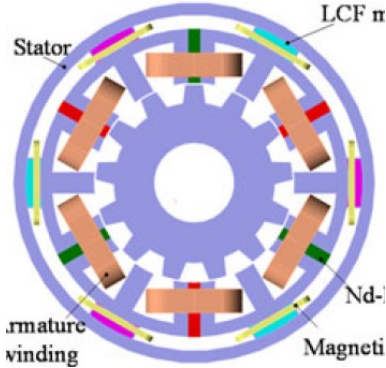
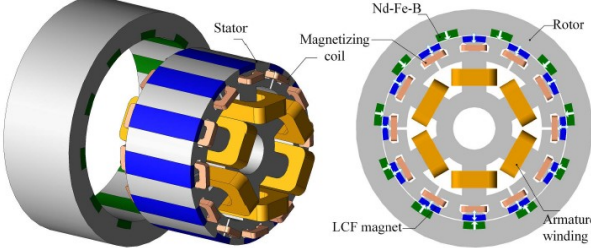


Fig. 1.8. Classification of the existing VFMMs.

The classification of VFMM topologies based on the PM-location and PM-coupling is shown in Table 1.1, the example of topology is marked red in the references.

Table 1.1. Classification of VFMM topologies.

PM-location	PM-coupling	Topology example	References
Rotor-PM	Single		[OST02] [OST03] [LIU08] [LIU09] [LIU10] [KAT14] [IBR15a] [IBR15b] [SUN15] [SAK13] [JIA15] [SOU22]
	Series		[SAK09] [YAN18c] [ZHA21] [SAK20] [HUA17a] [ZHU17] [ZHA18] [YAN19c] [XU21] [WAN15a] [SAK11]
	Parallel		[CHE05] [SAK09] [WU14] [ZHO16] [WAN19] [CHE09] [HU20b] [TSU21] [ZHE19]
	Series-parallel		[ATH17] [HUA19a] [YAN20] [YAN21] [YAN22] [LIU22] [SAK21] [QIA21]

	Single		[GON09] [YU11a] [YU11b] [YU15] [YAN14a] [YAN16g] [YAN16a] [YAN14b]
Stator-PM	Series		[LI14] [YAN14c] [YAN19a]
	Parallel		[LI11a] [LI11b] [LIU14a] [YAN16d] [LI21] [YAN16c] [YAN16b] [YAN17b] [YAN16e] [YAN18d] [YAN16f] [YAN18e] [YAN17c] [JIA22] [YAN17d]
	Magnetic-gearing effect		[LIU14b] [YAN14c] [WAN15b] [YAN16h] [YAN18g]

To illustrate the tradeoffs of various rotor-PM VFMM, the key characteristics of the conventional series, parallel, and series-parallel VFMMs are compared as listed in Table 1.2. Besides, a comprehensive comparison between the series coupling and parallel coupling in VFMM has been conducted in [ATH17] [HUA19a], which found that parallel coupling

requires lower current to achieve intentional demagnetization, while the remagnetizing current is lower in series coupling due to the help of the HCL PMs. In general, the flux variation range is wider in parallel coupling machine, while series-type is more advantageous in improving the torque density due to the improvement of the working point of LCF PMs. Thus, the series-parallel VFMMs can reach a balanced tradeoffs between the series - and parallel -VFMMs.

Table 1.2. Comparison of series-, parallel-, and series-parallel-type rotor-PM VFMMs.

Types	Series	Parallel	Series-parallel
Torque capability	●	○	●
Flux regulation range	○	●	◐
Max. magnetizing current level	○	◐	●
On-load demagnetization	●	○	●
Structure simplicity	●	◐	◐

●: excellent, ◐: medium, ○: poor

1.4 Modelling of Memory Machines

1.4.1 Magnetic Properties

To achieve stable performance in conventional PM machines under normal conditions, the constant PMs have a linear demagnetization region which superimposes a recoil line. These PMs have high coercivity and do not undergo irreversible demagnetization issue under normal operating conditions. Conversely, LCF PMs such as AlNiCo have low coercivity and therefore, cannot be used in conventional PM machines where high coercivity magnets is required such as NdFeB and Samarium Cobalt (SmCo). While, in VFMMs, the properties of LCF PMs can be well utilized as presented below [XIE20a]:

- 1) The magnetization level of LCF PMs can be easily adjusted by a current pulse. After the current pulse is removed, the magnetization level can settle down on a certain level, which is called as memorizing magnetization level. This property is based on the nonlinear demagnetization curve
- 2) The magnetization level can be regulated online in VFMM, which is hardly achieved in conventional PM machines [LYU20a].

The operating points of the LCF PM are determined by the intersections of recoil line and load

line depicted on the H-axis as presented in Fig. 1.9. Consequently, by applying different remagnetizing or demagnetizing current pulses in LCF PMs, the operating points can be adjusted along the preset recoil lines. For example, at the beginning, the operating point is at P_1 . When a demagnetizing current pulse is injected, the operating point will move to F and G as shown in Fig. 1.9. After the demagnetizing current pulse is withdrawn, the operating point will move along another recoil line and settle down at the new operating point P_2 . Conversely, when injecting a remagnetizing current pulse, the operating point will move along the trajectory of P_2 -C-D-E-B and return to P_1 .

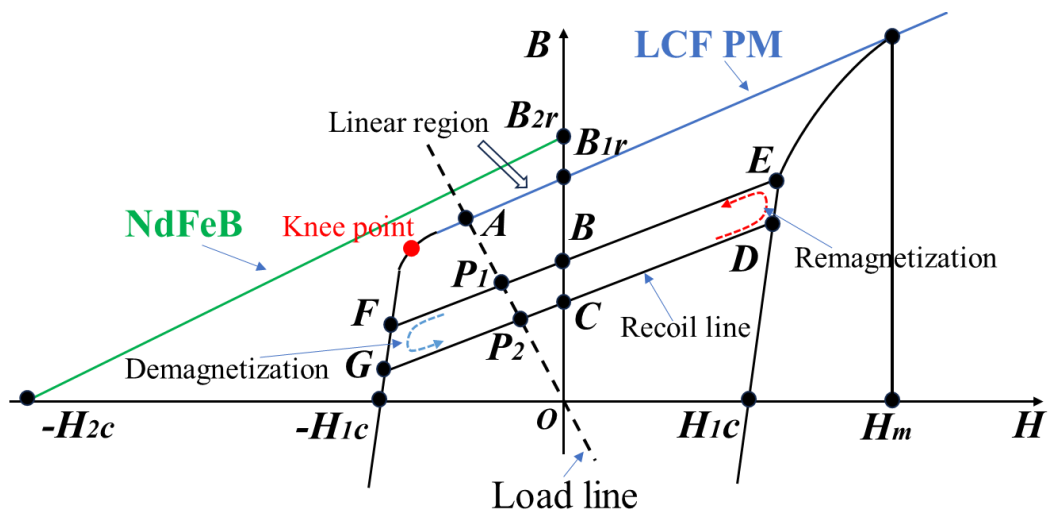


Fig. 1.9. Illustration of hysteresis characteristic of HCF PM and LCF PM.

There are also other magnet materials such as Ferrite and SmCo PMs can be applied in VFMM. Their hysteresis curves are depicted in Fig. 1.10, and their characteristics are listed and compared in Table 1.3.

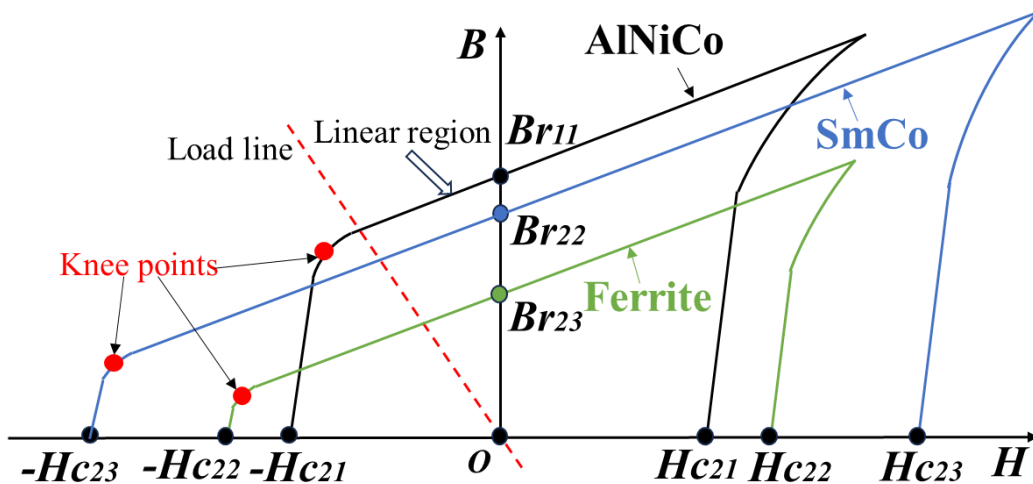


Fig. 1.10. Hysteresis curves of three LCF PMs.

Table 1.3. Comparisons of PM materials [WAN19].

PM materials	Remanence (T)	Coercive force (kA/m)	Maximum energy product (kJ/m ³)
AlNiCo9	1.05	111	72
Ferrite Y40	0.44~0.46	330~354	37.6~41.8
SmCo 066805	0.7	318	80
NdFeB N45UH	1.32~1.36	979	342~366

1.4.2 Modelling Methods

In the existing literature, three common modelling methods were presented: Hysteresis Model (HM), Magnetic Equivalent Circuit (MEC), and Finite-element Method (FEM), as shown in Fig. 1.11.

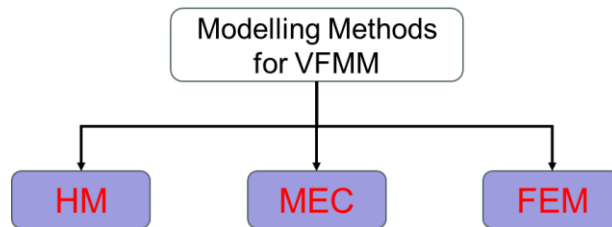


Fig. 1.11. Modelling methods for VFMM.

- **Hysteresis model (HM)**

To achieve better controllability of PM flux linkage in VFMMs, the hysteresis relationship should be modeled precisely. The remagnetization and demagnetization properties of LCF PMs has been modeled by different methods such as Frolich model, Presaich model, and piecewise linear model.

[YAN17a] developed a new virtual linear hysteresis model to rapidly identify the on-load demagnetization effect as shown in Fig. 1.12, which can be regarded as the extended line of the upper recoil line of the LCF PM. In this case, LCF PM can be considered as a magnet with a linear reversible demagnetization characteristic.

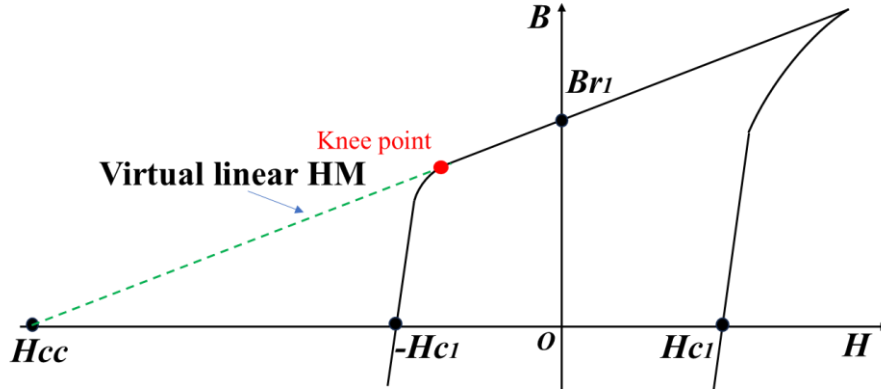


Fig. 1.12. Schematic of virtual linear hysteresis model.

In [WU19], a piecewise-linear hysteresis model for LCF-PM was proposed as depicted in Fig. 1.13. The HM of LCF PM is divided into several minor loops, during the MS manipulation, the operating point of the LCF PM moves along a hysteresis curve where it tracks the major BH-loop, and then moves back along the minor loop. It is assumed that the coercivity value of the major hysteresis loop and all the minor hysteresis loops are the same, while the remanence values are different. Therefore, the LCF PM can be partially magnetized.

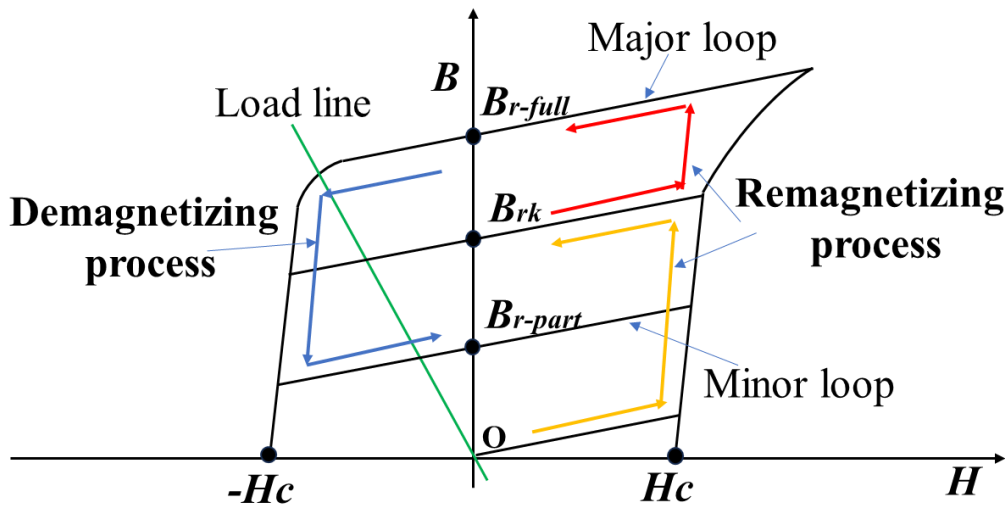


Fig. 1.13. Piecewise-linear hysteresis model of LCF-PM.

- **Magnetic equivalent circuit (MEC)**

Based on the PM magnetic circuits of VFMM, the MEC can be divided into parallel circuit and series circuit as shown in Fig. 1.14., the main flux through the air gap in the parallel circuit is the sum of two parallel branches, as shown in Fig. 1.14(a) [CHE05] [ZHO16] [WU14].

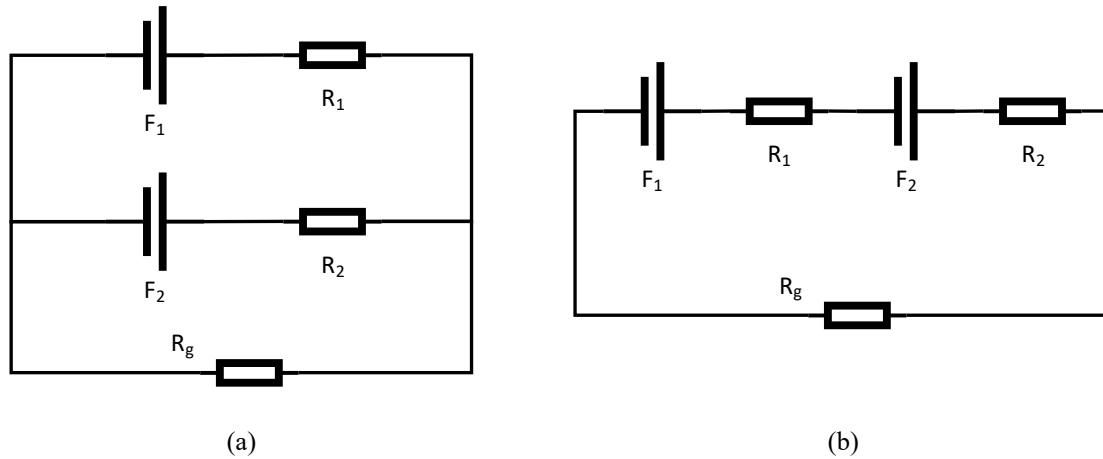


Fig. 1.14. Equivalent magnetic circuits of hybrid VFMM: (a) Parallel hybrid VFMM. (b) Series hybrid VFMM.

Conversely, in the series hybrid circuit [SAK09] [HUA17a] [ATH17], the flux linkage flows forward through constant PMs and variable PMs as shown in Fig. 1.14(b). Hence, the constant PM flux linkage always assists the variable PMs for stabilizing the operating points of the variable PMs. In [SON17], the MEC modelling method for VFMM was illustrated in detail, the magnetic-field intensity H_m within the PM was calculated. Accordingly, the PM operating point was equivalently expressed as a point on the B – H curve of the PM.

- **Finite-element method (FEM)**

[YU11b] combined the time-stepping FEM analysis method with a piecewise-linear hysteresis model to analysis a kind of DC-excited memory motors, both steady-state and transient performances. [ZHU11] utilized the same method to analysis the stator-PM doubly salient flux memory motor.

In [LEE08], the magnetic characteristics of permanent magnets in VFMM was analyzed by using a coupled FEM and Preisach modeling. In [GE18], the FEM was adopted to calculate the total PM torque and individual PM torques produced by different PMs, which was utilized to analyze the torque components separately.

1.5 Control of Memory Machines

Since the variable MS brings an extra freedom for the control of VFMM, the MS control becomes the crucial point in the control algorithm. The control of MS includes MS estimation and MS manipulation. The MS control for VFMM is illustrated in Fig. 1.15.

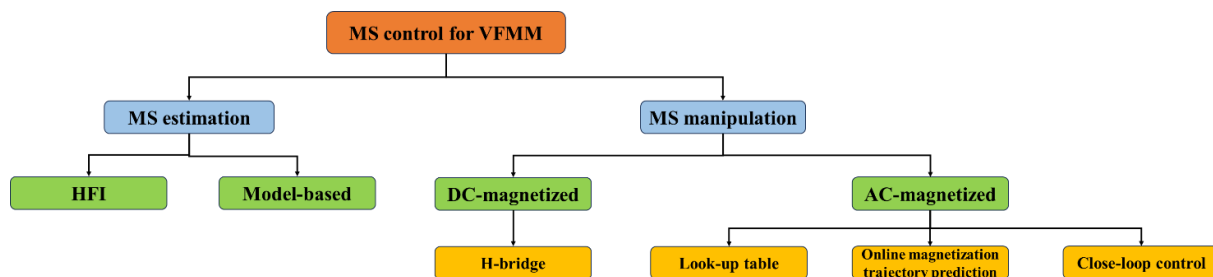


Fig. 1.15. Schematic of MS control for VFMM.

1.5.1 Magnetization State Estimation

Since MS control is crucial for VFMM, the MS online estimation under different loads and speed can improve the efficiency of MS manipulation. The PM flux linkage can be tested offline, and under this condition can be regarded as the MS since the machine is not operating. However, when the machine is operating, the measurements of MS by equipment are not easy. Besides, the PM flux linkage is also affected by the dynamic operating conditions. Therefore, the accurate estimation methods of the MS under different loads and in the whole speed range are highly desirable for VFMM.

The MS estimation methods in [YAN18f] [JIA15] [SAK11] [SAK09] [CHE05] [ZHO16] [WU14] can be classified as two main methods: high frequency injection (HFI) [JIA15] based method and model-based method [WU14].

- **HFI based MS estimation**

The MS estimation method of HFI based-method estimating the PM flux linkage mainly have two solutions: the d -axis high-frequency inductance [SAK11] variable with saturation levels, and the PM electrical high-frequency resistance [JIA15] [ZHO16], which changes under different MSs due to the magneto resistive effects. Magneto resistance is defined as a material's resistivity changing with the application of a magnetic field. The advantage of this method is it can be used in the whole speed range and including the standstill state. [JIA15] investigated the MS estimation using the magneto resistive effect. [ZHO16] analyzed the magneto resistive effect for three kinds of PM material: SmCo, ferrite magnets and NdFeB, which illustrated that the controlled demagnetization and unintentional demagnetization can be distinguished by the estimated high frequency resistance.

- **Model based MS estimation**

BEMF estimation is usually adopted in the model-based method to estimate MS, which estimates the stator flux linkage values by the machine terminal voltages and currents. This

must be applied during the machine operating. In this case, estimating the MS for the machine at standstill cannot be realized. Besides, the parameters of the machine including dq -axis inductances, stator resistance are needed to improve the MS estimation accuracy [SAK09].,

1.5.2 Magnetization State Manipulation

There are two main strategies for the control method of MS for VFMMs based on the machine magnetized type: the DC-magnetized machines and the AC-magnetized machines [JAY19].

DC-magnetized VFMMs need extra DC magnetizing coils to achieve the MS control. By applying the magnetizing current pulse, a field can be imposed on the PMs to remagnetize and demagnetize the MSs. To achieve the MS control, H-bridge converter is usually equipped to control the magnetizing current pulse.

- **H-bridge converter**

The flux controller of VFMM is different from the conventional one, since it needs to produce a temporary current pulse, controllable in both magnitude and direction. In [YU11b] [YANG14], the magnetizing current pulse controller consisted of a buck converter and an H-bridge converter as illustrated in Fig. 1.16, where the former functions to control the magnitude of the magnetizing current and the latter serves to control the direction and duration of the magnetizing current.

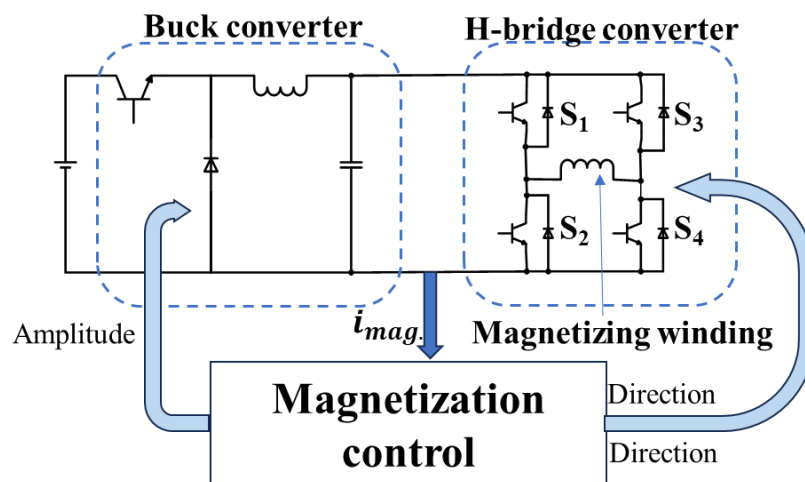


Fig. 1.16. MS control by H-bridge converter.

In [YAN19b], the MS control circuit based on the H-bridge converter was adopted to study the MS characteristics of a VFMM. The current pulse close-loop control method is combined with the generated PWM signals. As a result, the current pulse of the required amplitude and direction is obtained effectively.

Fig. 1.17 shows the control block diagram based on the MS control method, which mainly consists of the armature winding controller, the MS controller, and the PM flux linkage observer. The armature winding controller utilizes the traditional outer speed loop and inner current loop control.

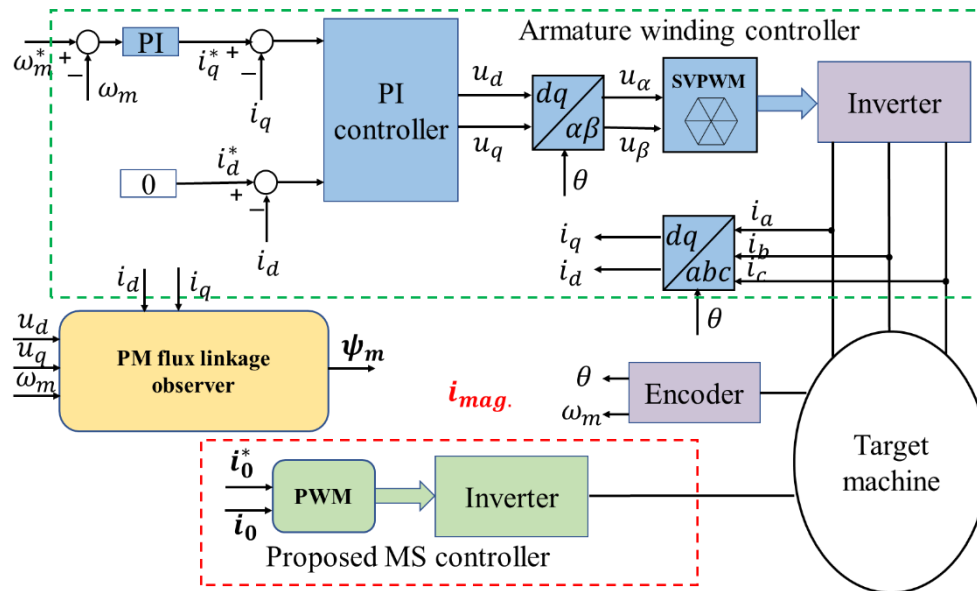


Fig. 1.17. Control block diagram in [YAN19a].

In [YAN19b], for the constant-torque region, the control method for the investigated machine was similar to that for the conventional PM machines. Due to the unity saliency ratio, the $I_d = 0$ control is utilized. On the other hand, the conventional FW control and PM demagnetization control are combined in the constant power region. The overall block diagram of the proposed control strategy is shown in Fig. 1.18. The block of L&R means inductance and resistance. The control circuit mainly includes two modules, i.e., drive and FW control modules; the former is based on a space vector pulse width modulation (SVPWM) and the latter adopts a negative feedback control. The core part of the magnetization control circuit is a single-phase H-bridge converter similar to the PWM chopper [LIU14d]. The amplitude of the current pulse can be regulated by means of a single current close-loop control.

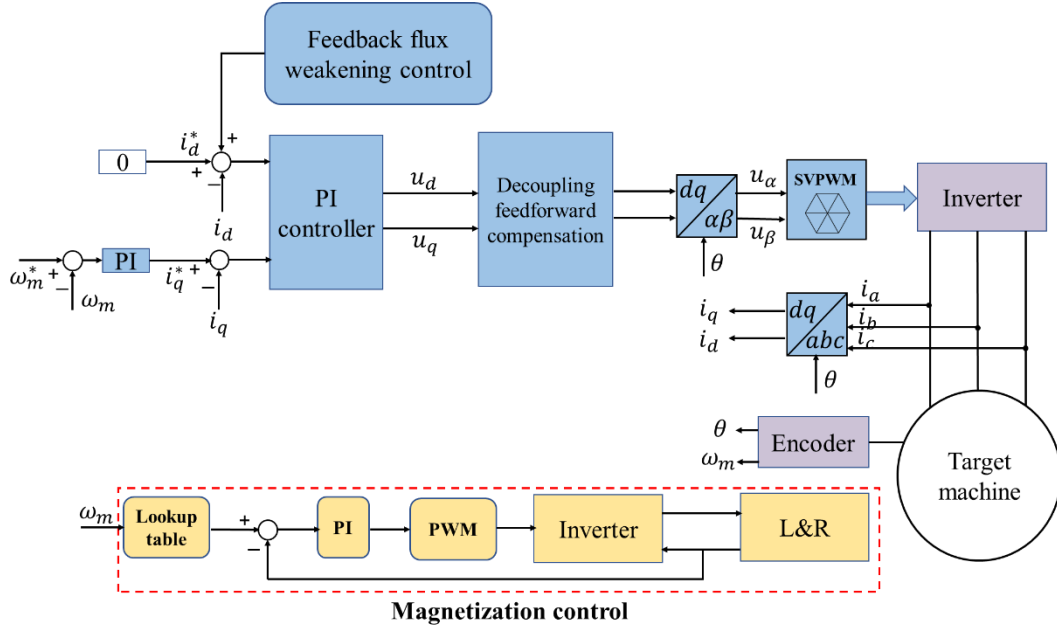


Fig. 1.18. Overall block diagram in [YAN19b].

In AC-magnetized VFMM, the stator winding currents can be utilized to achieve demagnetization and remagnetization for the MSs, in which the d -axis current dominates the effect. Therefore, the magnetizing current pulse is usually injected into the d -axis current. This type is much more popular in the existing research due to without requiring extra equipment [YAN18a] [LYU20a] [CHE20] [LYU20b] [YU14] [HU21] [MAE14] [GAG14] [GAG16] [ZHO22a] [ATH18] [ZHO23b] [MAS15] [JIA22b]. There are three kinds of MS control methods for AC-magnetized VFMM: Look-up table (LUT) [LYU20b], Online magnetization trajectory prediction [CHE20] [YU14] [GAG14], and Close-loop control [MAE14] [GAG16] [ATH18].

- **Look-up table method**

[LYU20b] proposed a novel MS selection method utilizing LUT for VFMM to guard against the overvoltage during uncontrolled generator fault prevention as well as extend the operation region of the machine.

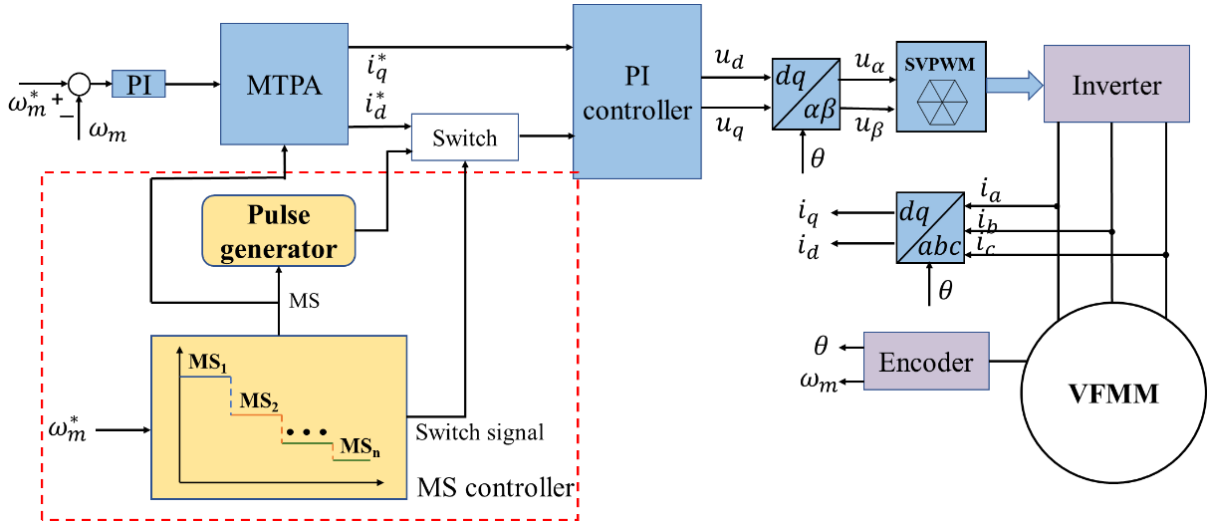


Fig. 1.19. Schematic diagram of MS selection method in [LYU20b].

Fig. 1.19 shows the schematic diagram of the proposed MS selection method for VFMM in [LYU20b]. Since VFMM is still a kind of PM machines, the FOC is also applied to VFMM. In the MS selection method, there are two modes: normal operating mode and magnetizing mode. When the machine operates in the normal mode, an MTPA controller is utilized based on the LUT as shown in Fig. 1.20 to make full use of the reluctance torque at low speed region for the VFMM. The machine under different MSs have different parameters such as PM flux linkage and dq -axis inductances, therefore, three separated sub-blocks are built in the MTPA controller. The sub-block is built by two-dimension, which contains the information of dq -axis currents and the torque and speed under each MS. To improve the efficiency of the control method, the information in the LUTs is tested in advance in the laboratory. During the operating of the machine, the sub-block is operating based on the present MS in the constant torque region. As a result, the dq -axis reference currents will be obtained from the LUTs according to the present torque and speed detected from the control system. In addition, a MS controller is utilized to achieve the MS manipulation for the machine. When a MS manipulation command is received, the operating mode will switch from the normal mode to the magnetizing mode according to the signal from the MS controller. And the target MS can be obtained based on the LUT which contains the target speed. Then, based on the correlation of MS and d -axis magnetizing current pulse, the pulse generator will generate a corresponding d -axis magnetizing current pulse to inject into the current controller to achieve the MS manipulation.

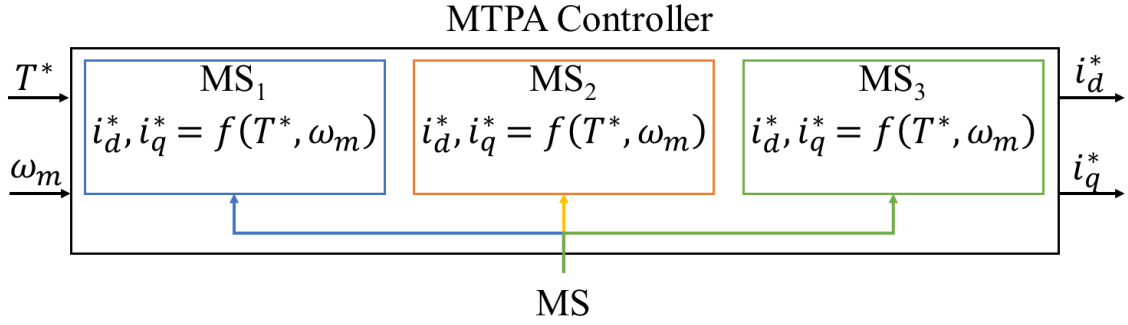


Fig. 1.20. Schematic diagram of MTPA controller.

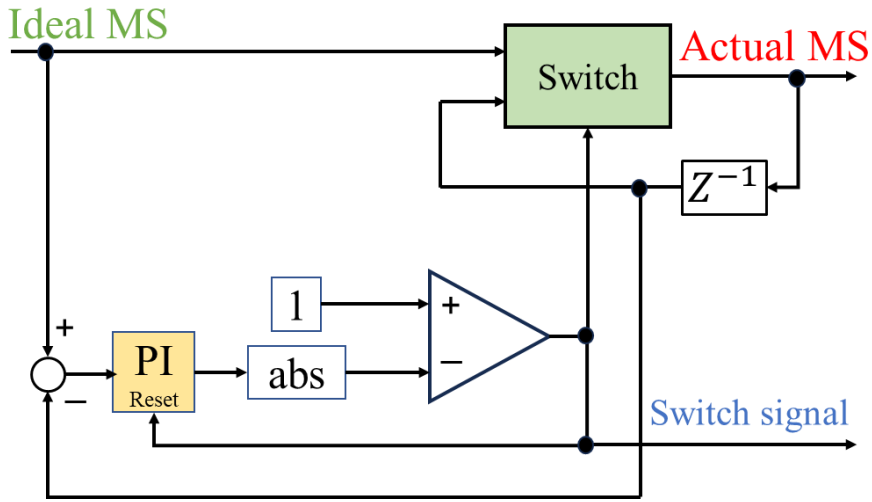


Fig. 1.21. Illustration of proposed MS hysteresis controller in [YAN16f].

In the MS control method, as the speed is utilized as the condition for MS manipulation, when the machine operates near the boundary speed between two neighboring MSs, the MS may be manipulated repeatedly, which will have bad impact on the control system and increase the MS manipulation times and will bring extra losses. To avoid this kind of issue, a hysteresis controller was proposed in [YAN16f] during MS manipulation as shown in Fig. 1.21. When the ideal MS command is generated according to the machine operating speed, the difference between the ideal MS and the actual MS can be obtained and will be sent to a proportional-integral (PI) controller. When the output of the PI controller achieves the preset threshold, the MS manipulation command will be sent to the pulse generator to achieve the MS manipulation. The PI controller will be reset. Therefore, the frequency of the MS manipulation can be effectively reduced by the MS hysteresis controller.

- **Online magnetization trajectory prediction**

In [CHE20], an online current trajectory prediction and control method for the magnetization current in a VFMM was proposed as presented in Fig. 1.22.

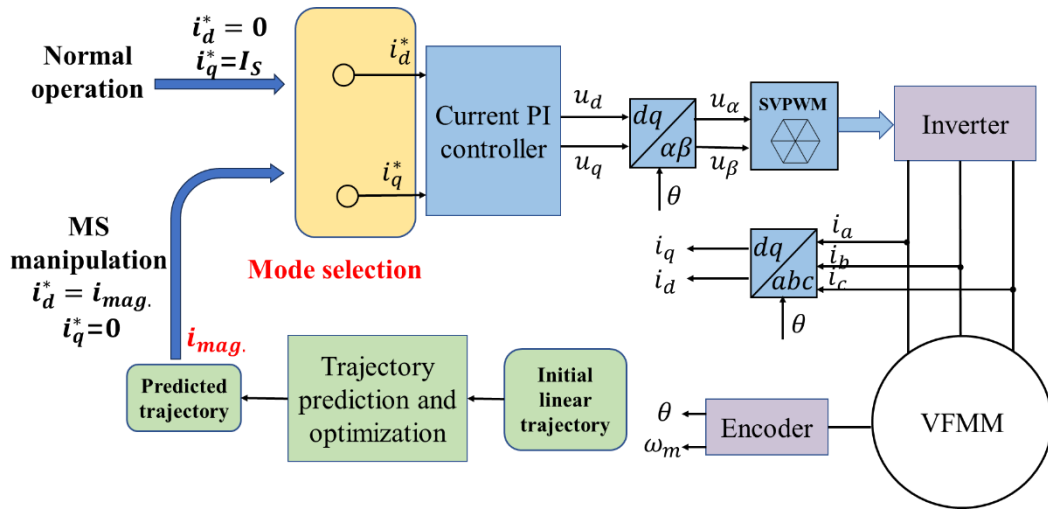


Fig. 1.22. Trajectory prediction and FOC-based machine control system in [CHE20].

The machine speed and the DC-link voltage are two of the major concerns in the MS manipulation trajectory prediction. The MS manipulation can be executed at different speeds. Moreover, the DC-link voltage can be variable in certain applications, e.g., electric vehicles using battery to feed the DC voltage. The battery voltage is variable due to discharge level and operating temperature. These two aspects affect the machine voltage and cause different manipulation trajectories.

The DC-link voltage, the machine speed, and the d -axis current are measured and used in the trajectory prediction algorithm, so that the predicted trajectory can be adjusted according to different machine operating conditions. The trajectory is then transferred to the mode selection to determine whether the machine is controlled in normal operation or the MS manipulation. During the MS manipulation, the d -axis current command is replaced by the predicted trajectory, and q -axis current command is set by zero.

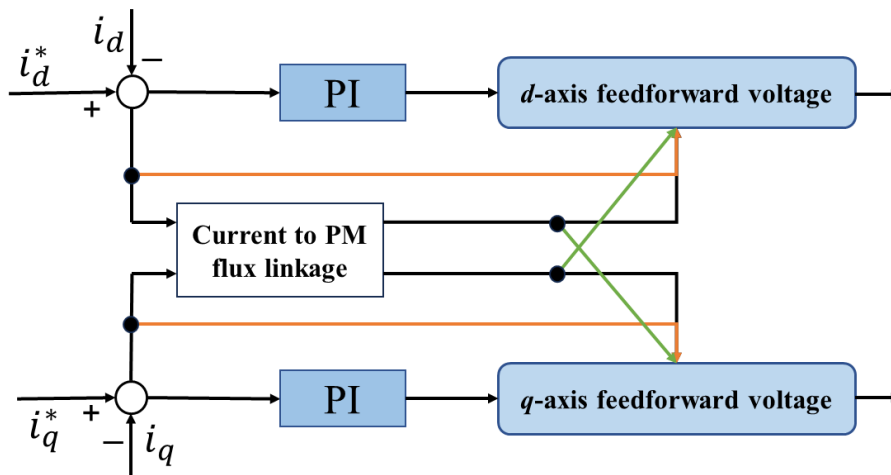


Fig. 1.23. Feed-forward current controller in [CHE20].

The increased current manipulation speed requires high-response current controller. Usually, PI gains in standard PI regulators are increased to satisfy the high bandwidth requirement. However, the higher PI gains can lead to current overshoot, deteriorating the control accuracy. Fig. 1.23 presents the current controller with feed-forward compensation. The feed-forward method compensates the required resistance voltage, induction voltage, and rotating voltage in the MS manipulation.

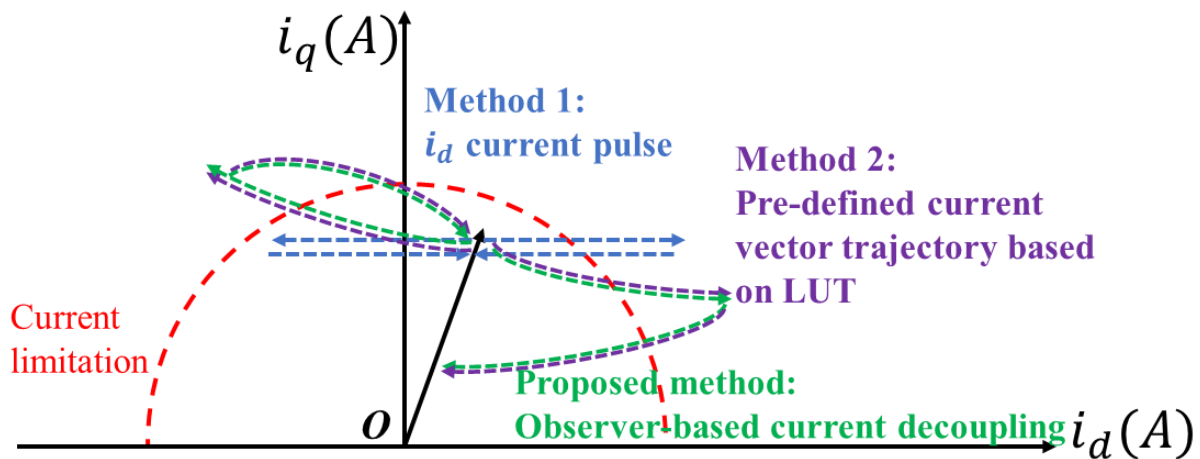


Fig. 1.24. Possible solutions for smooth torque control during MS process in [YU14].

To change the magnetization state, several possible solutions are shown in Fig. 1.24. There are two existing solutions: direct d -axis current pulse injection and using predefined current vector trajectory LUTs. The simplest method is giving a d -axis current pulse (blue line in Fig. 1.24) to the machine to achieve the desired MS. This method is feasible under no-load and low load conditions. Otherwise, a severe pulsating torque can be produced. The second method is based on LUTs. To produce smooth torque, q -axis current should be reduced as d -axis current increases under loaded conditions based on a prerecorded current trajectory in a LUT (red dotted line in Fig. 1.24).

However, time-intensive experiments are required because every loaded condition and MS corresponds to a different current trajectory. [YU14] proposed an observer based current decoupling method (green dotted line in Fig. 1.24) for smooth torque control during the MS manipulation process under loaded conditions. The overall control block diagram is shown in Fig. 1.25.

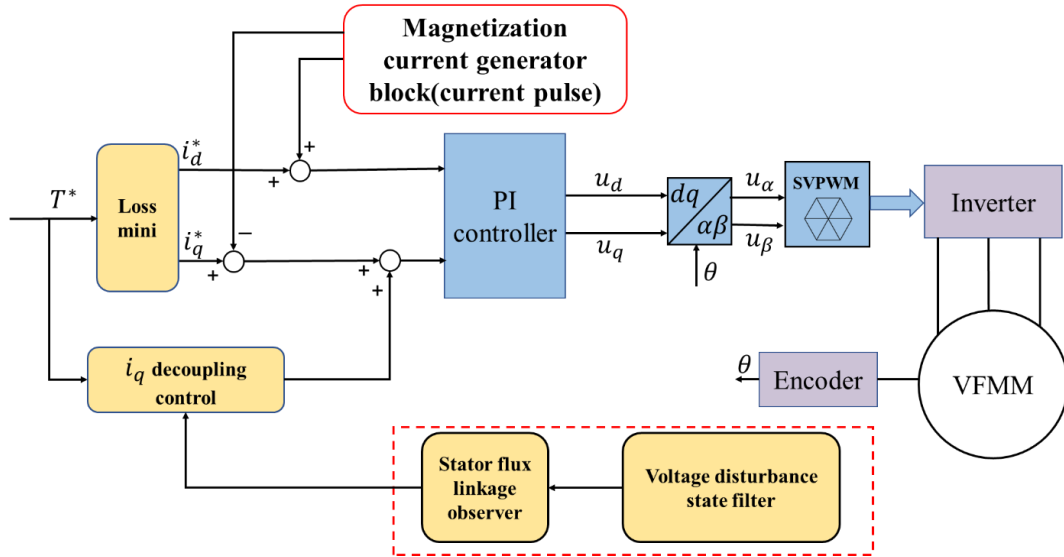


Fig. 1.25. Observer-based current decoupling control method in [YU14].

In [YU14], the MS was set within the limit of maximum MS based on the machine properties, speed, and available DC-bus voltage. For the observer based current decoupling method, the d -axis current command is generated to achieve the target magnetization level. The decoupling current can be generated based on the torque equation and estimated flux. The flux estimation is a key issue for accurate torque control. Then, a cascaded stator flux observer structure was used to mitigate the flux estimation error caused by parameter variations. The structure of the stator flux observer was shown in Fig. 1.26. It consisted of a stator current observer in the first stage and a Gopinath style stator flux linkage observer based on a voltage model [WAN12].

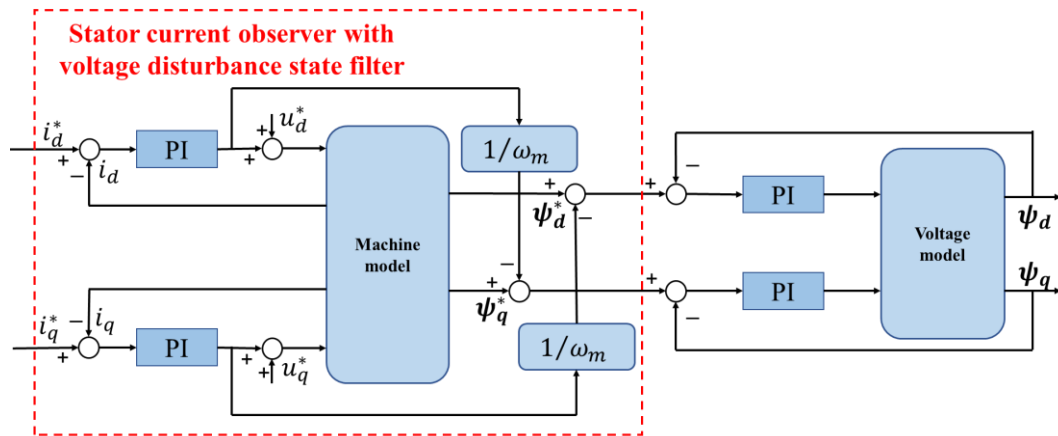


Fig. 1.26. Flux observer structure in [YU14].

In [GAG14], a reverse rotating current vector trajectory was proposed to increase MS in VFMMs, while mitigating the inherent dynamic voltage limitation. The basis of the method was a partial inverse model solution where the current vector was selected such that voltage component terms cancel the contributions of other terms. In the synchronous reference frame,

the method has an elliptical path where the ratio of the major to minor radius was set by the ratio of L_d and L_q , and rotation was in the reverse direction but at the same frequency as the electric fundamental of the machine. Therefore, the current vector trajectory was relatively more stationary in the stationary reference frame. In [GAG16], the existing methods for MS control were extended, organized into families of trajectory solutions, and analyzed along with a new method based on a straight line stationary frame flux linkage trajectory.

- **Close-loop control**

The configuration of the MS close-loop control proposed in [MAE14] is presented in Fig. 1.27, which consisted of the motor control and the control of the magnetizing current. Fig. 1.28 shows the configuration of the current control unit for high-speed control of d -axis current. During the MS manipulation, the magnetizing current command i_d^* is converted into a d -axis voltage command value using the inverse motor model. In other words, the d -axis current i_d is controlled by a feed-forward voltage command during magnetization. Further, the q -axis current i_q is controlled by a feedback current command. The magnetization control is configured to be a combination of the two controls. After the MS control finishes, the d -axis current control returns to feedback control. Then, the high-speed magnetizing current control and torque ripple control can be realized.

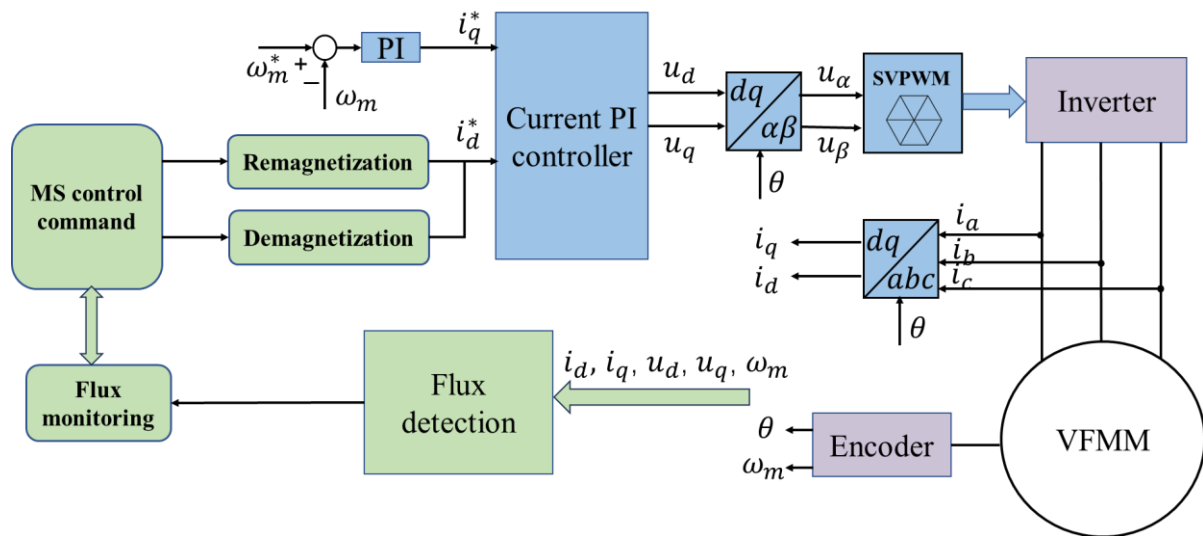


Fig. 1.27. Control configuration in [MAE14].

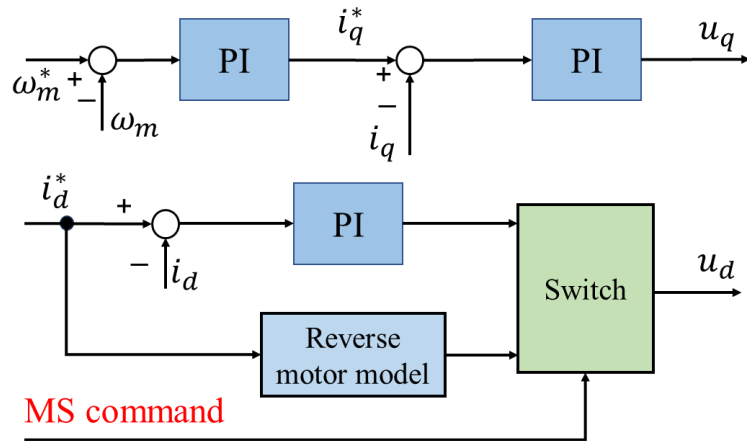


Fig. 1.28. Configuration of current control in [MAE14].

[QIA13] proposed a drive control system to realize the MS close-loop control as shown in Fig. 1.29. For the armature controller, it adopted a conventional dual close-loop control scheme, where the outer speed loop adopted a PID regulator to perform speed control, and the inner current loop used a hysteresis regulator to perform current chopping control. By comparing the command speed with the actual speed, the command armature current was resulted. Then, by comparing the command current with the actual current, the hysteresis regulator signal was generated. By logically combining the hysteresis regulator signal with the phase conduction signal, which depends on the mode of operation, the firing signal of each power switch in the armature inverter can be obtained. For the MS controller, it consisted of flux linkage observer, magnetizing current controller and current distributor. Magnetizing current controller control mode was similar to the armature current control operation mode. Obviously, the current distributor is one of the most important modules.

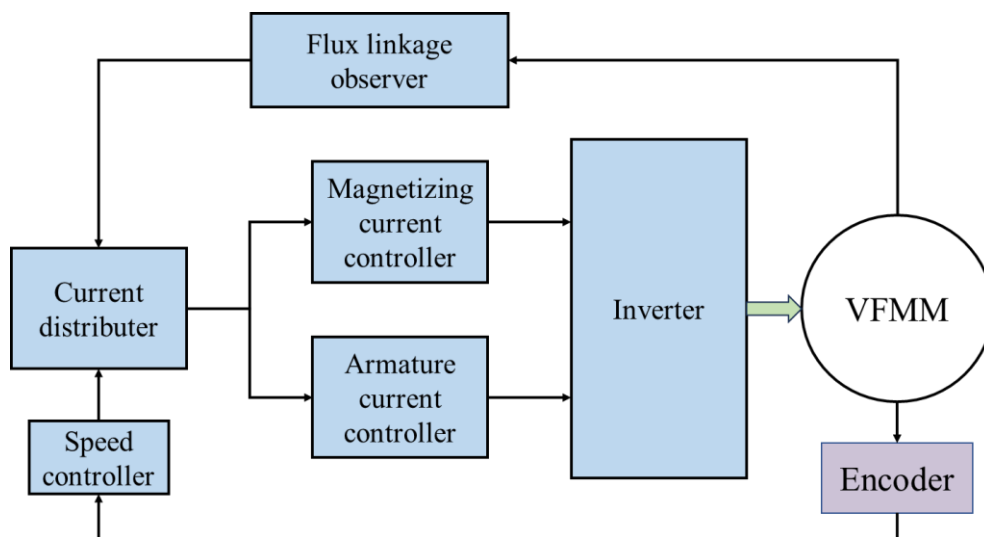


Fig. 1.29. Block diagram of drive control system in [QIA13].

Fig. 1.30 shows how the current distributor works in further details, where the optimal allocation of armature current and exciting current can be achieved.

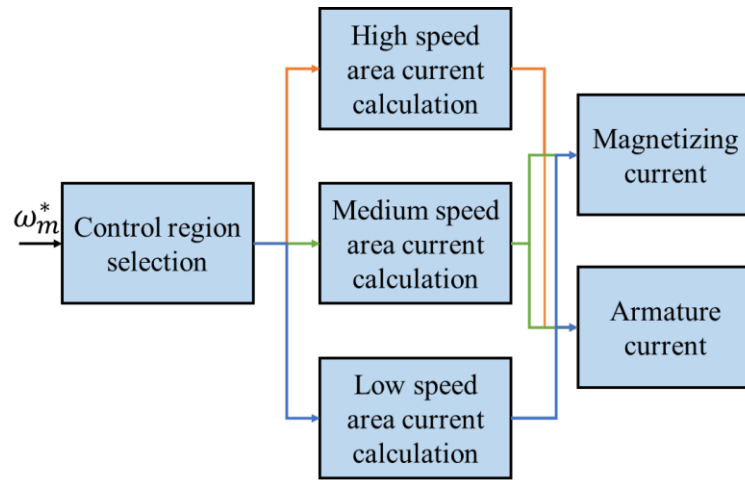
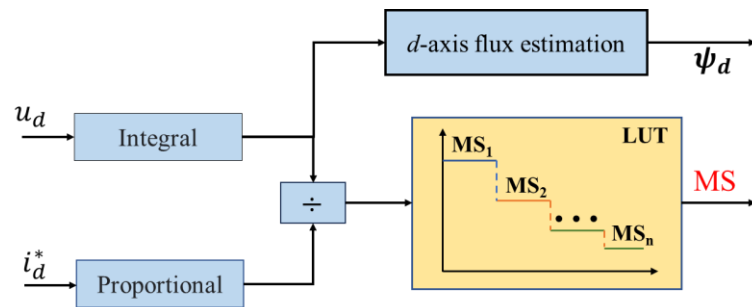
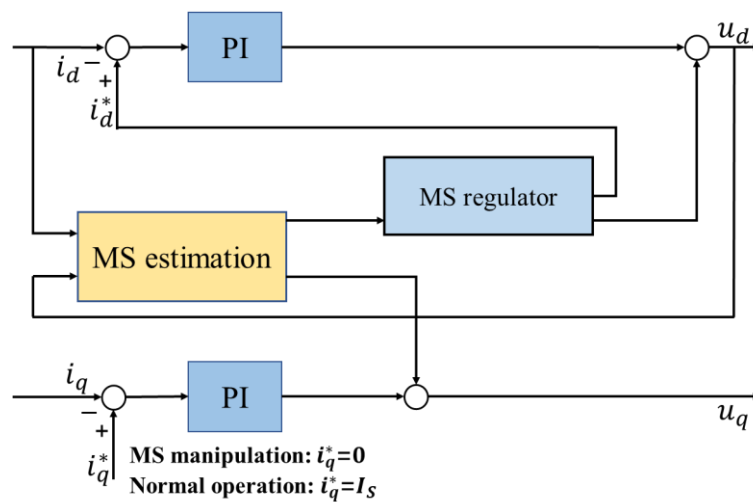


Fig. 1.30. Current distributor in [QIA13].



(a)



(b)

Fig. 1.31. MS estimation and close-loop control diagrams in [HU20a]. (a) MS estimation. (b) close-loop MS control.

[HU20a] proposed an on-line magnetization state estimation and close-loop control method as

shown in Fig. 1.31. The close-loop MS controller contained three major parts, i.e., the MS estimation, the MS regulator, and the dq -axis current controller.

In [ATH18], close-loop control can be achieved by manipulating the flux using deadbeat-direct torque and flux control algorithm while maintaining a nearly constant torque during MS change when the required current and voltage are within limits. Fig. 1.32 shows the schematic of the control strategy for driving cycle loss minimization with close-loop control. For MS control, LUT provides a d -axis flux command for minimum steady state loss with consideration for demagnetization due to the magnetic fields produced by the load current. This can also be achieved using loss models for MS control similar to the loss minimization methods for conventional machines. A deadbeat-direct torque and flux control algorithm is then used to maintain the desired torque and for manipulating the flux to change or maintain MS.

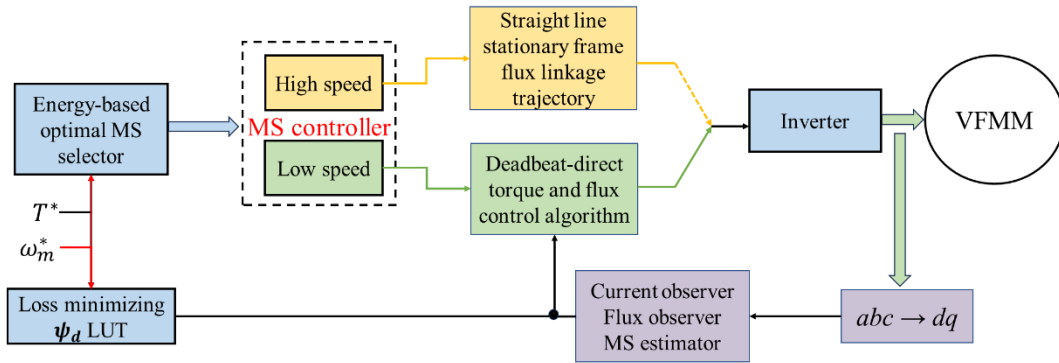


Fig. 1.32. Schematic diagram of loss minimization strategy with close-loop control in [ATH18].

The energy-based optimal MS selector provides a magnetization command based on a tradeoff between the energy required to change MS and the loss reduction that can be achieved by changing MS. For a detailed discussion of the transient losses during MS manipulations refer to [YU11b]. To decide the optimal MS, a LUT or a loss model to estimate the losses as a function of MS levels, torque and speed are obtained during calibration. To limit the number of MS changes, magnetization command is changed if the energy loss reduction over a fixed interval is greater than the energy required to change MS.

Feedback required for the close-loop MS control was obtained using a model reference adaptive MS estimation method developed in [GON09]. Besides, in [QIA19], The flux observer based on model reference adaptive theory was proposed for the close-loop flux control for VFMM.

● **Comparison and evaluation**

The summary of the above MS manipulation methods is listed in Table 1.4.

Table 1.4. Summary of presented approaches' advantages and disadvantages.

MS control methods	H-bridge converter	Look-up table	Online magnetization trajectory prediction	Close-loop control
Ref.	[YU11b] [YAN19] [YAN19b] [YAN14a]	[LYU20b]	[CHE20] [YU14] [GAG14]	[MAE14] [GAG16] [ATH18]
Pros	<ul style="list-style-type: none"> ✓ combining speed control and flux control ✓ magnitude, direction and duration of magnetizing current can be controlled separately ✓ flux control is more efficient 	<ul style="list-style-type: none"> ✓ adapt MTPA with MS control method ✓ establish relationship of voltage and flux, d-axis current and speed ✓ a hysteresis controller for MS manipulation 	<ul style="list-style-type: none"> ✓ online current trajectory prediction ✓ continuous real-time control ✓ control accuracy is high 	<ul style="list-style-type: none"> ✓ I_d was controlled by combination of FB current control and FF voltage control. ✓ high-speed magnetizing current control was realized ✓ control accuracy is higher
Cons	<ul style="list-style-type: none"> ✗ need additional hardware equipment ✗ more complicated structure ✗ no consideration of control transition smoothness 	<ul style="list-style-type: none"> ✗ obtained from offline test ✗ necessarily prior experiments ✗ control accuracy is not high 	<ul style="list-style-type: none"> ✗ still open-loop control ✗ control algorithm is more complicated ✗ Relatively high dependence on motor parameters 	<ul style="list-style-type: none"> ✗ magnetization changes under no-load condition ✗ Relatively high dependence on motor parameters

1.6 Scope and Contributions of the Thesis

1.6.1 Research Motivation

Based on the review above, the trend of the control for VFMM can be highlighted as follows:

1) As the crucial part of the control for VFMM, the solution to make the MS manipulation steady and smooth is desirable for the high performance in the control system. [YU14] focused on the dynamic disturbance caused by MS manipulation and proposed a smooth torque control method by utilizing a voltage disturbance state filter to make the MS manipulation smooth. While the optimal timing of MS manipulation to achieve the desired effect can make algorithm simple and is still needed.

2) Generally, the amplitude of the magnetizing current pulse to achieve MS manipulation is very large, and some are even several times or more than ten times the rated current, which will bring significant disturbance to the control system. In [ZHO23c], a speed controller based on linear active disturbance rejection compensation model was proposed to reduce the speed fluctuations caused by the MS manipulation. The transient performance during MS manipulation needs further investigation.

3) Since the magnetizing current pulse is injected into the d -axis armature current, it needs enough voltage to support the demand current. This brings a big challenge for the control system, especially in the flux weakening region, where the voltage controller is almost saturated. Therefore, the voltage limitation must be considered during MS manipulation. While in the existing research, the effect of the voltage constraints on the MS manipulation is always ignored.

4) Since the LCF PMs can be demagnetized by the negative current pulse, the negative d -axis armature current for flux weakening control can also cause the demagnetization of the LCF PMs. This kind of demagnetization can change the PM flux linkage unintentionally, and make the MS out of control, which will affect the performance of the machine drive system. Besides, the authors of [WU14] observed that cross-coupling between HCF PMs and LCF PMs in hybrid PM VFMM can demagnetize the LCF PMs unintentionally. Although this issue can be improved through the design of the different arrangement of the two kinds of PMs, the control method during MS manipulation is still desirable.

5) The conditions for MS manipulation have brought some attentions. The speed is usually set as the condition of MS manipulation, which is easy to implement and popular in the existing

literature [LYU20b] [MAS15] [ZHO22a] [ZHO22b]. As the main feature of the MS, PM flux linkage is also used as the condition for MS manipulation [CHE22] [HU20a]. [HU21] proposed an efficiency-based MS manipulation method, an efficiency map under different MSs was measured in advance. A flexible MS manipulation method that can be adjusted based on the real-time operating state is still needed.

In order to explore the applicability of VFMM in industry and daily life, the research in this thesis mainly focuses on the MS manipulation method and solutions to improve the dynamic performance, which will be presented in detail next section.

1.6.2 Research Outline

The structure of this thesis is presented in Fig. 1.33.

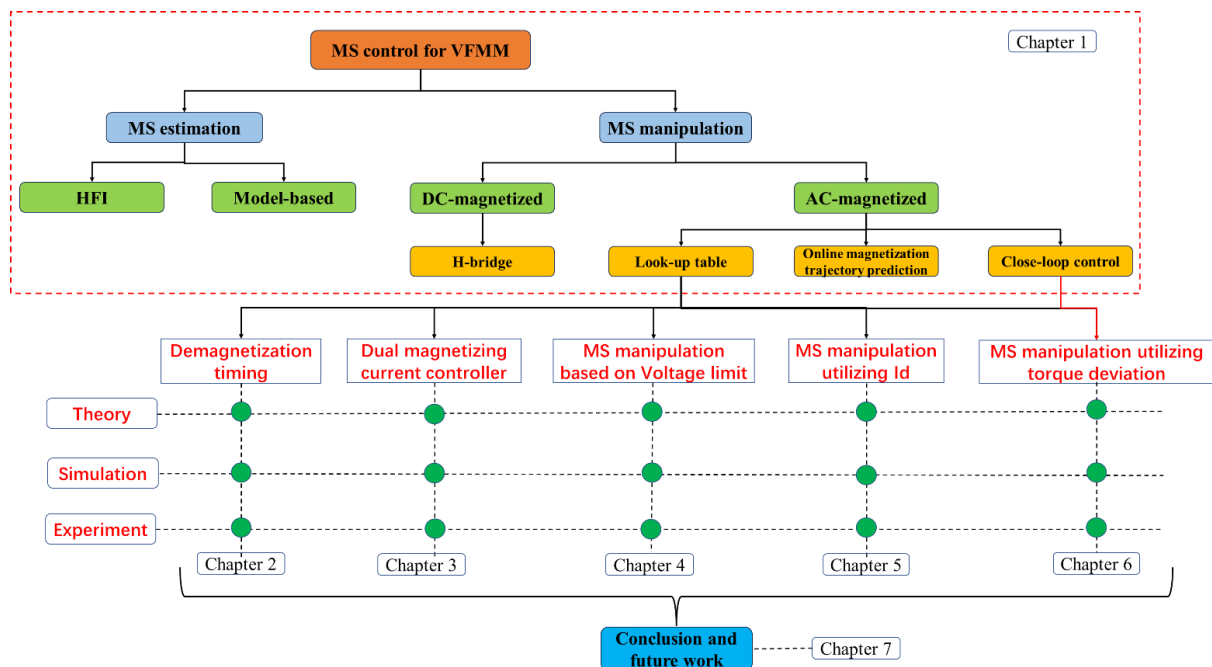


Fig. 1.33. Outline of research.

This thesis is organized as follows:

In chapter 2, the instant of demagnetization for hybrid magnet memory machine (HMMM) is investigated. A demagnetization grid is proposed based on the torque-speed curves under different magnetization states (MSs). A look up table (LUT) containing the information of speed and torque on the intersections of the torque-speed curves is then used to determine the best instant of demagnetization for HMMM. The performance of proposed demagnetization process is simulated and experimentally validated on the HMMM control system.

In chapter 3, a novel dual magnetizing current controller for VFMM is proposed aiming to

mitigate the speed fluctuation during MS manipulation. Firstly, the magnetizing properties of the investigated HMMM are tested and researched offline. The effect of amplitude and time duration of the magnetizing current pulse on its magnetizing capability is investigated. Secondly, the proposed dual magnetizing current controller is designed based on the dynamic mathematical model for VFMM. A model-based torque calculation is utilized and a LUT with the parameters under each magnetization state including the magnetizing current pulse and dq -axis inductances is established. Then, the experiments are carried out on the investigated HMMM control system. The measured results of the transient performance on both remagnetization and demagnetization show that the proposed dual magnetizing current controller can significantly mitigate the speed fluctuation and has better transient performance than the conventional single magnetizing current method.

In chapter 4, a novel MS control method for HMMM based on modified voltage limitation is proposed. The effect of the voltage limitation on the MS manipulation is analyzed. The circumcircle of the voltage vector hexagon is utilized as the modified voltage limitation instead of the inscribed circle to simplify the algorithm. The maximum amplitude of the magnetizing current pulse under real-time voltage limitation can be calculated and utilized as the boundary for MS manipulation. Within the boundary, the target MS can be achieved. When the MS is limited, the proposed MS control method also provides solutions to achieve the target MS by calculating the optimal operating speed. The experimental validations are carried out on the HMMM control system to verify the feasibility of the proposed MS control method.

In chapter 5, a novel MS control method is proposed to eliminate the unintentional demagnetization (UD) of LCF PM for VFMM. In the proposed method, the amplitude of demagnetization d -axis current pulse is determined from a look-up table with the relationship between the demagnetization d -axis current pulse and the MS change intersections, and subsequently used as the condition for the MS manipulation. A PM flux linkage estimation is adopted to monitor the UD all the time and the amplitude of d -axis current is controlled within the amplitude of the demand demagnetization d -axis current pulse to avoid the UD in the whole speed range. The inverter nonlinearity is compensated to improve the estimation accuracy. The experiment validation is conducted on HMMM drive system to illustrate the UD issue and to verify the PM flux linkage estimation method and the proposed MS control method.

In chapter 6, a novel MS control method is proposed by utilizing torque deviation for VFMM to achieve the MS close-loop control. Firstly, the relationship between the MSs and the demand magnetizing current pulses is built into a LUT, which also contains information on the flux

linkages and the dq -axis inductances under different MSs. Afterwards, a model-based torque calculation is adopted for the torque estimation, and then, the torque deviation between the present MS and target MS is used to generate the MS switch signal, which will determine the type of MS manipulation. Subsequently, the torque deviation will also be used for real-time monitoring of MS. Finally, experiments are carried out on a HMMM control system for validation.

1.6.3 Contributions

The major contributions in this thesis include:

- 1) An optimal demagnetization grid is built to determine the best instant of demagnetization. The VFMM can be regarded as a group of PMSMs with the same topology and different PM flux linkages and inductances. The torque is the same on the interactions of the branch of torque-speed curves, which form the demagnetization grid. Then, MS manipulation on the demagnetization grid can be smooth and steady. This solution is also tested for remagnetization process.
- 2) A dual magnetizing current controller is proposed to mitigate the speed fluctuation during MS manipulation. The torque variation caused by the injected d -axis magnetizing current pulse can be calculated. Then, a q -axis current pulse is compensated to reduce the torque variation. As a result, the speed fluctuation can be improved.
- 3) A MS control method based on modified voltage limitation is proposed. The circumcircle of the voltage vector hexagon is utilized as the modified voltage limitation instead of the inscribed circle to simplify the algorithm. Then, the modified voltage limitation is utilized as the boundary for MS manipulation to achieve the demand MS.
- 4) A MS control method to eliminate the unintentional demagnetization issue is proposed. Since the MS can be changed only when the amplitude of the magnetizing current pulse is bigger than the previous one. The amplitude of demagnetization d -axis current pulse is used as the condition for the MS manipulation. Then, the amplitude of d -axis current is controlled within the amplitude of the demand demagnetization d -axis current pulse to avoid the UD issue in the whole speed range. A PM flux linkage estimation is adopted to monitor the UD issue, and the inverter nonlinearity is compensated to improve the estimation accuracy.
- 5) A MS control method utilizing torque deviation is proposed to achieve the MS close-loop control. Since torque contains the information of PM flux linkage and dq -axis inductances, it

can be sensitive during MS manipulation under the same operating state. A model-based torque calculation is adopted for the torque estimation, and then, the torque deviation between the present MS and target MS is used to generate the MS switch signal.

Publications:

Yan Jia, Z.Q. Zhu, Qiang Wei, Jianghua Feng, Shuying Guo, Yifeng Li, and Liang Hu, “A novel dual magnetizing current controller to mitigate speed fluctuation during magnetization state manipulation for variable flux memory machines” (Digital Object Identifier or DOI: 10.1109/TEC.2024.3359950) Accepted for publication by IEEE Transactions on Energy Conversion.

Yan Jia, Z. Q. Zhu, L. Xu, J. H. Feng, S. Y. Guo, Y. F. Li, and L. Hu, “A novel magnetization state control method utilizing torque deviation for variable flux memory motor,” *2022 25th International Conference on Electrical Machines and Systems (ICEMS)*, Chiang Mai, Thailand, 2022, pp. 1-5. accepted for publication by IEEE Transactions on Industry Applications.

Yan Jia, Z. Q. Zhu, Dawei Liang, J. H. Feng, S. Y. Guo, Y. F. Li, and L. Hu, “A novel magnetization state control method to eliminate the unintentional demagnetization of low-coercive force permanent magnet for a hybrid magnet memory motor,” *2022 International Conference on Electrical Machines (ICEM)*, Valencia, Spain, 2022, pp. 1096-1102. Submitted to IEEE Transactions on Industry Applications and revised.

Yan Jia, Z.Q. Zhu, Qiang Wei, Jianghua Feng, Shuying Guo, Yifeng Li, and Liang Hu, “Novel magnetization state control method based on modified voltage limitation for hybrid magnet memory machine”. Submitted to IEEE Transactions on Energy Conversion and under review.

Yan Jia, Z. Q. Zhu, J. H. Feng, S. Y. Guo, Y. F. Li, L. Hu, and H. Yang, “Investigation on the timing of demagnetization for variable flux memory motor,” *2022 IEEE 5th International Electrical and Energy Conference (CIEEC)*, Nanjing, China, 2022, pp. 3473-3478.

CHAPTER 2 DEMAGNETIZATION TIMING CONTROL FOR HYBRID MAGNET MEMORY MACHINE

In this chapter, the instant of demagnetization for hybrid magnet memory machine (HMMM) is investigated. A demagnetization grid is proposed based on the torque-speed curves under different magnetization states (MSs). This provides a solution for smooth MS manipulation.

2.1 Introduction

The adjustable MS of LCF PMs provides extra freedom for the control of variable flux memory machine (VFMM). Some researchers have investigated the magnetizing characteristics of VFMM [QIA18] [LIU08] [OST03] [LEE08] [LIU09] [LYU19] [LIU10] [GAG17]. [QIA18] analyzed the magnetic properties of LCF PMs and the operating principle of the combined magnetic-pole memory motor. [LIU08] analyzed the influence of different PM shapes on the PM demagnetization pattern of VFMM. The air gap flux density and demagnetizing magnetomotive force had been investigated by equivalent magnetic circuit method and geometric analytical method [OST03]. In [LEE08], a demagnetizing characteristic analysis method was proposed by using coupled Preisach modeling and finite element method (FEM). In [LIU09], the variation characteristics of flux density and field intensity of trapezoidal PM in the VFMM under different demagnetizing magnetomotive forces were analyzed by a two-step FEM. The influences of key design parameters on the on-load demagnetization effect of a switched flux hybrid magnet memory machine were analyzed with the aid of the FEM and frozen permeability method [LYU19]. In [LIU10], the PM remagnetizing characteristics of a VFMM were analyzed by considering the PM hysteresis. The magnet temperature effects on magnetization manipulation and maximum torque properties in VFMM were investigated and the magnet temperature was used as an input to manipulate magnetization [GAG17]. These papers mainly focused on the modeling methods and magnetic properties of VFMM.

Some researchers focused on the MS manipulation for VFMM [FUK15] [YAN19b] [YAN14a] [CHE20] [YU14] [GAG14] [MAE14] [GAG16] [ATH18] [MAS15] [HU21]. Different MSs were selected in terms of minimization of the loss over a driving cycle [FUK15]. [YAN19b] proposed a stepwise magnetization control strategy by utilizing a LUT and a single-phase H-bridge converter to avoid the continuous and frequent adjustment of the PM flux-linkage. A

time-divisional online magnetization strategy combining an H-bridge converter and a Buck converter was proposed in [YAN14a]. An online current trajectory prediction and control method for the magnetization current in a VFMM was proposed in which the machine speed and the DC-link voltage are used as the key index [CHE20]. [YU14] proposed a smooth torque control method by utilizing a voltage disturbance state filter during the magnetization state manipulation under nonzero speed and load conditions. A reverse rotating current vector trajectory method was proposed as a partial inverse model solution to allow MS to be increased at higher speeds [GAG14]. In [MAE14], a high-speed magnetizing current control was realized by the combination of the feedback current control and the feedforward voltage control. [GAG16] proposed a new method based on a straight-line stationary frame flux linkage trajectory for MS control of VFMM. [ATH18] proposed a close-loop MS control method to enable reliable loss minimization control. In [MAS15], a whole vector control algorithm for the VFMM was proposed, and the magnets were demagnetized proportionally as the speed increases according to a table relating the PM states and the d -axis current limits. An efficiency-based magnetization state switch control was proposed in [HU21]. In the above research, the MS control methods were investigated and combined with current control methods to improve the performance during MS manipulation.

The demagnetization process of MS can be treated as an extra method of flux weakening control for VFMM. The performance of magnetization dynamic process and the perfect instant of demagnetization to make the MS manipulation much more smoothly are still needed for further investigation.

In this chapter, the instant, number and performance of demagnetization for VFMM are investigated. Firstly, the topology and the parameters of HMMM and its magnetizing characteristics are illustrated, and the difference in mathematical models between VFMM and the conventional PMSM is analyzed. Secondly, the demagnetization characteristics based on the maximum power output current trajectory for VFMM is investigated. Then, a demagnetization grid (DG) is proposed based on torque-speed curves under different MSs, and a LUT containing the information of the intersections of the torque-speed curves is built and used to determine the best instant of demagnetization for VFMM. Finally, experiment validation based on the proposed method are carried out on the HMMM control system. The transient performance and optimal numbers of demagnetization for the machine are tested. The measured results verify that the proposed demagnetization control method exhibits better performance on the demagnetization grid.

2.2 Machine Topology And Mathematical Model

2.2.1 Machine Topology

The topology of the investigated HMMM with bypass airspace barriers [YAN19c] is shown in Fig. 2.1. It has 21 stator slots and 4 rotor poles, and uses AlNiCo as the LCF PM and NdFeB as the HCF PM. The HCF and LCF magnets are geometrically separated within one PM rotor pole, forming a dual layer structure. The radially magnetized LCF PMs are located nearby the airgap, which can be demagnetized easily, and the circumferentially magnetized HCF PMs are placed on the two sides of the LCF magnet. This series structure arrangement of hybrid PMs can combine the advantages of high torque capability of HCF PMs and wide flux regulation merit of LCF PMs and prevent the unintentional demagnetization risk of the LCF PMs. Besides, the airspace barriers and adjacent iron bridges are designed at the d -axis position, which can effectively reduce the oversized inverter power rating and required fully demagnetizing current pulse level. Due to the presence of the upper-side iron bridge and airspace barrier, a short-circuiting path for the HCF PM magnetic fields will occur at the flux-weakened state.

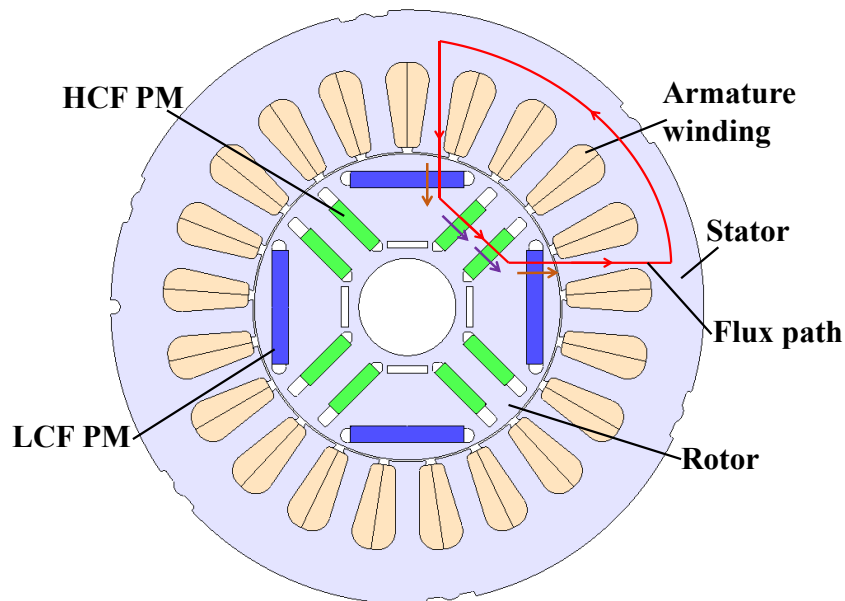
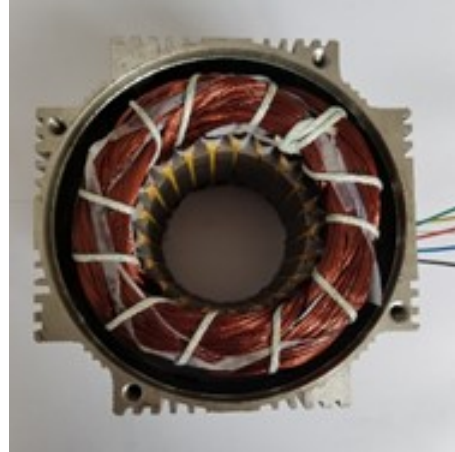


Fig. 2.1. Topology of investigated HMMM.

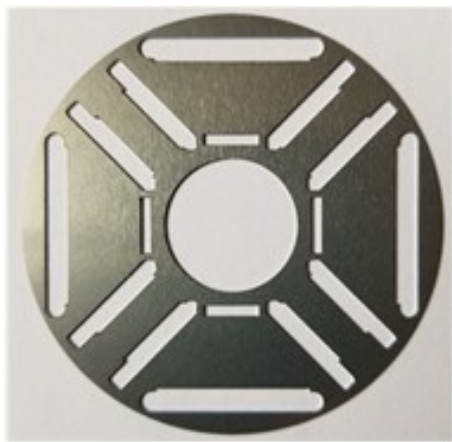
The photos are presented in Fig. 2.2.



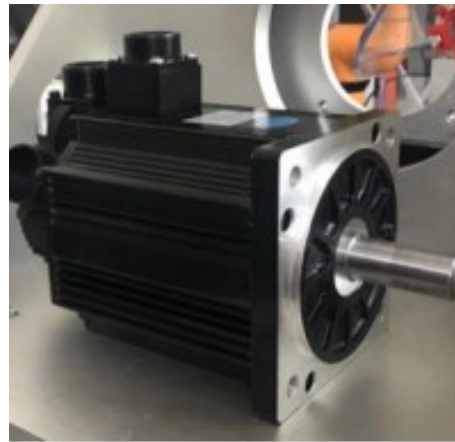
(a)



(b)



(c)



(d)

Fig. 2.2. Photos of HMMM. (a) Stator. (b) Stator with armature windings. (c) Rotor laminations. (d) Appearance.

As shown in Fig. 2.1, there is no extra magnetizing coil in the HMMM. The magnetizing current pulse is injected into the d -axis armature current to achieve MS manipulation.

The main parameters of the investigated HMMM prototype are listed in Table 2.1.

Table 2.1. Main parameters of investigated HMMM prototype.

Item	Symbol	Value
Rated power	P	1100W
Rated current (RMS)	I_m	7.5A
Rated speed	n	1500 r/min
Rated voltage	V	220V
Number of pole pairs	p	2
Phase resistance	R	1.9 Ω
HCF PM grade	-	N35SH
LCF PM grade	-	AlNiCo 9
HCF PM coercivity	-	915 kA/m
LCF PM coercivity	-	112 kA/m
HCF PM remanence	-	1.2T
LCF PM remanence	-	1.0T
Steel grade	-	35CS440

As above mentioned, the LCF PMs and HCF PMs are made of AlNiCo and NdFeB, respectively. Their B-H curves are depicted in Fig. 2.3. For LCF PMs, the hysteresis curve of AlNiCo can allow its operating points to move flexibly.

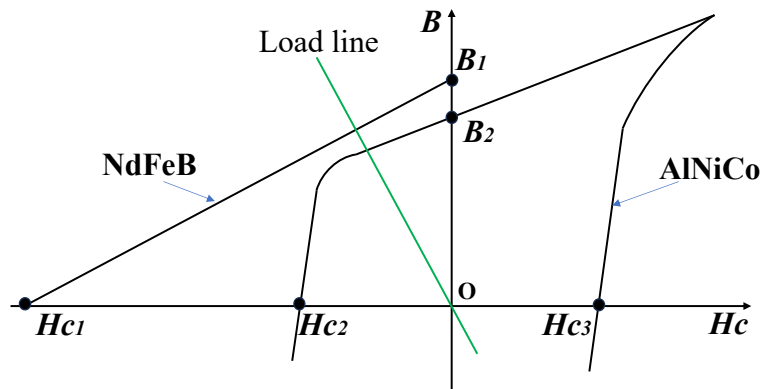


Fig. 2.3. BH curves for NdFeB and AlNiCo (B: Flux density, Hc: magnetic field strength).

The simplified electric equivalent circuit of the machine is illustrated in Fig. 2.4, where F_{Nd} , F_{Al} , R_{Nd} , and R_{Al} represent the intrinsic magnetic motive force and magnetic reluctances of NdFeB magnets and AlNiCo magnets, respectively. R_g represents the air-gap reluctance. The reluctance of leakage path is represented by R_{g1} .

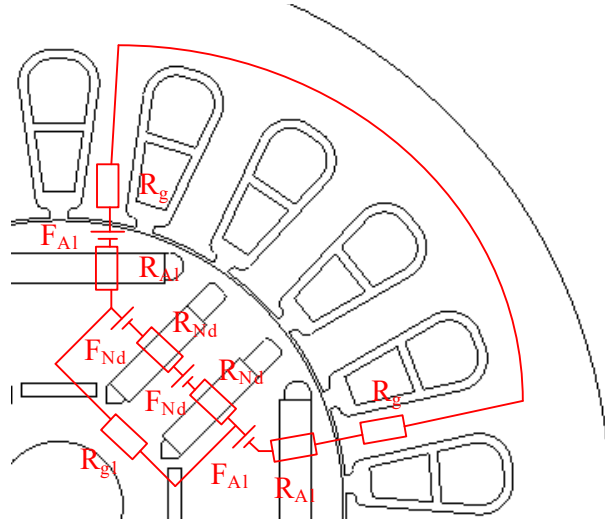


Fig. 2.4. Equivalent magnetic circuit of hybrid VFMM.

A magnetization ratio (MR) is used to represent the MS level. When the magnetization ratio is 0%, the flux linkage is 0.124 Wb. When the magnetization ratio is 100%, the flux linkage is 0.195 Wb. The flux linkages and the dq -axis inductances against the magnetization ratio are shown in Fig. 2.5. When the MS changes, the dq -axis inductances and the flux linkages change synchronously. Thus, when the MS control is processed, the change in dq -inductances must be considered. Here, the effect of magnetic saturation and temperature on the flux linkages and dq -axis inductances is neglected, which will be further investigated together with MS control.

For the investigated machine, due to its magnetizing properties in Fig. 2.5, chapter 2 – chapter 5 mainly focus on the MR from 0% - 100%, chapter 6 focuses on the MR from -100% - 0%, which will be investigated in detail in the following chapters.

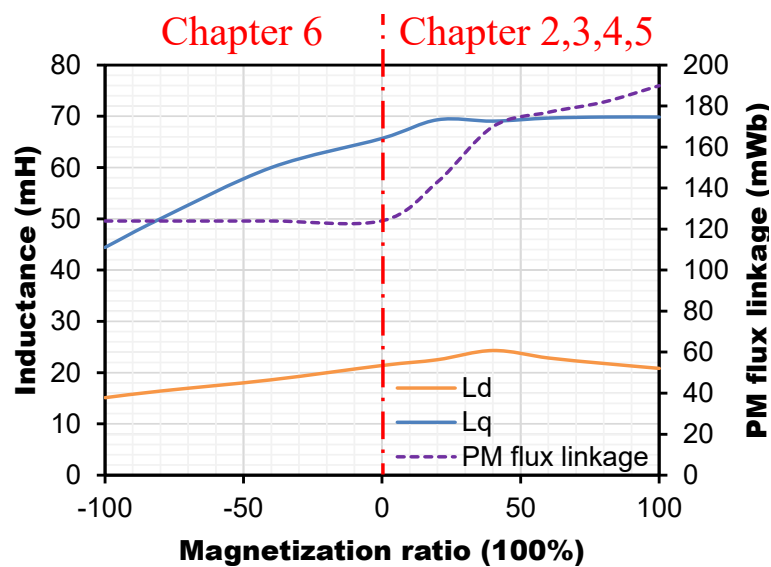


Fig. 2.5. PM flux linkage and dq -axis inductances against magnetization ratio.

2.2.2 Mathematical Model

In the conventional PMSM model, the permanent magnet flux linkage ψ_m is usually regarded as a constant, while it in VFMM will change during the process of MS manipulation. Therefore, the dq -axis mathematical model for VFMM considering the process of MSs manipulation is referred to as dynamic mathematical model and can be expressed as:

$$u_d = Ri_d + L_d \frac{di_d}{dt} + \frac{d\psi_m(i_{mag.})}{dt} - \omega L_q i_q \quad (2.1)$$

$$u_q = Ri_q + L_q \frac{di_q}{dt} + \omega L_d i_d + \omega \psi_m(i_{mag.}) \quad (2.2)$$

where i_d and i_q are the dq -axis stator currents, L_d and L_q are the dq -axis inductances, $i_{mag.}$ is the magnetizing current pulse, $\psi_m(i_{mag.})$ is the permanent magnet flux linkage, which is adjusted by the magnetizing current pulse, R is the winding resistance, u_d and u_q are the dq -axis voltages, ω is the electrical angular speed.

Then, the electromagnetic torque equation is:

$$T_e = 1.5p[\psi_m(i_{mag.})i_q + (L_d - L_q)i_d i_q] \quad (2.3)$$

where p is the pole pair number of VFMM.

2.3 Demagnetization Analysis for VFMM

Flux-weakening methods for PMSM are generally based on the voltage and current magnitude constraints, which are the limited DC bus voltage (V_m) and the motor rated current (I_m), respectively. It can be expressed as

$$\begin{cases} i_d^2 + i_q^2 \leq I_m^2 \\ V_d^2 + V_q^2 \leq V_m^2 \end{cases} \quad (2.4)$$

where V_d and V_q are the dq -axis voltages, and I_m and V_m are the current and voltage magnitude limits.

Without considering the change of MS, VFMM is the same as a conventional PMSM according to the mathematical model. As VFMM is essentially a special kind of PMSM, (2.4) is also suitable for VFMM. The current trajectories in dq -axis current coordinate system for the salient-pole VFMM can be illustrated in Fig. 2.6. The demagnetization manipulation is considered in the trajectories. In Fig. 2.6, X $(-i_{c1}, 0)$ point on the horizontal axis is the center

point of the voltage initial limit ellipse. i_{c1} is the characteristic current of the VFMM under initial MS₁ ($i_{c1} = \psi_{m1}/L_{d1}$), ψ_{m1} is the initial PM flux linkage. With the speed increasing from ω_1 to ω_2 , the intersection of voltage limit ellipse and current limit circle moves from A to C. Then, for the demagnetization process at speed ω_2 , the center point of the voltage limit ellipse moves from X ($-i_{c1}, 0$) to Y ($-i_{c2}, 0$). i_{c2} is the characteristic current of the VFMM under MS₂. This makes the intersection of voltage limit ellipse and current limit circle move from C to B. As the speed keeps increasing to ω_3 , the intersection of voltage limit ellipse and current limit circle moves from B to E. When demagnetization manipulates at ω_3 , the center point of the voltage limit ellipse moves from Y ($-i_{c2}, 0$) to Z ($-i_{c3}, 0$). i_{c3} is the characteristic current of the VFMM under MS₃. At the same time, the intersection of voltage limit ellipse and current limit circle moves from E to D. When the speed increases to ω_4 , the intersection of voltage limit ellipse and current limit circle moves from D to F.

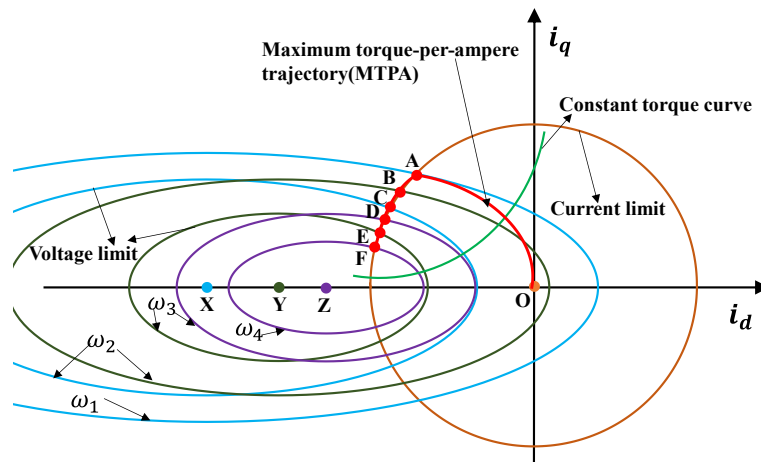


Fig. 2.6. Illustration of current trajectory for salient-pole VFMM. Speed: $\omega_1 < \omega_2 < \omega_3 < \omega_4$.

The current trajectories for conventional PMSM will go along curve 'OA' at the maximum torque-per-ampere (MTPA) region, then turn into the flux weakening region from A to F directly along the current limit. The current trajectories for VFMM at the MTPA region are the same as PMSM, while due to the demagnetization manipulations, the current trajectories of VFMM at the flux weakening region move along ACBEDF on the current limit circle, which are more complicated. It is assumed here that the demagnetization occurs in the flux weakening region.

On the curve 'OA', the machine operates in the constant torque region. The voltage is relatively sufficient, and the torque must be maintained at the maximum value to ensure acceleration performance. When the PM linkage decreases by demagnetization, the torque will decrease, which will reduce the acceleration performance. Therefore, there is no benefit for

demagnetization in the constant torque region.

On the curve ‘AF’, also called as flux weakening region, the machine operates on the intersection points of the current and voltage limits. Due to the voltage limits, flux weakening control is essential for the speed extension. A negative increasing d -axis current will be generated by the flux weakening control method [BOL14], which will reduce the induced voltage and extend the speed. Demagnetization in this region will reduce the PM linkage, which can also reduce the voltage. In other words, the demagnetization process can also be treated as a method of flux weakening. Therefore, demagnetization on curve ‘AF’ can be combined with the flux weakening control to realize the stable operation of the motor in this area.

2.4 Best Instant of Demagnetization

Demagnetization manipulation is very crucial in the whole control method for VFMM. Demagnetization manipulation at a suitable instant can make the transition of the demagnetization process smooth and stable, which can improve the control performance of the motor.

The PM flux linkage and dq -axis inductances are different under different MSs. Therefore, a VFMM can be regarded as a group of specific PMSMs under different MSs. The main parameters of this group of specific PMSMs are the same except for the PM flux linkage and dq -axis inductances. Then, the torque-speed characteristics of this group of PMSMs can be obtained. The torque-speed characteristic curves under several MSs are illustrated in Fig. 2.7. It can be observed that these torque-speed characteristic curves have some intersections, which means the torque under the different MSs of the VFMM are the same on these intersections.

According to (2.3), when the MS changes, the torque changes a lot due to the change of PM flux linkage, which will affect the performance of the motor a lot. Therefore, the important aim for VFMM demagnetization control is to reduce or even eliminate the influence of torque change caused by the MS manipulation. Based on the analysis above, demagnetization manipulation on these intersections of equal torque will eliminate the torque fluctuation. In this chapter, these intersections are called as demagnetization points (DPs). These DPs form a grid, which is called demagnetization grid (DG), as shown in Fig. 2.7. This DG can be obtained under different loads, not only for the maximum torque-speed characteristic curve. Demagnetization process on the DG can make the torque switching smooth and stable. This does not mean that the more DPs on the DG, the better. Each MS manipulation will bring

oscillations to the control system due to the large amplitude of the magnetizing current pulse. Therefore, the optimal numbers of MS manipulation need to be determined aiming to minimize the impact of MS control on dynamic performance of the control system. This will be evaluated and discussed in section 2.5.3 for the investigated machine.

To determine the demagnetization points for the VFMM in the flux weakening region, a LUT is adopted. Since the VFMM at each MS presents different torque-speed characteristics, a series of torque-speed characteristics curves can be obtained first, just as illustrated in Fig. 2.7. Then, the intersections of various torque-speed characteristic curves can be obtained. Based on the offline measuring the relationship between the MS and the magnitude of the d -axis current pulse, and the relationship between the MSs and the intersections of the torque-speed characteristics, a table of a DG containing several DPs can be built as shown in Table 2.2.

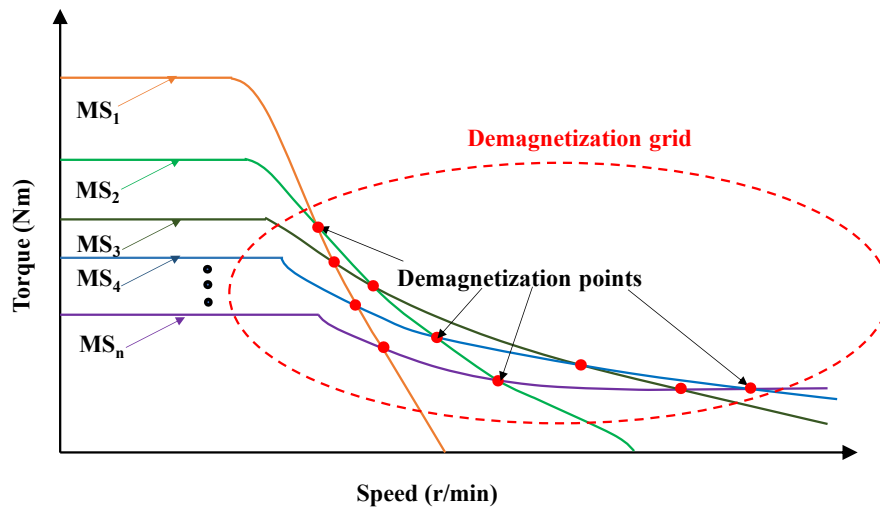


Fig. 2.7. Torque-speed characteristics under different MSs.

Table 2.2. Demagnetization points of each MS.

Change of MS	Magnetizing current pulse	Demagnetization points
MS ₁ to MS ₂	$-I_{mag,12}$	(Torque ₁₂ , Speed ₁₂)
MS ₁ to MS ₃	$-I_{mag,13}$	(Torque ₁₃ , Speed ₁₃)
... MS ₁ to MS _n	$-I_{mag,1n}$... (Torque _{1n} , Speed _{1n})
MS ₂ to MS ₃	$-I_{mag,23}$	(Torque ₂₃ , Speed ₂₃)
MS ₂ to MS ₄	$-I_{mag,24}$	(Torque ₂₄ , Speed ₂₄)
... MS ₂ to MS _n	$-I_{mag,2n}$... (Torque _{2n} , Speed _{2n})
MS ₃ to MS ₄	$-I_{mag,34}$	(Torque ₃₄ , Speed ₃₄)
... MS _m to MS _n	$-I_{mag,mn}$... (Torque _{mn} , Speed _{mn})

As shown in Table 2.2, each DP is a coordinate value with two dimensions containing torque and speed, which means demagnetization manipulation on these DPs must meet the torque condition and the speed condition at the same time.

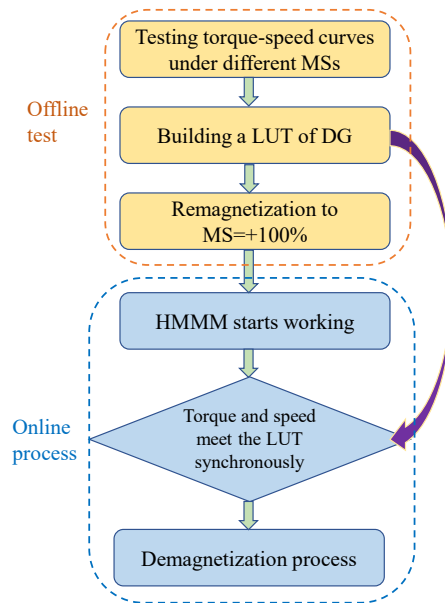


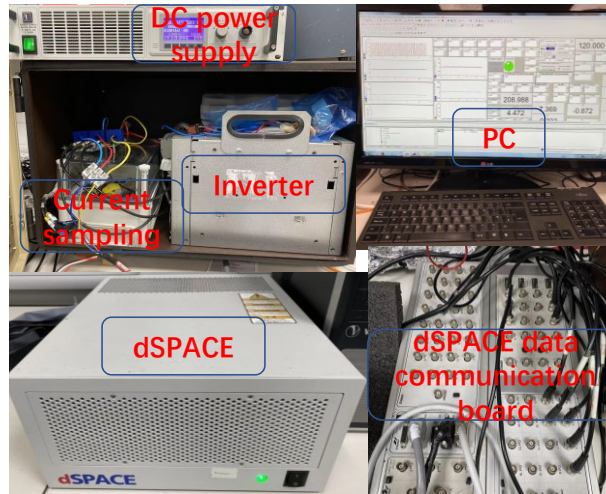
Fig. 2.8. Process of determining instant of demagnetization.

Combining with the prototype HMMM, the process to determine the best instant of demagnetization is illustrated in Fig. 2.8. The offline measurements to build the LUT of DG is necessary in this process. Remagnetization is also required based on the magnetizing properties of the HMMM. Then, the online demagnetization process can be realized according to the offline measurements. It needs to mention that although this method is verified on the HMMM in this chapter, it is applicable to all kinds of VFMM.

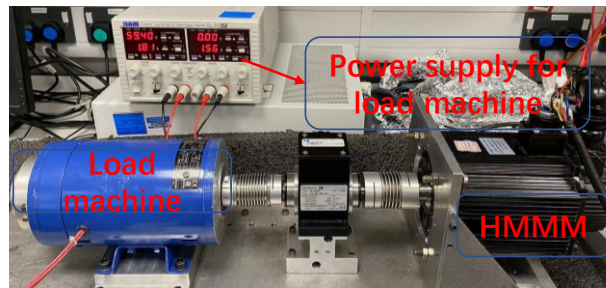
2.5 Experimental Validation

2.5.1 Test Rig

The experiment platform is shown in Fig. 2.9. The investigated machine is controlled by a three-phase IGBT inverter which is produced by Semikron. The external current sampling module is connected between the inverter and the machine. The dSPACE is used to realize the interaction of analog and digital quantities between the inverter and the control model in the computer (PC) that is employed to compile the algorithm of the control system and monitor control data. The PWM frequency and sampling frequency are 10 kHz. The switching frequency of the inverter is 10k Hz. A load machine is connected to the HMMM. A set of DC power supplies are connected to this test rig.



(a)



(b)

Fig. 2.9. Test platform for HMMM. (a) Experiment and control equipment. (b) Prototype and test rig.

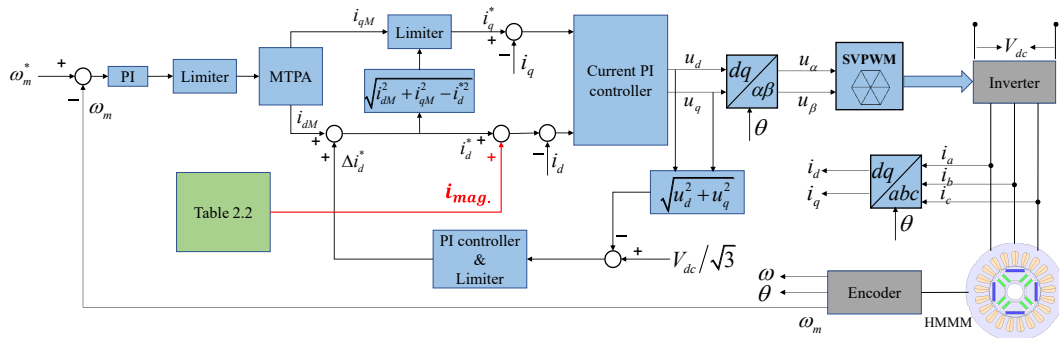


Fig. 2.10. Overall control system for experimental validation.

The overall control system for the tests is presented in Fig. 2.10. A conventional single magnetizing current pulse control method is adopted. The magnetizing current pulse is generated by the LUT 2.2 in section 2.4. The parameters for the speed PI controller are $k_p = 0.01$, $k_i = 0.001$. The parameters for current PI controller are $k_p = 50$, $k_i = 50$, for both dq -axis currents. The limit for current PI controller is $2V_{dc}/3$. The parameters for voltage PI controller are $k_p = 0$, $k_i = 0.5$. The parameters for the PI controller are tested one by one to find out the optimal one. The limiters for the speed PI controller and the voltage PI controller are I_m , which

is 7.5 A for the machine. The limiter for i_{qM} is $\sqrt{i_{dM}^2 + i_{qM}^2} - i_d^*$.

2.5.2 Performance on Demagnetization Points

First, the test on the performance of MS manipulation on the intersection and on the other points are compared. The schematic diagram is shown in Fig. 2.11. Three switch points are selected, switch point 1 (before the intersection), intersection, switch point 2 (after the intersection). “Switch points” means the “MS manipulation points”. The main parameters for the experiments are listed in Table 2.3.

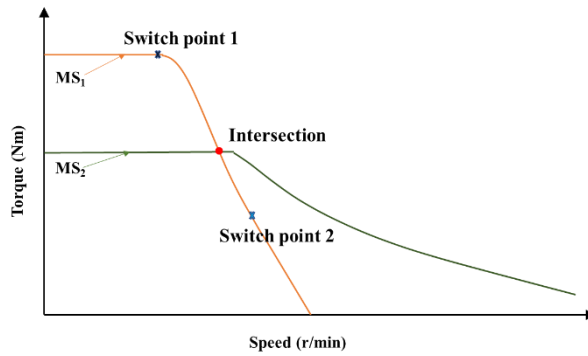


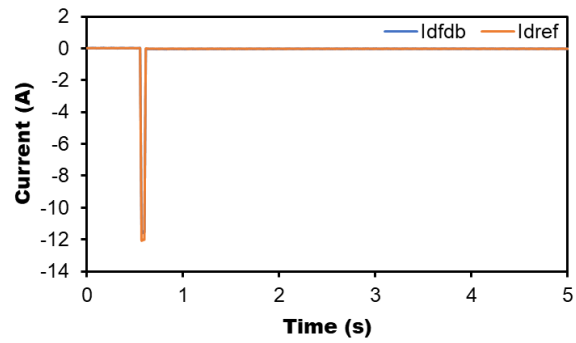
Fig. 2.11. Schematic diagram of MS manipulation performance comparison.

Table 2.3. Main parameters for MS manipulation performance comparison.

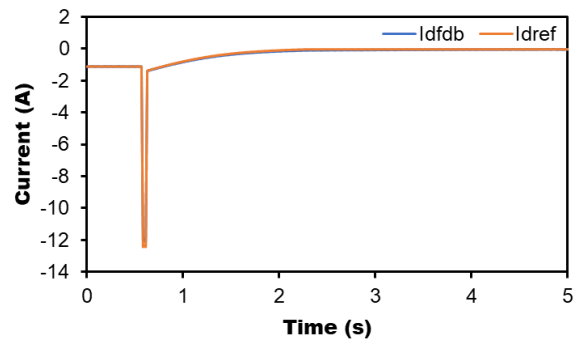
Item	Symbol	Value
DC link voltage	V_{dc}	80V
Rated current (RMS)	I_m	7.5A
PM flux linkage at MS ₁	ψ_{m1}	0.182Wb
d -axis inductance at MS ₁	L_{d1}	20.0mH
q -axis inductance at MS ₁	L_{q1}	14.2mH
PM flux linkage at MS ₂	ψ_{m2}	0.145Wb
d -axis inductance at MS ₂	L_{d2}	17.3mH
q -axis inductance at MS ₂	L_{q2}	11.0mH
Demagnetization current pulse	$I_{mag.12}$	-12A
Speed on switch point 1	Speed ₁	300r/min
Speed on intersection	Speed ₂	450r/min
Speed on switch point 2	Speed ₃	500r/min

The measured results are shown in Fig. 2.12. The demagnetizations on the three switch points with the same demand demagnetizing current pulse are tested. It can be observed that the speed fluctuation caused by the MS manipulation on the intersection is smaller than on the other two switch points as shown in Fig. 2.12(c). The demagnetization measured results meet expectations. After demagnetization process, the dq -axis currents can be controlled very well as shown in Fig. 2.12(a) and Fig. 2.12(b). The gradually changing in d -axis current after the MS manipulation is caused by PM flux linkage reduction. The demagnetization process decreases the PM flux linkage of the machine. Then, the flux-weakened degree is reduced, and the integral part in the voltage PI control decreases gradually after the MS change. After the demagnetization, the degree of flux weakening region decreases, which leads to the reduction in the amplitude of d -axis armature current at steady state. The spike caused by the demagnetization process in the dq -axis voltages and torque as shown in Fig. 2.12(e) and Fig. 2.12(d) is not a problem since the system inertia can filter it out.

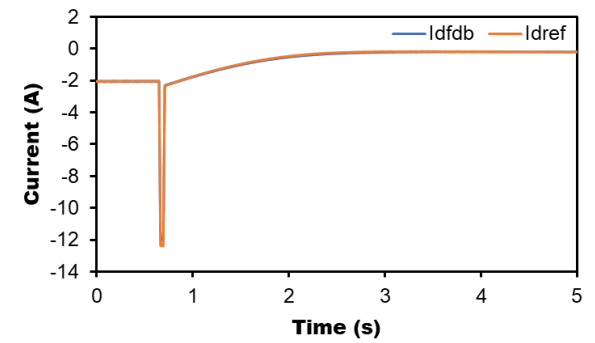
Switch point 1



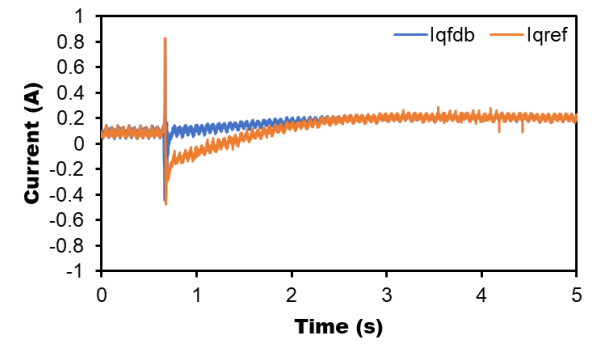
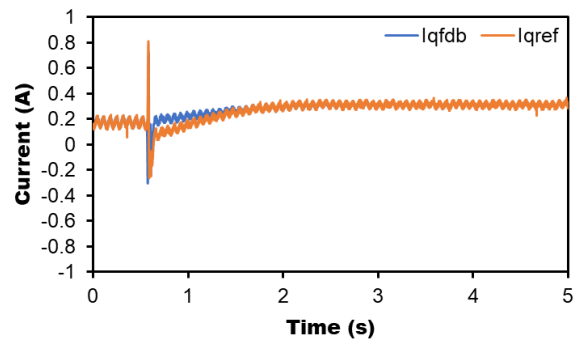
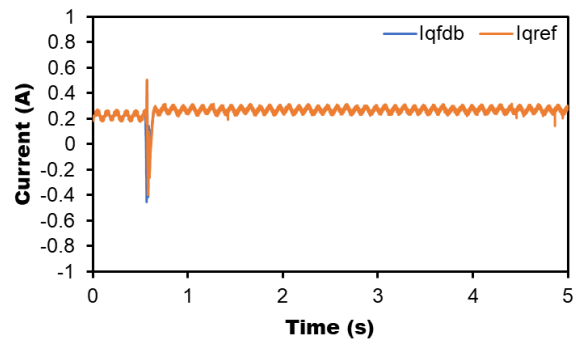
Intersection



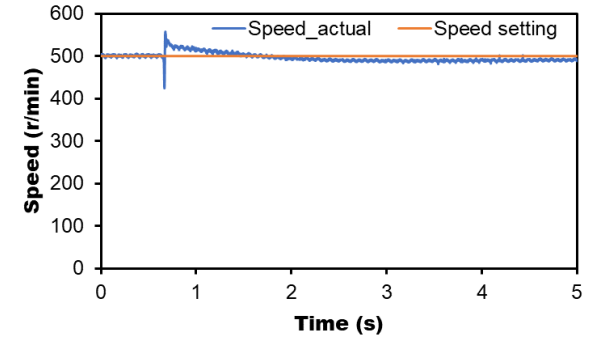
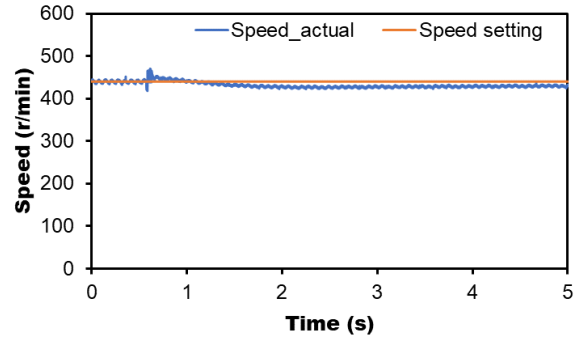
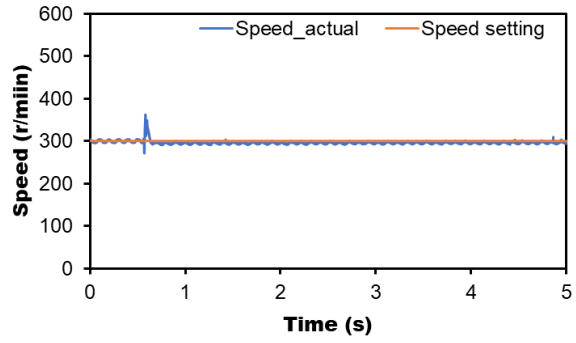
Switch point 2



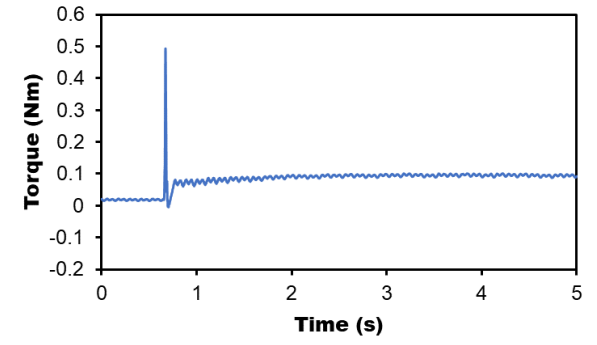
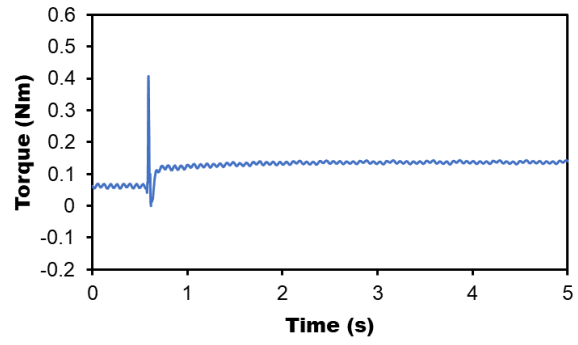
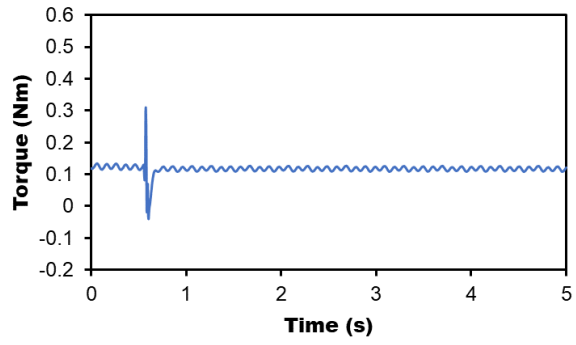
(a) d -axis current



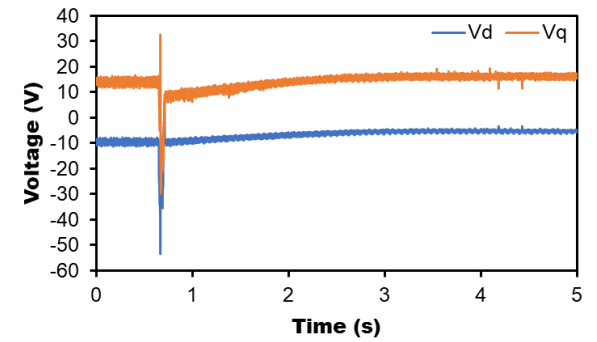
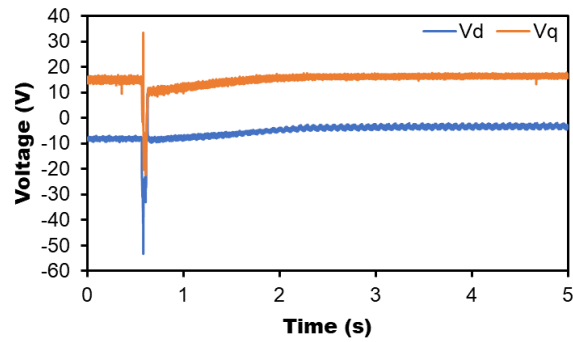
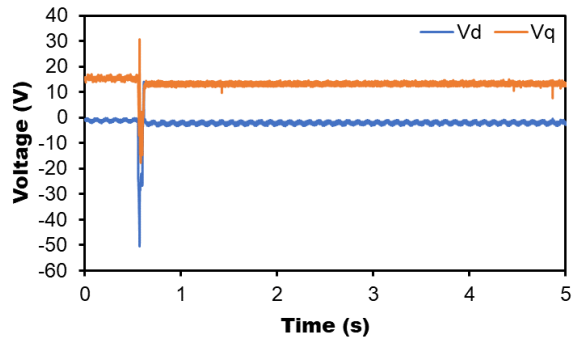
(b) q -axis current



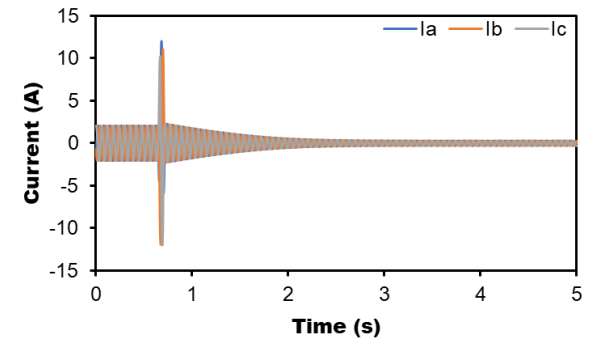
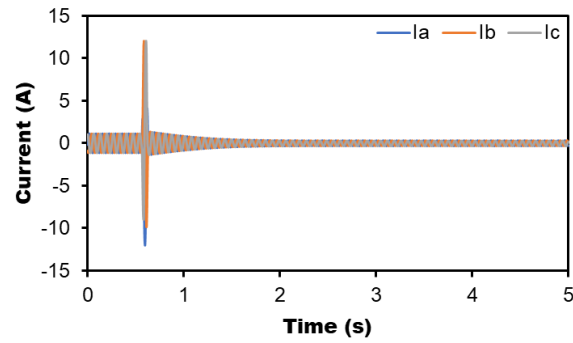
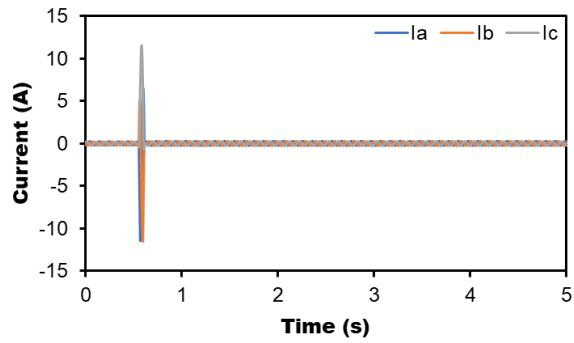
(c) Speed



(d) Torque



(e) dq -axis voltages



(f) Three-phase currents

Fig. 2.12. Measured results of demagnetization with -12 A demagnetizing current pulse on three points. (a) d -axis current. (b) q -axis current. (c) Speed. (d) Torque. (e) dq -axis voltages. (f) Three-phase currents.

2.5.3 Optimal Number of Demagnetization Instants

In Fig. 2.13, the demagnetization is only processed once, the oscillations caused by the MS manipulation are significant, especially in the q -axis current and torque, which means that it is not the optimal number for demagnetization instants. Then, under the same experimental conditions, the dual demagnetization on the DPs to achieve the same MS are tested. Three MSs are selected including the same initial MS and final MS as the test in Fig. 2.13. The schematic diagram is shown in Fig. 2.14. The main parameters are listed in Table 2.4.

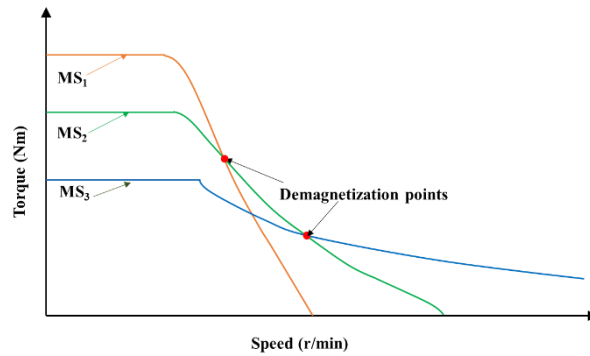
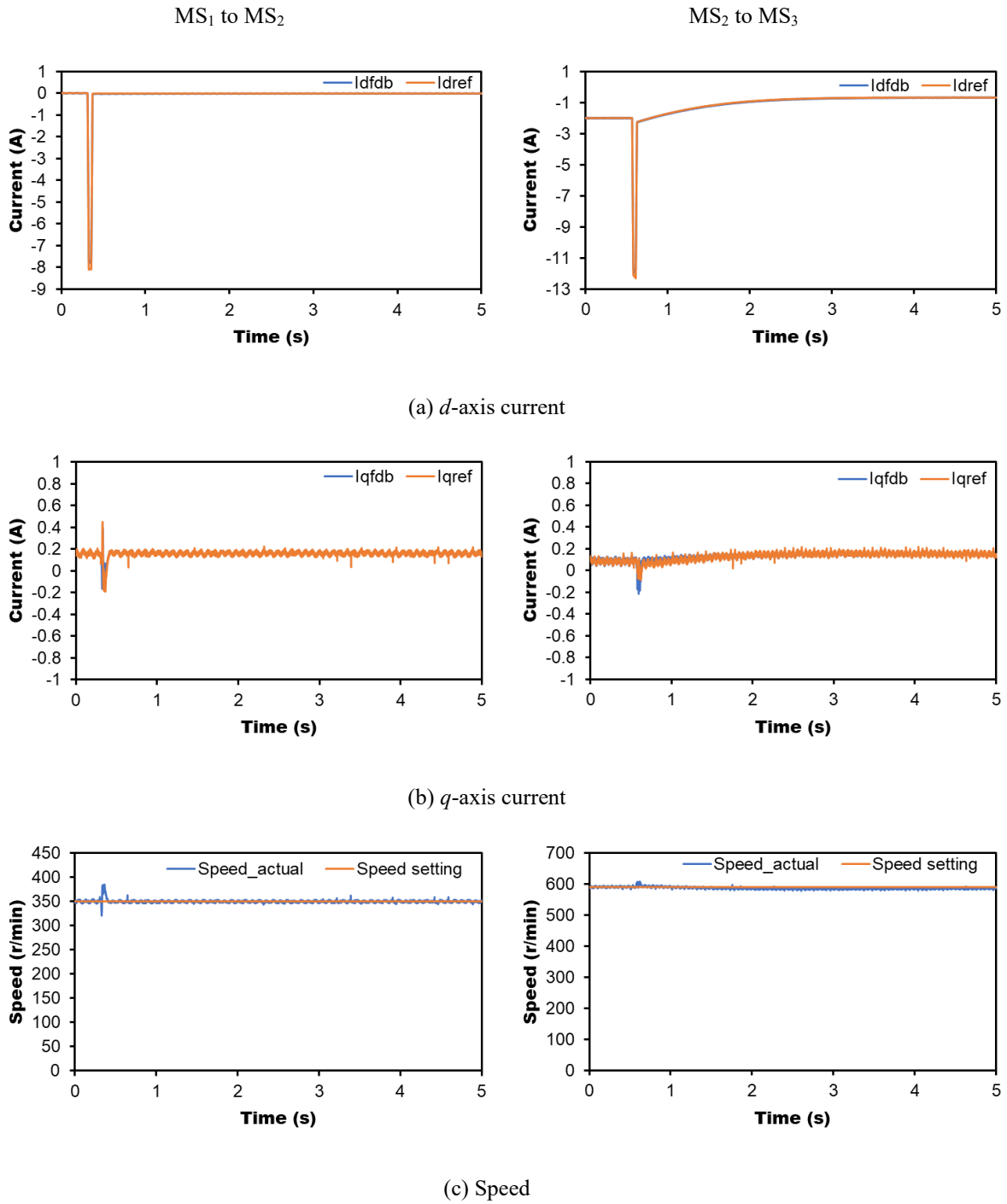


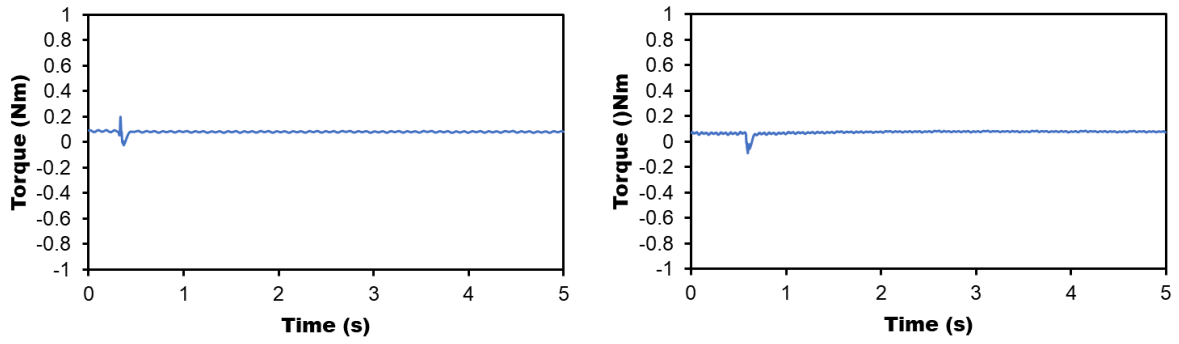
Fig. 2.13. Schematic diagram of dual demagnetization.

Table 2.4. Main parameters for dual demagnetization test.

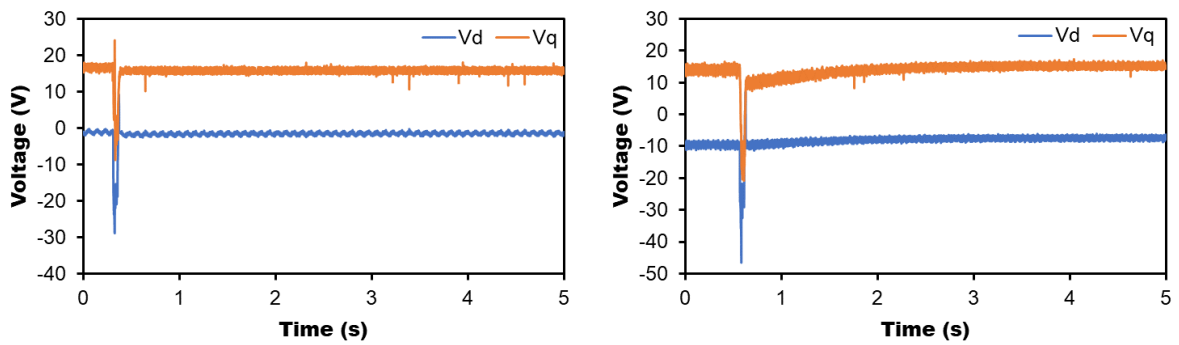
Item	Symbol	Value
DC link voltage	V_{dc}	80V
Rated current (RMS)	I_m	7.5A
PM flux linkage at MS ₁	ψ_{m1}	0.182Wb
d -axis inductance at MS ₁	L_{d1}	20.0mH
q -axis inductance at MS ₁	L_{q1}	14.2mH
PM flux linkage at MS ₂	ψ_{m2}	0.17Wb
d -axis inductance at MS ₂	L_{d2}	18.7mH
q -axis inductance at MS ₂	L_{q2}	12.6mH
PM flux linkage at MS ₃	ψ_{m3}	0.145Wb
d -axis inductance at MS ₃	L_{d3}	17.3mH
q -axis inductance at MS ₃	L_{q3}	11.0mH
Demagnetization current pulse1	$I_{mag.12}$	-8A
Demagnetization current pulse2	$I_{mag.23}$	-12A

The measured results are shown in Fig. 2.14. The fluctuation in q -axis current, speed and torque during MS manipulation as shown in Fig. 2.14(b), Fig. 2.14(c) and Fig. 2.14(d) is mitigated comparing with the measured results in Fig. 2.12. The changes between MSs such as the PM flux linkage and dq -axis inductances become small, the oscillations caused by the MS manipulation will be reduced.

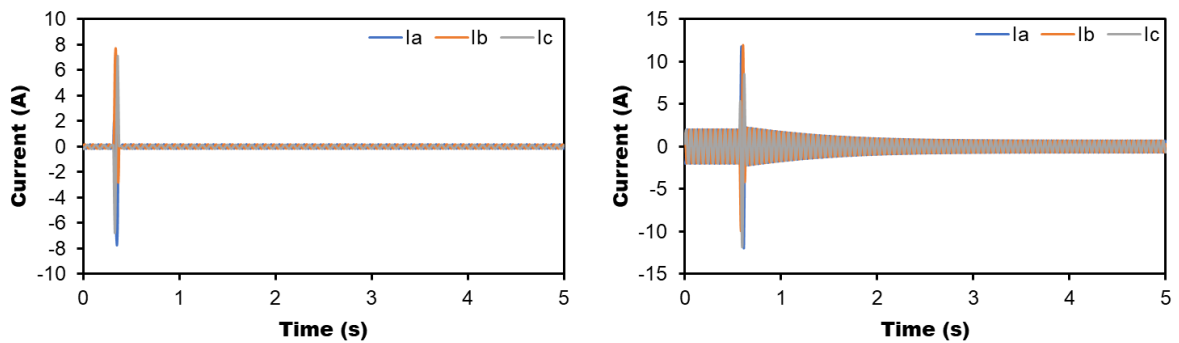




(d) Torque



(e) dq -axis voltages



(f) Three-phase currents

Fig. 2.14. Measured results of dual demagnetization. (a) d -axis current. (b) q -axis current. (c) Speed. (d) Torque. (e) dq -axis voltages. (f) Three-phase currents.

To further verify the optimal number of demagnetization instant, demagnetization for three times is tested. Four MSs are selected with the same initial MS and final MS. The scheme is shown in Fig. 2.15. The main parameters are listed in Table 2.5.

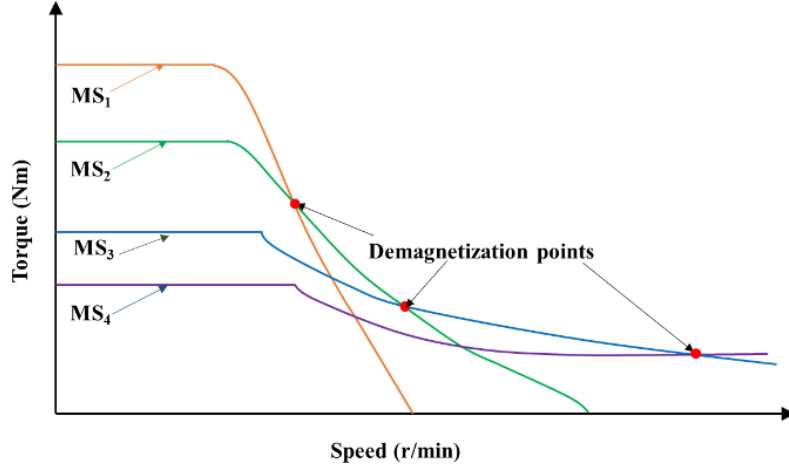


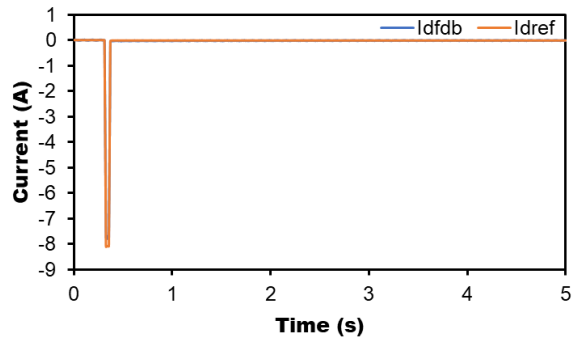
Fig. 2.15. Schematic diagram of demagnetization for three times.

Table 2.5. Main parameters for demagnetization three times test.

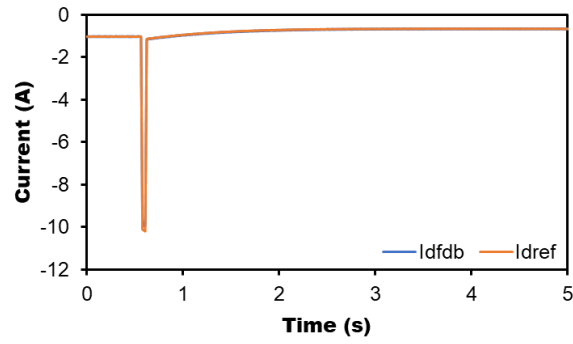
Item	Symbol	Value
DC link voltage	V_{dc}	80V
Rated current (RMS)	I_m	7.5A
PM flux linkage at MS ₁	ψ_{m1}	0.182Wb
d -axis inductance at MS ₁	L_{d1}	20.0mH
q -axis inductance at MS ₁	L_{q1}	14.2mH
PM flux linkage at MS ₂	ψ_{m2}	0.17Wb
d -axis inductance at MS ₂	L_{d2}	18.7mH
q -axis inductance at MS ₂	L_{q2}	12.6mH
PM flux linkage at MS ₃	ψ_{m3}	0.158Wb
d -axis inductance at MS ₃	L_{d3}	18.0mH
q -axis inductance at MS ₃	L_{q3}	11.6mH
PM flux linkage at MS ₄	ψ_{m4}	0.145Wb
d -axis inductance at MS ₄	L_{d4}	17.3mH
q -axis inductance at MS ₄	L_{q4}	11.0mH
Demagnetization current pulse1	$I_{mag.12}$	-8A
Demagnetization current pulse2	$I_{mag.23}$	-10A
Demagnetization current pulse3	$I_{mag.34}$	-12A

The measured results are shown in Fig. 2.16. The speed fluctuations caused by MS manipulation can rarely be observed with the times of MS manipulation increasing in Fig. 2.16(c). While this does not mean that the more times of MS manipulation, the better. The MS manipulation causes a larger magnetizing current pulse in the drive system, which will cause significant fluctuation in three-phase currents. The oscillation in dq -axis voltages and three-phase currents are still very significant in Fig. 2.16(e) and Fig. 2.16(f), and this cannot be avoided due to the injection of magnetizing current pulse with large amplitude. Therefore, considering the performance during MS manipulation and the effects due to the magnetizing current pulse, dual demagnetization for the investigated HMMM to achieve the final MS is an optimal option.

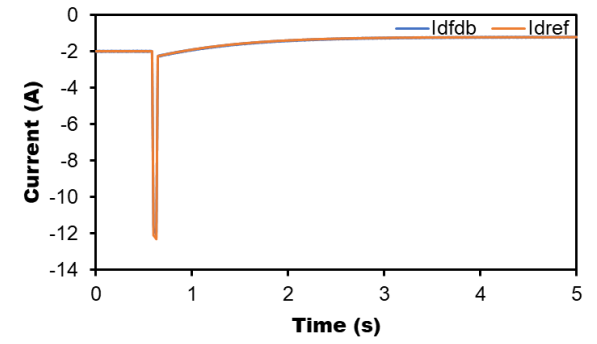
MS₁ to MS₂



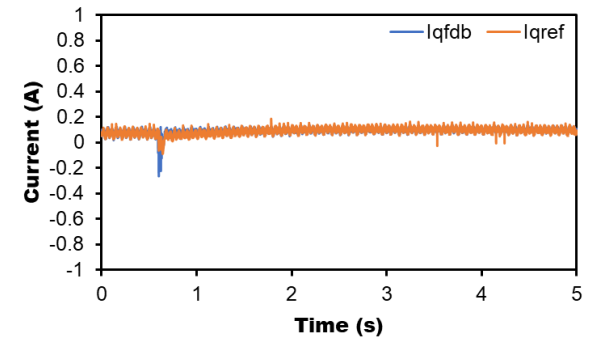
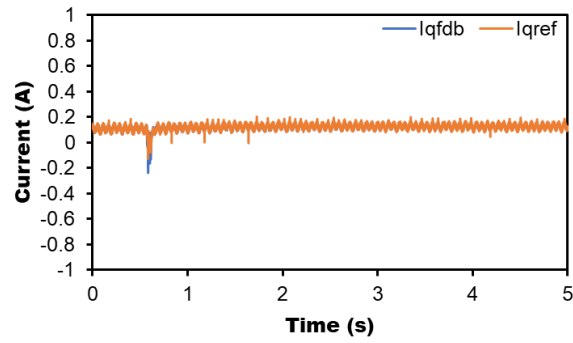
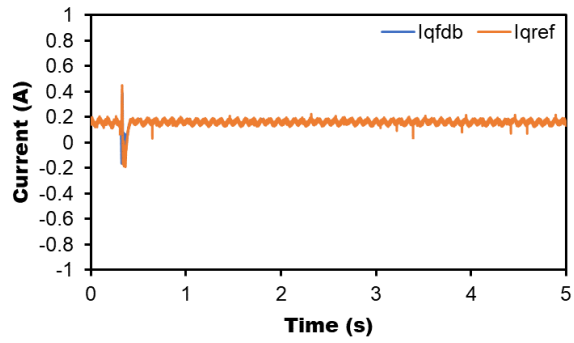
MS₂ to MS₃



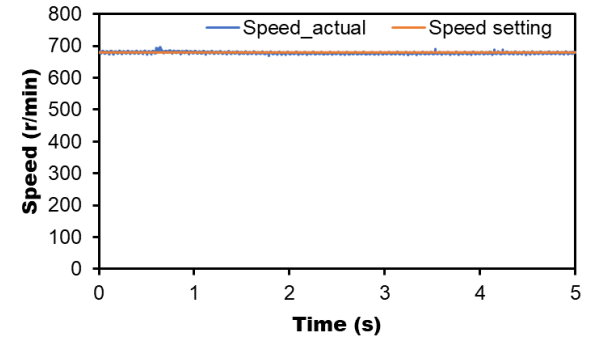
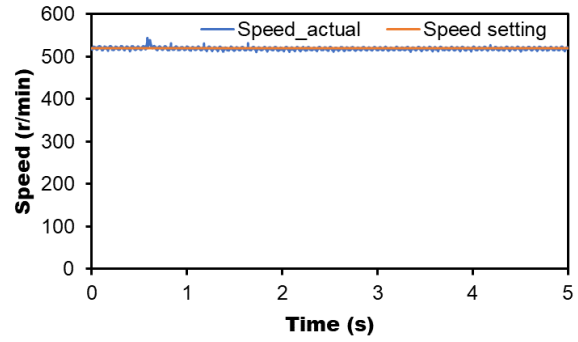
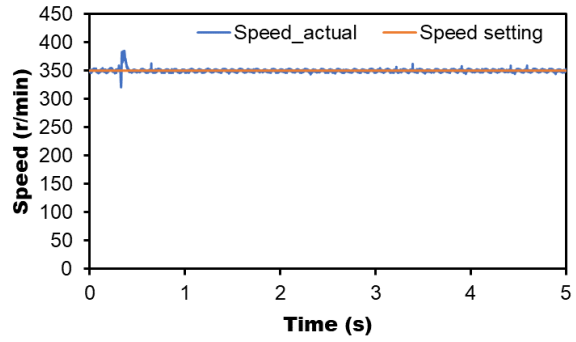
MS₃ to MS₄



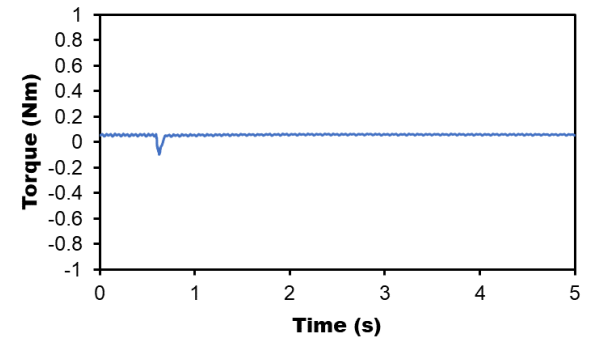
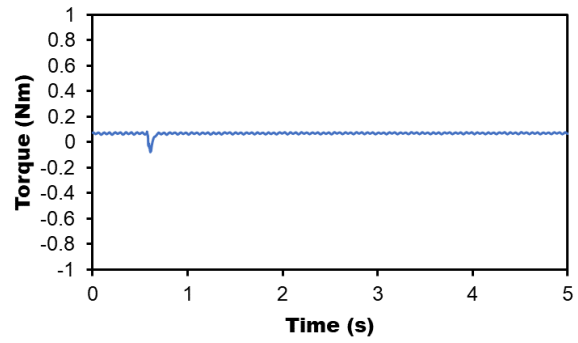
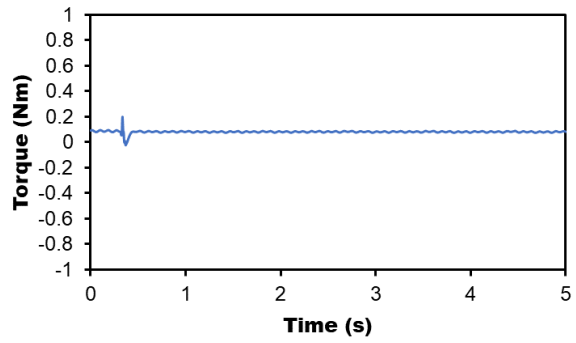
(a) *d*-axis current



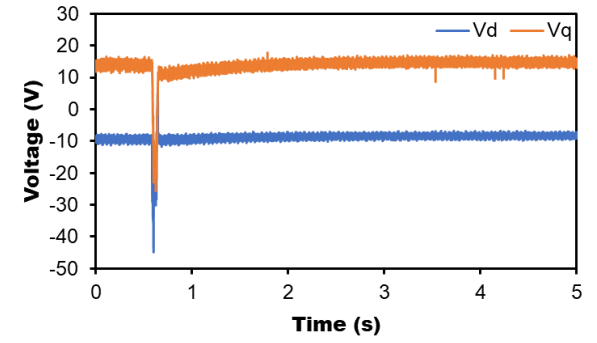
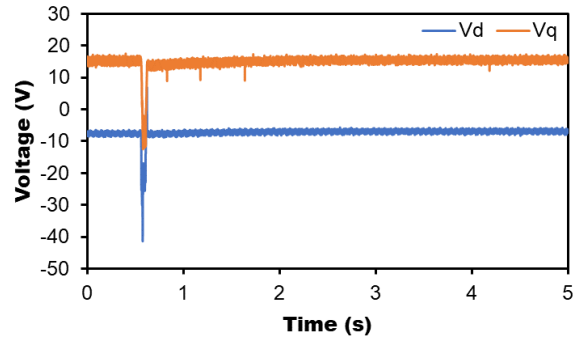
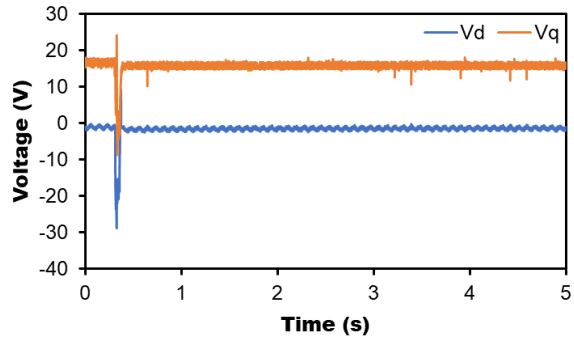
(b) *q*-axis current



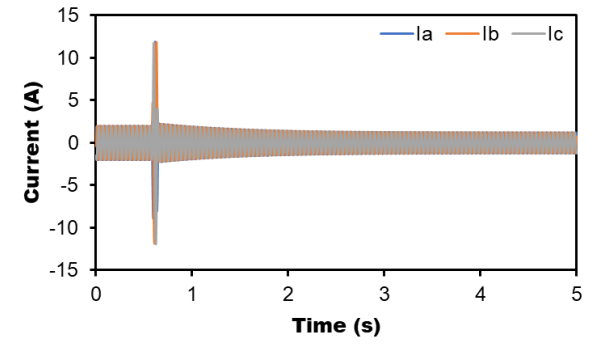
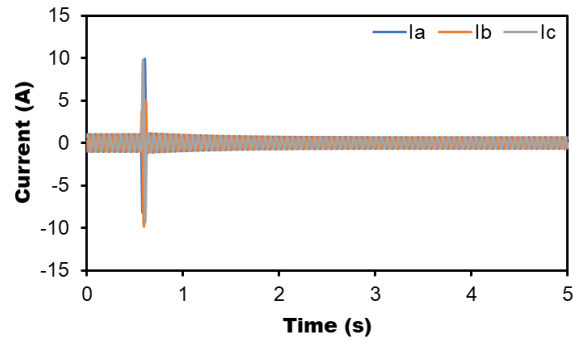
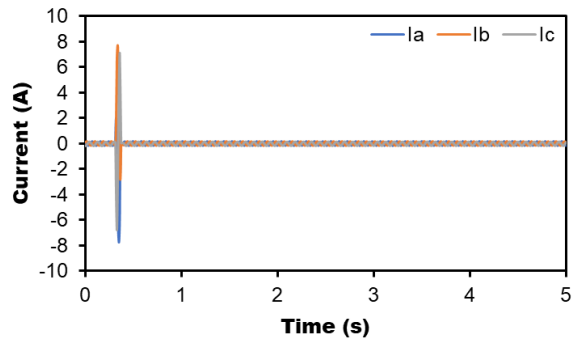
(c) Speed



(d) Torque



(e) dq -axis voltages



(f) Three-phase currents

Fig. 2.16. Measured results of MS manipulation for three times. (a) d -axis current. (b) q -axis current. (c) Speed. (d) Torque. (e) dq -axis voltages. (f) Three-phase currents.

2.5.4 Verification on Remagnetization

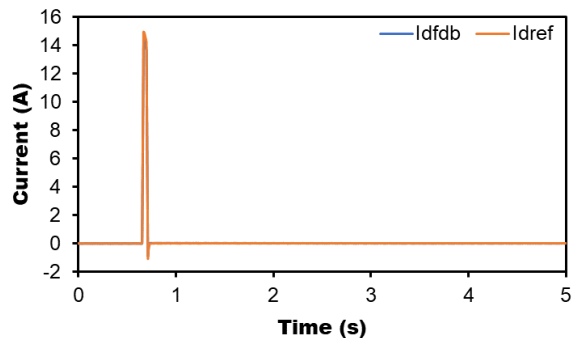
First, the test on the performance of MS remagnetization on the intersection and on the other points are compared as the same as the demagnetization validation in section 2.5.2. Three switch points are selected, the switch point 1 (before the intersection), the intersection point, and the switch point 2 (after the intersection). The main parameters for the experiments are listed in Table 2.6.

Table 2.6. Main parameters for MS remagnetization performance comparison.

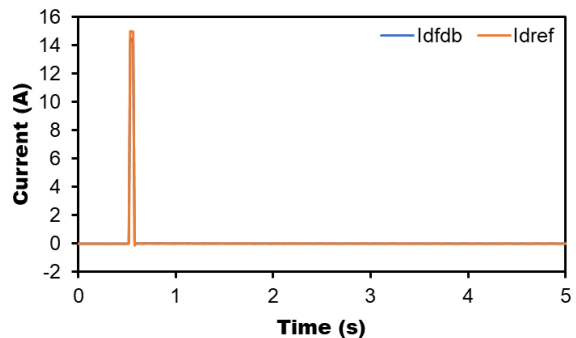
Item	Symbol	Value
DC link voltage	V_{dc}	80V
Rated current (RMS)	I_m	7.5A
PM flux linkage at MS ₁	ψ_{m1}	0.125Wb
d -axis inductance at MS ₁	L_{d1}	15.1mH
q -axis inductance at MS ₁	L_{q1}	7.83mH
PM flux linkage at MS ₂	ψ_{m2}	0.18Wb
d -axis inductance at MS ₂	L_{d2}	20.0mH
q -axis inductance at MS ₂	L_{q2}	14.2mH
Remagnetization current pulse	$I_{mag.12}$	15A
Speed on switch point 1	Speed ₁	300r/min
Speed on intersection	Speed ₂	200r/min
Speed on switch point 2	Speed ₃	100r/min

The measured results are shown in Fig. 2.17. The remagnetizations on the three selected switch points with the same demand remagnetizing current pulse are tested. It can be observed that the speed fluctuation caused by the MS manipulation on the intersection point is much smaller than on the other two switch points as shown in Fig. 2.17(c), which is the same as the demagnetization validation and consistent with the theoretical analysis.

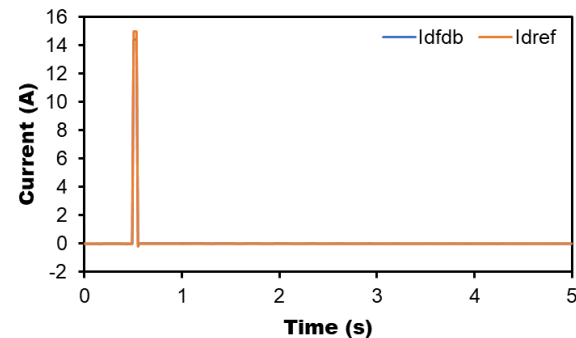
Switch point 1



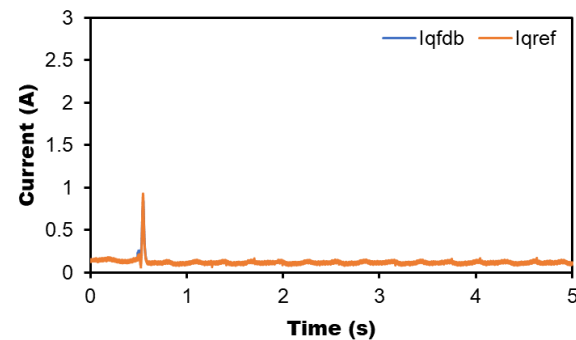
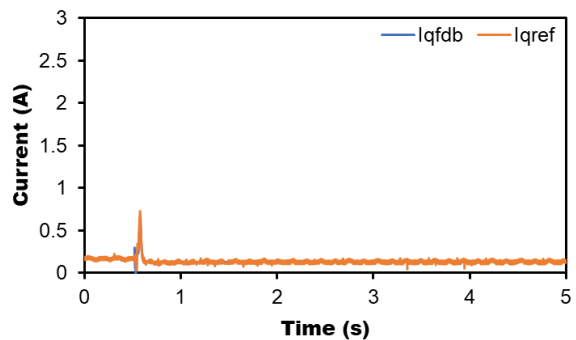
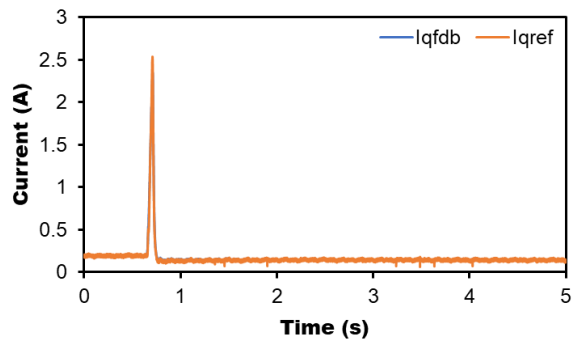
Intersection point



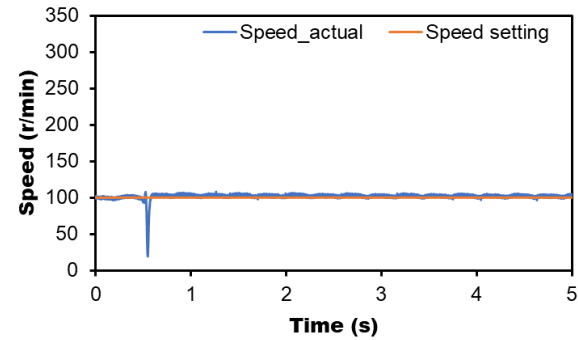
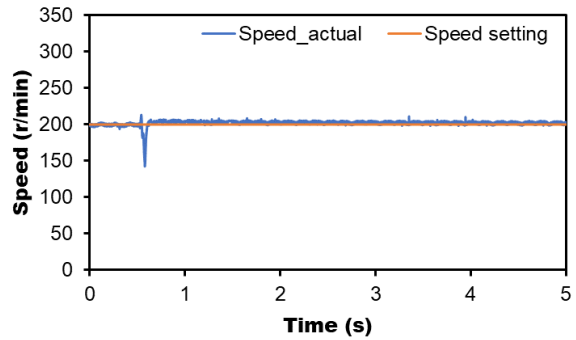
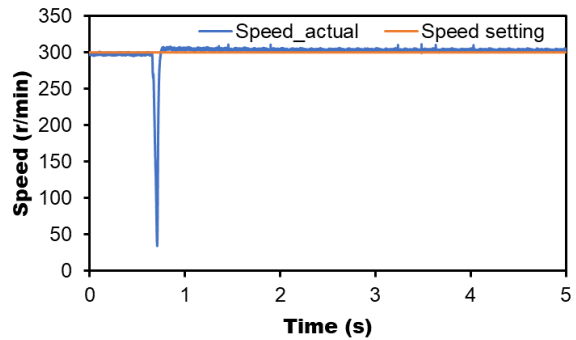
Switch point 2



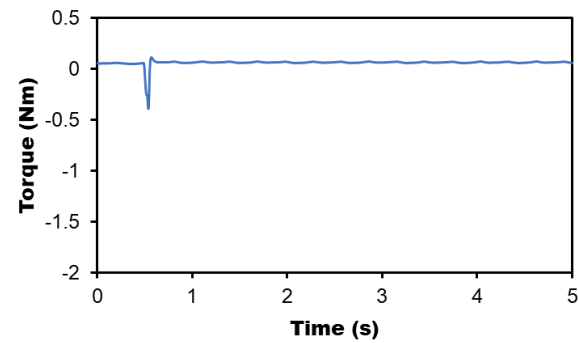
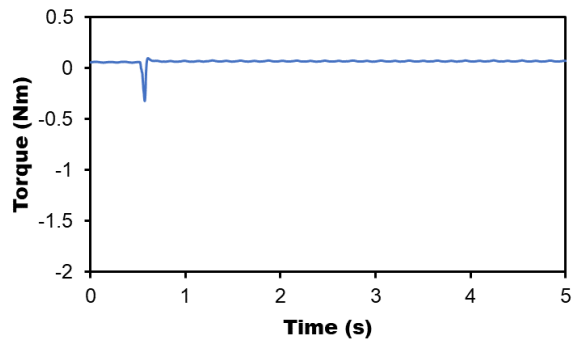
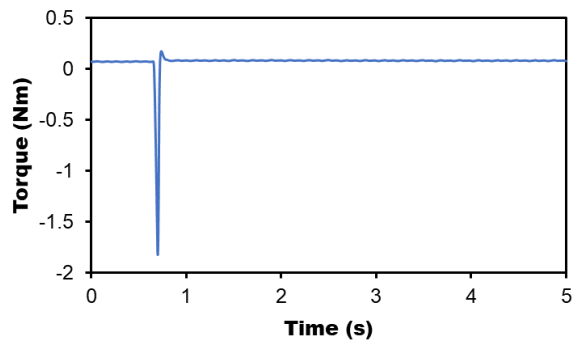
(a) d -axis current



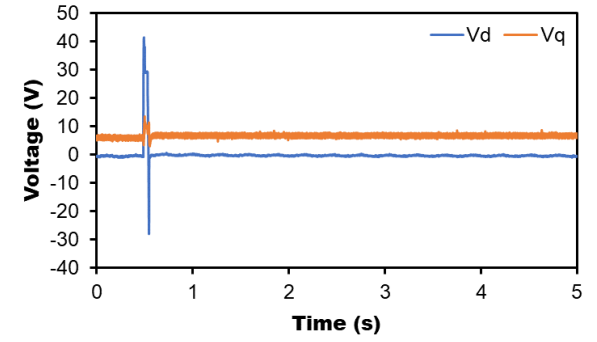
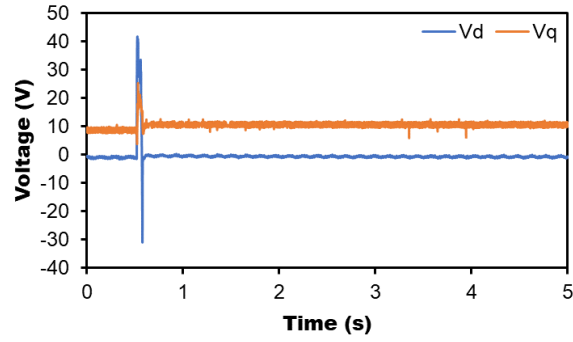
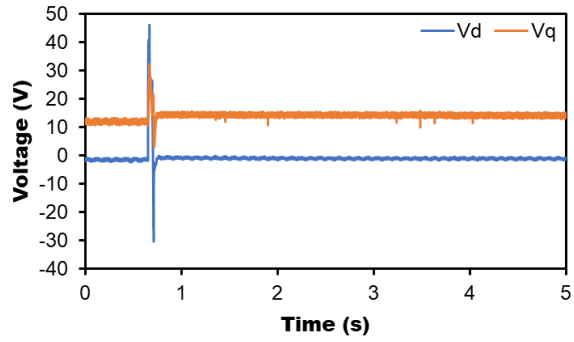
(b) q -axis current



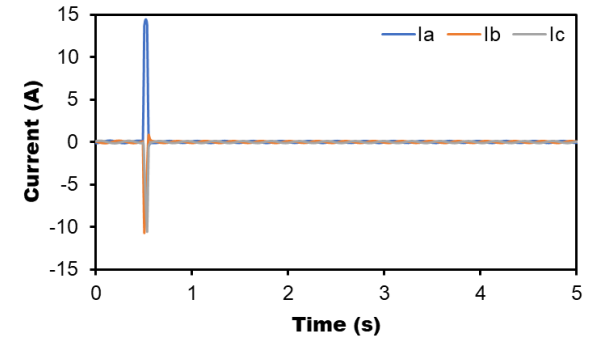
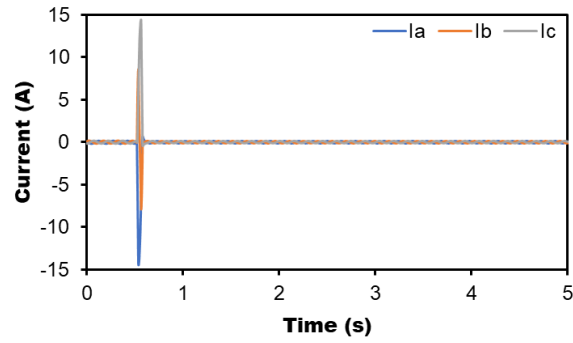
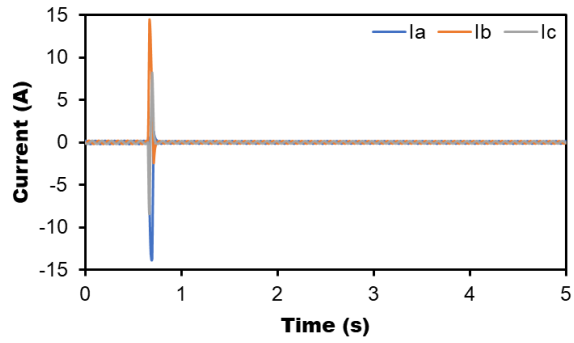
(c) Speed



(d) Torque



(e) *dq*-axis voltages



(f) Three-phase currents

Fig. 2.17. Measured results of remagnetization with 15 A remagnetizing current pulse on three points. (a) *d*-axis current. (b) *q*-axis current. (c) Speed. (d) Torque. (e) *dq*-axis voltages. (f) Three-phase currents.

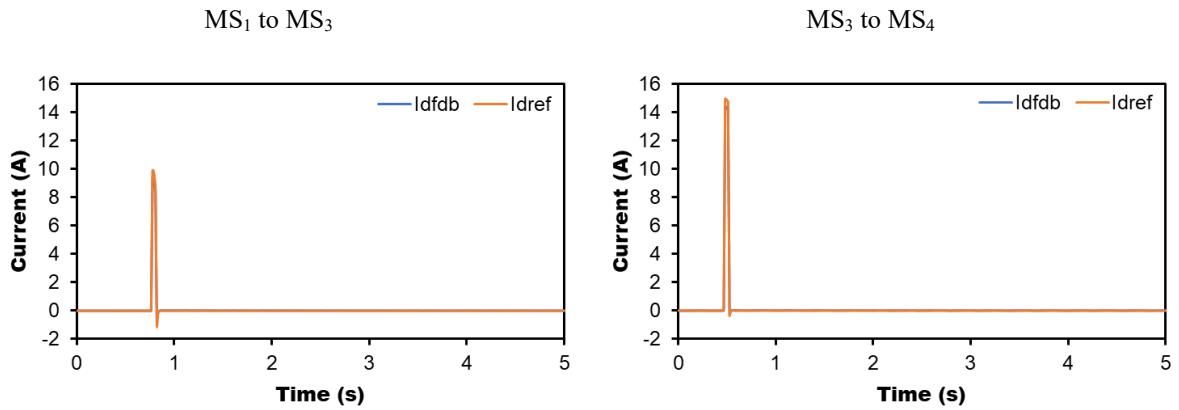
Then, the tests for the optimal number of remagnetization are processed with dual and three times, respectively. The initial MS and final MS are the same as the once remagnetization above. The main parameters are listed in Table 2.7. MS₁, MS₃, and MS₄ are selected for the dual remagnetization test, and the measured results are shown in Fig. 2.18. MS₁, MS₂, MS₃, and MS₄ are selected for the remagnetization three times test, and the measured results are shown in Fig. 2.19.

Table 2.7. Main parameters for remagnetization three times test.

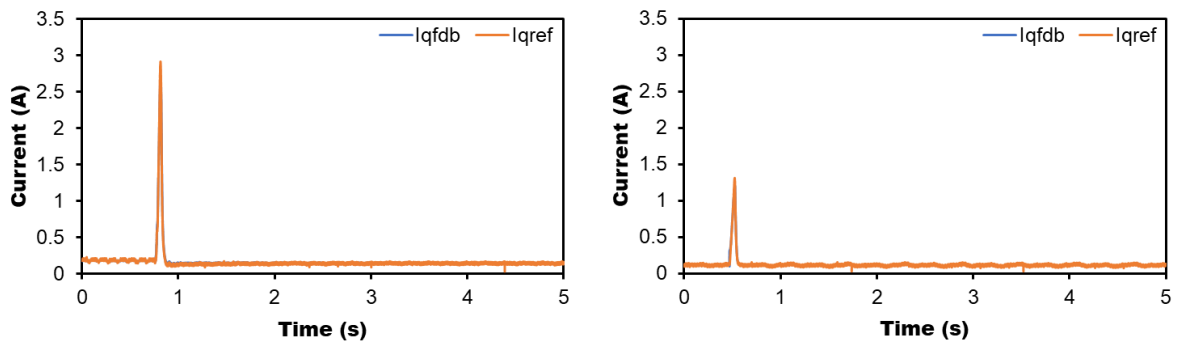
Item	Symbol	Value
DC link voltage	V_{dc}	80V
Rated current (RMS)	I_m	7.5A
PM flux linkage at MS ₁	ψ_{m1}	0.125Wb
d -axis inductance at MS ₁	L_{d1}	15.1mH
q -axis inductance at MS ₁	L_{q1}	7.83mH
PM flux linkage at MS ₂	ψ_{m2}	0.145Wb
d -axis inductance at MS ₂	L_{d2}	16.5mH
q -axis inductance at MS ₂	L_{q2}	10.0mH
PM flux linkage at MS ₃	ψ_{m3}	0.17Wb
d -axis inductance at MS ₃	L_{d3}	19.0mH
q -axis inductance at MS ₃	L_{q3}	13.0mH
PM flux linkage at MS ₄	ψ_{m4}	0.18Wb
d -axis inductance at MS ₄	L_{d4}	20.0mH
q -axis inductance at MS ₄	L_{q4}	14.2mH
Remagnetization current pulse1	$I_{mag.12}$	5A
Remagnetization current pulse2	$I_{mag.23}$	10A
Remagnetization current pulse3	$I_{mag.34}$	15A

It can be observed that the oscillations caused by remagnetization are much larger than the demagnetization performance in section 2.5.3. With the large amplitude of positive remagnetizing current pulse, the machine is flux enhanced significantly. The change in torque is too drastic to reduce its impact. This is different from the demagnetization test and cannot be avoided due to the injection of remagnetizing current pulse with large amplitude. Since

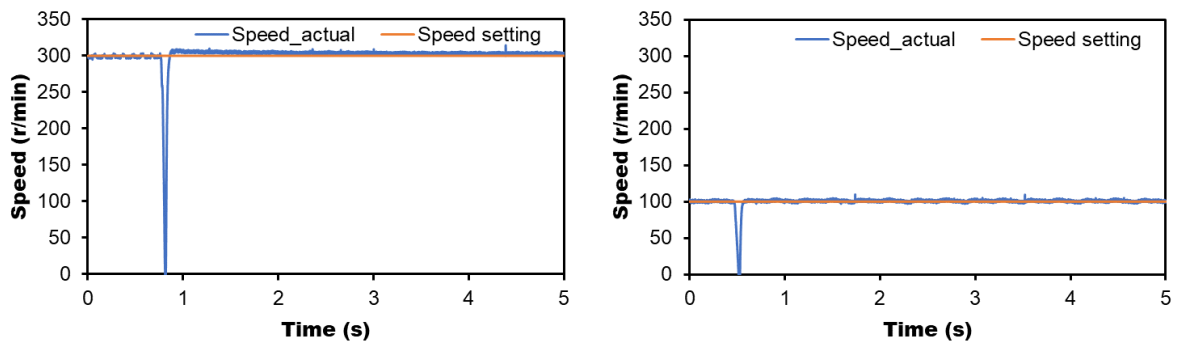
remagnetization is usually processed in the low-speed region or offline before the machine is operating to improve the torque performance. Therefore, considering the performance during remagnetization and the effects due to the remagnetizing current pulse, remagnetization once for the investigated HMMM to achieve the final MS is an optimal option.



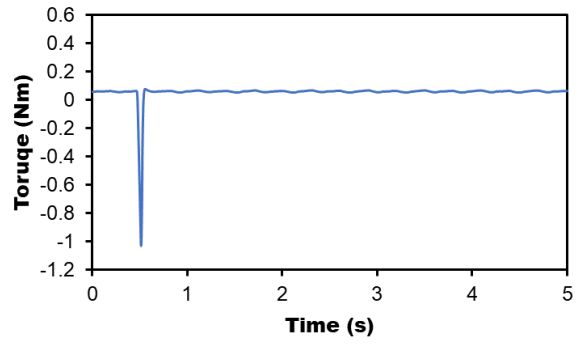
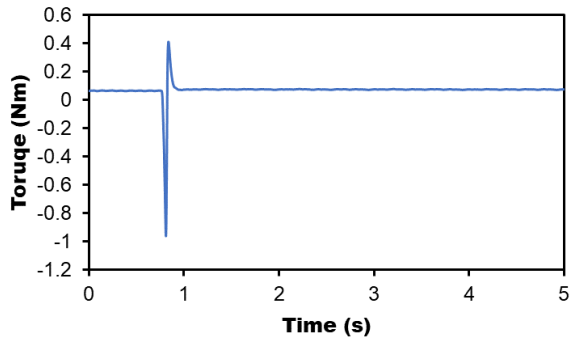
(a) d -axis current



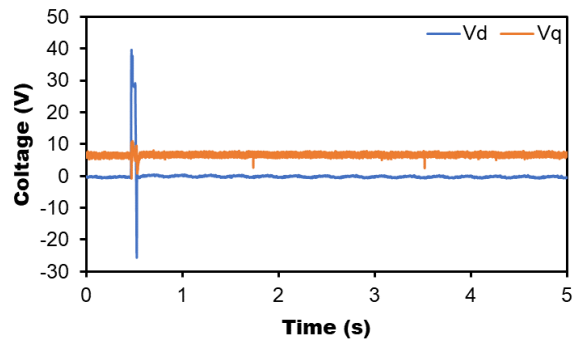
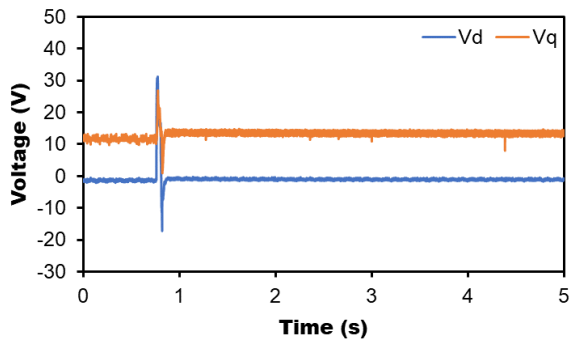
(b) q -axis current



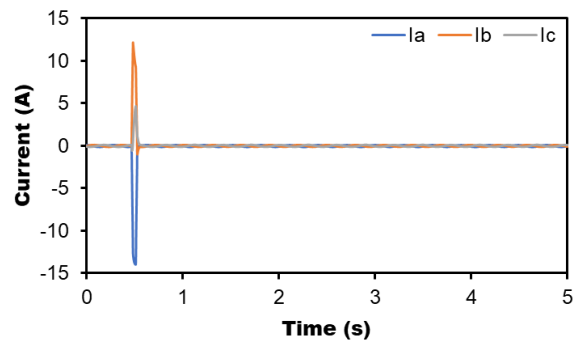
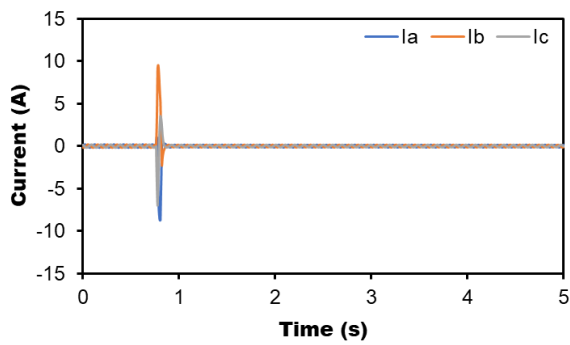
(c) Speed



(d) Torque



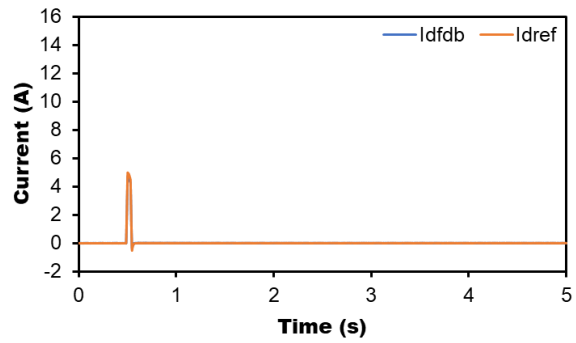
(e) dq -axis voltages



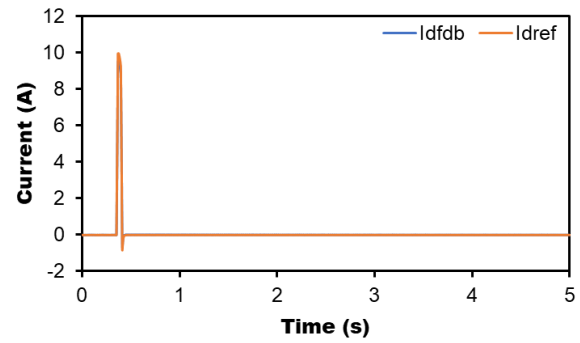
(f) Three-phase currents

Fig. 2.18. Measured results of dual remagnetization. (a) d -axis current. (b) q -axis current. (c) Speed. (d) Torque. (e) dq -axis voltages. (f) Three-phase currents.

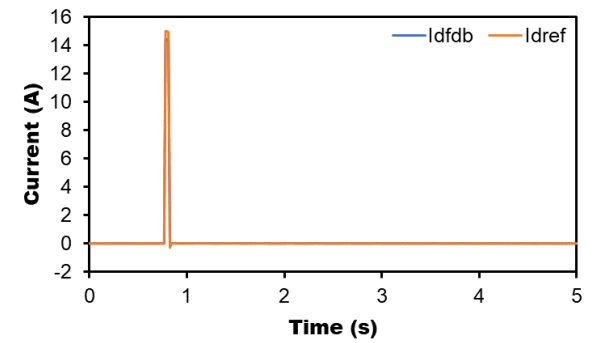
MS₁ to MS₂



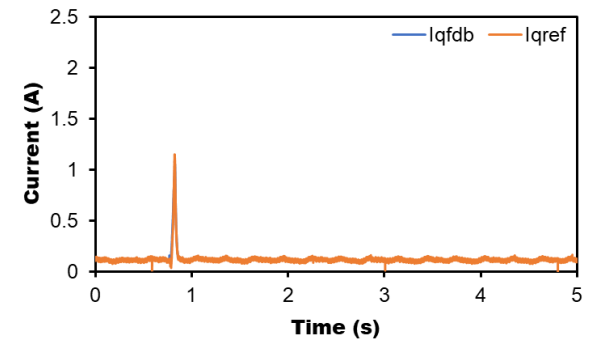
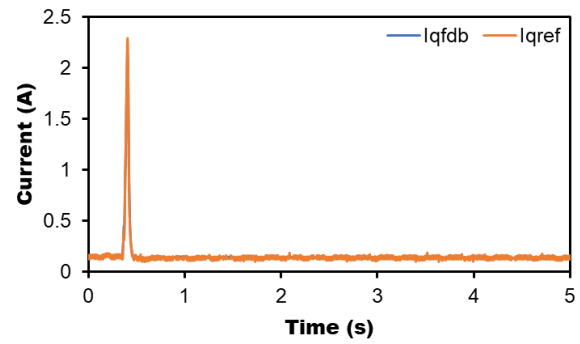
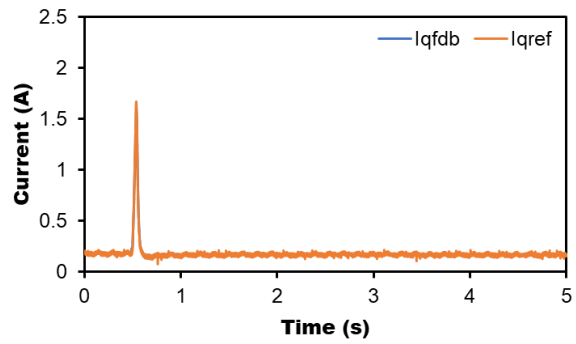
MS₂ to MS₃



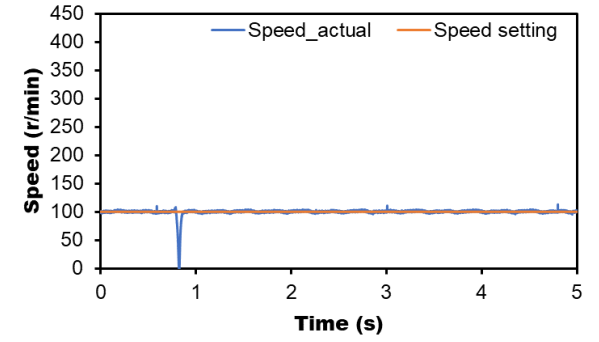
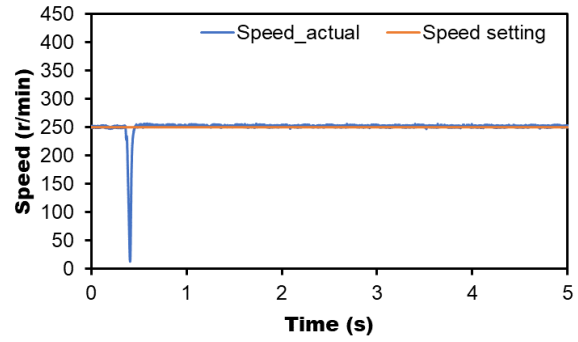
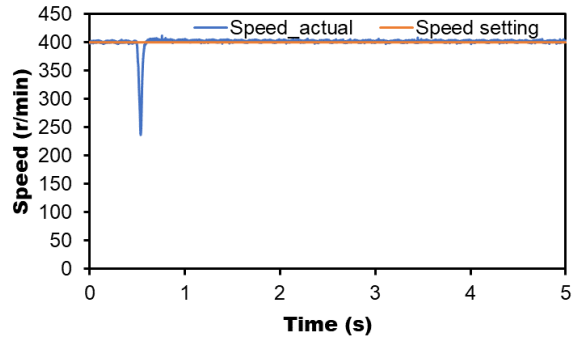
MS₃ to MS₄



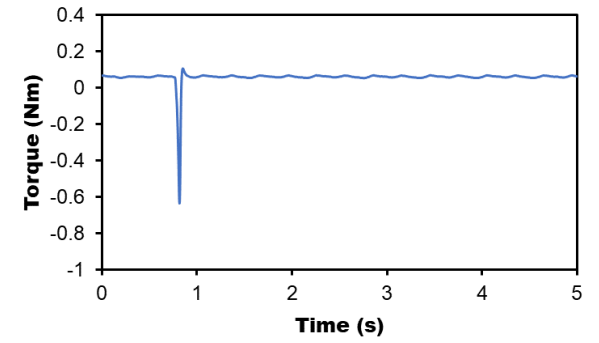
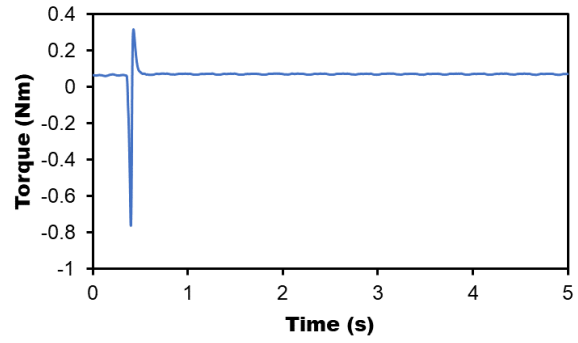
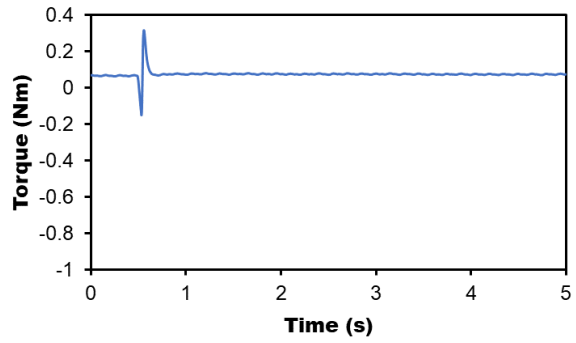
(a) d -axis current



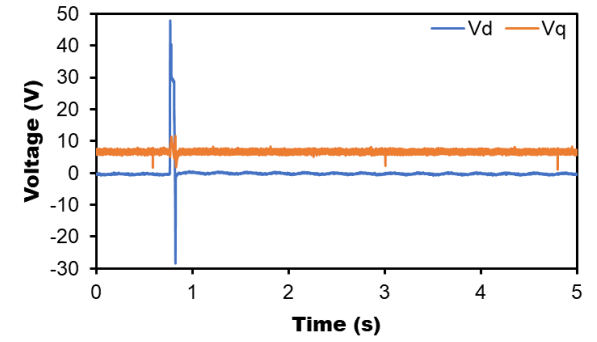
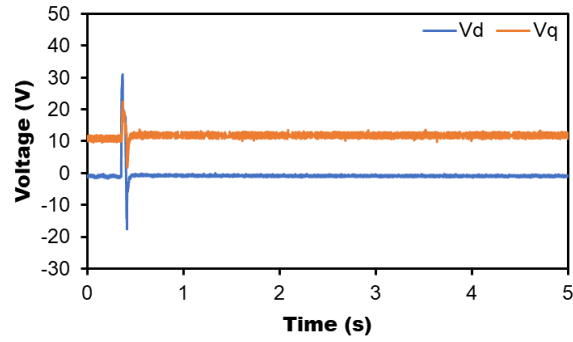
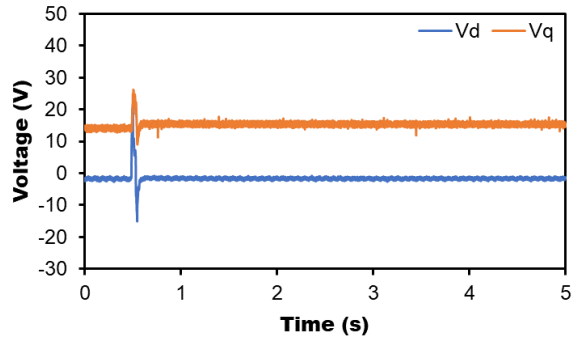
(b) q -axis current



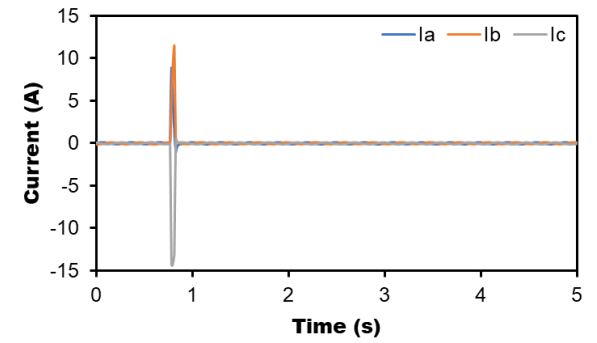
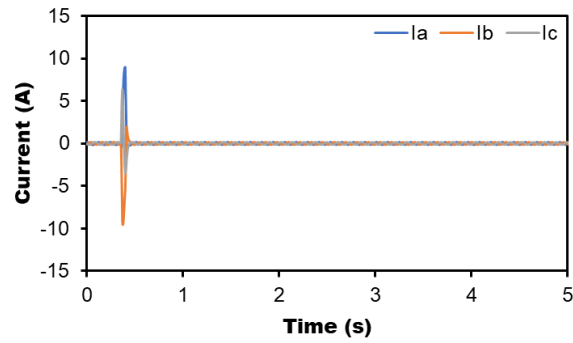
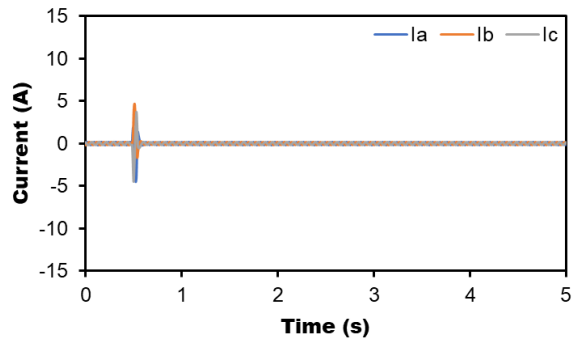
(c) Speed



(d) Torque



(e) dq -axis voltages



(f) Three-phase currents

Fig. 2.19. Measured results of remagnetization for three times. (a) d -axis current. (b) q -axis current. (c) Speed. (d) Torque. (e) dq -axis voltages. (f) Three-phase currents.

2.6 Conclusion

In this chapter, the instant, number, and performance of demagnetization for HMMM are investigated. A demagnetization grid (DG) is proposed based on the torque-speed curves of VFMM under different MSs. Demagnetization manipulation on the DG can mitigate the fluctuation in speed caused by injected magnetizing current pulse, which can be regarded as the best instant for demagnetization. Based on the analysis, a look up table containing the torque and speed information on the intersections of the torque-speed curves is used to determine demagnetization instant for VFMM. The measured results of demagnetization on the HMMM drive system show better performance on the DG, and dual demagnetization to achieve the final MS for the machine is optimal. The investigation on demagnetization is also tested on remagnetization.

CHAPTER 3 DUAL MAGNETIZING CURRENT CONTROLLER TO MITIGATE SPEED FLUCTUATION DURING MAGNETIZATION STATE MANIPULATION

When the fluctuation still affects the performance during MS manipulation or the MS manipulations are not processed on the proposed demagnetization grid, to further mitigate the speed fluctuation and improve the transient performance during MS manipulation, a novel dual magnetizing current controller is proposed. Based on the dynamic mathematical model, a q -axis current pulse is injected to compensate the torque fluctuation caused by the d -axis magnetizing current pulse, which forms a dual magnetizing current controller during MS manipulation.

3.1 Introduction

In the existing research, some scholars analyzed the topologies of VFMM [ZHU17] [HUA17a] [HUA19a] [HUA19b]. In [HUA19a], the properties of the parallel and series hybrid PM VFMMs based on the interior PM machine topology were investigated and compared. The series-type VFMM had better demagnetization withstand capability and higher torque density than the parallel-type VFMM, while the unbalanced magnetic pole arrangement makes series-type VFMM bear more evident unipolar end effect than parallel-type VFMM [HUA19b]. Thus, the parallel and series HMMM were proposed to combine the synergies of both kinds of VFMM [YAN20] [XIE20b] [ATH17] [YAN16d].

Some scholars focused on the magnetizing characteristics of the PMs in VFMM [ZHO16] [HU20b] [LIU09] [LEE08] [LYU19] [LIU08] [LIU10] [GAG17] [TAK18] [LIU23]. In [LIU09], the irreversible PM demagnetization phenomena of the VFMM under different demagnetizing magnetomotive forces were observed and investigated. A coupled finite element analysis and Preisach modeling technique were presented in [LEE08] for a VFMM to analyze the demagnetization characteristics.

The influences of design parameters on on-load demagnetization characteristics of the switched flux hybrid magnet memory machine were analyzed [LYU19], such as rotor pole numbers, split

ratio, PM thickness, rotor pole width. The influence of different PM shapes on the PM demagnetization pattern of VFMM was analyzed in [LIU08]. In [LIU10], the PM remagnetizing state of VFMM was evaluated by using finite element method incorporating with a hysteresis model. [GAG17] investigated the effects of magnet temperature on magnetization properties, such as current and flux vectors required for magnetization and demagnetization, maximum torque performance, and trajectories used for magnetization state manipulation, and a technique to mitigate the effects of magnet temperature on magnetization manipulation was also proposed.

As the crucial part for VFMM control, the MS manipulation methods were researched by many scholars [YAN19b] [YAN14a] [YU11b] [YAN18] [LYU20a] [CHE20] [LYU20b] [YU14] [HU21] [MAE14] [GAG14] [GAG16] [ZHO22a] [ATH18] [ZHO23a] [MAS15] [JIA22b] [ZHO24] [ZHO23c]. For DC magnetized VFMMs, the magnetizing current pulse (MCP) was always applied on the DC magnetizing coils combined with an H-bridge converter [YAN19b] [YAN14a] [YU11b]. For AC magnetized VFMMs, a MCP was injected into d -axis current to regulate MS without requiring extra equipment, which was much more popular in the existing research [YAN18] [LYU20a] [CHE20] [LYU20b] [YU14] [HU21] [MAE14] [GAG14] [GAG16] [ZHO22a] [ATH18] [ZHO23a] [MAS15] [JIA22b]. The transient performance during MS manipulation also brought some attentions. [ZHO23c] proposed a speed controller based on linear active disturbance rejection compensation model to reduce the speed fluctuations caused by the MS manipulation. In [ZHO24], a q -axis current reverse control method was proposed to reduce the speed fluctuation caused by the MS control, the q -axis current would be reverse directly when the torque was negative.

In this chapter, to improve the transient performance during MS manipulation for VFMM, a q -axis current pulse is injected at the same time as the injection of d -axis MCP a novel dual magnetizing current controller is proposed to mitigate the speed fluctuation. Firstly, the magnetizing properties, and the topology of the investigated HMMM are analyzed. The correlation between the MSs and the corresponding MCPs is tested offline, and the magnetizing capability of different amplitudes and time durations for the MCP is analyzed. Secondly, the torque fluctuation caused by the d -axis MCP is calculated by a model-based torque calculation. A q -axis current pulse is injected to compensate the torque fluctuation. Then, the dual magnetizing current controller is formed. Besides, a look-up table (LUT) based on the MS properties of the investigated machine are adopted to build the dual magnetizing current controller. Then, based on the HMMM control system, the transient performances of

remagnetization and demagnetization of the proposed dual magnetizing current controller are tested and compared with the conventional single magnetizing current method. The measured results show that the proposed method can mitigate the speed fluctuation caused by the MS manipulation significantly and present better dynamic performance comparing with the conventional method.

3.2 Machine Properties

3.2.1 Magnetizing Current Properties

In the experiments, the effect of the delay of data transmission and the response time of the whole experiment system cannot be ignored. Therefore, to ensure the magnetizing capability, the d -axis magnetizing current pulse is set as a trapezoidal wave, of which the amplitude time duration is 30 ms, and the time duration for both rising slope and falling slope is 10 ms. The schematic diagram of MS manipulation process is depicted in Fig. 3.1.

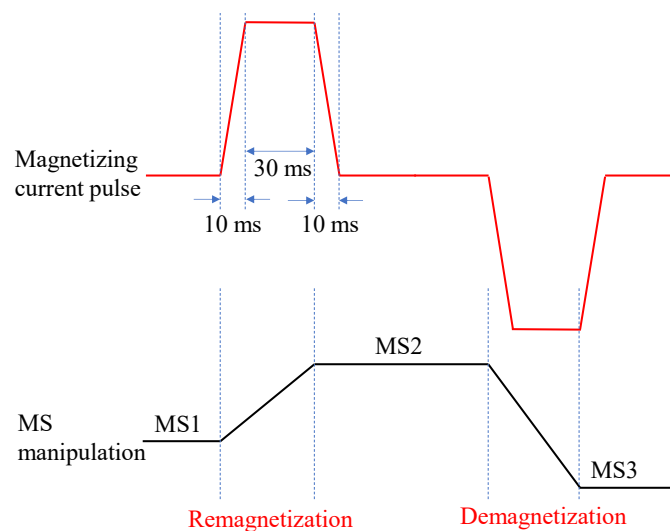


Fig. 3.1. Schematic diagram of MS manipulation.

1) Amplitude of magnetizing current pulses

The PM flux linkage (ψ_m) adjustment range of the investigated HMMM under laboratory conditions is from 0.125 to 0.195 Wb. A set of positive MCPs with amplitudes of 5, 10, 15, 20, and 25 A are used to test the MS remagnetization process. A set of negative MCPs with amplitudes of 2, 5, 8, 10, 12, and 15 A are used to test the MS demagnetization process. The MCP is set as a trapezoidal wave with 50 ms amplitude duration and 15 ms for both rising slope and falling slope for the offline tests. The test procedure is as follows. First, injecting a MCP into the d -axis armature current of the investigated machine stationarily. Second, the

investigated machine is rotated by the load machine under 200 r/min, and its back electromotive force (EMF) can be measured offline, which is utilized to calculate ψ_m .

$$u_q = Ri_q + L_q \frac{di_q}{dt} + \omega L_d i_d + \omega \psi_m \quad (3.1)$$

When the investigated machine is rotated by the load machine, there are no dq -axis currents, and u_q can be treated as back EMF, then ψ_m can be obtained:

$$\psi_m = u_q / \omega \quad (3.2)$$

Then, the correlation between ψ_m and the corresponding MCP can be obtained. ψ_m can be regulated from 0.125 to 0.195 Wb by a positive MCP with amplitude of 25 A, and conversely from 0.195 to 0.125 Wb by a negative MCP with amplitude of 15 A, as depicted in Fig. 3.2. The demagnetization is easier than the remagnetization for the investigated machine. These offline measured results can be built into a LUT for MSs and the corresponding MCPs. It should be noted that the initial electromagnetic d -axis must be at the zero position of the encoder to make sure that the MCP can be completely added to the d -axis current. The rotor is not locked when injecting magnetizing current pulse, and the speed is controlled to 0. To reduce the measurement errors, each offline magnetization operation is performed 5 times, the results depicted in Fig. 3.2 are the average values. This also applies for the following offline time duration test section.

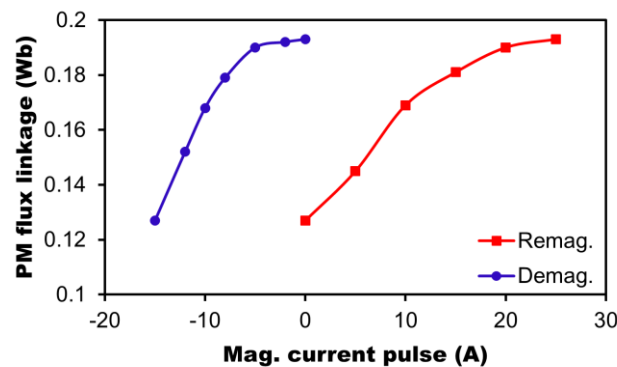


Fig. 3.2. Relationship between PM flux linkage and amplitude of magnetizing current pulse with 50 ms duration.

It is noted that this LUT just represents the maximum magnetizing capability for the machine and provides the correlation between the magnetizing current pulses and the MSs. When the machine is operating in the control system, the actual magnetizing capability should be readjusted according to the real-time operating conditions.

2) Time duration of magnetizing current pulses

The current pulse with different time duration is injected offline to test the influence of the current pulse time duration on the magnetizing capability.

The trapezoidal current pulse with an amplitude of 10 A under a set of time durations of 5, 10, 20, 30, 40, 50, and 60 ms are tested on remagnetization and demagnetization, respectively. The remagnetization is processed from the minimum ψ_m 0.125 Wb, which can be increased to 0.169 Wb by a 10 A MCP. The demagnetization is tested from the maximum ψ_m 0.195 Wb, which can be decreased to 0.17 Wb by a -10 A MCP. The measured results are presented in Fig. 3.3. Ignoring the measurement errors, when the duration of the current pulse is less than 30 ms, its capability of ψ_m adjustment decreases, especially for the demagnetization process.

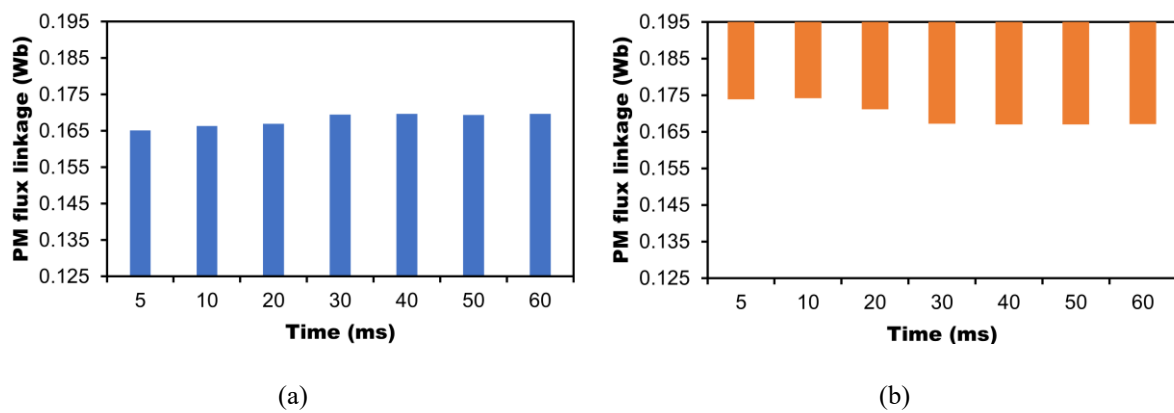


Fig. 3.3. Off-line measured PM flux linkages of 10 A current pulse with different time duration. (a) Remagnetization. (b) Demagnetization.

To verify the above measured results, the injected MCP with an amplitude of 15 A is also tested with the same conditions of the MCP with an amplitude of 10 A. The measured results are shown in Fig. 3.4, which are basically consistent with the measured results in Fig. 3.3. This is mainly due to the response time of the whole experiment system and the delay of data transmission, which cannot be neglected in the experiments. Therefore, the minimum time duration of MCP is 30 ms to ensure the MS reach to the target, especially for the demagnetization process. Considering the responsiveness of the inverter components, the MCP has a 10 ms slope for both rising slope and falling slope.

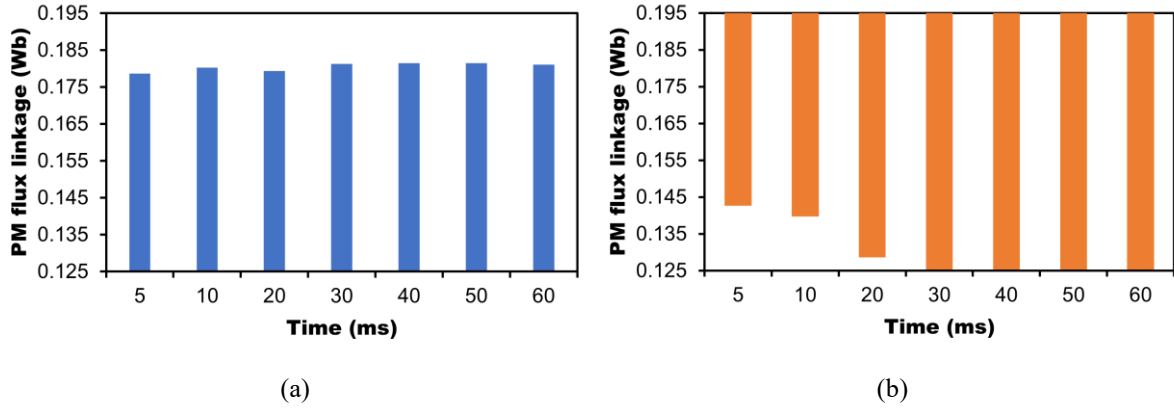


Fig. 3.4. Off-line measured PM flux linkages of 15 A current pulse with different time duration. (a) Remagnetization. (b) Demagnetization.

3.2.2 Magnetization State Properties

As depicted in Fig. 3.2, ψ_m of the HMMM can be adjusted from 0.125 to 0.195 Wb. Each ψ_m represents a MS, and under each MS the dq -axis inductances (L_d , L_q) change.

The effects of magnetic saturation on L_d and L_q are considered. The finite element analysis results of L_d and L_q under different dq -axis currents are presented in Fig. 3.5 and Fig. 3.6. Two MSs are selected: $\psi_m = 0.125$ Wb and $\psi_m = 0.176$ Wb. It can be observed that L_d is relatively stable. However, L_q varies by different q -axis current which changes from 100 mH to 60 mH.

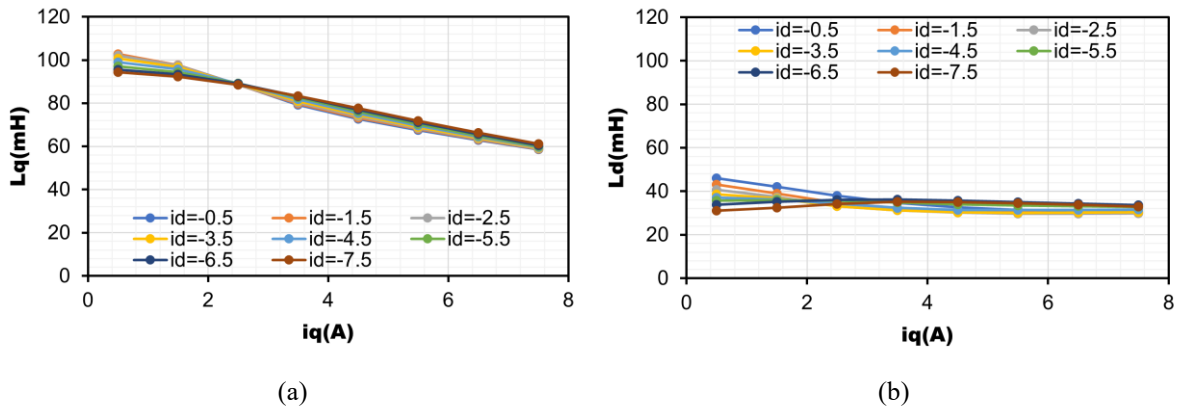


Fig. 3.5. dq -axis inductances under different dq -axis currents ($\psi_m = 0.125$ Wb). (a) q -axis inductance. (b) d -axis inductance.

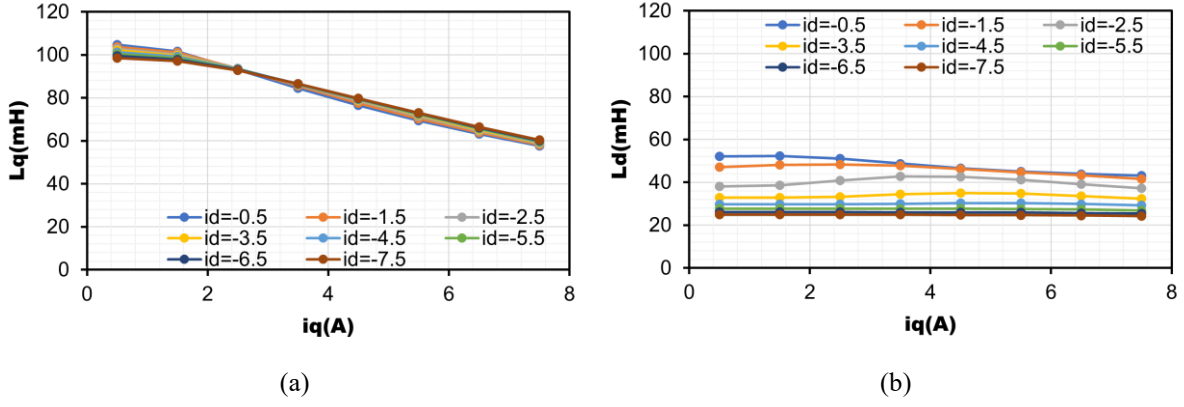


Fig. 3.6. dq -axis inductances under different dq -axis currents ($\psi_m = 0.176$ Wb). (a) q -axis inductance. (b) d -axis inductance.

The test procedure for determining L_d and L_q is as follows. First, injecting a magnetizing current pulse to manipulate the MS. Second, testing L_d and L_q by a LCR equipment offline and record the value. Then, repeat the previous two steps to obtain L_d and L_q under different MSs.

A magnetization ratio is used to define the MSs, 0% and 100% correspond to the minimum and maximum flux linkages, respectively. The relationship between L_d , L_q and the magnetization ratio is depicted in Fig. 3.7, and ψ_m is also illustrated. Here, the effects of other factors, e.g., temperature and magnetic saturation etc., on the parameters of the machine are ignored.

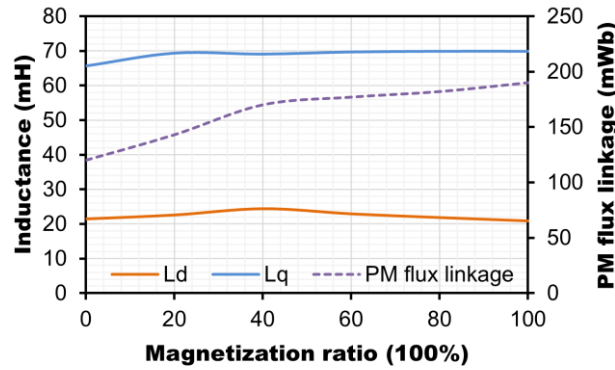


Fig. 3.7. Illustration of dq -axis inductances and PM flux linkages under different magnetization ratios.

3.3 Dual Magnetizing Current Method

3.3.1 Mathematical Model for VFMM

The mathematical model is expressed below and more details are illustrated in APPENDIX B.

$$\begin{cases} u_d = Ri_d + L_d \frac{di_d}{dt} + \frac{d\psi_m(i_{mag.})}{dt} - \omega L_q i_q \\ u_q = Ri_q + L_q \frac{di_q}{dt} + \omega L_d i_d + \omega \psi_m(i_{mag.}) \end{cases} \quad (3.3)$$

$$T_e = 1.5p[\psi_m(i_{mag.})i_q + (L_d - L_q)i_d i_q] \quad (3.4)$$

3.3.2 Design of Proposed Dual Magnetizing Current Controller

During the MS manipulation, ψ_m and L_d, L_q are affected by the injected MCP. Therefore, during MS manipulation, (3.4) can be expressed:

$$T_e = 1.5p[\psi_m(i_{mag.})i_q + (L_d(i_{mag.})) - L_q(i_{mag.}))(i_d + i_{mag.})i_q] \quad (3.5)$$

For the conventional MS manipulation, a single d -axis MCP is injected, which is called as single magnetizing current method here. Generally, the MCP is very large and will cause significant changes in torque, which is main torque oscillation during the MS manipulation. The torque oscillation will directly cause the speed fluctuation.

The parameters of the machine before MS manipulation are set as $\psi_{m1}, L_{d1}, L_{q1}$, and the parameters under the target MS are set as $\psi_{m2}, L_{d2}, L_{q2}$. Then, the torque before MS manipulation and during MS manipulation can be expressed as:

$$T_{e1} = 1.5p[\psi_{m1}i_q + (L_{d1} - L_{q1})i_d i_q] \quad (3.6)$$

$$T_{e2} = 1.5p[\psi_{m2}i_q + (L_{d2} - L_{q2})(i_d + i_{mag.})i_q] \quad (3.7)$$

To compensate the torque oscillation caused by the magnetizing current pulse, a q -axis current pulse Δi_q is injected during the MS manipulation. Then, (3.7) can be expressed as:

$$T_{e2} = 1.5p[\psi_{m2} + (L_{d2} - L_{q2})(i_d + i_{mag.})](i_q + \Delta i_q) \quad (3.8)$$

The ideal situation by injected this q -axis current is that the torque change can be eliminated, which means T_{e2} in (3.8) equals to T_{e1} in (3.6). Then, Δi_q can be obtained:

$$\Delta i_q = \frac{T_{e1} - T_{e2}}{1.5p[\psi_{m2} + (L_{d2} - L_{q2})(i_d + i_{mag.})]} \quad (3.9)$$

This compensated q -axis current pulse will be injected into i_q during MS manipulation. The amplitude of Δi_q can be obtained by (3.9). Based on the analysis in section 3.2.2, the time duration should be 30 ms just as the same as the d -axis MCP. Thus, the dual magnetizing current controller is achieved. Compared with the single magnetizing current method, the proposed

dual magnetizing current method is aimed at mitigating the speed fluctuation caused by the sudden change in torque.

3.3.3 Design of Torque Calculation and Look-up Table

A model-based torque calculation is employed to calculate the injected q -axis magnetizing current. Since the L_d , L_q and ψ_m change with the adjustment of MSs, this characteristic must be taken into account in the design of torque calculation. The torque calculation is shown in Fig. 3.8. The cut-off frequency of LPF is 10 Hz.

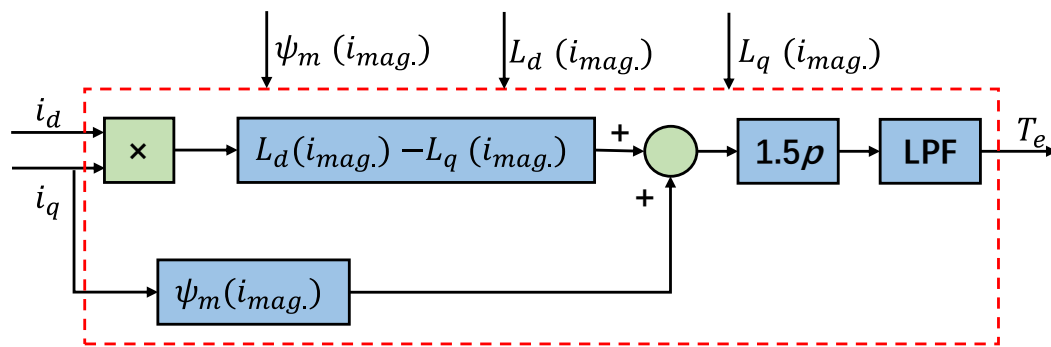


Fig. 3.8. Model-based torque calculation.

This torque calculation can also be utilized to evaluate the torque transient performance during MS manipulation.

According to the MS properties of the investigated machine, a LUT is built. The MSs with the corresponding MCPs and the information of L_d , L_q and ψ_m under each MS are listed in detail in the LUT. The design of the LUT is presented in Fig. 3.9.

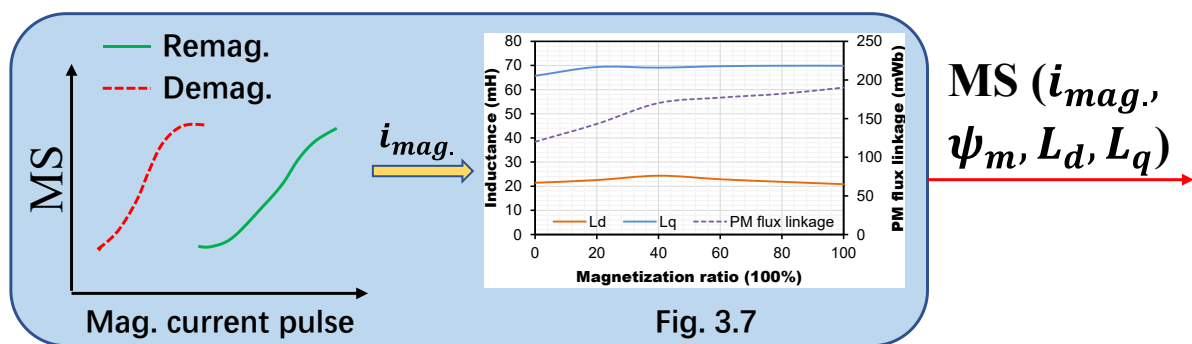


Fig. 3.9. Scheme of look-up table.

3.3.4 Scheme of Proposed Dual Magnetizing Current Method

The proposed dual magnetizing current method is illustrated in Fig. 3.10. When a MS manipulation command occurs, the parameters under the present MS_1 and the target MS_2 can

be obtained from the LUT. The corresponding d -axis MCP can also be gained. The torque under these two MSs can be calculated by the model-based torque calculation. Then, according to (3.9), the injected q -axis MCP Δi_q can be obtained. The output of the dual magnetizing current controller is the dq -axis MCPs.

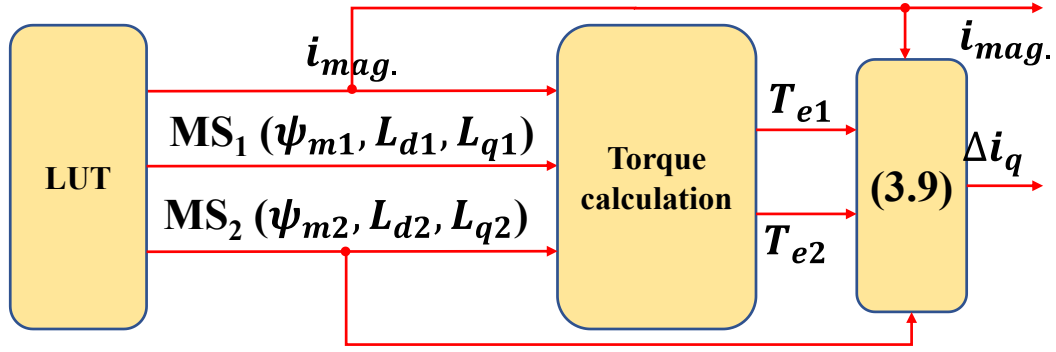


Fig. 3.10. Scheme of proposed dual magnetizing current method.

3.4 Simulation and Discussion

3.4.1 Control System

The scheme of the whole control system to test the proposed dual magnetizing current controller on the investigated machine is illustrated in Fig. 3.11.

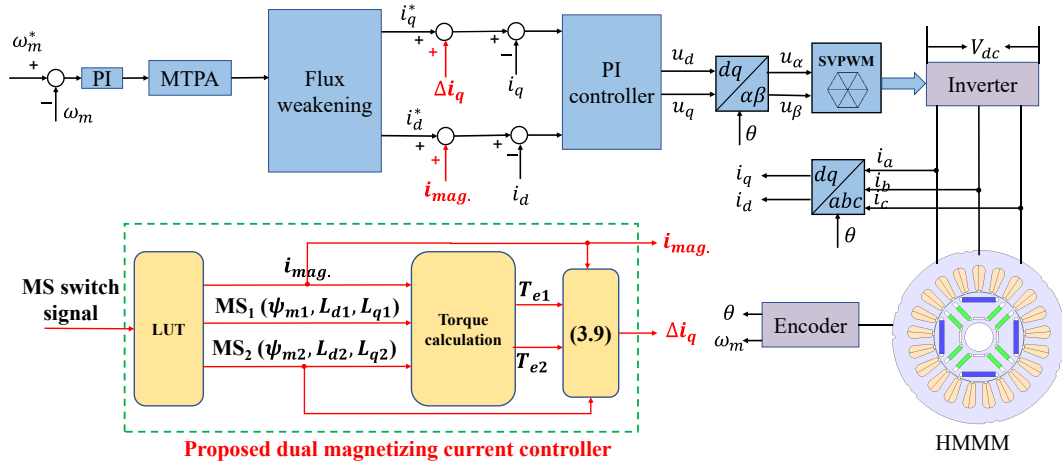


Fig. 3.11. Schematic of overall investigated machine control system.

where u_d and u_q are the voltage components in the dq -axis, u_α and u_β are the voltage components in the $\alpha\beta$ -axis, ω_m^* and ω_m are the reference and actual mechanical angular velocity, θ is the electrical angle, i_d^* and i_q^* are generated by control algorithm of maximum torque per ampere (MTPA) and flux weakening control and set as the reference of the current PI controller, i_a , i_b , and i_c are the respective three-phase currents. The torque observer is

referred to Fig. 3.8. The flux weakening and PI controller are referred to Fig. 1.6. Since the output of flux weakening will affect dq -axis currents as presented in Fig. 1.6, dq -axis currents are depicted as the outputs of flux weakening block to simplify the schematic block. The parameters for PI controllers are same as Fig. 2.10.

When the machine is operating in the constant torque region, the MTPA is adopted to take the full advantage of the reluctance torque. In the flux weakening region, the feedback flux weakening control algorithm proposed in [KIM97b] is utilized which is more robust against the parameter variation. i_{mag} is added into i_d^* directly, and Δi_q is added into i_q^* directly.

3.4.2 Simulation Analysis

The main parameters for simulation are listed in Table 3.1. The DC-link voltage is set as 80 V. Three MSs and two operating speeds are selected to simulate the feasibility of the proposed dual magnetizing current controller.

Table 3.1. Main parameters of simulation.

Quantity	Value
DC link voltage V_{dc}	80 V
Operating speed n_1	300 r/min
Operating speed n_2	500 r/min
ψ_{m1} at MS ₁	0.125 Wb
L_{d1} at MS ₁	21.4 mH
L_{q1} at MS ₁	65.7 mH
ψ_{m2} at MS ₂	0.169 Wb
L_{d2} at MS ₂	24.3 mH
L_{q2} at MS ₂	69.1 mH
ψ_{m3} at MS ₃	0.195 Wb
L_{d3} at MS ₃	20.8 mH
L_{q3} at MS ₃	69.9 mH
Remagnetization current pulse MS ₁ to MS ₂	10 A
Demagnetization current pulse MS ₃ to MS ₂	-10 A

The remagnetization is simulated under 300 r/min in the constant torque region from MS1 to MS2, which is regulated by a 10 A MCP. The simulation results of the conventional single magnetizing current method and the proposed dual magnetizing current controller are presented in Fig. 3.12 and Fig. 3.13, respectively. The d-axis MCPs are kept the same in both methods as shown in Fig. 3.12(b) and Fig. 3.13(b). The “fbd” in I_{qfdb} is the abbreviation of feedback in Fig. 3.12(a), which represents the actual q-axis current for the current PI controller, and this

also applies on d-axis current. An extra q-axis magnetizing current pulse Δi_q is compensated in the proposed method in Fig. 3.13(a). The speed fluctuation during MS manipulation by the conventional method is more than 50 r/min in Fig. 3.12(c), which is mitigated to less than 10 r/min by the proposed method in Fig. 3.13(c). Besides, the oscillations in torque are reduced in Fig. 3.13(d). The performance improvement of the proposed method is significant.

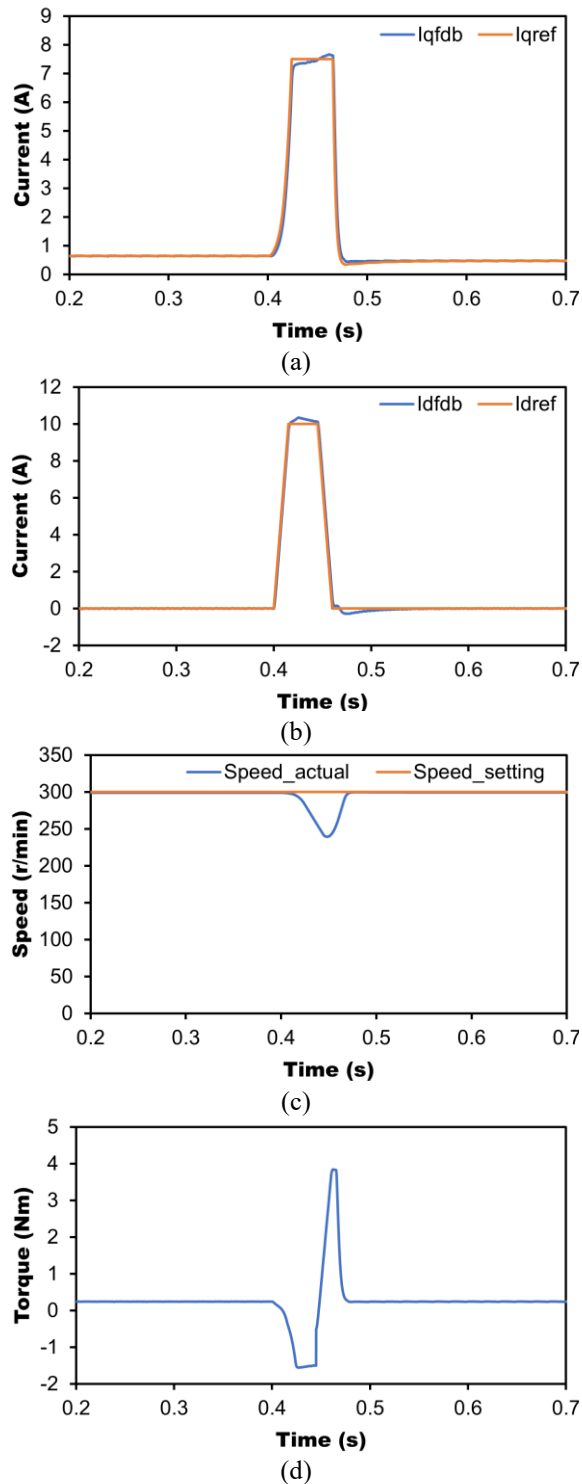


Fig. 3.12. Simulation results of remagnetization with 10 A MCP by conventional single magnetizing current method. (a) q -axis current. (b) d -axis current. (c) Speed. (d) Torque.

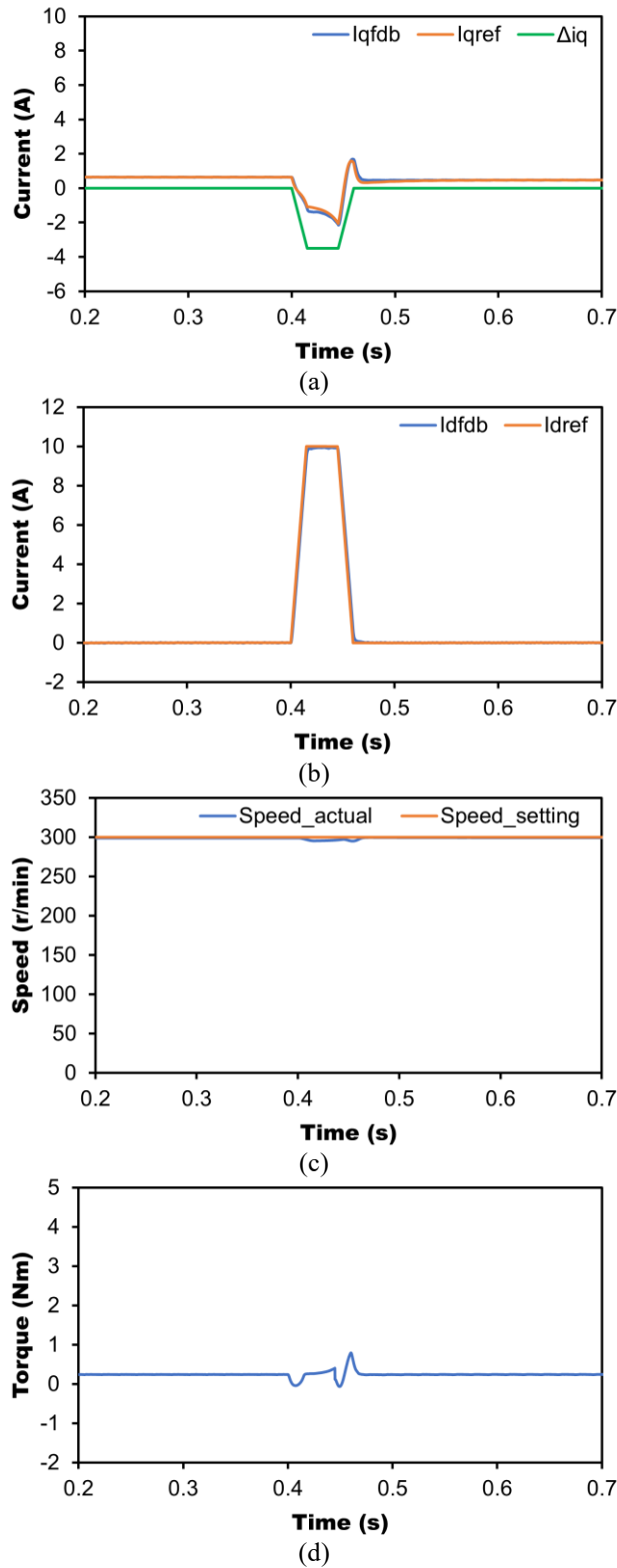


Fig. 3.13. Simulation results of remagnetization with 10 A MCP by proposed dual magnetizing current controller. (a) q -axis current. (b) d -axis current. (c) Speed. (d) Torque.

The demagnetization is simulated under 500 r/min in the flux weakening region from MS3 to MS2 by a -10 A MCP. The simulation results are presented in Fig. 3.14 and Fig. 3.15. The speed fluctuation during MS manipulation almost disappears by the proposed method in Fig.

3.15(c), which is more than 30 r/min by the conventional method in Fig. 3.14(c). The feasibility of the proposed method is well validated by simulation.

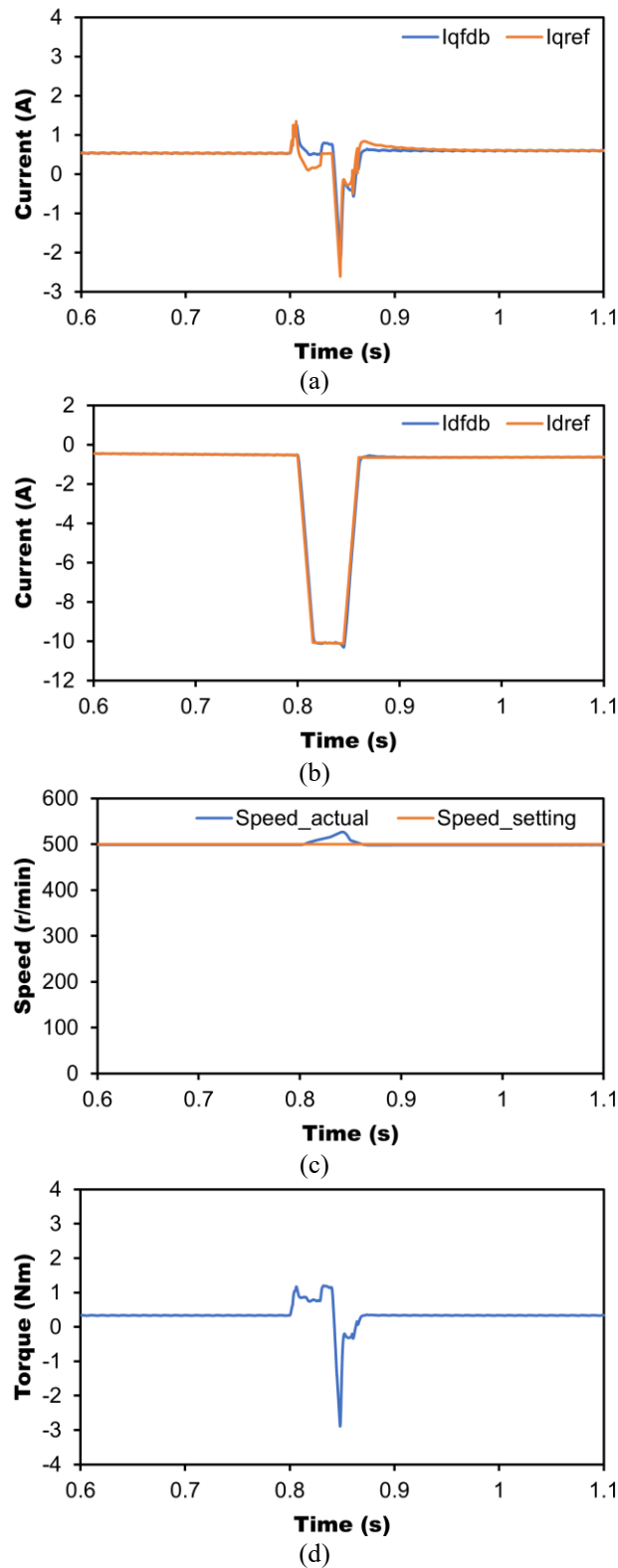
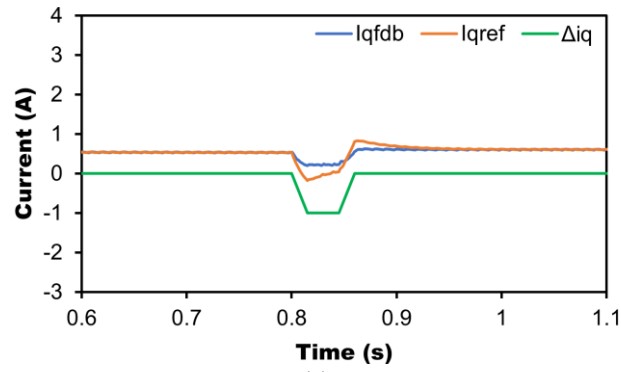
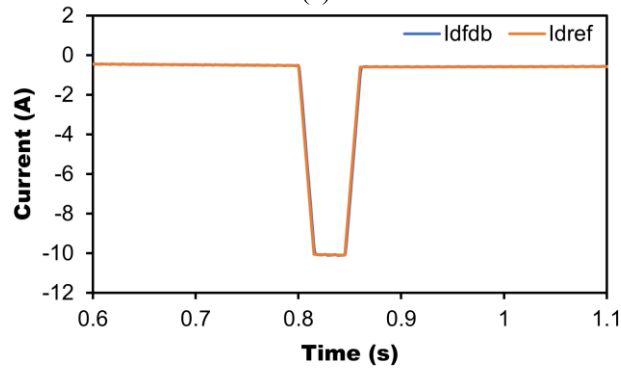


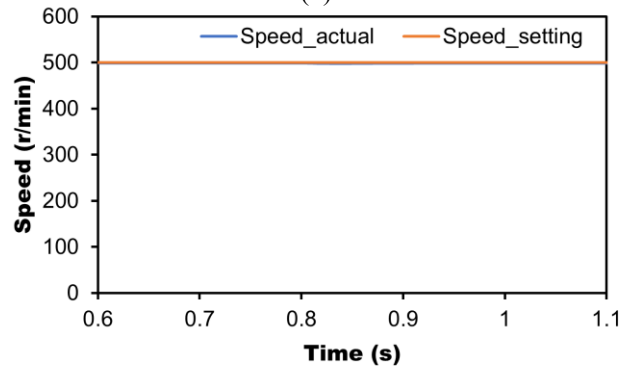
Fig. 3.14. Simulation results of demagnetization with -10 A MCP by conventional single magnetizing current method. (a) q -axis current. (b) d -axis current. (c) Speed. (d) Torque.



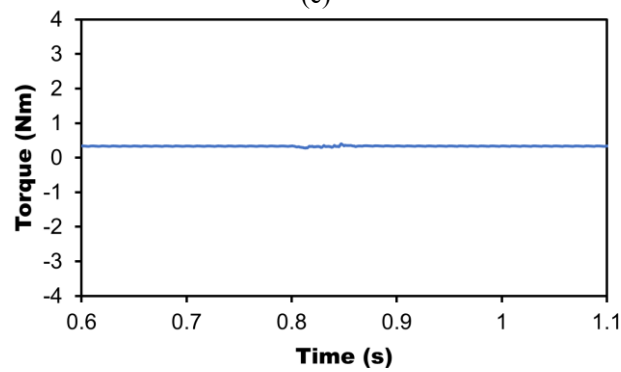
(a)



(b)



(c)



(d)

Fig. 3.15. Simulation results of demagnetization with -10 A MCP by proposed dual magnetizing current controller. (a) q -axis current. (b) d -axis current. (c) Speed. (d) Torque.

3.5 Experiments and Analysis

3.5.1 Remagnetization Transient Performance

The main parameters for the transient performance experiments of remagnetization are listed in Table 3.2, which are obtained according to the test method in section 3.2.2. The DC link voltage is set as 80V. Since the remagnetization in constant torque stage can enhance the torque performance of the machine, and the operating speed of the remagnetization experiments is set at 300 r/min that the machine is working in the constant torque stage. The initial MS₁ is set at the minimum one, of which ψ_{m1} is 0.125 Wb. Then, two more MSs are selected for the experiments. The value of the remagnetization current pulse from MS₁ to MS₂ is 10 A, and from MS₁ to MS₃ is 15 A. Based on the analysis in section 3.2, the trapezoidal MCP is with 30 ms amplitude duration and 10 ms for both rising slope and falling slope.

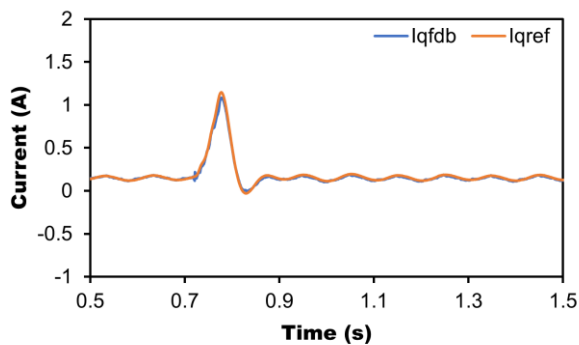
Table 3.2. Main parameters of remagnetization test.

Quantity	Value
DC link voltage V_{dc}	80 V
Operating speed	300 r/min
ψ_{m1} at MS ₁	0.125 Wb
L_{d1} at MS ₁	21.4 mH
L_{q1} at MS ₁	65.7 mH
ψ_{m2} at MS ₂	0.169 Wb
L_{d2} at MS ₂	24.3 mH
L_{q2} at MS ₂	69.1 mH
ψ_{m3} at MS ₃	0.181 Wb
L_{d3} at MS ₃	22.9 mH
L_{q3} at MS ₃	69.7 mH
Remagnetization current pulse MS ₁ to MS ₂	10 A
Remagnetization current pulse MS ₁ to MS ₃	15 A

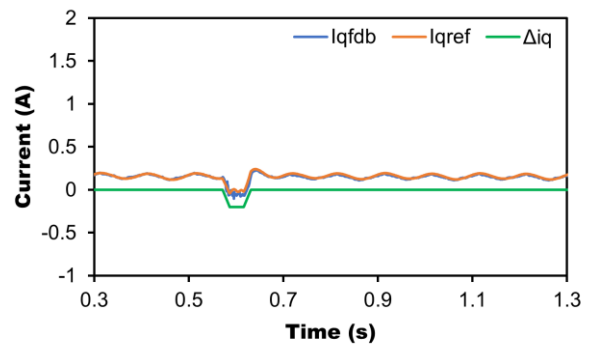
The measured results of the remagnetization transient performance with 10 A MCP are shown in Fig. 3.16. The control algorithm of the conventional method is presented in Fig. 2.10. With the conventional single magnetizing current method, the injected i_{mag} causes significant

increasing in torque as shown in Fig. 3.16(I, d). Due to the sudden increasing in d -axis current, the operating speed has a significant reduction from 300 to 200 r/min in Fig. 3.16(I, c). This leads to the increasing in q -axis current by the self-adjustment of the speed PI controller. Although this process is transient, the sudden oscillations have a bad effect on the dynamic performance of the VFMM driving system. With the proposed dual magnetizing current controller, i_{mag} keeps the same as the conventional one as presented in Fig. 3.16(b), and thus, the magnetizing capability is not affected. Then, the generated Δi_q in Fig. 3.16(II, a) almost eliminates the speed fluctuation in Fig. 3.16(II, c). Meanwhile, the oscillations in q -axis current and torque also are mitigated in Fig. 3.16(II, d). The experimental validation which is carried out at low torque is aimed to make sure that there is enough voltage margin for MS manipulation, especially for large magnetizing current pulse or in the flux weakening region. The comparisons of the measured results show the proposed dual magnetizing current pulse can mitigate the fluctuations significantly. The load machine is a brushed DC excitation motor. The ripple is caused by that the shaft of the load machine is not completely aligned with the investigated machine.

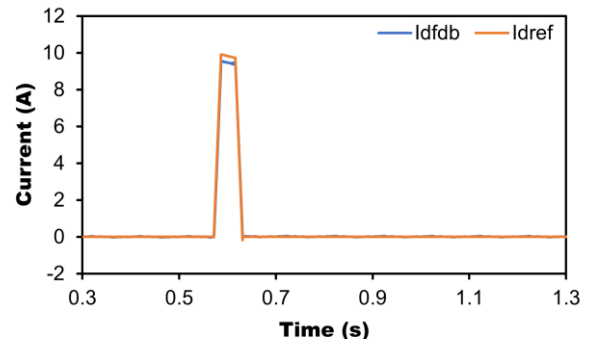
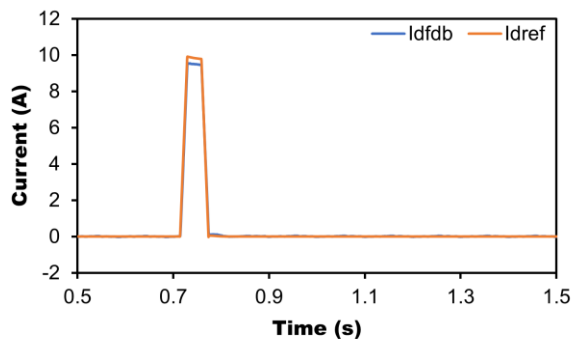
(I) Conventional single magnetizing current method



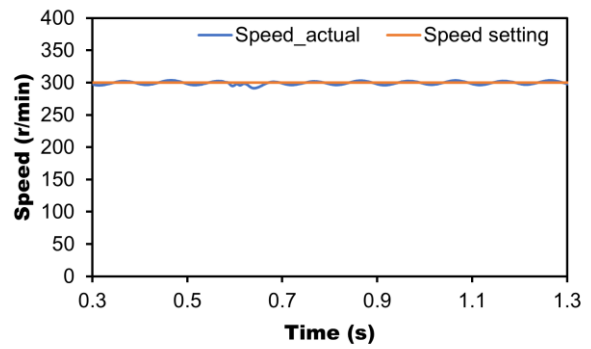
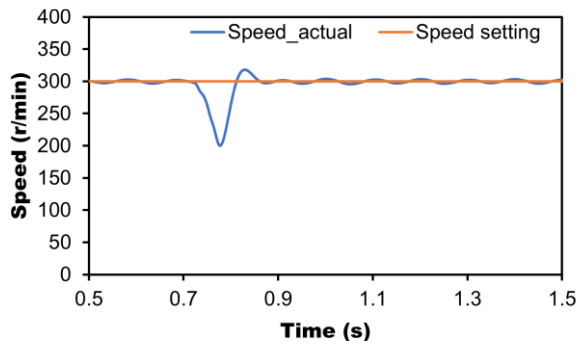
(II) Proposed dual magnetizing current method



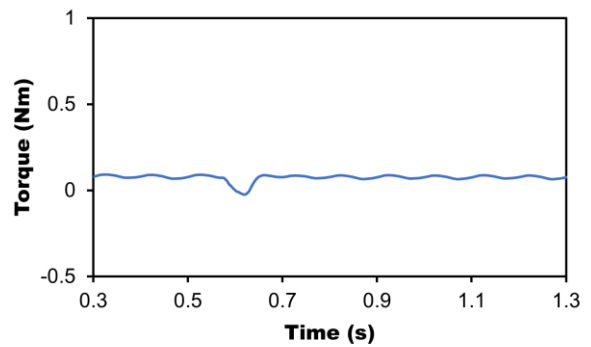
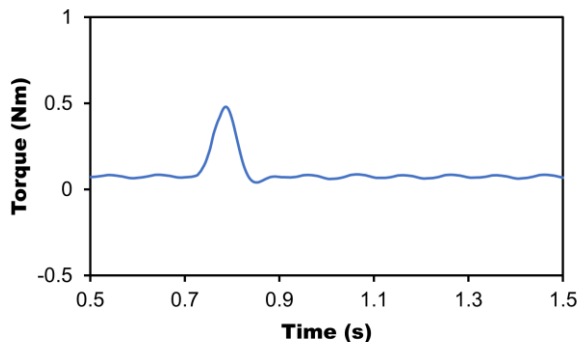
(a)



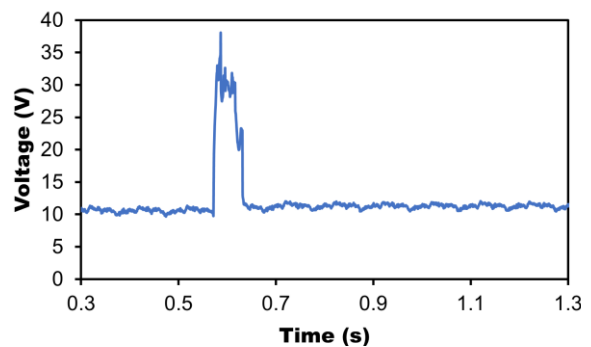
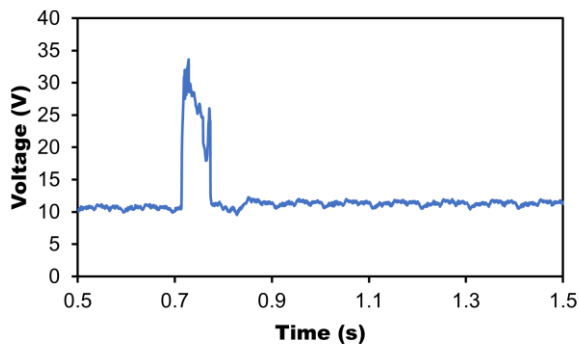
(b)



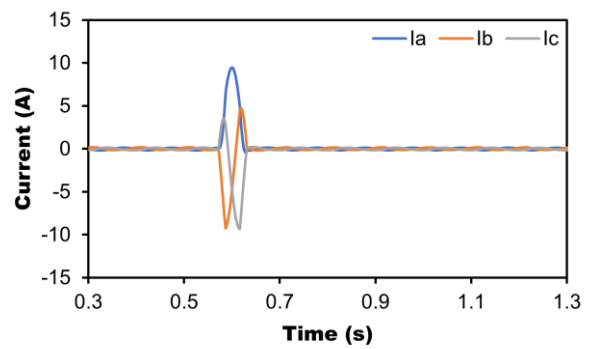
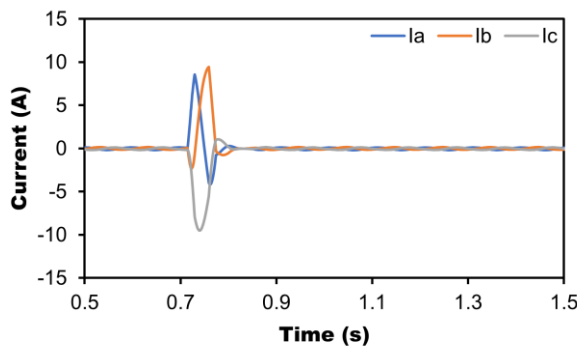
(c)



(d)



(e)

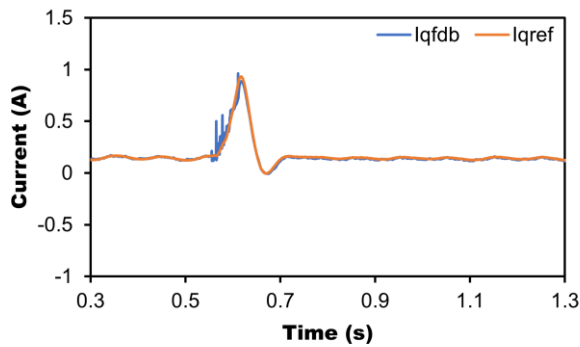


(f)

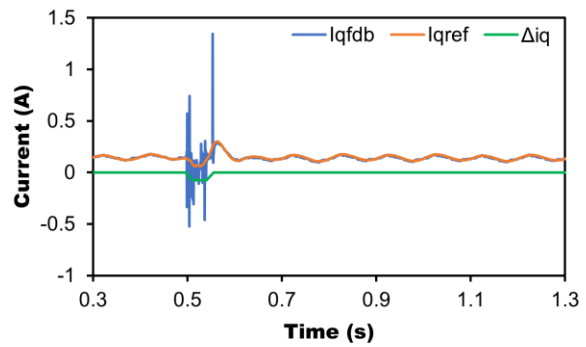
Fig. 3.16. Measured results of remagnetization with 10 A magnetizing current pulse, (I) conventional single magnetizing current method and (II) proposed dual magnetizing current controller. (a) q -axis current. (b) d -axis current. (c) Speed. (d) Torque. (e) Amplitude of dq -axis voltage vectors' sum. (f) Three-phase currents.

The experiment validation is processed on the remagnetization with 15 A magnetizing current pulse to verify the feasibility of the proposed method. The measured results for the conventional single magnetizing current method and the proposed dual magnetizing current controller are compared in Fig. 3.17. With the proposed method, the speed fluctuations caused by the MS manipulation are reduced to less than 20 r/min comparing with more than 80 r/min by the single magnetizing current method as shown in Fig. 3.17(c). Besides, the sudden changes in q -axis current and torque are improved by the proposed method. Although the voltage shown in Fig. 3.17(II, e) increases a little, it is still under the voltage limitation, the performance of MS manipulation is not influenced. The remagnetization performance with the proposed method is verified on the speed of 300 r/min, but it is definitely feasible for the whole speed range and all the other magnetizing current pulses.

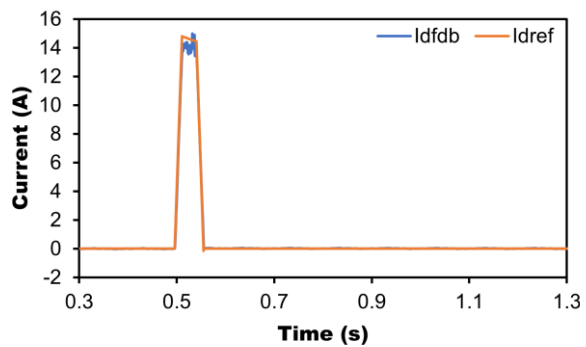
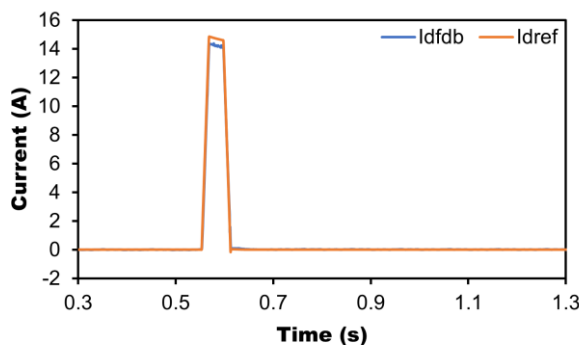
(I) Conventional single magnetizing current method



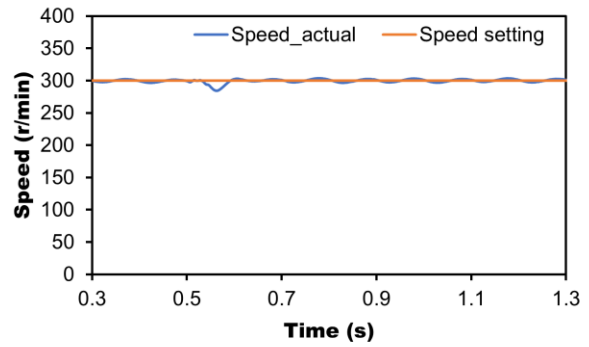
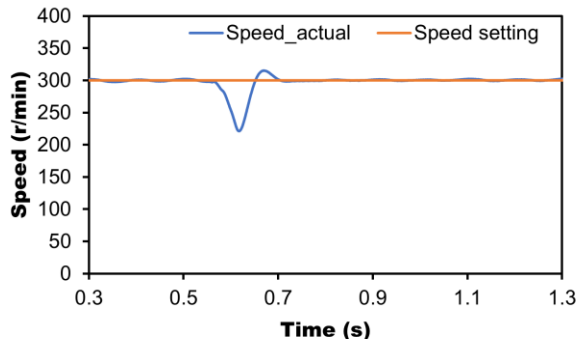
(II) Proposed dual magnetizing current method



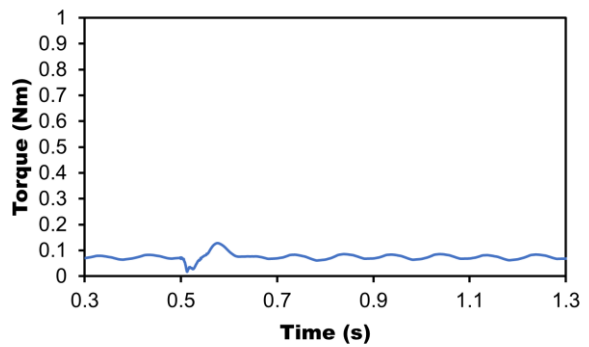
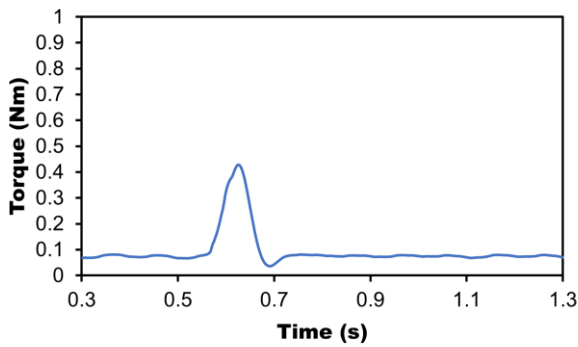
(a)



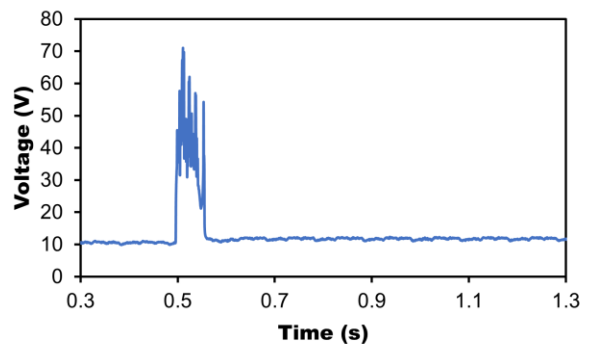
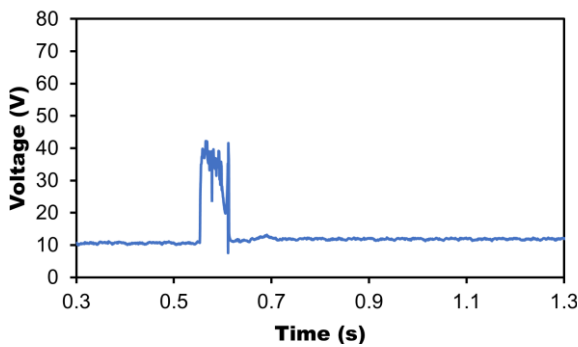
(b)



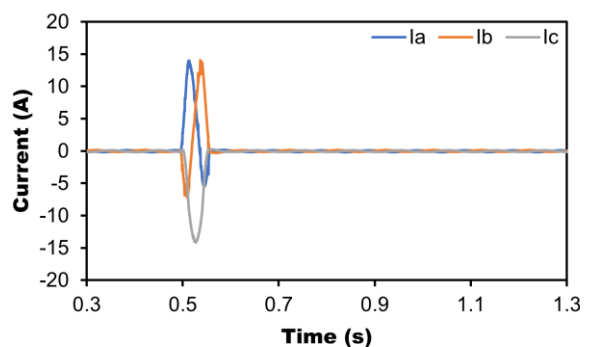
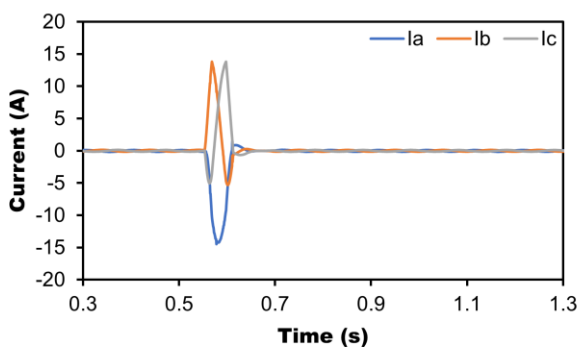
(c)



(d)



(e)



(f)

Fig. 3.17. Measured results of remagnetization with 15 A magnetizing current pulse, (I) conventional single magnetizing current method and (II) proposed dual magnetizing current controller. (a) q -axis current. (b) d -axis current. (c) Speed. (d) Torque. (e) Amplitude of dq -axis voltage vectors' sum. (f) Three-phase currents.

3.5.2 Demagnetization Transient Performance

To experimentally demonstrate the demagnetization transient performance, the initial MS_1 is set at the maximum one, of which ψ_{m1} is 0.195 Wb. The main parameters for the transient performance experiments of demagnetization are listed in Table 3.3. Since demagnetization process can reduce the PM flux linkage and extend the speed of the machine, its function is just like the flux weakening method. Therefore, demagnetization in flux weakening region will benefit the performance for the machine control system. Here, the experiments are processed under the envelope of the maximum torque speed curve. The operating speed of the demagnetization experiments is set at 500 r/min that the machine is working in the flux weakening region. Two MSs are selected for the transient performance experiments except for the initial MS_1 . The value of the demagnetization current pulse from MS_1 to MS_2 is -10 A, and that from MS_1 to MS_3 is -15 A.

Table 3.3. Main parameters of demagnetization test.

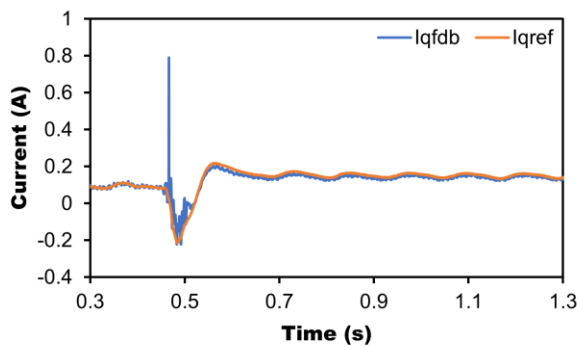
Quantity	Value
DC link voltage V_{dc}	80 V
Operating speed	500 r/min
ψ_{m1} at MS_1	0.195 Wb
L_{d1} at MS_1	20.8 mH
L_{q1} at MS_1	69.9 mH
ψ_{m2} at MS_2	0.169 Wb
L_{d2} at MS_2	24.3 mH
L_{q2} at MS_2	69.1 mH
ψ_{m3} at MS_3	0.125 Wb
L_{d3} at MS_3	21.4 mH
L_{q3} at MS_3	65.7 mH
Demagnetization current pulse MS_1 to MS_2	-10 A
Demagnetization current pulse MS_1 to MS_3	-15 A

The measured results of the demagnetization transient performance with -10 A MCP are compared in Fig. 3.18 for the conventional single magnetizing current method and the proposed dual magnetizing current controller.

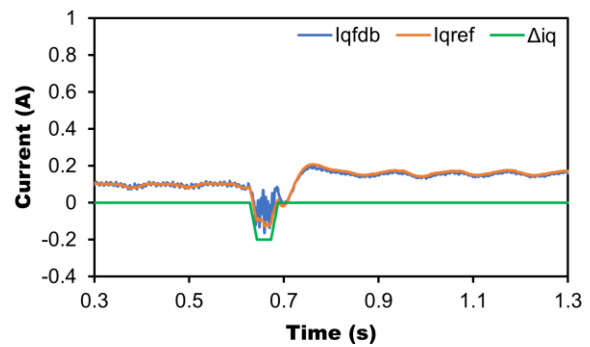
After the demagnetization process, the PM flux linkage reduces. Then, the degree of the flux weakening region reduces or even completely back to the constant torque region. This leads to the change of d -axis current at steady state as shown in Figs. 3.18(b). The injected Δi_q of the proposed dual magnetizing current controller is depicted in Fig. 3.18(II, a). The speed fluctuations are almost eliminated by the proposed method comparing with the single magnetizing current method as shown in Figs. 3.18(I, c) and (II, c). The spikes in the voltage and q -axis current caused by the demagnetization process as shown in Fig. 3.18(a) and Fig. 3.18(e) in both methods are not an issue since the inertia system can filter them out.

From the comparison of the measured results, the proposed dual magnetizing current controller shows better performance in speed fluctuations mitigation.

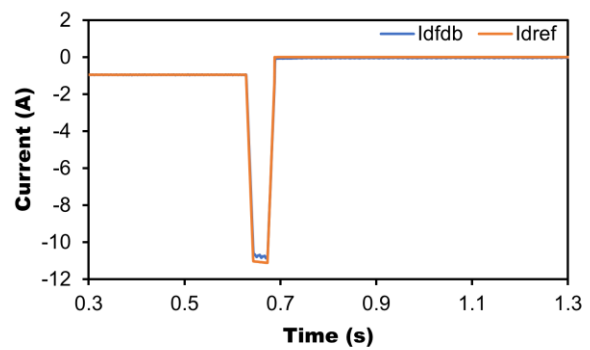
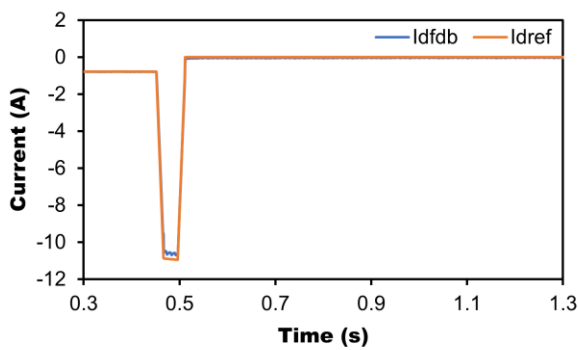
(I) Conventional single magnetizing current method



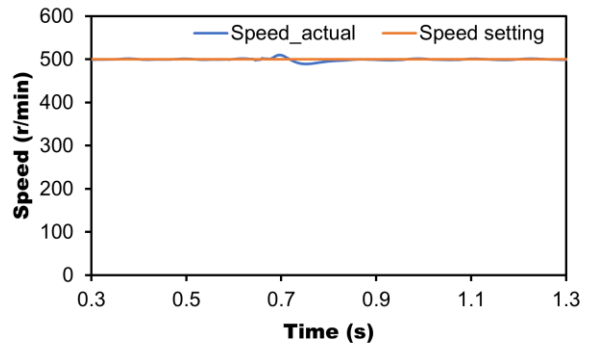
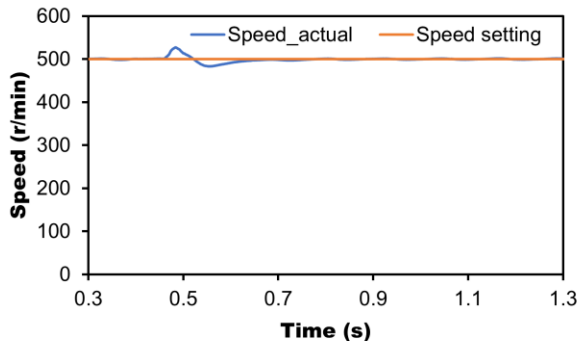
(II) Proposed dual magnetizing current method



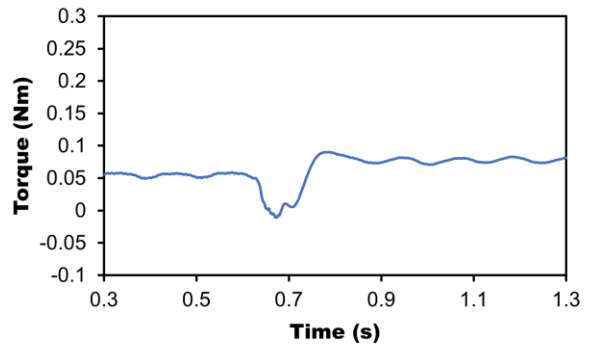
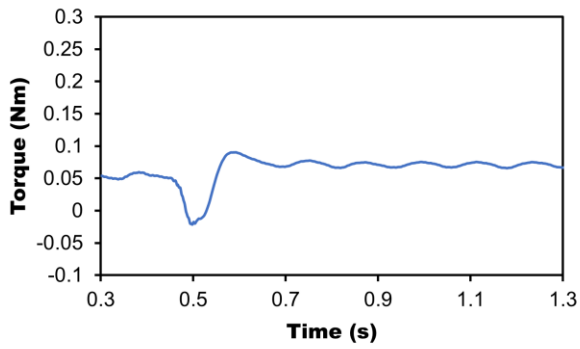
(a)



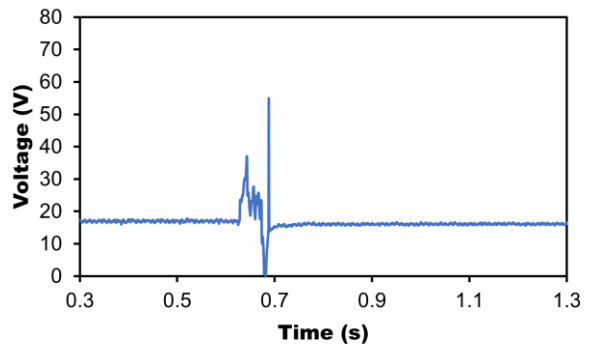
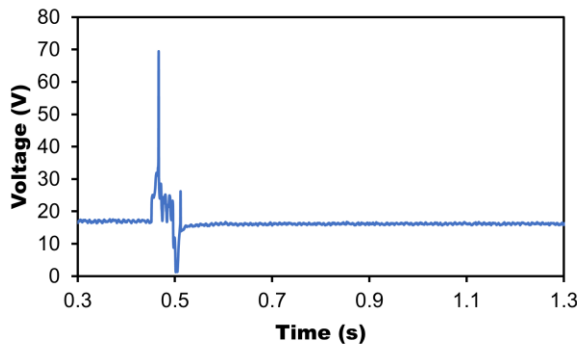
(b)



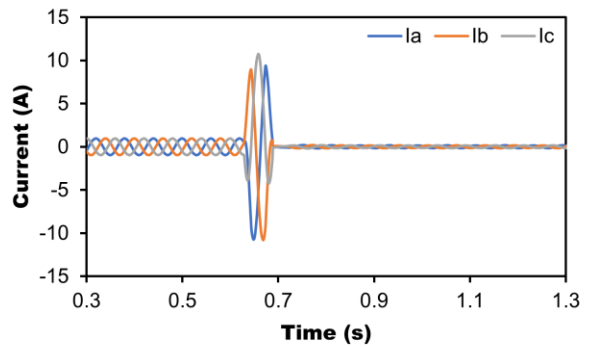
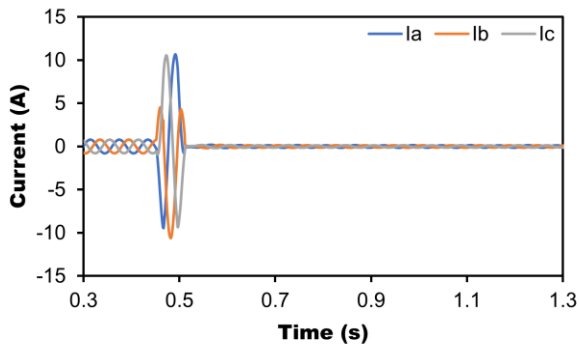
(c)



(d)



(e)

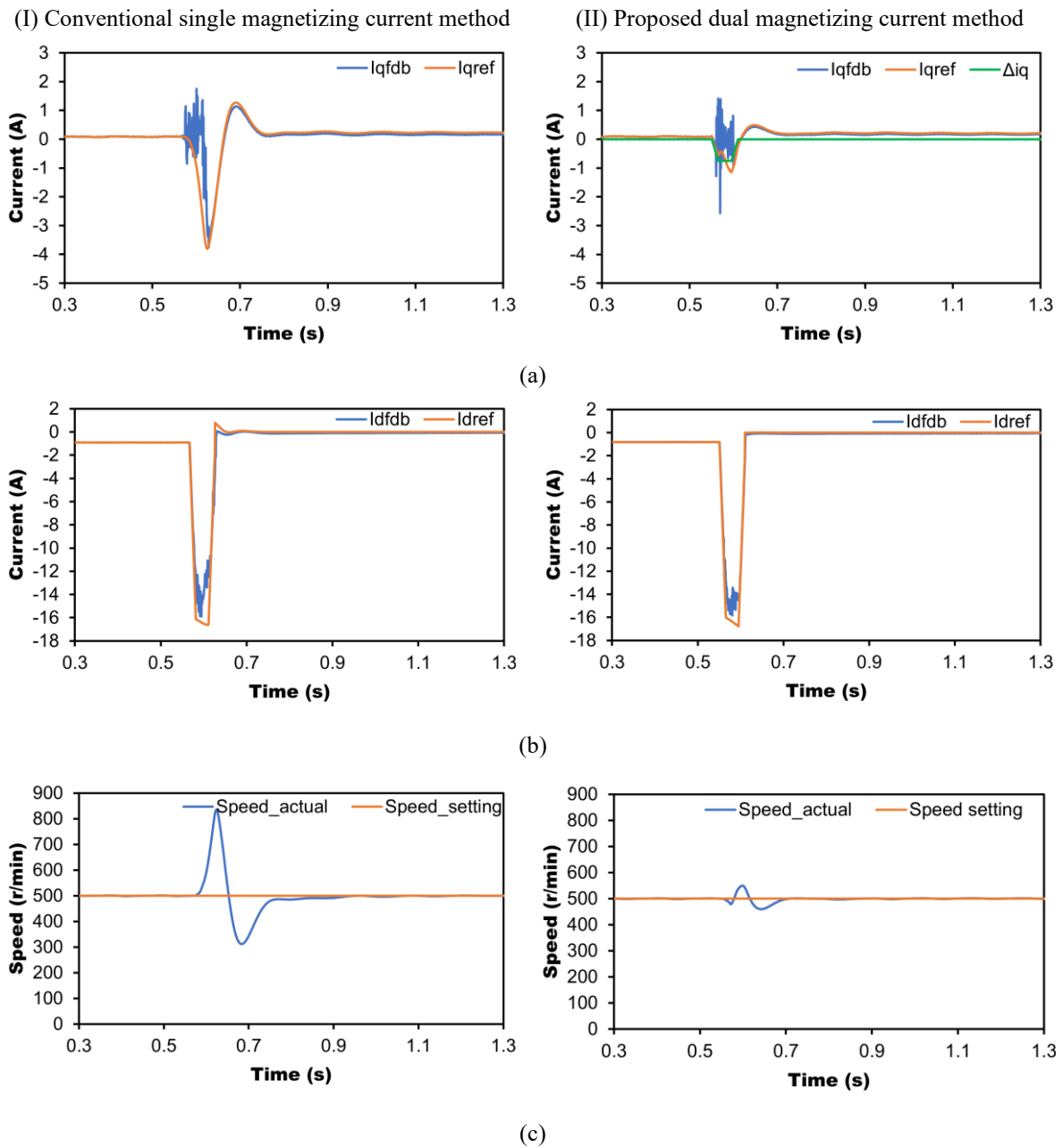


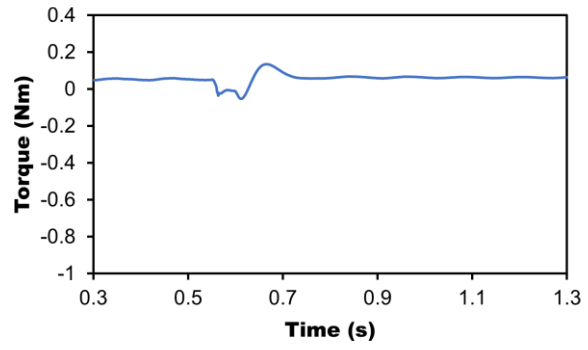
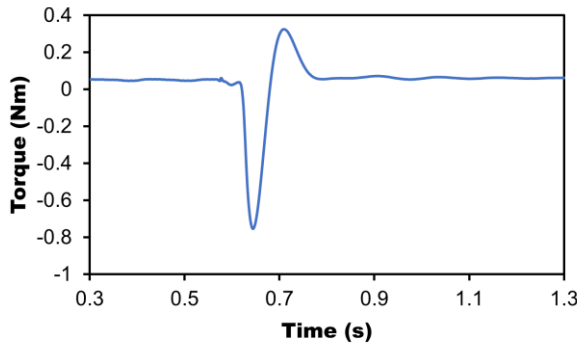
(f)

Fig. 3.18. Measured results of demagnetization with -10 A magnetizing current pulse, (I) conventional single magnetizing current method and (II) proposed dual magnetizing current controller. (a) q -axis current. (b) d -axis current. (c) Speed. (d) Torque. (e) Amplitude of dq -axis voltage vectors' sum. (f) Three-phase currents.

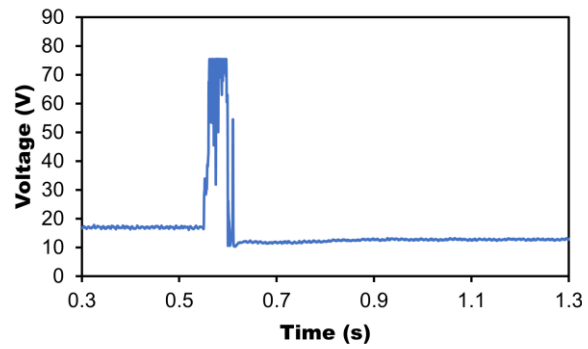
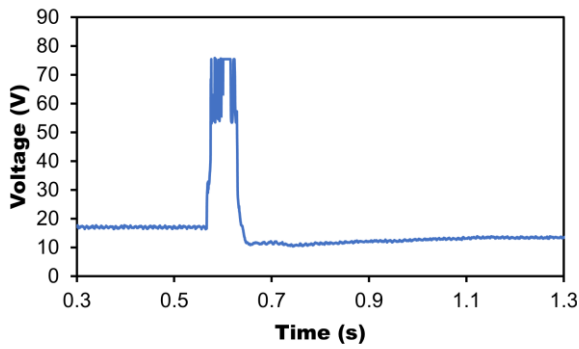
To further validate the performance of the proposed dual magnetizing current method, the demagnetization is tested with -15 A MCP. The measured results of the single magnetizing current method and the proposed dual magnetizing current method are compared in Fig. 3.19.

With the amplitude of the MCP increasing, the speed fluctuations increase significantly, which is more than 800 r/min with the conventional single magnetizing current method. While the proposed method mitigates it to less than 50 r/min as shown in Fig. 3.19(II, c). Further, the proposed method also significantly reduces the oscillations in the q -axis current and torque caused by the MS manipulation as shown in Fig. 3.19(II, a) and Fig. 3.19(II, d).

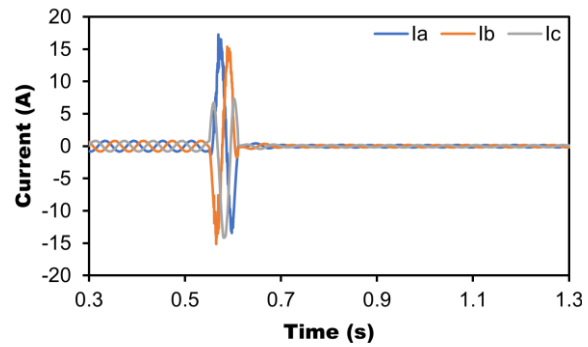
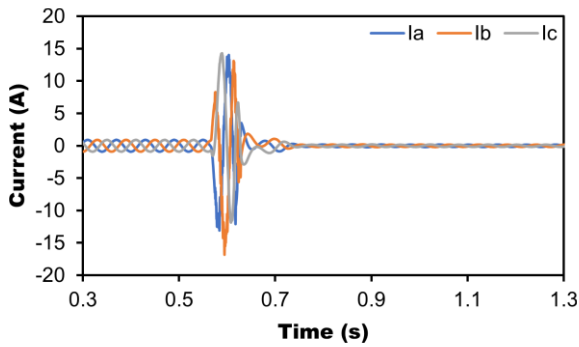




(d)



(e)



(f)

Fig. 3.19. Measured results of demagnetization with -15 A magnetizing current pulse, (I) conventional single magnetizing current method and (II) proposed dual magnetizing current controller. (a) q -axis current. (b) d -axis current. (c) Speed. (d) Torque. (e) Amplitude of dq -axis voltage vectors' sum. (f) Three-phase currents.

Overall, the proposed dual magnetizing current controller can significantly mitigate the speed fluctuation caused by the MS manipulation and shows much better transient performance.

3.6 Conclusion

In this chapter, a novel dual magnetizing current controller is proposed to mitigate the speed fluctuation caused by the MS manipulation and improve the transient performance for VFMM control system. The properties of the magnetizing current pulse are illustrated in detail. The

correlation between the magnetizing current pulses and the MSs is established, and the effects of the amplitude and time duration of the magnetizing current pulse on its magnetizing capability are tested and analyzed. Based on the dynamic mathematical model of VFMM, a dual magnetizing current controller is designed. A q -axis current pulse is injected to compensate the torque fluctuation caused by the d -axis MCP. A model-based torque calculation is employed. A LUT is built based on the MS properties of the investigated machine. The transient performance experiments are validated on a HMMM control system, and the remagnetization and demagnetization are tested, respectively. The measured results by using the single magnetizing current method and the proposed dual magnetizing current method are compared and analyzed.

The measured results show that compared with the conventional method, the proposed dual magnetizing current method can significantly mitigate the speed fluctuation caused by the injected magnetizing current pulse with large amplitude and has much better transient performance during the MS manipulation. The speed fluctuations are reduced by more than 80% compared to conventional methods. Therefore, the feasibility of the proposed dual magnetizing current controller is well validated experimentally.

CHAPTER 4 MAGNETIZATION STATE CONTROL CONSIDERING THE EFFECT OF VOLTAGE LIMITATION

Since the amplitude of magnetizing current pulse is usually very large, it needs enough voltage margin to support the demand magnetizing current pulse. Then, the effect of voltage limitation on the capability of magnetizing cannot be ignored. In this chapter, a novel magnetization state (MS) control method for a hybrid magnet memory machine (HMMM) based on modified voltage limitation is proposed.

4.1 Introduction

As a kind of permanent magnet synchronous machine (PMSM), variable flux memory machines (VFMMs) persist the advantages of high efficiency and low loss and can further improve the efficiency due to the special feature of changeable magnetizing level in permanent magnet (PM) by a current pulse. Due to adoption of low-coercive force (LCF) PM and often combined with high-coercive force (HCF) PM, the different arrangements of the PMs show significantly different performance for VFMM [YAN19d] [XIE20a]. The adjustability of magnetization state (MS) brings an extra freedom for control of VFMM [CHE20] [YAN18] [HU21] [LYU20a] [TAK18] [YAN19b] [HUA17a]. Thus, since its concept was proposed in 2001 [OST01], more and more scholars have begun to devote themselves to the research on the related topics [YAN18b], including various VFMM topologies [YU11b] [ZHU17] [LIU23] [HUA19a] [HU20b] [HUA19b] [ZHO16] [ZHA18] [YAN20] [YAN19c] and control strategies [CHE22] [ZHO22a] [ZHO22b] [LYU23] [ZHO23a] [ZHO24] [ZHO23c].

In [CHE22], a sinusoidal current pulse was utilized for MS manipulation to design the bandwidth of a linear extended state observer, which was employed to estimate the sum of the PM induced voltage and the disturbance voltage for the current controller modification, and then, the estimated q -axis voltage is utilized to build the PM flux linkage observer. The active-disturbance-rejection control method is firstly adopted in the MS control. However, the sinusoidal current pulse will introduce large copper loss. In [ZHO22a], a flux weakening control method combining feedforward and feedback approaches was employed to tradeoff between the fast response and robustness of current regulation during the MS manipulation for VFMM. Only two MSs were selected to reduce the manipulations of MS, and when the speed

reached to the intersection of the torque-speed curves, the MS was manipulated. The fluctuation caused by the MS manipulation was ignored since it was only processed once. A fuzzy PI feedforward current controller was adopted in [ZHO22b] to reduce the effects of inaccurate parameters, the MS manipulation time was adjusted for the first time according to the available voltage. In [LYU23], the remagnetization and demagnetization boundaries were set inside the maximum torque-speed envelopes of two selected MSs, and the machine was kept working within the boundaries to avoid frequent MS manipulations. However, the range of MS adjustment was reduced, which would affect the capability of MS manipulation. In [ZHO23a], the position sensorless control was applied to VFMM, the dq -axis inductances were measured in advance and updated into sliding-mode observer, and the normalization of extended EMF was adopted to keep the bandwidth constant. While the dynamic performance of position estimation during MS manipulation was still needed to improve. [ZHO24] proposed a q -axis current reverse control method to reduce the speed fluctuation during MS manipulation. When the torque was detected as negative caused by the injected magnetizing current pulse, the q -axis current was reverse directly. A super-twisting sliding mode torque observer was re-structured as the disturbance observer. In [ZHO23c], a model-compensation linear active disturbance rejection speed controller was employed for VFMM speed regulation systems to reduce both the torque and speed fluctuations. An extended state observer was employed to provide real-time estimation of disturbances. In the above two papers, the fluctuation caused by MS manipulation was investigated and mitigated, and the torque pulsation and speed fluctuation were analyzed and compensated directly, but the algorithms were complex.

In existing research, the effect of the voltage constraints on the MS manipulation is always ignored. In this chapter, a novel MS control method based the modified voltage limitation is proposed for VFMM. Firstly, the topology and the magnetizing properties of the investigated HMMM are illustrated. The pattern of the magnetizing current pulse is introduced. The relationship between the MSs and the magnetizing current pulse is tested offline and built into a look-up table (LUT). Secondly, the mathematic model and the voltage constraint for VFMM control are presented. Thirdly, the effect of voltage limitation on the MS manipulation is analyze, and the current controller with the decoupling feedforward compensation is introduced. The circumcircle rather than the inscribed circle of the voltage vector hexagon is utilized as the voltage limitation. Based on the simplified voltage limitation, the maximum amplitude of the magnetizing current pulse under real-time operating conditions can be obtained, which is utilized as the boundary for MS manipulation in the proposed MS control method. Within the

boundary, the target MS can be achieved. otherwise, the MS will be limited, and in this case, the proposed MS control method also provides solutions to achieve the target MS by calculating the optimal operating speed. Then, the overall control strategy with the proposed MS control method is illustrated. Finally, the experimental validation is conducted on the HMMM drive system. The feasibility of the proposed MS control method is verified both on remagnetization and demagnetization.

4.2 Mathematical Model for VFMM

4.2.1 VFMM Model

The mathematical model is expressed below and more details are illustrated in APPENDIX B.

$$\begin{cases} u_d = R(i_d + i_{mag.}) + L_d \frac{d(i_d + i_{mag.})}{dt} + \frac{d\psi_m(i_{mag.})}{dt} - \omega L_q i_q \\ u_q = R i_q + L_q \frac{d i_q}{dt} + \omega L_d (i_d + i_{mag.}) + \omega \psi_m(i_{mag.}) \end{cases} \quad (4.1)$$

4.2.2 Voltage and Current Constraints

The voltage and current constraints for VFMM are expressed as:

$$\begin{cases} u_d^2 + u_q^2 \leq V_m^2 \\ i_d^2 + i_q^2 \leq I_m^2 \end{cases} \quad (4.2)$$

where I_m is the rated current of the machine, and V_m is the maximum voltage magnitude, which depends on the DC bus voltage and the PWM control method.

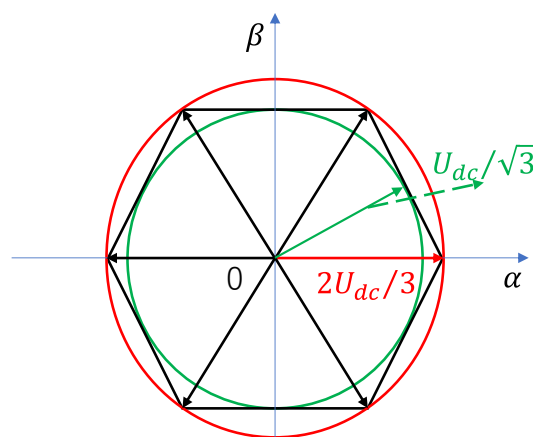


Fig. 4.1. Schematic diagram of space vector voltage limit circle.

The space vector voltage limit circle is depicted in Fig. 4.1. Generally, the ideal operating performance region for the machine control is inside the inscribed circle of the hexagon, where

the voltage vector is working in the linear region. In this case, the voltage limit for machine control can be expressed as

$$V_m = U_{dc}/\sqrt{3} \quad (4.3)$$

where U_{dc} is the dc-link voltage.

4.3 Magnetization State Control Based on Voltage Limitation

4.3.1 Effect of Voltage Limitation on MS Manipulation

Since i_{mag} is usually very large for VFMM, this will consume a lot of energy during MS manipulation, which will cause the insufficient voltage issue to hardly achieve the target MS. Therefore, the effect of voltage limitation during MS manipulation must be considered.

The torque-speed curve is depicted in Fig. 4.2. In the whole speed range, the maximum envelope can also be treated as the voltage limitation, especially in the flux weakening region. The MS manipulation is available under the maximum envelope, and its capability is affected by the voltage limitation. Once the voltage is limited, the current will be out of control, and the performance of the machine control system will be affected, especially for the MS control.

The available voltage for MS manipulation can be calculated by:

$$V_{MS}^2 = V_m^2 - (u_d^2 + u_q^2) \quad (4.4)$$

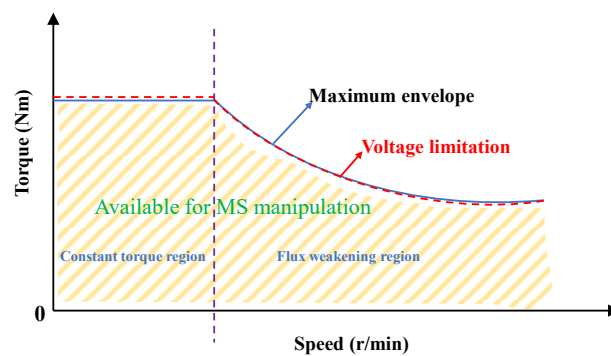


Fig. 4.2. Torque speed curve for VFMM.

4.3.2 Modified Voltage limitation During MS Manipulation

Due to i_{mag} has at least 30 ms time duration on the amplitude as shown in Fig. 3.1, the main part to determine whether the voltage is enough to achieve MS manipulation is still the steady component. Therefore, the dynamic differential component can be neglected. Then, the voltage model during MS manipulation can be expressed as

$$\begin{cases} u_d = R(i_d + i_{mag.}) - \omega L_q i_q \\ u_q = R i_q + \omega L_d (i_d + i_{mag.}) + \omega \psi_m (i_{mag.}) \end{cases} \quad (4.5)$$

Combine (4.5) with the voltage limit in (4.2):

$$(R(i_d + i_{mag.}) - \omega L_q i_q)^2 + (R i_q + \omega L_d (i_d + i_{mag.}) + \omega \psi_m (i_{mag.}))^2 = U_{dc}^2/3 \quad (4.6)$$

Then, the maximum $i_{mag.}$ under real-time operating conditions can be obtained.

However, utilizing (4.6) to calculate the maximum $i_{mag.}$ under real-time operating conditions is too complex. The solution of (4.6) for maximum $i_{mag.}$ is too time consuming to perform in real time. According to the voltage limit circle in Fig. 4.1, the circumcircle of the hexagon is the maximum voltage vector boundary in the field-oriented control (FOC) algorithm, which is usually used as the limitation of the dq -axis voltages in the current controller as illustrated in Fig. 4.3. It can be expressed as

$$\begin{cases} |u_d| \leq 2U_{dc}/3 \\ |u_q| \leq 2U_{dc}/3 \end{cases} \quad (4.7)$$

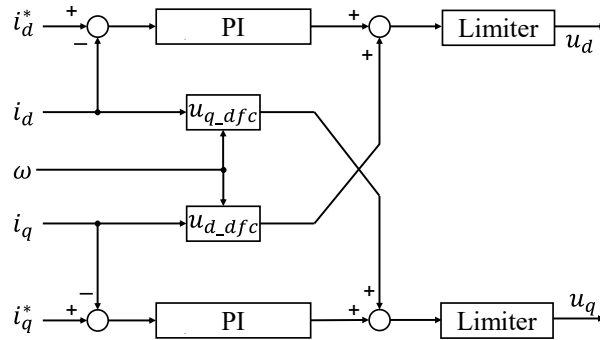


Fig. 4.3. Current controller with decoupling feedforward compensation [MOR94].

where i_d^* and i_q^* are the reference dq -axis stator currents. In the current controller, the decoupling feedforward compensation is utilized to solve the cross-coupling effects. The decoupling feedforward compensation voltages for VFMM are expressed as:

$$u_{q_dfc} = \omega L_d i_d + \omega \psi_m (i_{mag.}) \quad (4.8)$$

$$u_{d_dfc} = -\omega L_q i_q \quad (4.9)$$

As $i_{mag.}$ is injected into the d -axis current, the output of the d -axis current PI controller u_d will be affected directly. When u_d is limited, the actual d -axis current cannot follow the reference very well. Therefore, the limitation of u_d is set as the modified voltage limitation during MS

manipulation in this chapter, which is expressed as:

$$|R(i_d + i_{mag.}) - \omega L_q i_q| \leq 2U_{dc}/3 \quad (4.10)$$

Then, the maximum $i_{mag.}$ under real-time operating conditions can be easily obtained:

$$|i_{mag.}| \leq (2U_{dc}/3 + \omega L_q i_q)/R - |i_d| \quad (4.11)$$

Comparing with the algorithm to calculate the maximum $i_{mag.}$ in (4.6), the modified method is significantly simplified. It is noted that the overmodulation algorithm must be considered in this modified voltage limitation for MS manipulation.

4.3.3 Proposed MS Control Method Based on Modified Voltage Limitation

Since the voltage limitation must be considered during the MS manipulation, a novel MS control method based on the modified voltage limitation is proposed in this chapter as presented in Fig. 4.4.

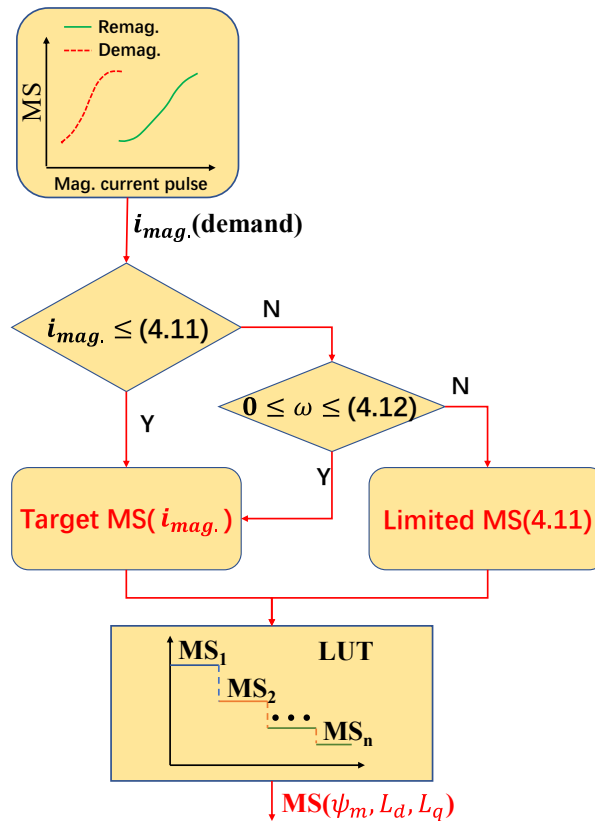


Fig. 4.4. Scheme of proposed MS control method.

When a MS manipulation command is generated, the demand $i_{mag.}$ to achieve the target MS can be obtained by the LUT in Fig. 3.9. The demand $i_{mag.}$ will be compared with the maximum $i_{mag.}$ calculated by (4.11), which provides a boundary for MS manipulation. The target MS can

be achieved within the boundary. If the amplitude of the demand i_{mag} is bigger than the maximum value, the MS will be limited. Then, the optimal operating speed to achieve the target MS can be obtained from (4.10), which can be expressed as:

$$\omega \leq (2U_{dc}/3 + R(i_d + i_{mag}))/L_q i_q \quad (4.12)$$

If the calculated speed is equal to or smaller than 0, the target MS is beyond the magnetizing capability of the machine under the operating conditions. In this case, the output of i_{mag} will be set as the maximum i_{mag} . Then, the MS manipulation will be processed to the limited MS, and the corresponding parameters under the limited MS will be feedback to the control algorithm.

4.3.4 Overall Control Strategy

The overall control system of the proposed MS control method on the HMMM is shown in Fig. 4.5. The outer loop control is the speed close-loop control. The setting speed ω^* is the main input of the control system. To take full advantage of the saliency of the machine, the maximum torque per ampere (MTPA) control is employed in the control algorithm. To mitigate the influence of the parameters during MS manipulation, the feedback flux weakening control method [KIM97b] is adopted in the control algorithm. After processed by the speed controller, MTPA controller and flux-weakening controller, the reference value of the current loop (i_d^* , i_q^*) is obtained. Then, the control process enters the inner loop control: the current close-loop control. As aforementioned, in the proposed MS control method, the overmodulation algorithm must be considered in the space vector pulse width modulation (SVPWM). i_{mag} is injected into the reference d -axis current. Each MS contains a set of dq -axis inductances and PM flux linkage (ψ_m, L_d, L_q), which will feedback into the algorithms of the MTPA controller and the current controller. The parameters for PI controllers are the same as Fig. 2.10. The flux weakening, MTPA, and PI controller are referred to Fig. 1.6. Since the output of flux weakening will affect dq -axis currents as presented in Fig. 1.6, dq -axis currents are depicted as the outputs of flux weakening block to simplify the schematic block.

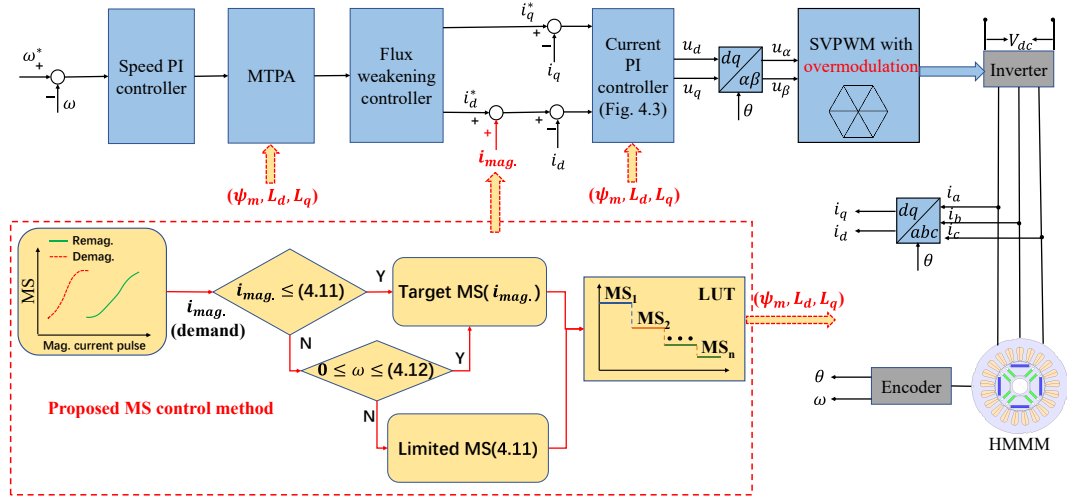


Fig. 4.5. Scheme of overall control system.

In Fig. 4.5, i_a , i_b , and i_c are the three-phase currents, respectively, u_α and u_β are the voltage components in the $\alpha\beta$ -axis, θ is the actual electrical angle.

4.4 Experimental Validation

4.4.1 Remagnetization Experimental Validation

The remagnetization process can enhance the flux linkage for the VFMM, which can improve the torque performance. Therefore, the remagnetization generally is processed at the starting stage or in the low-speed region.

Table 4.1. Main parameters of remagnetization validation.

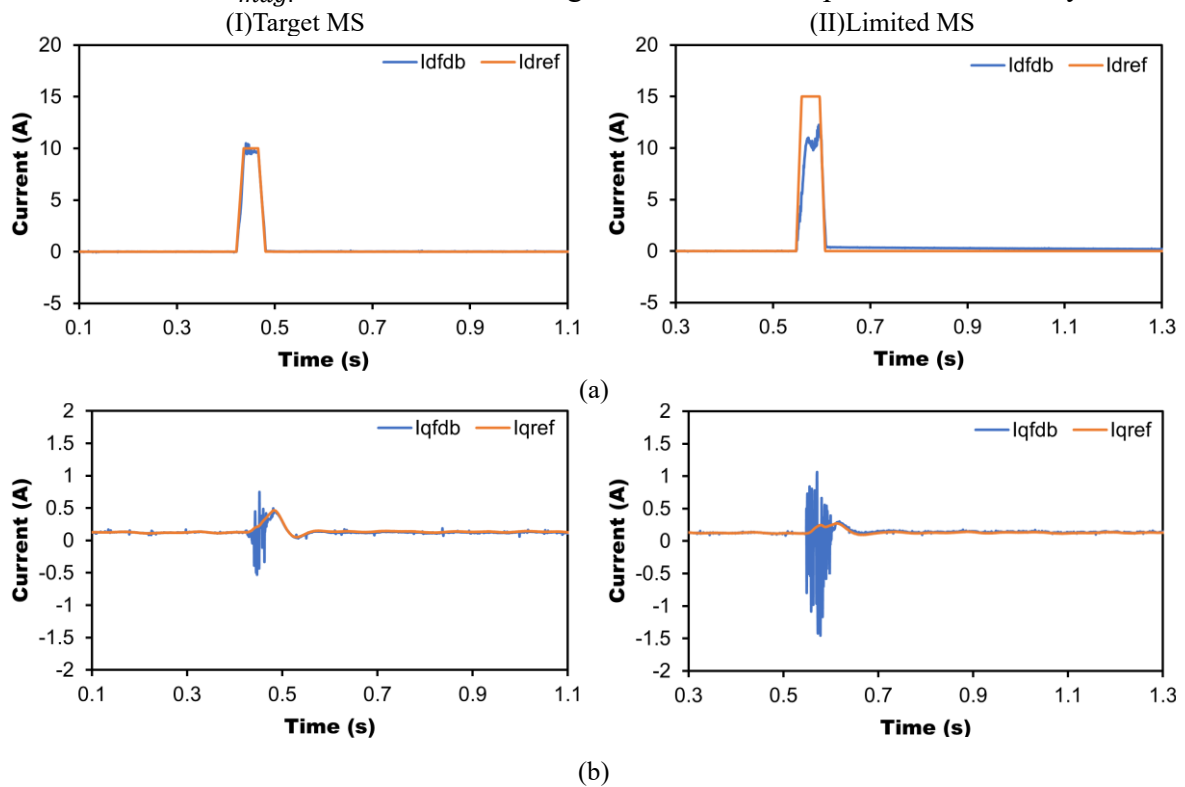
Item	Symbol	Value
DC link voltage	V_{dc}	50V
Rated current (RMS)	I_m	7.5A
Operating speed	n	200r/min
PM flux linkage at MS ₁	ψ_{m1}	0.125Wb
d -axis inductance at MS ₁	L_{d1}	15.1mH
q -axis inductance at MS ₁	L_{q1}	7.8mH
PM flux linkage at MS ₂	ψ_{m2}	0.169Wb
d -axis inductance at MS ₂	L_{d2}	19.0mH
q -axis inductance at MS ₂	L_{q2}	13.0mH
Remagnetization current pulse	$i_{mag.12}$	10A

In this chapter, the remagnetization validation is tested in the constant torque region. Two MSs are selected to complete the experiment. The main parameters are listed in Table 4.1. The DC-link voltage is set at 50 V, the operating speed is 200 r/min. The demand remagnetizing current pulse from MS₁ to MS₂ is 10 A.

Under the real-time operating conditions for the remagnetization experiment, the calculated maximum i_{mag} based on the proposed modified voltage limitation is 11 A. The measured results of the remagnetization from MS₁ to MS₂ are shown in Fig. 4.6(I). The same conventional controller as Chapter 3 is adopted here.

Since the demand i_{mag} is under the limitation, the actual current can reach to the target as shown in Fig. 4.6(I, a). u_d is quickly under control after a brief saturation in Fig. 4.6(I, c). During the voltage saturation, a small disturbance occurs in the q -axis current in Fig. 4.6(I, b). The MS manipulation brings significant disturbance for the system, especially on the transient of injecting i_{mag} , which is presented on speed and torque performance in Fig. 4.6(I, d) and Fig. 4.6(I, e). The significant fluctuations can also be found in three-phase currents as shown in Fig. 4.6(I, f). The torque changes as expected in Fig. 4.6(I, e), while it is out of control in Fig. 4.6(II, e) due to the limit of MS.

Since the demand i_{mag} is not limited, the target MS can be manipulated successfully.



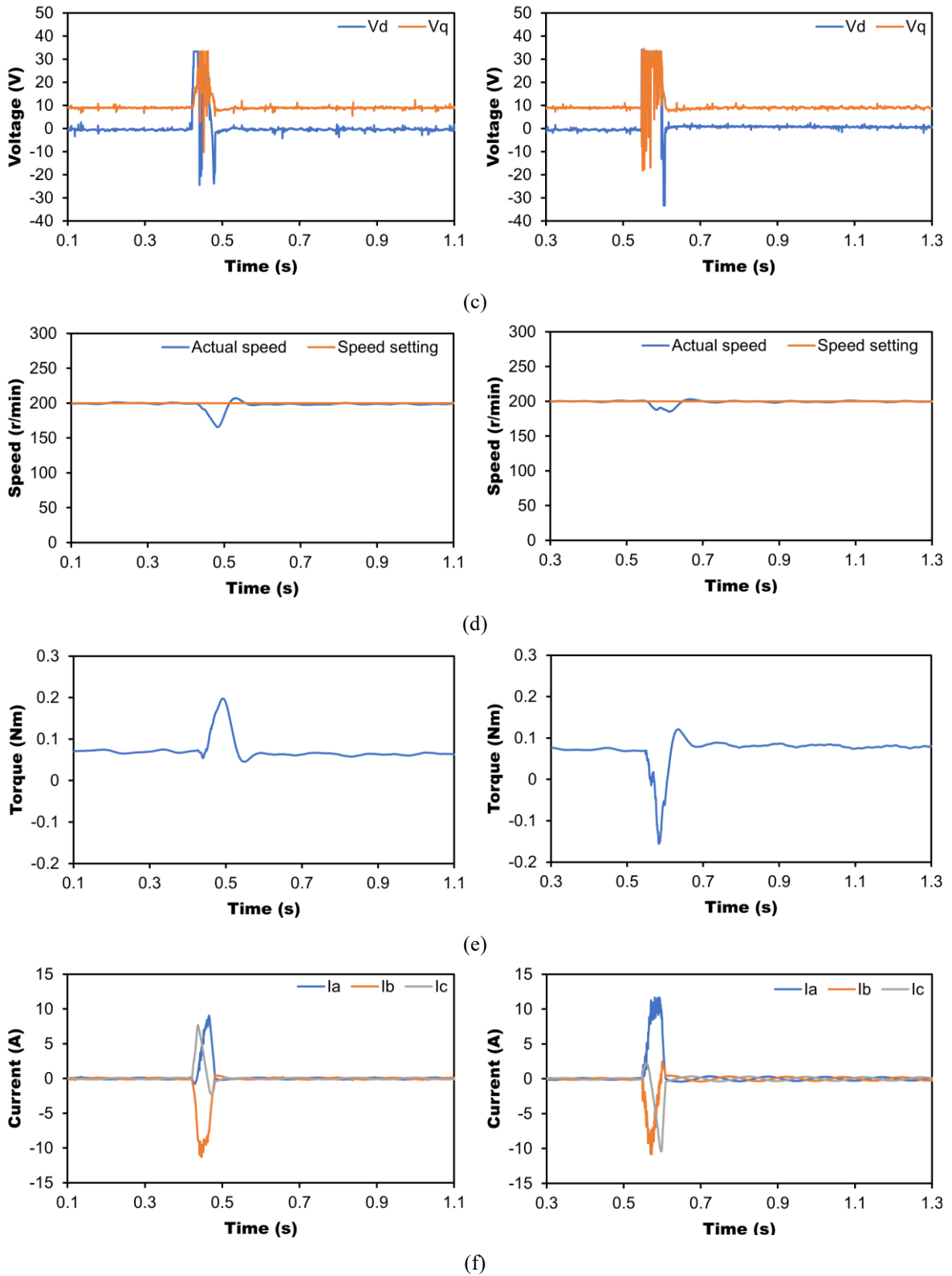


Fig. 4.6. Remagnetization validation in constant torque region. (I) Achieve target MS, (II) Limited MS due to voltage limitation. (a) d -axis current. (b) q -axis current. (c) dq -axis voltages. (d) Speed. (e) Torque. (f) Three-phase currents.

Then, the demand i_{mag} beyond the limitation is tested. The operating conditions keep the same as above. The demand i_{mag} is 15 A, which is bigger than the maximum value. To achieve the

target MS, the optimal speed is calculated, which is less than 0 as calculated by (4.12). Therefore, the final MS can only reach to the limited state. The measured results are shown in Fig. 4.6(II).

The actual i_{mag} is limited at 11 A as shown in Fig. 4.6(II, a). Due to the voltage limitation, u_d keeps saturation during the whole MS manipulation in Fig. 4.6(II, c). Since i_{mag} is limited, the current is out of control, which leads to the significant disturbance in q -axis current in Fig. 4.6(II, b). In this case, the performance of torque and speed is abnormal as shown in Fig. 4.6(II, e) and Fig. 4.6(II, d).

Since i_{mag} is constrained to the limitation value, the final MS is not manipulated to the target and only reaches to the limited MS, and more fluctuations in currents and torque occur. Based on the proposed MS control method, the parameters under the final MS are still obtained since the MS is known.

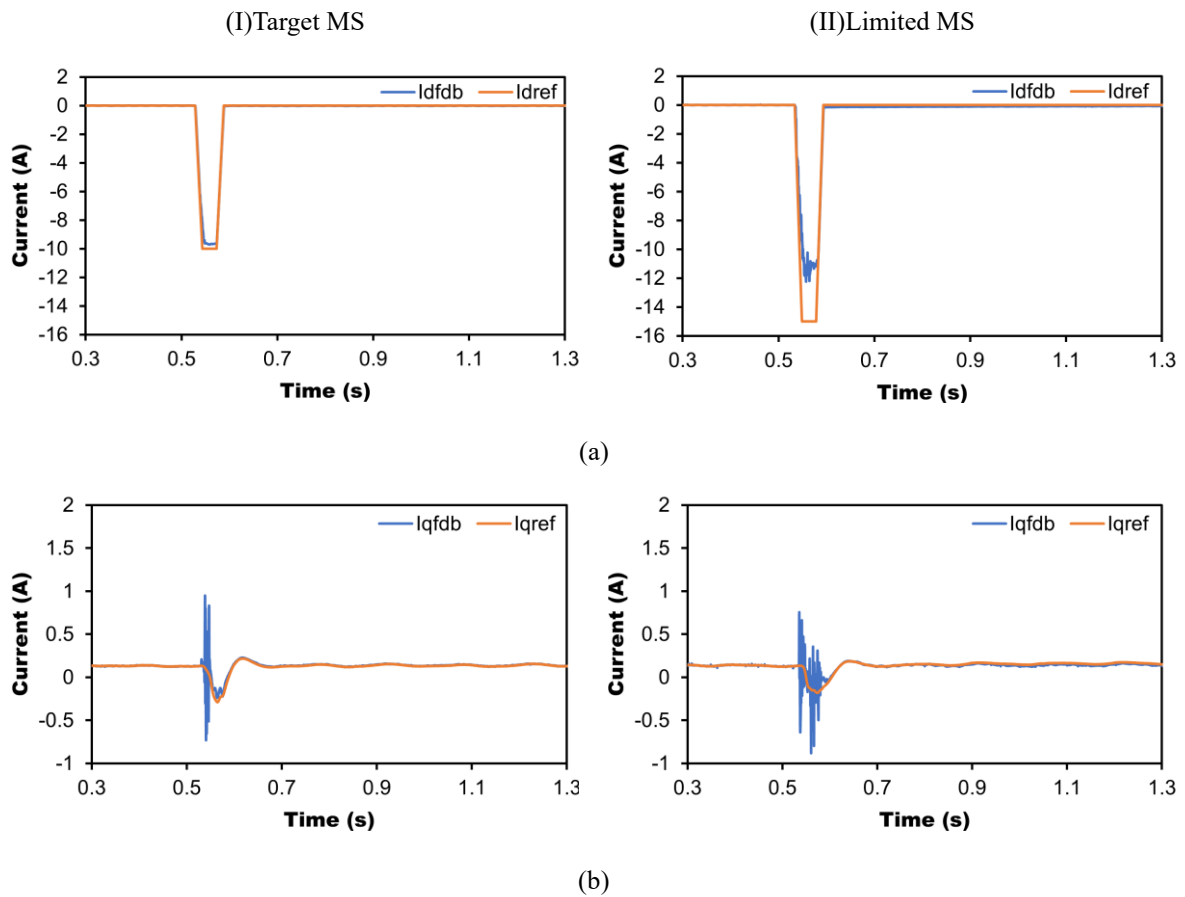
4.4.2 Demagnetization Experimental Validation

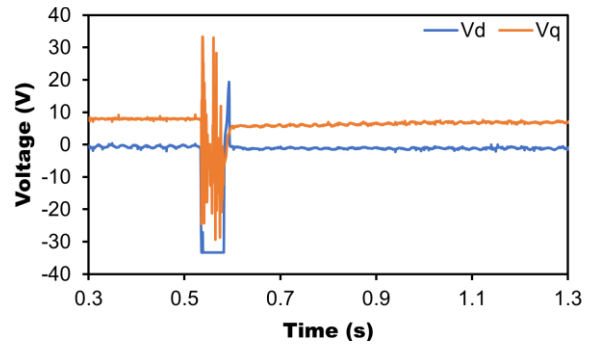
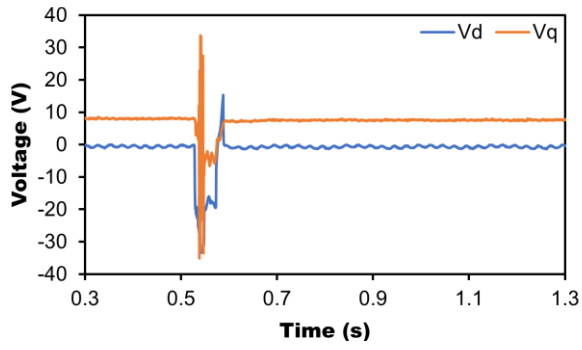
Three MSs are selected to test the demagnetization performance. The main parameters are listed in Table 4.2. First, the demagnetization manipulation is tested in the constant torque region at 200 r/min, the same speed as the remagnetization validation. The MS is demagnetized from MS₁ to MS₃. The measured results are shown in Fig. 4.7(I).

Table 4.2. Main parameters of demagnetization validation.

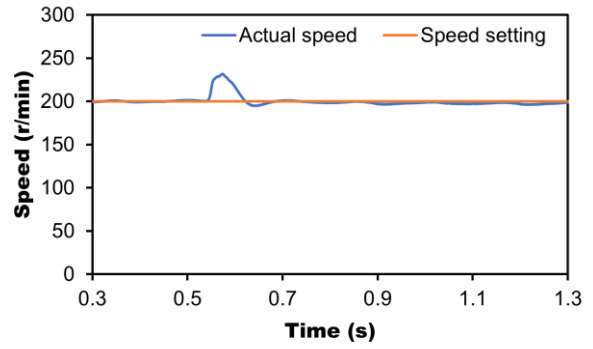
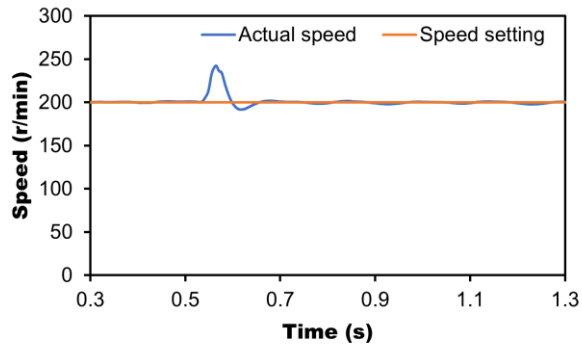
Item	Symbol	Value
DC link voltage	V_{dc}	50V
Rated current (RMS)	I_m	7.5A
Operating speed ₁	n_1	200r/min
Operating speed ₂	n_2	700r/min
PM flux linkage at MS ₁	ψ_{m1}	0.195Wb
d -axis inductance at MS ₁	L_{d1}	20.1mH
q -axis inductance at MS ₁	L_{q1}	15.0mH
PM flux linkage at MS ₂	ψ_{m2}	0.19Wb
d -axis inductance at MS ₂	L_{d2}	20.5mH
q -axis inductance at MS ₂	L_{q2}	15.0mH
PM flux linkage at MS ₃	ψ_{m3}	0.168Wb
d -axis inductance at MS ₃	L_{d3}	18.7mH
q -axis inductance at MS ₃	L_{q3}	12.6mH
Demagnetization current pulse ₁	$I_{mag.12}$	-5A
Demagnetization current pulse ₂	$I_{mag.13}$	-10A

According to the real-time operating conditions, the amplitude of the calculated i_{mag} limitation is 11 A. The demagnetizing current pulse from MS₁ to MS₃ is -10 A, which is under the limitation. Therefore, the actual magnetizing current pulse can reach to the demand value as shown in Fig. 4.7(I, a). At the beginning of demagnetization process, the injected i_{mag} causes disturbance in the q -axis voltage and q -axis current in Fig. 4.7(I, c) and Fig. 4.7(I, b). Then, the voltage quickly resumes under control. The large demagnetizing current pulse leads to the reduction of torque in Fig. 4.7(I, e). The speed increases due to the reduction in torque in Fig. 4.7(I, d). To adjust the speed fluctuations, the q -axis current decreases in Fig. 4.7(I, b). The three-phase currents are shown in Fig. 4.7(I, f). Since the demand i_{mag} is satisfied, the final MS can reach to the target.

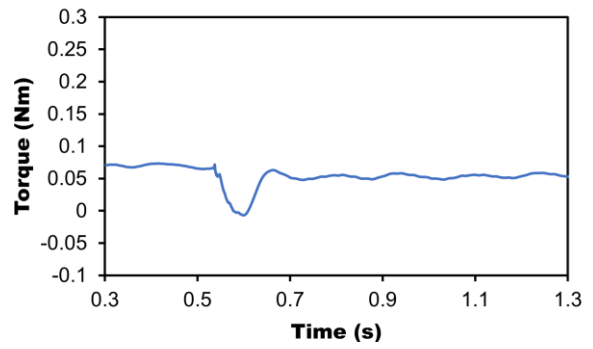
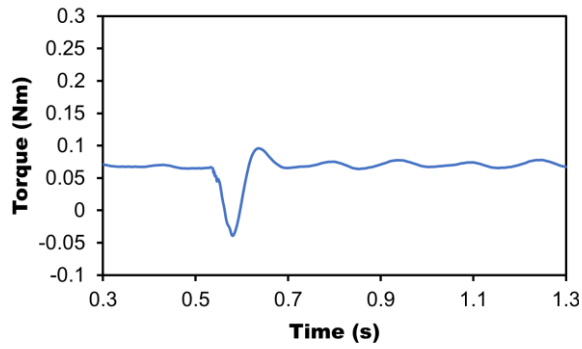




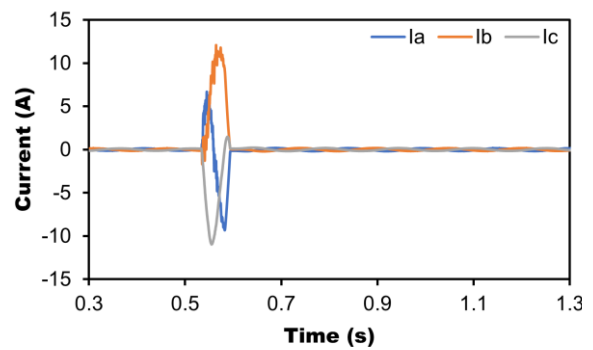
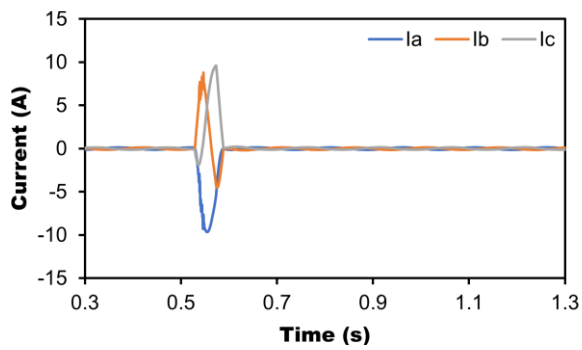
(c)



(d)



(e)



(f)

Fig. 4.7. Demagnetization validation in constant torque region. (I) Achieve target MS, (II) Limited MS due to voltage limitation. (a) d -axis current. (b) q -axis current. (c) dq -axis voltages. (d) Speed. (e) Torque. (f) Three-phase currents.

When the magnitude of the demand i_{mag} is beyond the limitation and exceeds the machine's magnetizing capability, the measured results are presented in Fig. 4.7(II). The demand i_{mag} for the MS manipulation is -15 A. Due to the magnitude is bigger than the limitation, the actual i_{mag} can only reach to -11 A as shown in Fig. 4.7(II, a). The d -axis voltage keeps saturation during MS manipulation in Fig. 4.7(II, c). The q -axis current is out of control in Fig. 4.7(II, b), and significant disturbance occurs. The speed, torque, and three-phase currents are shown in Fig. 4.7(II, d), Fig. 4.7(II, e), and Fig. 4.7(II, f), respectively.

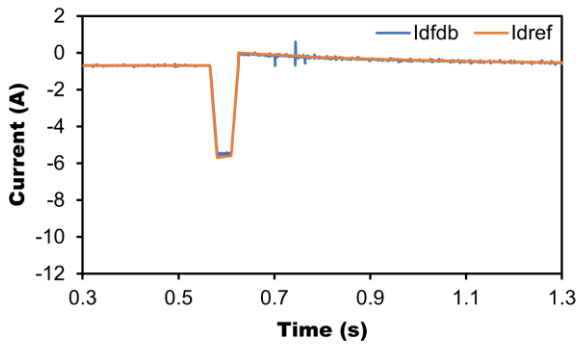
Due to the voltage limitation, the actual i_{mag} cannot reach to the demand value, the final MS can only be manipulated to the limited MS. The dynamic performance during the MS manipulation is worse than the successful target MS achievement.

Then, the demagnetization manipulation is tested in the flux weakening region to verify the proposed control method. The operating speed is 700 r/min. With the speed increasing, the voltage limitation shrinks, the limitation of i_{mag} reduces at the same time. Under the experimental conditions, the amplitude of the calculated limitation of i_{mag} by the modified voltage limitation is 9 A. The MS is demagnetized from MS₁ to MS₂, and the demand i_{mag} is -5 A, which is under the limitation. The measured results are shown in Fig. 4.8(I).

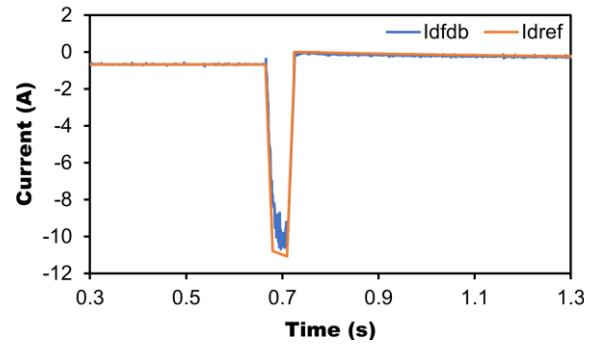
As there is enough voltage for the MS manipulation, the actual i_{mag} can reach to the demand value as shown in Fig. 4.8(I, a). The machine still operates in the flux weakening region after the MS manipulation. Therefore, after the sudden change caused by i_{mag} , the d -axis current gradually increases in the negative direction to restore the flux weakening control. The glitches in the voltage and current in Fig. 4.8(I, b) and Fig. 4.8(I, c) are the electromagnetic interference during the experiment and will be filtered out by the control system. Due to the increasing in d -axis current amplitude, the torque reduces during the demagnetization manipulation in Fig. 4.8(I, e). Then, the speed increases and be controlled quickly by the speed close-loop in Fig. 4.8(I, d). The three-phase currents are shown in Fig. 4.8(I, f).

Since i_{mag} reaches to the demand value, the MS is manipulated to the target MS, and the dynamic performance is stable.

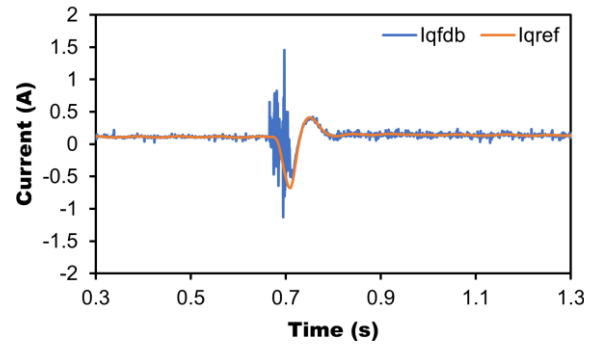
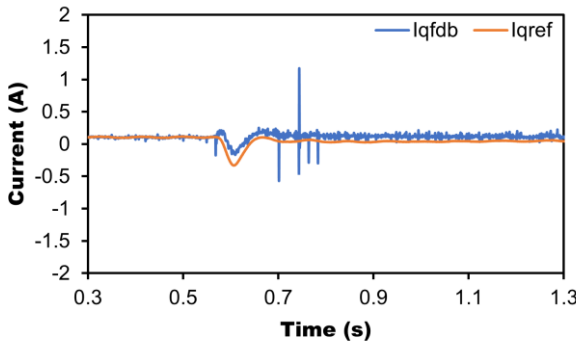
(I)Target MS



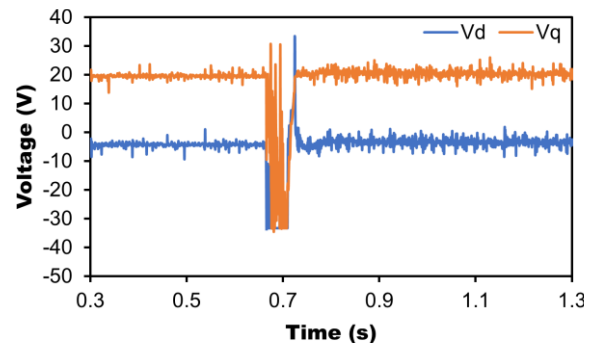
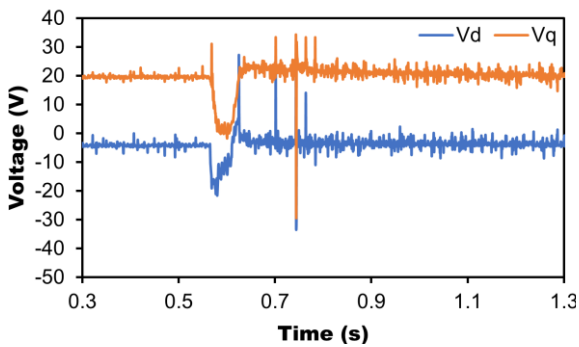
(II)Limited MS



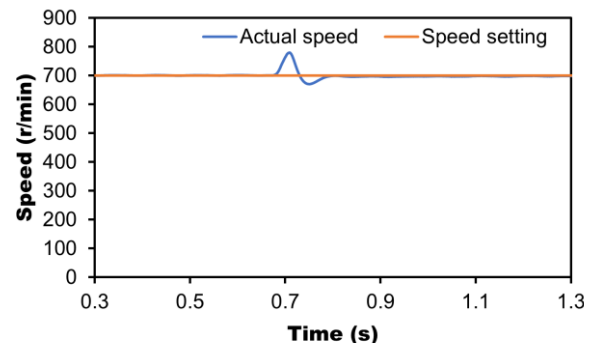
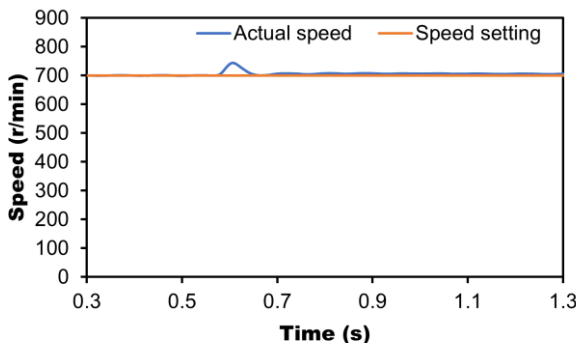
(a)



(b)



(c)



(d)

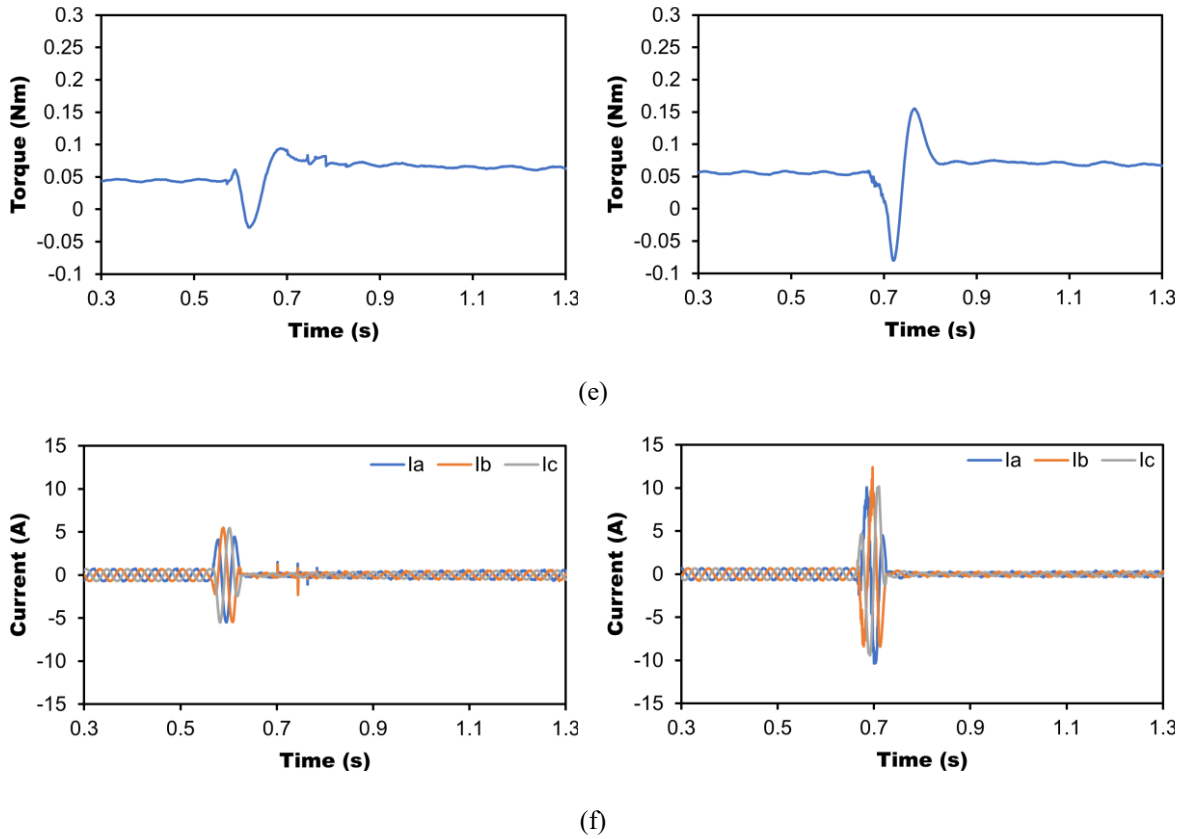


Fig. 4.8. Demagnetization validation in flux weakening region. (I) Achieve target MS, (II) Limited MS due to voltage limitation. (a) d -axis current. (b) q -axis current. (c) dq -axis voltages. (d) Speed. (e) Torque. (f) Three-phase currents.

Then, the demand i_{mag} increases to -10 A to test the proposed MS control method. The other experiment conditions keep the same as above. The measured results are shown in Fig. 4.8(II). The actual i_{mag} is limited to -9 A in Fig. 4.8(II, a). Due to the MS manipulation, the machine has almost exited the flux weakening control region. Therefore, after the MS manipulation, the amplitude of d -axis current is quite small. The d -axis voltage is saturated during the MS manipulation in Fig. 4.8(II, c), which indicates the current is out of control. This causes the disturbance in the current in Fig. 4.8(II, b). The performance of speed, torque, and three-phase currents are shown in Fig. 4.8(II, d), Fig. 4.8(II, e), and Fig. 4.8(II, f), respectively, which is not good due to the voltage limitation.

The solution to realize the target MS manipulation is decreasing the speed to 200 r/min, where the limitation of i_{mag} is 11 A based on the proposed MS control method. Then, the demand -10 A i_{mag} can be satisfied, and the target MS can be achieved as shown in Fig. 4.7(I).

The measured results show that the proposed MS control method can ensure the accuracy and efficiency of MS manipulation and improve the dynamic performance.

4.5 Conclusion

In this chapter, a novel MS control method based the modified voltage limitation is proposed for VFMM and is tested on the investigated HMMM control system. The effect of the voltage limitation on the MS manipulation is analyzed. The circumcircle rather than the inscribed circle of the voltage vector hexagon is utilized as the voltage limitation. Based on the simplified voltage limitation, the maximum amplitude of the magnetizing current pulse under real-time operating conditions can be calculated, which is utilized as the boundary for MS manipulation in the proposed MS control method. Within the boundary, the target MS can be achieved. When the MS is limited, the proposed MS control method also provides solutions to achieve the target MS by calculating the optimal operating speed. The fluctuation caused by the voltage limitation during MS manipulation can be reduced more than 50 % by the proposed method. The feasibility of the proposed MS control method is well validated on the investigated machine drive system.

CHAPTER 5 MAGNETIZATION STATE CONTROL UTILIZING *D*-AXIS CURRENT TO ELIMINATE UNINTENTIONAL DEMAGNETIZATION OF LOW-COERCIVE FORCE PERMANENT MAGNET

Since the MS can be demagnetized by negative current pulse, the large amplitude of negative flux weakening current can also cause demagnetization, which can be defined as unintentional demagnetization (UD) issue. In this chapter, a novel MS control method is proposed to eliminate the UD issue of low-coercive force permanent magnet (PM) for variable flux memory machine (VFMM).

5.1 Introduction

For conventional permanent magnet synchronous machine (PMSM) drive systems, a continuous negative *d*-axis current is necessary in the flux weakening region to extend the speed, which will cause additional losses and reduce the efficiency of the drive system. A variable flux memory machine (VFMM) can solve this major issue in PMSM systems. The special low-coercive force (LCF) permanent magnet (PM) in VFMM can be remagnetized and demagnetized by a current pulse, and its magnetization state (MS) can be memorized after the magnetizing current pulse is removed. Once the MS is memorized, it can be changed again only when the amplitude of the current pulse is bigger than before [JIA22b]. Then, the PM flux linkage can be regulated without the need of a continuous flux weakening current. Therefore, the efficiency of the VFMM system can be improved significantly.

The adjustment of the MS in VFMMs can be achieved by two different strategies: separate direct current (DC) magnetization coils or the stator AC armature windings in PMSMs [YAN18b]. For the DC magnetized VFMM, a current pulse can be applied by an H-bridge converter on the DC magnetizing coils to manipulate the MS of LCF PMs [YU11b] [YAN19b] [LIU14a] [WU15] [YAN14a]. [YAN19b] proposed a stepwise magnetization control strategy by dividing the overall operating envelop into several regions based on the torque-speed characteristic curve under various PM MSs. Due to the DC magnetizing coils and the extra equipment to control the magnetizing current pulse, the structure for the DC magnetized VFMM is much more complicated.

For AC magnetized VFMM, a d -axis current pulse is utilized to regulate the MS of LCF PMs [LYU20a] [LYU20b] [MAS15] [YU14] [GAG14] [HU21] [MAE14] [CHE20] [GAG16] [ATH18]. The look up table (LUT) MS control methods were utilized in [LYU20b] and [MAS15], which contained the relationship between the MS and the d -axis current pulse. The speed was set as the condition of MS manipulation, this was easy to implement and popular in the existing literature. [YU14] and [GAG14] focused on the MS control under load condition and in high-speed region, in which the current and voltage limitations have caused big challenges for MS manipulation, but it was ignored in the most research. The efficiency and accuracy of the magnetizing current control during MS manipulation were improved in [HU21] and [MAE14], while the disturbances caused by the magnetizing current pulse were not mentioned. In [CHE20] [GAG16] [ATH18], the online MS control methods were investigated, which were more efficient than the methods based on LUT, but the algorithms were very complicated.

Since the LCF PMs can be demagnetized by an additional negative d -axis current pulse, the negative d -axis armature current for flux weakening control can also cause the demagnetization of the LCF PMs when the machine operates in the flux weakening region. This kind of demagnetization can change the PM flux linkage unintentionally, and make the MS out of control, which will affect the performance of the machine drive system. The MS represents a reference state for MS manipulation. The MS manipulation is processed from the present MS to the target MS. The accuracy of the present MS can make sure the MS reaches the demand. This is designated in this chapter as the unintentional demagnetization (UD) issue for VFMM. Since the UD issue is rarely considered in the existing MS control literature for VFMM, it will be the research subject in this chapter.

In this chapter, a novel MS control method is proposed to eliminate the UD issue by utilizing the d -axis current for VFMMs. Firstly, the topology of the investigated hybrid magnet memory machine (HMMM) and its PM properties are illustrated. The characteristics of the dq -axis inductances which are affected by the change of MSs are analyzed. Secondly, the conventional control methods in the whole speed range for VFMM are illustrated. Thirdly, a PM flux linkage estimation is adopted to detect the UD issue. To ensure the accuracy of the PM flux linkage estimation, the voltage source inverter (VSI) nonlinearity is compensated. The initial MS manipulation is set for the proposed MS control method. Then, a LUT containing the relationship between the MSs and the demagnetization d -axis current pulses is established. Then, when the flux weakening d -axis current under certain MS reaches to the value of the

previous demagnetization current pulse, the MS is manipulated. The proposed MS controller is designed and the overall control system for the HMMM is illustrated. Finally, the experiment validation is presented to verify the proposed MS control method on the investigated machine drive system.

5.2 Control Method for VFMM

5.2.1 Mathematical Model of VFMM

The mathematical model is expressed below and more details are illustrated in APPENDIX B.

$$u_d = Ri_d + L_d \frac{di_d}{dt} + \frac{d\psi_m(i_{mag.})}{dt} - \omega L_q i_q \quad (5.1)$$

$$u_q = Ri_q + L_q \frac{di_q}{dt} + \omega L_d i_d + \omega \psi_m(i_{mag.}) \quad (5.2)$$

$$T_e = 1.5p[\psi_m(i_d)i_q + (L_d - L_q)i_d i_q] \quad (5.3)$$

5.2.2 Field-Oriented Control for VFMM

Except for the adjustability of MS, VFMM is still a PMSM. The field-Oriented control (FOC) method is constrained by the machine rated current and DC bus voltage by:

$$\begin{cases} i_d^2 + i_q^2 \leq I_m^2 \\ u_d^2 + u_q^2 \leq V_m^2 \end{cases} \quad (5.4)$$

where I_m is the current magnitude limit and V_m is the voltage magnitude limit.

At steady state, (5.1) and (5.2) can be expressed as

$$\begin{cases} u_d = Ri_d - \omega L_q i_q \\ u_q = Ri_q + \omega(L_d i_d + \psi_m) \end{cases} \quad (5.5)$$

where ψ_m is the steady state permanent magnet flux.

Based on the above analytical model, the current trajectories in dq -axis current plane for the salient-pole and non-salient-pole VFMM can be illustrated in Fig. 5.4.

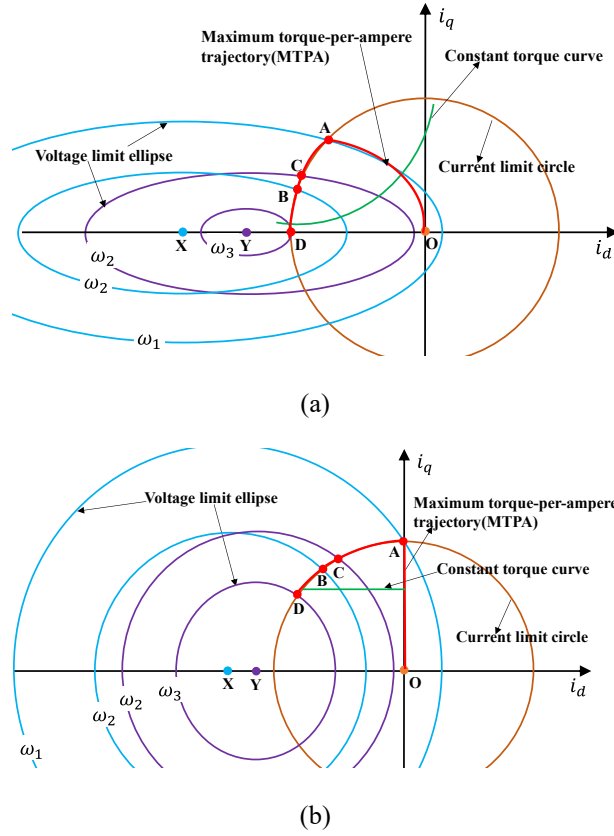


Fig. 5.1. Maximum power output current trajectory for VFMM. (a) Salient-pole VFMM ($L_d \neq L_q$). (b) Non-salient-pole VFMM ($L_d = L_q$). Speed: $\omega_1 < \omega_2 < \omega_3$.

In Fig. 5.1, demagnetization is illustrated at speed ω_2 . X point on the horizontal axis is the center point of the voltage initial limit ellipse before demagnetization process, and Y point is the center point of the voltage limit ellipse after demagnetization process. The coordinate values of X and Y are $(-I_c, 0)$, where I_c ($I_c = \psi_m/L_d$) is the characteristic current of the VFMM. The PM flux is changed by the demagnetization, and thus, the center of the voltage limit ellipse moves.

The current trajectories for VFMM will go along the curve 'OA' at the constant torque region, and then turn into the flux weakening region along ABCD due to the demagnetization manipulation in Fig. 5.1.

On the curve 'OA', the machine operates in the constant torque region. In this region, by considering the maximum torque per Ampere (MTPA) curve, i_d can be expressed as

$$\begin{cases} i_d = 0 & (L_d = L_q) \\ i_d = \frac{-\psi_m(i_d) + \sqrt{(\psi_m(i_d))^2 + 8(L_d - L_q)^2 i_s^2}}{4(L_d - L_q)} & (L_d \neq L_q) \end{cases} \quad (5.6)$$

where i_s is the input current of the MTPA control. Then, i_q can be expressed as

$$i_q = \sqrt{i_s^2 - i_d^2} \quad (5.7)$$

On the curve 'AB', also called as flux weakening region, the machine operates on the intersection point of the current and voltage limits. By ignoring the stator resistance, the relationship between i_d and i_q on this curve can be expressed as

$$\begin{cases} i_d = \frac{-\psi_m(i_d) + \sqrt{\frac{V_m^2}{\omega^2} - (L_q i_q)^2}}{L_d} \\ i_d^2 + i_q^2 = I_m^2 \end{cases} \quad (5.8)$$

(5.8) is usually used in the feedforward flux weakening control method. In this chapter, considering the high robustness, the voltage magnitude feedback flux-weakening [KIM97b] is adopted to analyze the performance of VFMM.

5.3 Proposed MS Controller Design

5.3.1 PM Flux Linkage Estimation

In Fig. 2.5, it can be observed that the PM flux linkage is more severely affected by the change of MS, especially from MR=+100% to MR=0%. To avoid the occurrence of the UD, the MS must be monitored all the time.

As shown in the steady state model (5.5), the derivative terms can be neglected. The corresponding rotor reference frame model for the estimation PM flux linkage becomes:

$$\omega \hat{\psi}_m = u_q - R i_q - \omega L_d i_d \quad (5.9)$$

where $\hat{\psi}_m$ is the estimated PM flux linkage.

Fig. 5.2 shows the scheme of on-line PM flux linkage estimation for VFMM. A low pass filter (LPF) is adopted here to filter out the high frequency components. The outputs of the PM flux linkage estimation are used to detect the UD when the VFMM is operating under the initial MS. When $\hat{\psi}_m$ is inconsistent with the value in Fig. 2.5, it can be determined that the UD has occurred. Then, the demagnetization process must be operated.

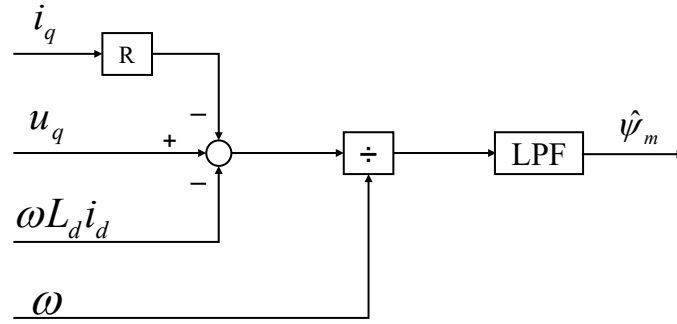


Fig. 5.2. On-line PM flux linkage estimation.

In (5.9), it can be observed that the voltage can affect the accuracy of the PM flux linkage estimation. Thus, the VSI nonlinearity compensation must be considered [ZHU21] [KIM06] [LIU14c]. In this paper, the dead-time and turn on/off delay of the inverter are compensated based on the reference [LIU14c].

5.3.2 Initial MS Manipulation

In the starting stage of the machine, the larger the starting torque, the better. According to (5.1) - (5.3), the electromagnetic torque is mainly affected by the PM torque in the low-speed region. The larger the PM flux linkage, the larger the q -axis voltage and the electromagnetic torque. Thus, the initial MS for VFMM is generally magnetized to forward saturation at first, i.e., $MR=+100\%$. Then, the MTPA control can be adopted in the constant torque region to utilize the saliency torque. This will enhance the operation performance of VFMM in the constant torque region.

As mentioned earlier, the UD issue is mainly caused by the negative d -axis armature current. It can be seen in (5.6), the negative d -axis armature current generated by the MTPA control is affected by the difference between dq -axis inductances. The bigger the difference of dq -axis inductances, the larger the amplitude of the negative d -axis armature current, which may be large enough to cause the UD issue in the constant torque region. In the flux weakening region, due to the voltage limit ellipse and current limit circle, the amplitude of the negative flux weakening d -axis armature current will gradually increase with the increase of speed, which will also cause the UD issue. When the PM flux linkage estimation detects the UD issue, the first demagnetization manipulation must be operated. The MS switches from the initial MS_1 to MS_2 , and the first demagnetization d -axis current pulse $I_{dem.12}$ can be obtained.

5.3.3 Proposed MS Controller

The proposed MS controller is based on a LUT of MSs. Therefore, the LUT must be built first.

The VFMM has a group of torque-speed characteristic curves under different MSs. It has already been proved that MS manipulations on the intersections of these torque-speed characteristic curves are much smoother and steadier [JIA22a]. The scheme of the LUT of MSs is illustrated in Fig. 5.3, which contains the magnitude of the demand d -axis current pulse for the change of MSs, the torque and speed on these intersections.

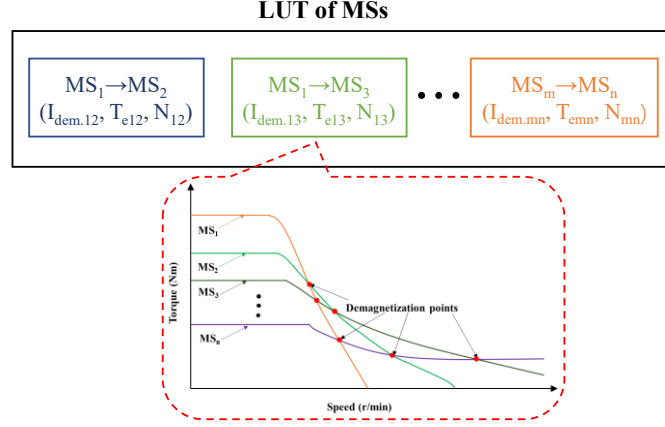


Fig. 5.3. Scheme of LUT of MSs.

Due to the properties of LCF PM, the PM linkage of VFMM can be either remagnetized or demagnetized and memorized by a magnetizing d -axis current pulse. Once the MS is changed to a certain level, it cannot be changed again unless the amplitude of d -axis current (the summation of d -axis armature current and injected d -axis magnetizing current pulse) is bigger than the magnitude of the demand magnetizing current pulse for the previous MS manipulation. In this chapter, the demand demagnetization d -axis current pulse ($I_{dem.}$) listed in the LUT is used as the condition of MS manipulation to avoid the UD issue. The MS control can be expressed as:

$$\begin{cases} |i_d| \leq |I_{dem.12}|, & MS_2 \\ |i_d| > |I_{dem.12}|, & MS_2 \rightarrow MS_3 \end{cases} \quad (5.10)$$

where $|I_{dem.12}|$ is the magnitude of the demand demagnetization d -axis current pulse from the initial MS_1 to MS_2 . The first-time demagnetization from the initial MS_1 to MS_2 is operated when the PM flux linkage estimation detects the UD issue. Then, the demagnetization d -axis current pulse $I_{dem.12}$ can be obtained from the LUT of MSs. This $I_{dem.12}$ will be used as the condition for the next demagnetization. That is when the absolute value of d -axis current $|i_d|$ is smaller than or equal to $|I_{dem.12}|$, the MS stays at MS_2 , when $|i_d|$ is bigger than $|I_{dem.12}|$, the MS will change from MS_2 to MS_3 or other MS, and so on. Therefore, the amplitude of the d -axis current is kept smaller than the amplitude of the demand d -axis demagnetizing current

pulse all the time, and the UD issue can be eliminated subsequently. The configuration of the proposed MS controller is shown in Fig. 5.4.

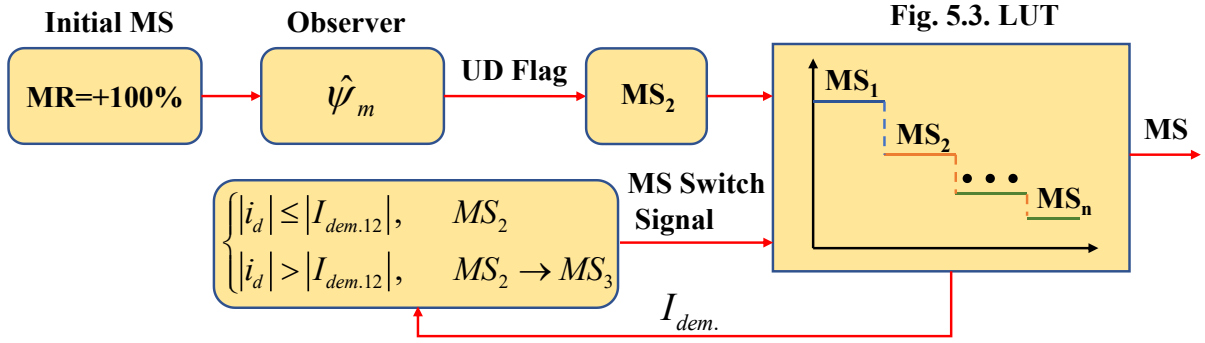


Fig. 5.4. Configuration of proposed MS controller.

5.3.4 Overall Control Strategy

The overall control system with the proposed MS control method for the HMMM is illustrated in Fig. 5.5, where V_{dc} is the DC-bus voltage of the three-phase inverter, i_a , i_b , and i_c are the three-phase currents, respectively, ω_m^* is the reference mechanical angular velocity, ω_m is the real mechanical angular velocity, θ is the actual electrical angle, i_{dM} and i_{qM} are the MTPA control dq -axis currents, which can be obtained by (5.6) and (5.7), Δi_d^* is the output of the flux-weakening control, i_d^* and i_q^* are the reference dq -axis currents for the current PI control.

As the initial MS is set at MR=+100%, the MTPA control is adopted in the constant torque region due to the saliency. As the speed of the HMMM becomes higher, when the magnitude of the output voltage of the current regulator is more than $V_m (V_{dc}/\sqrt{3})$, the machine operation enters the flux weakening control region, a negative d -axis current is generated by the voltage magnitude feedback control loop [KIM97b], which does not depend on the parameters of the machine. This will reduce the influence of the change of machine parameters on the control algorithm during the change of MS. For VFMM, the machine parameters including dq -axis inductances and PM flux linkage vary under different MSs, which has been considered in the flux weakening PI control [BED20]. The PM flux linkage ψ_m is manipulated in the proposed MS controller and will affect the current regulator. The MTPA controller and PI controller are referred to Fig. 1.6. The parameters and limits for PI controllers are same as Fig. 2.10.

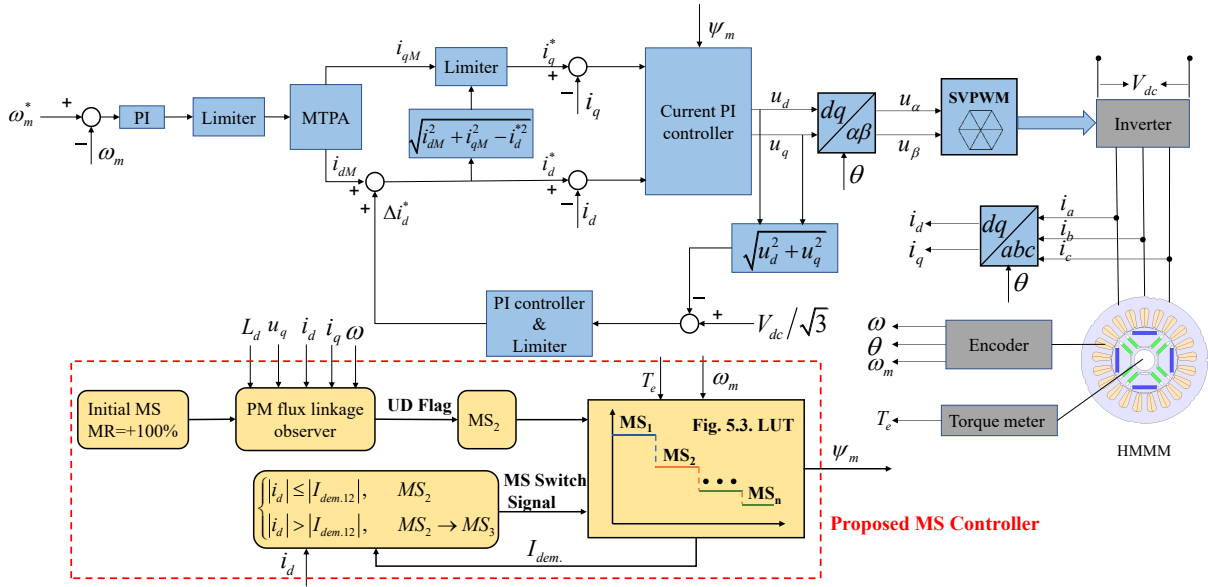


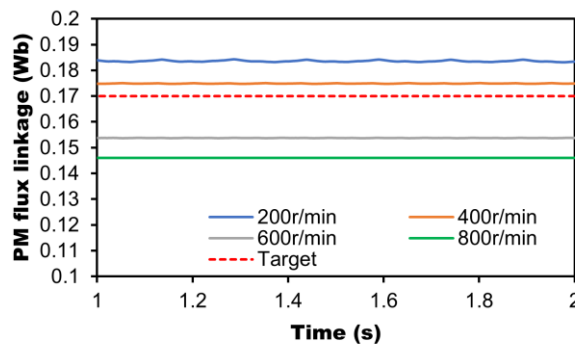
Fig. 5.5. Scheme of overall control system for HMMM.

5.4 Experiment Validation

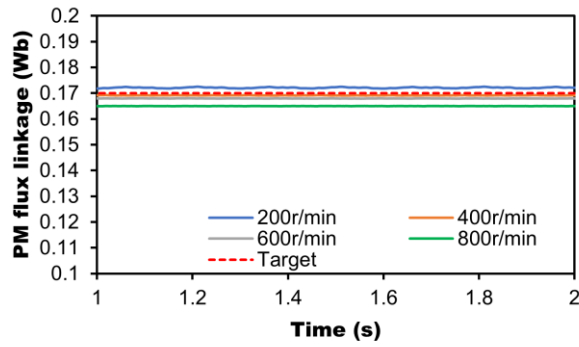
5.4.1 PM Flux Linkage Estimation

Based on the dSPACE platform for the investigated machine, the PM flux linkages under different speed/load operating conditions are estimated and the influence of VSI nonlinearity compensation is investigated.

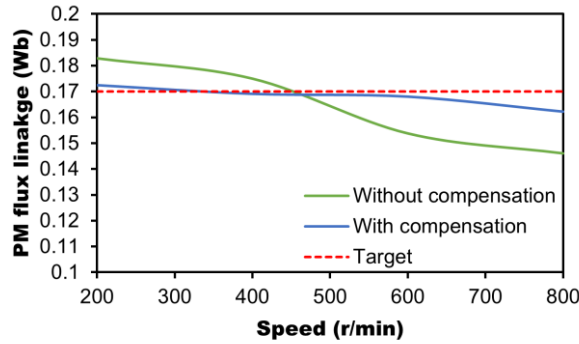
The machine is magnetized to the MS with PM flux linkage 0.17 Wb, which is the target for the PM flux linkage estimation test. The measured results are shown in Fig. 5.6. The estimated PM flux linkages under 200, 400, 600 and 800 r/min are recorded, respectively.



(a)



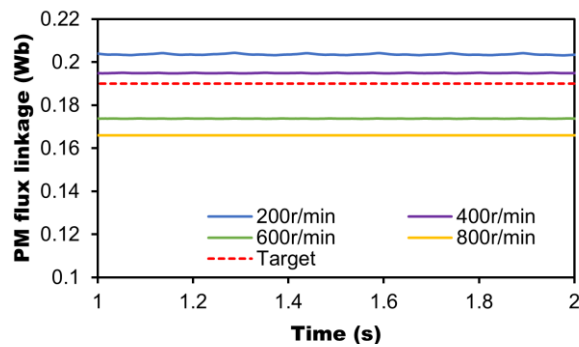
(b)



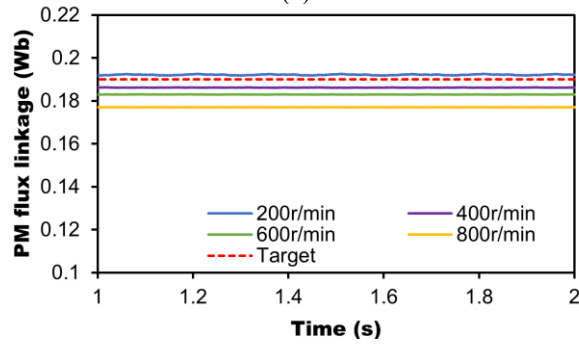
(c)

Fig. 5.6. PM flux linkage estimation. (a) Without VSI nonlinearity compensation. (b) With VSI nonlinearity compensation. (c) Comparison PM flux linkage with and without compensation against speed.

Without the VSI nonlinearity compensation, as the speed increases, the estimated PM flux linkage keeps decreasing, as shown in Fig. 5.6(a). All the estimated values under the four speed conditions are not close to the target value.



(a)



(b)

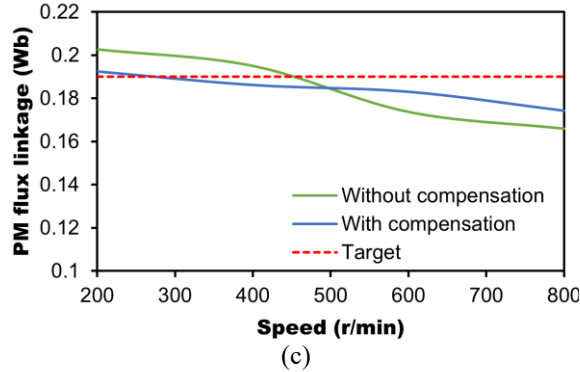


Fig. 5.7. PM flux linkage estimation for target 0.19 Wb. (a) Without VSI nonlinearity compensation. (b) With VSI nonlinearity compensation. (c) Comparison PM flux linkage with and without compensation against speed.

When the VSI nonlinearity is compensated, the estimated PM flux linkages under the four speed conditions are very close to the target, especially at 400 and 600 r/min. The error in the estimated PM flux linkage at 200 r/min is mainly due to low signal-to-noise ratio is low at low speed. At 800 r/min, the machine operates in the flux weakening region, the negative d -axis flux weakening current increases significantly, which will cause demagnetization in the LCF PM. Therefore, the estimated PM flux linkage decreases. This is evidence of the UD issue which will be further investigate in the next section. Further, The PM flux linkage estimation for target 0.19 Wb is tested and the measured results are presented in Fig. 5.7. The UD issue is more significant when the speed reaches to 800 r/min.

5.4.2 Verification of UD Issue

To verify the existence of the UD issue for the investigated machine, the machine is magnetized initially to the full remagnetization state under the laboratory condition. The estimated PM flux linkage reaches to 0.19 Wb and the measured results are shown in Fig. 5.8. With the speed increasing, the machine enters the flux weakening region. The amplitude of the negative d -axis current i_d keeps increasing. When i_d reaches to -2 A as shown in Fig. 5.8(a), the estimated PM flux linkage reduces from 0.19 Wb to 0.185 Wb, as can be seen in Fig. 5.8(b), i.e., UD occurs.

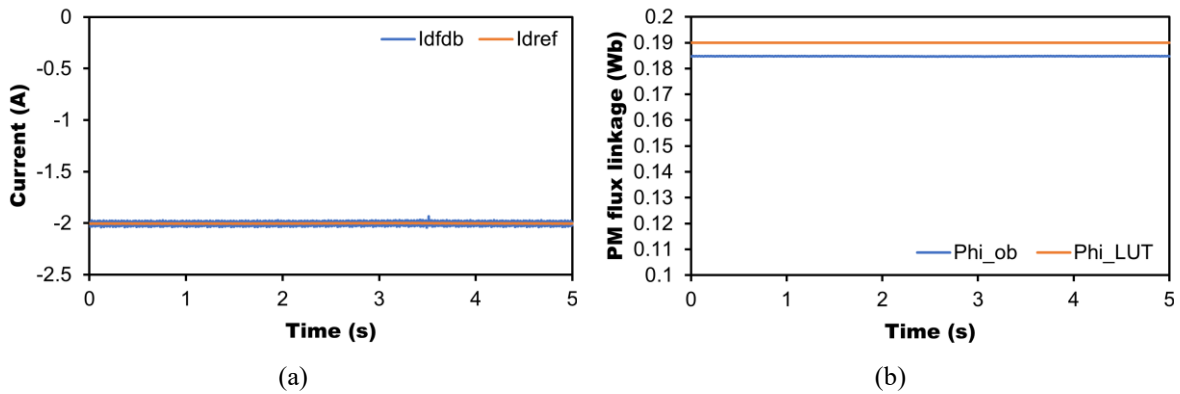


Fig. 5.8. UD issue under $i_d = -2$ A. (a) d -axis current. (b) Estimated PM flux linkage.

To further verify the UD issue, during the test the speed keeps increasing in the flux weakening region. When the speed increases to 650 r/min and $i_d = -4$ A as shown in Fig. 5.9(a), the estimated PM flux linkage further reduces from 0.185 Wb to 0.18 Wb as shown in Fig. 5.9(b), i.e., the UD issue becomes worse as $|i_d|$ increases. To avoid the UD issue and ensure the machine under control, the MS manipulation is required, as will be described in the next section.

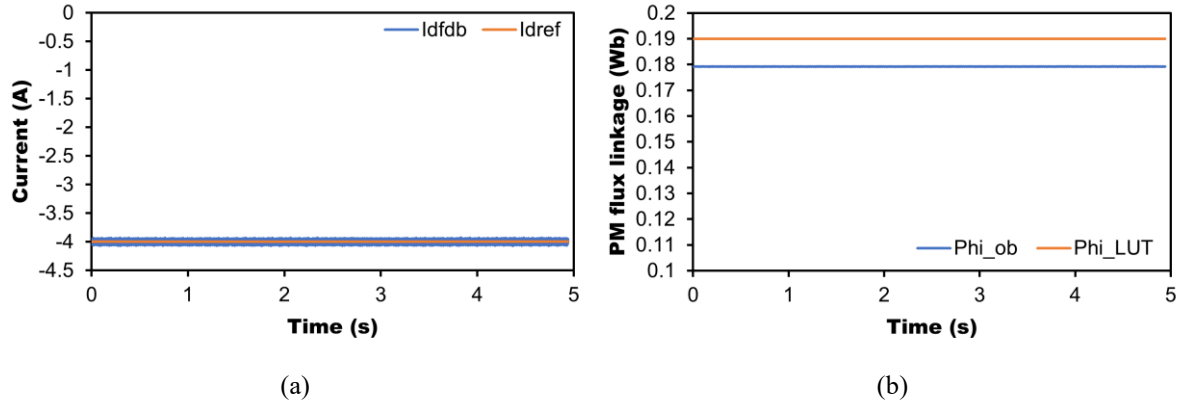


Fig. 5.9. UD issue under $i_d = -4$ A. (a) d -axis current. (b) Estimated PM flux linkage.

5.4.3 Verification of Proposed MS Control Method

The main parameters for the proposed MS control method experiments are listed in Table 5.1.

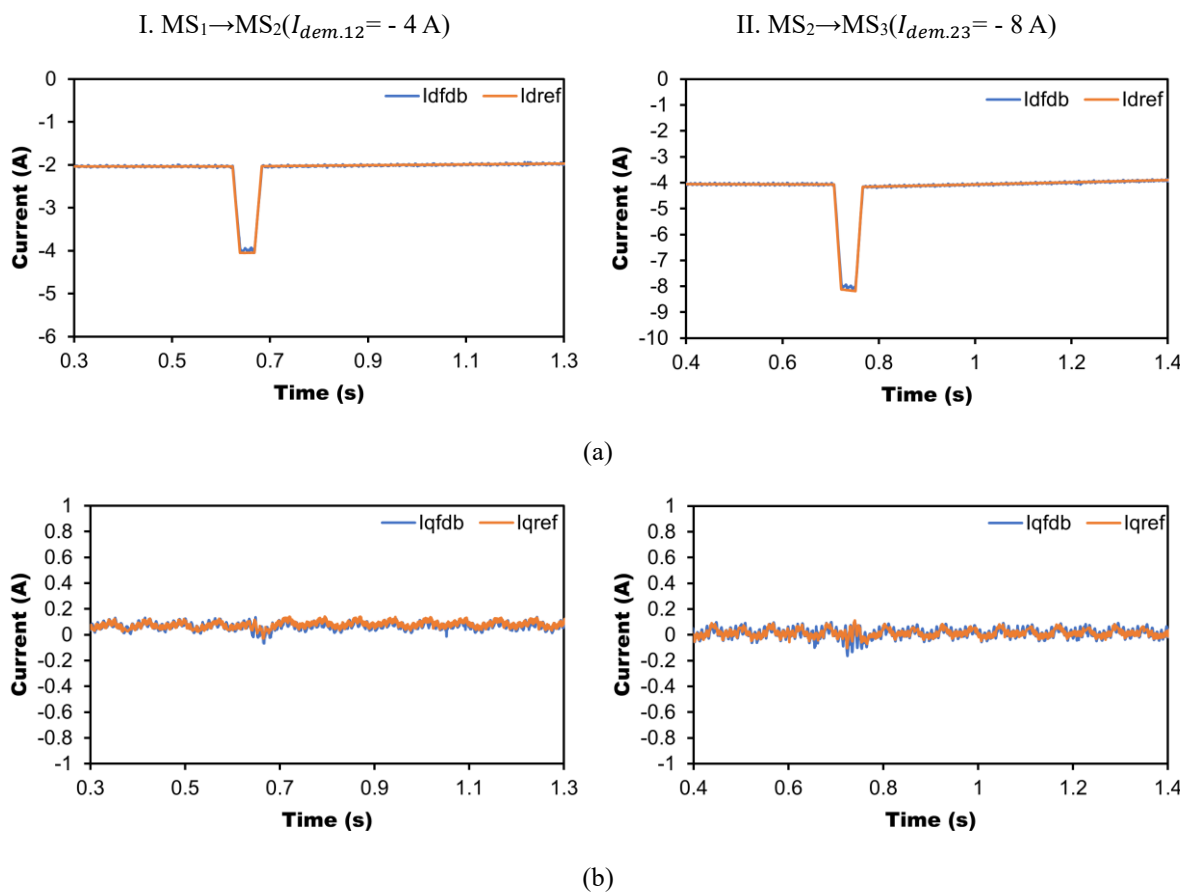
Table 5.1. Main parameters for experimental validation.

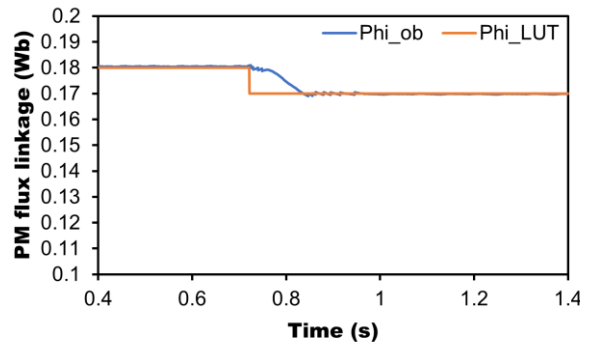
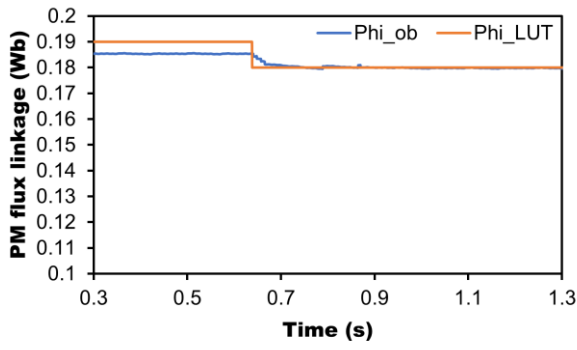
Item	Symbol	Value
DC link voltage	V_{dc}	80V
Maximum current (RMS)	I_{max}	7.5A
PM flux linkage at MS ₁	ψ_{m1}	0.19Wb
d-axis inductance at MS ₁	L_{d1}	20.8mH
q-axis inductance at MS ₁	L_{q1}	69.9mH
PM flux linkage at MS ₂	ψ_{m2}	0.18Wb
d-axis inductance at MS ₂	L_{d2}	22.7mH
q-axis inductance at MS ₂	L_{q2}	69.5mH
PM flux linkage at MS ₃	ψ_{m3}	0.17Wb
d-axis inductance at MS ₃	L_{d3}	24.3mH
q-axis inductance at MS ₃	L_{q3}	68.3mH
Demagnetization current from MS ₁ to MS ₂	$I_{dem.12}$	-4A
Demagnetization current from MS ₂ to MS ₃	$I_{dem.23}$	-8A

The parameters are obtained by the off-line tests in the laboratory. The DC link voltage is set as 80 V. Three MSs are selected for the experiments. The initial MS, i.e., MS₁, its corresponding PM flux linkage is 0.19 Wb, which is maximum value under the present laboratory condition. To reduce the fluctuation during MS manipulation, the other two MSs, i.e., MS₂ and MS₃, can be selected from the intersections of the torque-speed characteristic curves as illustrated in Fig. 5.3.

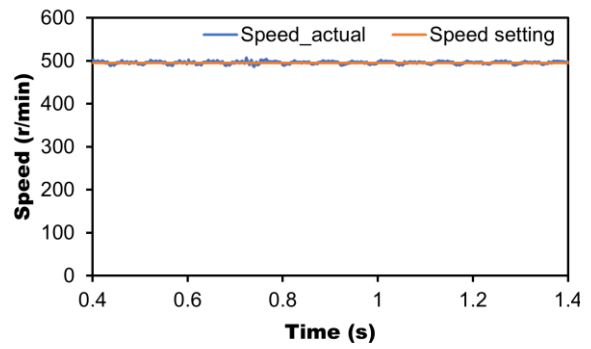
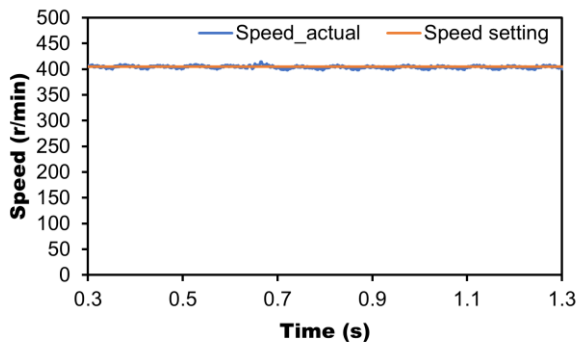
As the saliency of the investigated machine is not very high, the d -axis current for the MTPA control in the constant torque region will not cause the UD issue. Therefore, the experiment validation for the proposed MS control method is processed in the flux weakening region.

In the flux weakening region, $|i_d|$ keeps increasing. When the d -axis flux weakening current reaches to - 2 A, the difference between the initial PM flux linkage, MS₁, and the estimated PM flux linkage is beyond the threshold. The MS manipulation must be processed. MS₂ is selected as the next ideal MS, which needs a - 4 A demagnetizing current pulse to realize the MS manipulation. The measured results are shown in Fig. 5.10(I).

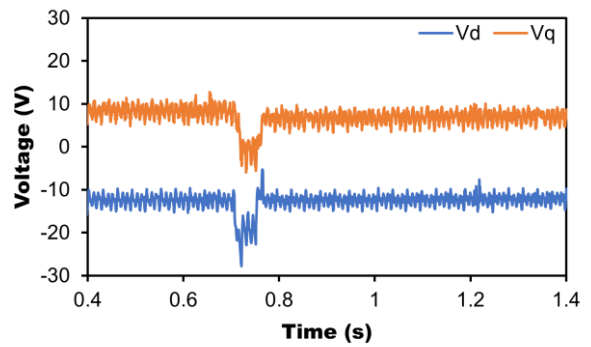
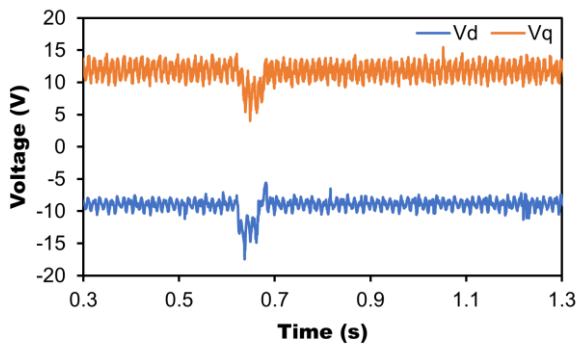




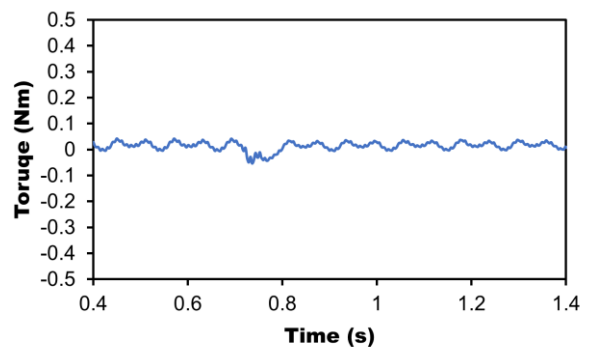
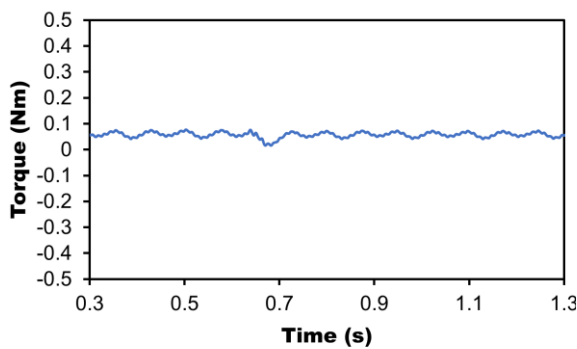
(c)



(d)



(e)



(f)

Fig. 5.10. Measured results of proposed MS control method, (I) MS₁ to MS₂ with -4 A demagnetizing current pulse, (II) MS₂ to MS₃ with -8 A demagnetizing current pulse. (a) *d*-axis current. (b) *q*-axis current. (c) PM flux linkage. (d) Speed. (e) *dq*-axis voltages. (f) Torque.

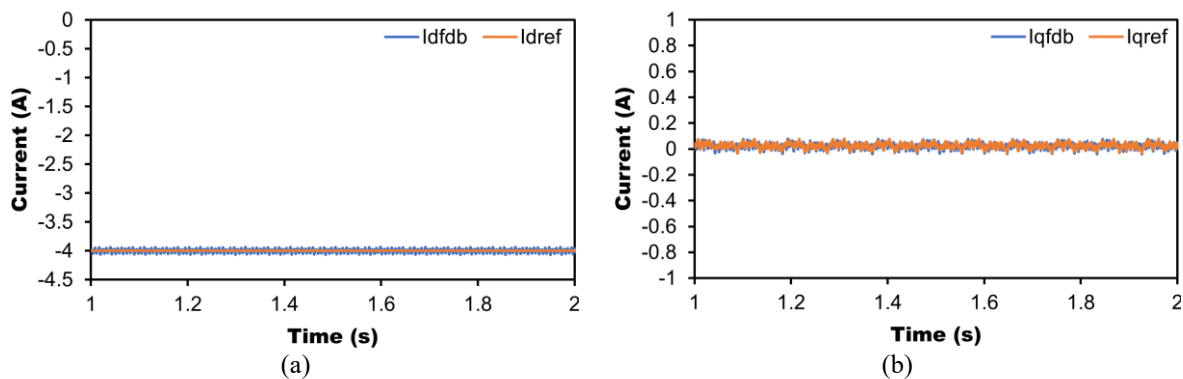
After the MS manipulation stage, MS₂, the demagnetizing current pulse is removed, but the d -axis current is still negative since the machine is still operating in the flux weakening region as shown in Fig. 5.10(I, a). Then, the estimated PM flux linkage will be the value under the present MS₂, which is close to the LUT value as shown in Fig. 5.10(I, c). The estimated PM flux linkage can also be the indication of a successful MS manipulation. As mentioned earlier, the MS manipulation timing is selected on the intersection of the torque-speed curves under MS₁ and MS₂, and consequently, only minor speed fluctuation will be caused by the MS manipulation as shown in the speed in Fig. 5.10(I, d). The glitch in the d -axis voltage in Fig. 5.10(I, e) during the MS manipulation will not affect the performance of the machine since it can be filtered by the control system. The q -axis current and the three-phase currents are shown in Fig. 5.10(I, b) and Fig. 5.10(I, f), respectively.

When the d -axis current reaches to -4 A, another MS manipulation is processed, as shown in Fig. 5.10(II).

The next MS, MS₃, is to make the MS manipulation smoother, which needs a -8 A magnetizing current pulse. In this case, the PM flux linkage reduces, the degree of flux weakening also decreases, the flux weakening d -axis current generated by the voltage magnitude feedback control starts to gradually decrease in amplitude due to the PI integrator, Fig. 5.10(II, a).

After the MS manipulation stage, MS₃, the estimated PM flux linkage is consistent with the LUT value, Fig. 5.10(II, c). The fluctuation in speed becomes negligible, Fig. 5.10(II, d). The q -axis current, dq -axis voltages, and the three-phase currents are shown in Fig. 5.10(II, b), Fig. 5.10(II, e), and Fig. 5.10(II, f), respectively.

As a comparison of the proposed MS control method, the measured results of the machine operating in the flux weakening without MS manipulation are shown in Fig. 5.11. When the d -axis current is -4 A in Fig. 5.11(a), the PM flux linkage in Fig. 5.11(c) is smaller than the initial value, which is set as the correct value for the machine control. Although the machine works as normal, the UD issue has occurred and will become worse without MS manipulation control.



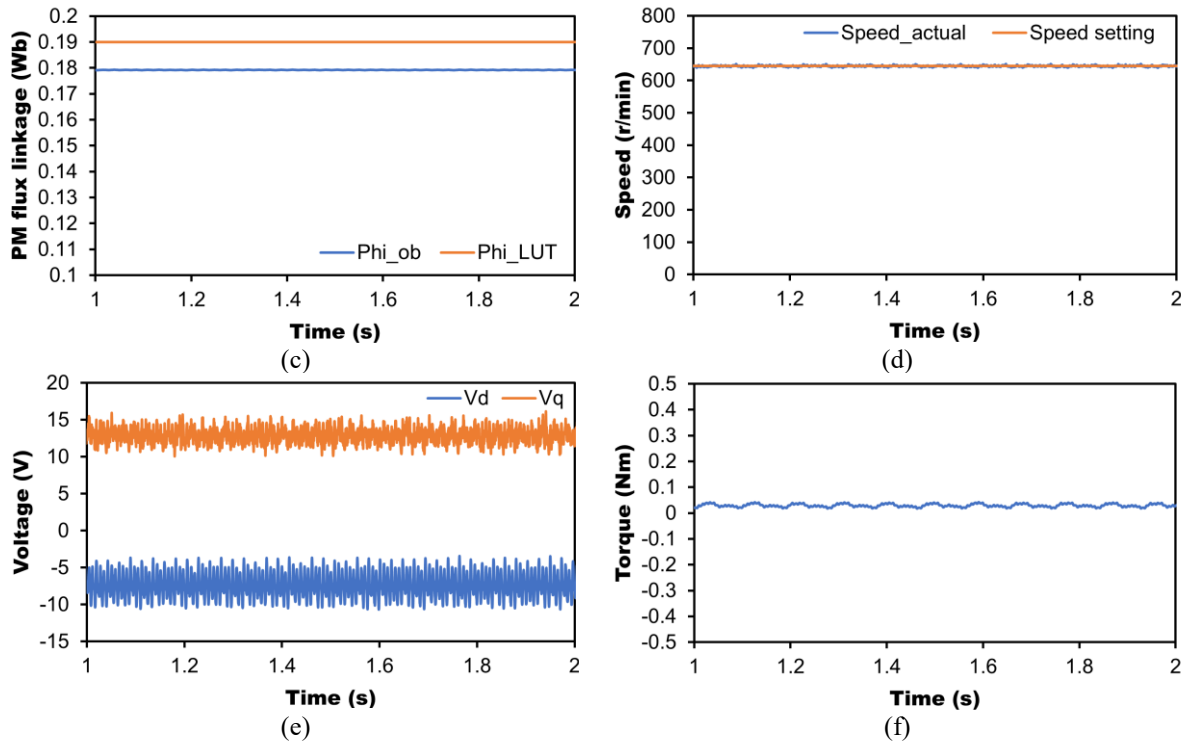
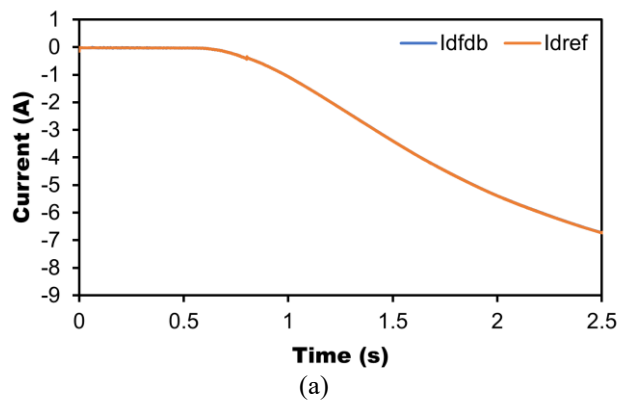
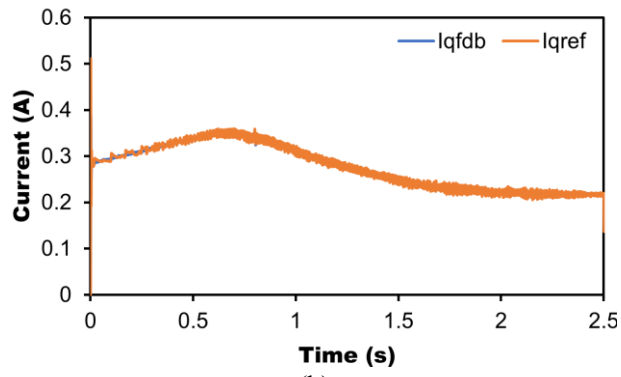


Fig. 5.11. Measured results without MS manipulation for UD. (a) d -axis current. (b) q -axis current. (c) PM flux linkage. (d) Speed. (e) dq -axis voltages. (f) Torque.

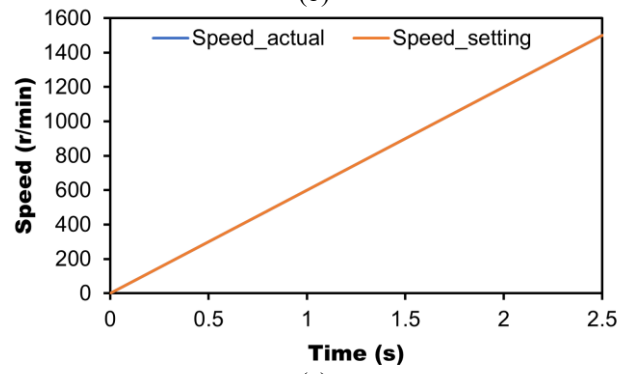
5.4.4 Dynamic Performance for Whole Speed Range

The dynamic performance from standstill to 1500 r/min for the investigated machine with and without the proposed method are tested and compared. To make sure the voltage margin is enough for MS manipulation, the DC-link voltage in this test is set as 100 V. A small load is added as 0.15 Nm. The other parameters are the same as listed in Table 5.1. The test results are presented in Fig. 5.12 and Fig. 5.13. With speed increasing, the amplitude of the negative d -axis armature current increases. According to the test in section 5.4.2, the UD issue will occur and become worse without the proposed method in Fig. 5.12. Although the machine can still work, the MS is not correct.

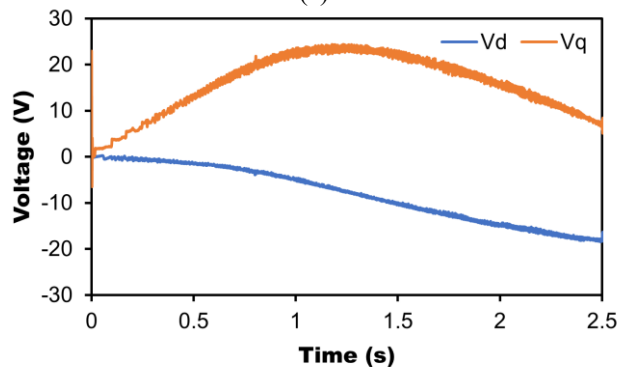




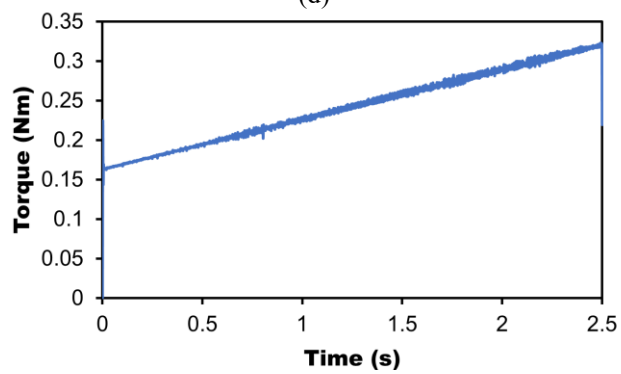
(b)



(c)



(d)



(e)

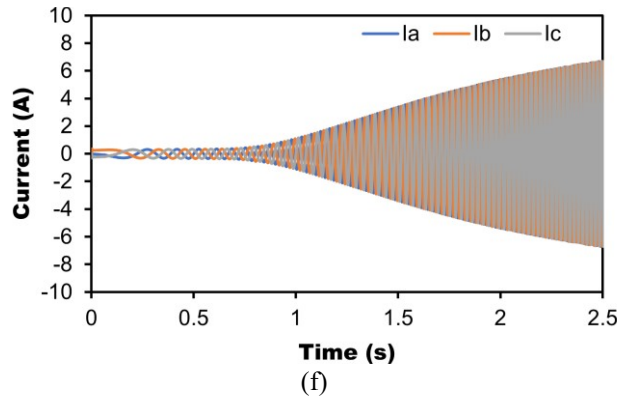
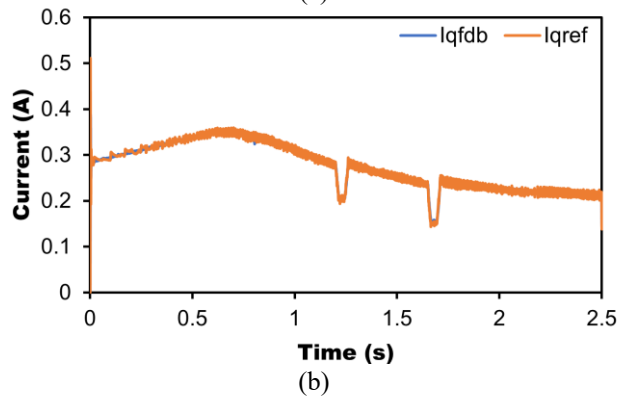
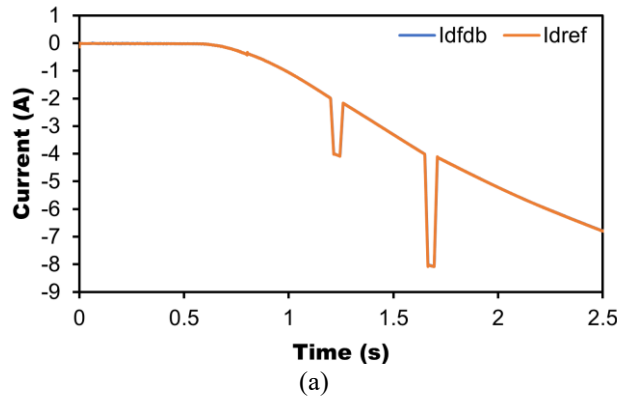


Fig. 5.12. Measured results from 0-1500 r/min without the proposed method. (a) d -axis current. (b) q -axis current. (c) Speed. (d) dq -axis voltages. (e) Torque. (f) Three-phase currents.

When the d -axis armature current reaches -2 A, the MS is manipulated to avoid the UD issue as shown in Fig. 5.13(a), and with the speed increasing, the next MS manipulation is processed when the d -axis armature current reaches -4 A. As shown in Fig. 5.13, the value of the d -axis current is kept under the amplitude of the demand magnetizing current pulse during the whole operating period. The potential UD issue can be avoided by the proposed MS control method. This technique can also be applied to other VFMMs with potential UD issue.



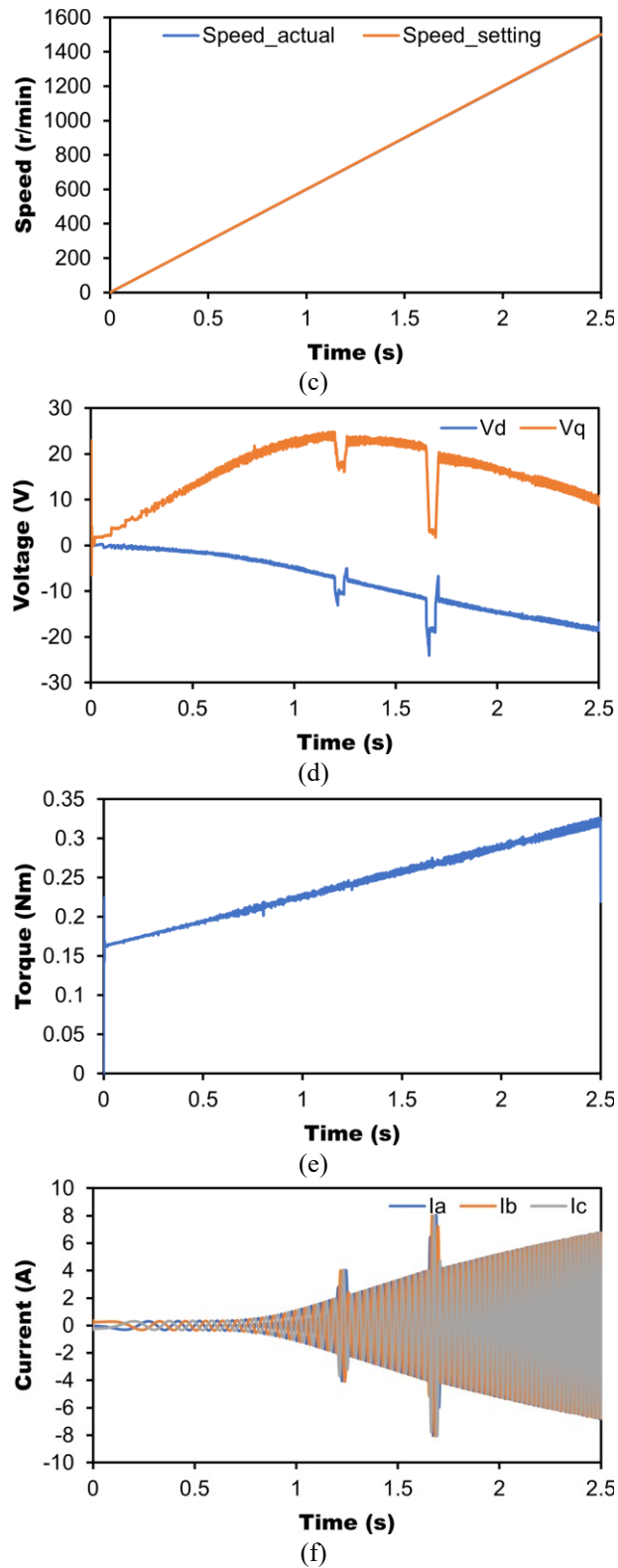


Fig. 5.13. Measured results from 0-1500 r/min with the proposed method. (a) d -axis current. (b) q -axis current. (c) Speed. (d) dq -axis voltages. (e) Torque. (f) Three-phase currents.

5.5 Conclusion

In this chapter, a novel MS control method is proposed to solve the UD issue of LCF PM for

VFMM. The demand demagnetization d -axis current pulse is used as the condition for the switch of MSs. When the amplitude of negative d -axis current reaches at the amplitude of the demand demagnetization d -axis current, the MS manipulation is processed. The value of the d -axis current is kept under the amplitude of the demand magnetizing current pulse during the whole operating period. The potential UD issue can be avoided by the proposed MS control method. Thus, the flux weakening d -axis current will not cause the UD issue in the proposed MS manipulation control method. A PM flux linkage estimation is adopted to monitor the UD issue, and the influence of VSI nonlinearity for PM flux linkage estimation is tested. Based on the HMMM drive system, the feasibility of the proposed MS control method is well verified experimentally.

CHAPTER 6 MAGNETIZATION STATE CLOSED-LOOP CONTROL UTILIZING TORQUE DEVIATION

For the investigated machine, PM flux linkage cannot represent the MS from MR= 0% to MR = -100% as presented in Fig. 2.5. In this case, a solution to determine the MS manipulation type is desired. In this chapter, a novel magnetization state (MS) control method is proposed by utilizing torque deviation for variable flux memory machine to achieve the MS close-loop control.

6.1 Introduction

The magnetization level of low-coercive force (LCF) permanent magnets (PM) can be enhanced or weakened by a current pulse, and the magnetization state (MS) can be memorized after the current pulse is withdrawn [OST01]. Since the adoption of LCF PMs, the MS of variable flux memory machine (VFMM) can also be changed by a current pulse. This property can expand the range of speed regulation and reduce the losses significantly compared with conventional permanent magnet synchronous machine (PMSM). Therefore, it began to receive much research attention since it was proposed.

In recent decades of research, a lot of topologies for VFMM have been proposed: single-PM (only LCF PM) and hybrid-PM (containing both LCF PM and HCF PM) [YAN18b], and the hybrid-PM type topology has become much more popular due to its prominent advantages. The hybrid-PM VFMM can be divided into series-type VFMM [HUA17a] and parallel-type VFMM [WU14] based on the PM magnetic circuit. The series-type VFMM has higher torque density and better demagnetization withstand capability [ZHU17] [HUA17b], which shows better performance in the machine drive system.

As the flux linkage is changeable, the MS control is the crucial point for VFMM control. In [MAS15], the speed was used as the condition of MS manipulation and the PMs were demagnetized proportionally as the speed increased. A linear extended state observer was used for the flux linkage estimation to achieve online MS manipulation and a linear active-disturbance-rejection-based current feedforward controller was adopted to optimize the control performance of current during the MS regulation [CHE22]. [HU20a] proposed a close-loop MS manipulation method whose MS estimation used manipulation signals self-sensing, and

the magnetizing current was controlled by an injected voltage, which also was used as the source of MS estimation. In [MAE14], the d -axis magnetizing current was converted into a d -axis voltage value, a feedforward voltage controller was used to control the d -axis current, and a feedback current controller was used to control the q -axis current during MS manipulation, and then, the close-loop MS control was achieved. [GAG16] proposed a straight-line stationary frame PM flux linkage trajectory method to realize high speed MS control based on maximizing the stationary frame voltage utilization, this method also reduced the torque ripple during the MS control. In [ATH18], the MS online estimation was utilized as feedback for close-loop control, and a deadbeat-direct torque and flux control framework was adopted to achieve precise torque control during MS regulation, besides, a high-speed flux trajectory generation method was utilized to allow MS manipulation at high speed. [YU14] focused on the smooth voltage control during the nonzero speed and loaded conditions MS manipulation, and then, a voltage disturbance state filter and an observer-based current decoupling method without a lookup table (LUT) were adopted to achieve this aim, while the MS control was still based on the speed changing. In [CHE20], an online current trajectory prediction and control method for the magnetization current was proposed, and the induction voltage was estimated to increase the MS manipulation speed, and then, the high control accuracy of the MS control was achieved. A reverse rotating current vector trajectory method was proposed to cancel the voltage component terms in the governing machine voltage equations, which allowed the MS control at higher speed [GAG14]. [HU21] proposed an efficiency-based MS switch method, an efficiency map under different MSs was measured in advance, and then the operating efficiency was calculated by the torque and speed, the MS that had better efficiency was selected according to the efficiency map. In [ZHO22a] [ZHO22b], the MS control was based on the speed, when the speed reached to the MS switch setting speed in a LUT, the MS manipulation was processed.

In the existing literature, the MS control usually was processed according to the machine speed or the flux linkage. It is easy to achieve MS control according to the machine speed, but it is open loop for MS control. The accuracy of PM flux linkage estimation is critical for the MS manipulation by PM flux linkage. The change of dq -axis inductances under different MSs also brings challenge for PM flux linkage estimation. In this chapter, a novel MS closed-loop control method based on the torque deviation for VFMM is proposed to achieve the MS close-loop control. Firstly, the investigated hybrid magnet memory machine (HMMM) topology is illustrated, and the relationship between the MSs and the magnetizing current pulse is built.

The property of the dq -axis inductances affected by the MS change is revealed. Secondly, a look up table based on the machine properties is built, which contains the information on the dq -axis inductances and the flux linkages under different MSs and the corresponding magnetizing current pulse. A model-based torque calculation is adopted to estimate the steady state torque of the machine. A novel MS control method by utilizing the deviation of the calculated torque between the present MS and the target MS is proposed. Then, the overall control algorithm combining with the proposed MS control method for the investigated HMMM is illustrated. The simulation for the proposed MS control method is processed to verify its feasibility. Finally, the proposed MS control method is validated on the HMMM experimental platform, and the feasibility of the proposed MS control method is well validated.

6.2 Proposed MS Control Method

6.2.1 Proposed MS Control Method

In the existing literature, the MS control was usually processed according to the machine speed or PM flux linkage. It is easy to achieve MS control according to the machine speed, but it is open loop for MS control. The accuracy of PM flux linkage estimation is critical for the MS manipulation by PM flux linkage. Despite of the magnetic saturation effect, the change of dq -axis inductances under different MSs also brings challenge for PM flux linkage estimation. The proposed MS control method based on electromagnetic torque deviation provides a closed-loop MS control solution, and the influence of changes in dq -axis inductance is considered.

The MS control method proposed in this chapter is illustrated in Fig. 6.1. On receiving the MS change command, the present MS and the target MS with related parameters can be obtained from the LUT. The torque calculation is referred to Fig. 3.8. Then, the torque calculation will calculate the steady state torque under these two MSs. The observed torque T_{e_pms} under the present MS is compared with the observed torque T_{e_tms} under the target MS. When the torque deviation exceeds the set threshold λ , if T_{e_tms} is smaller than T_{e_pms} , a demagnetization signal is generated, and conversely, a remagnetization signal is generated. Otherwise, a non-magnetization signal is generated. In this chapter, the threshold is set as 5% of the torque under the present MS. 5% of torque is usually an indicator to measure torque accuracy in industrial applications. The torque deviation is within 5%, which is qualified. Then, the LUT will generate the demand d -axis magnetizing current pulse according to the MS switch signal. Therefore, the MS close-loop control can be achieved. The torque calculation will also be used

to monitor the MS to make sure the target MS is achieved.

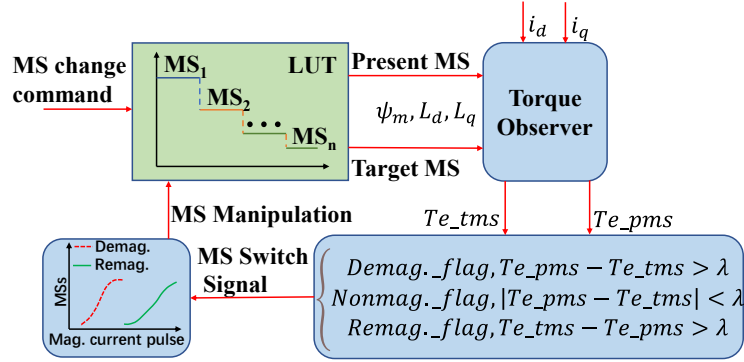


Fig. 6.1. Schematic of proposed MS control method.

For example, if the PM flux linkage of the target MS is larger than the present value, remagnetization is required. But if the torque deviation between the target MS and present MS is within the threshold, MS manipulation is unnecessary. For the investigated machine, PM flux linkage cannot represent the MS from MR= 0% to MR = -100%. In this case, it is also required to calculate torque deviation to determine the MS manipulation type.

6.2.2 Overall Control Strategy

The overall control strategy with the proposed MS control method is illustrated in Fig. 6.2. The maximum torque per ampere (MTPA) control is adopted in the constant torque region due to the saliency of the investigated machine, and the voltage magnitude feedback flux-weakening control [KIM97b] is adopted in the flux weakening region considering the high robustness.

In Fig. 6.2, I_m is the machine rated current, V_{dc} is the DC-link voltage, ω_m is the real mechanical angular velocity, ω_m^* is the reference mechanical angular velocity, θ is the actual electrical angle, u_α and u_β are the voltage components in the $\alpha\beta$ stationary coordinate system, i_a , i_b , and i_c are the three-phase currents, respectively, i_{dM} and i_{qM} are the MTPA control dq -axis currents, Δi_d^* is the output of the voltage magnitude feedback flux-weakening control, i_d^* and i_q^* are the reference dq -axis currents for the current PI control, which are composed of the MTPA control current and the flux weakening control current, i_{mag} is the d -axis magnetizing current pulse generated by the proposed control method. The d -axis magnetizing current pulse is added to the reference d -axis current directly. The torque observer is referred to Fig. 3.8. The MTPA controller is referred to Fig. 1.6. The parameters and limits for PI controllers are the same as Fig. 2.10.

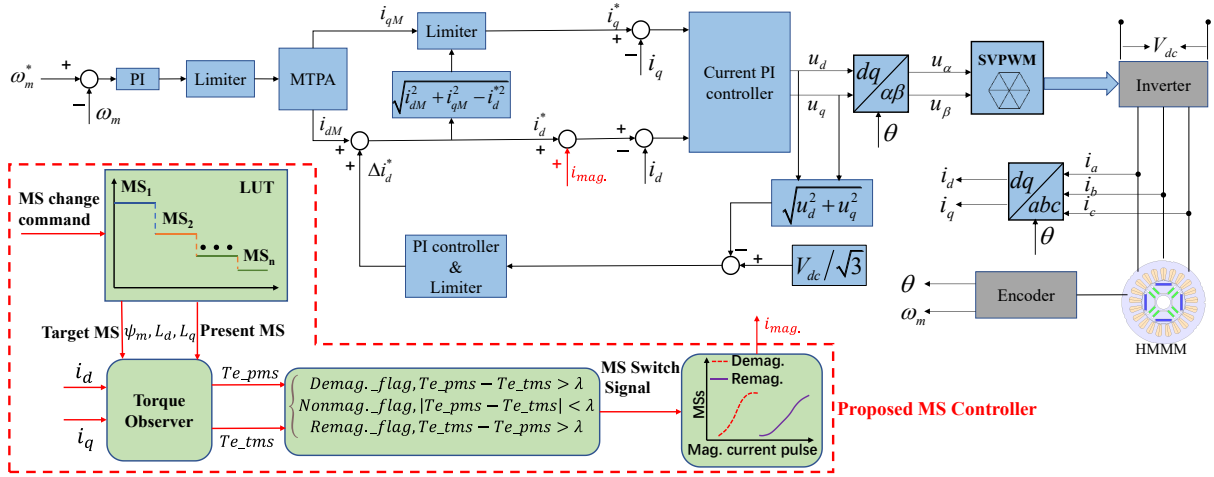


Fig. 6.2. Schematic of overall control method.

6.3 Simulation and Discussion

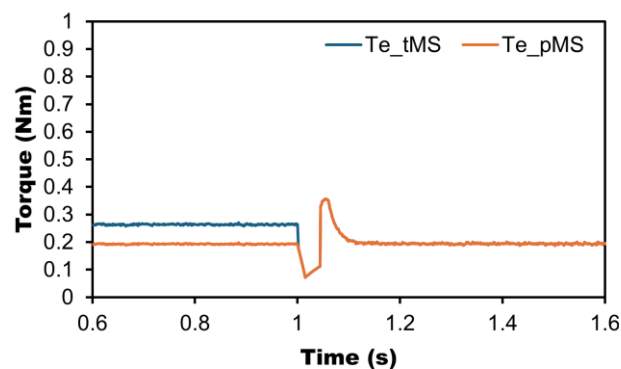
The main parameters of the investigated HMMM and the simulation system are listed in Table 6.1. Three MSs are selected to simulate the proposed MS control method: MR1=0%, MR2=40%, and MR3=100%, respectively. The corresponding magnetizing current pulses are also illustrated.

Table 6.1. Main parameters of simulation system.

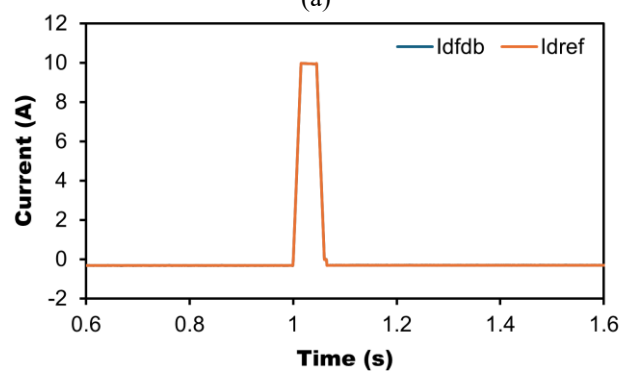
Item	Value	Symbol
DC link voltage	80V	V_{dc}
PM flux linkage at MR1=0%	0.124Wb	ψ_{m1}
d -axis inductance at MR1=0%	21.4mH	L_{d1}
q -axis inductance at MR1=0%	65.7mH	L_{q1}
PM flux linkage at MR2=40%	0.169Wb	ψ_{m2}
d -axis inductance at MR2=40%	24.3mH	L_{d2}
q -axis inductance at MR2=40%	69.1 mH	L_{q2}
PM flux linkage at MR3=80%	0.18Wb	ψ_{m3}
d -axis inductance at MR3=80%	22.9mH	L_{d3}
q -axis inductance at MR3=80%	69.7mH	L_{q3}
PM flux linkage at MR4=100%	0.195Wb	ψ_{m4}
d -axis inductance at MR4=100%	20.8mH	L_{d4}
q -axis inductance at MR4=100%	69.9mH	L_{q4}
Remag. current from MR1 to MR2	10A	$I_{rem.12}$
Remag. current from MR1 to MR3	15A	$I_{rem.13}$
Demag. current from MR4 to MR2	-10A	$I_{dem.42}$
Demag. current from MR4 to MR1	-15A	$I_{dem.41}$
Operating speed	200r/min	n

6.3.1 Remagnetization Simulation

At first, the MS of the machine is set as MR1. The remagnetization is simulated from MR1 to MR2, the simulation results are shown in Fig. 6.3. When the torque under the target MS is bigger than the torque under the present MS, the remagnetization is needed. Based on the LUT, the MS is switched from MR1 to MR2 by injecting a 10 A remagnetizing current pulse. After the MS manipulation, the torque reduces and this is caused by the decreasing in q-axis current, due to the change of machine parameters. The “fdb” in I_{qfdb} is the abbreviation of feedback, which represents the actual q-axis current for the current PI controller in Fig. 6.3(c). The performance of dq -axis voltages, speed, and three-phase currents during remagnetization are shown in Fig. 6.3(d), Fig. 6.3(e), and Fig. 6.3(f), respectively. As the outcome of the control system, the torque during the MS manipulation is affected significantly. The spikes in dq -axis voltages are due to no filter in the simulation.



(a)



(b)

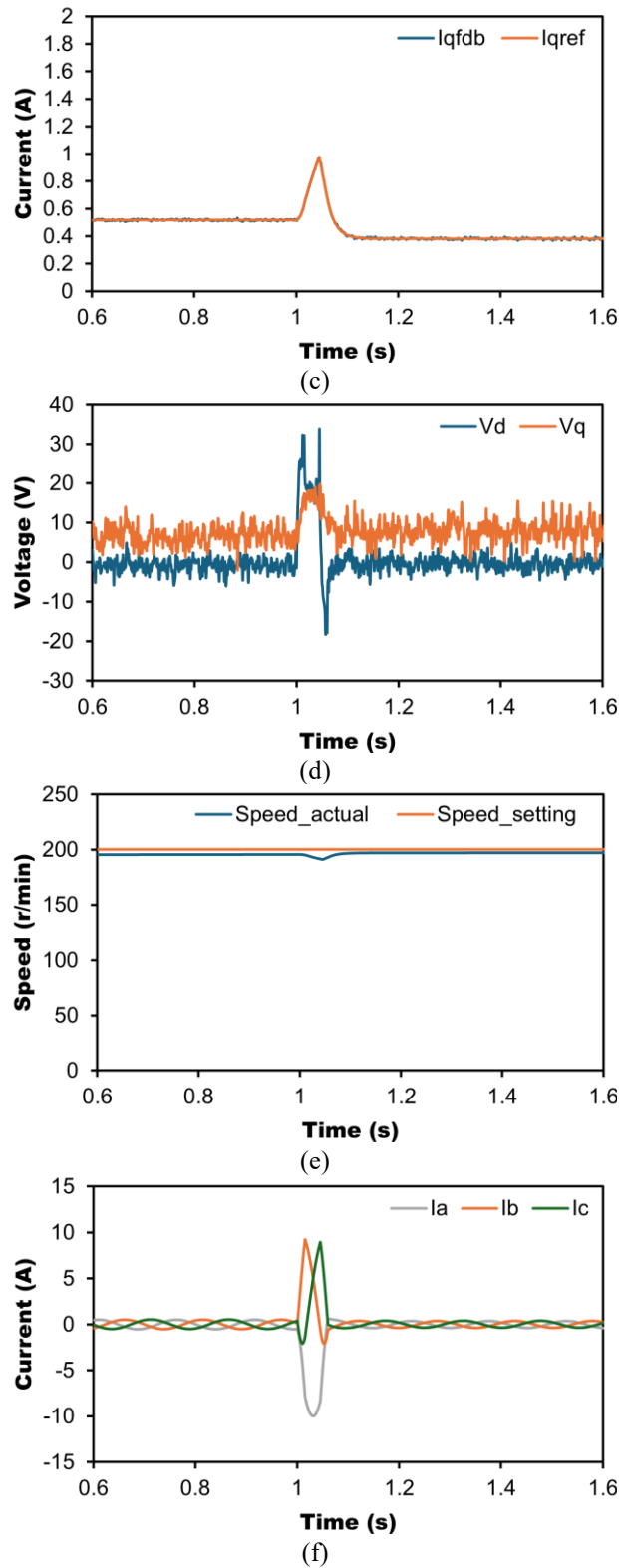
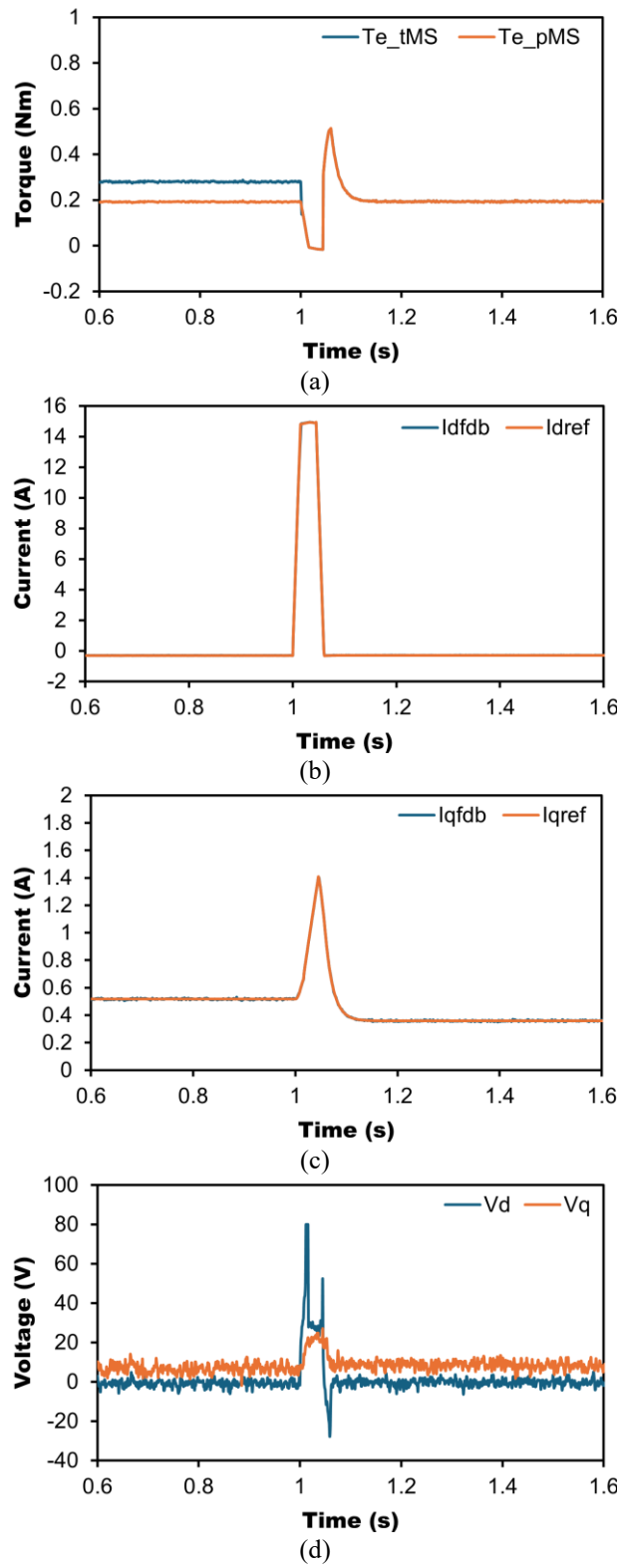


Fig. 6.3. Simulation results of remagnetization with 10 A magnetizing current pulse. (a) Calculated torque. (b) d -axis current. (c) q -axis current. (d) dq -axis voltages. (e) Speed. (f) Three-phase currents.

To further test the proposed MS control method, a demanded 15 A magnetizing current pulse for remagnetization from MR1 to MR3 is simulated. The simulation results are presented in

Fig. 6.4. With the amplitude of magnetizing current pulse increasing, the fluctuations in q -axis current, dq -axis voltages, and speed caused by MS manipulation increase.



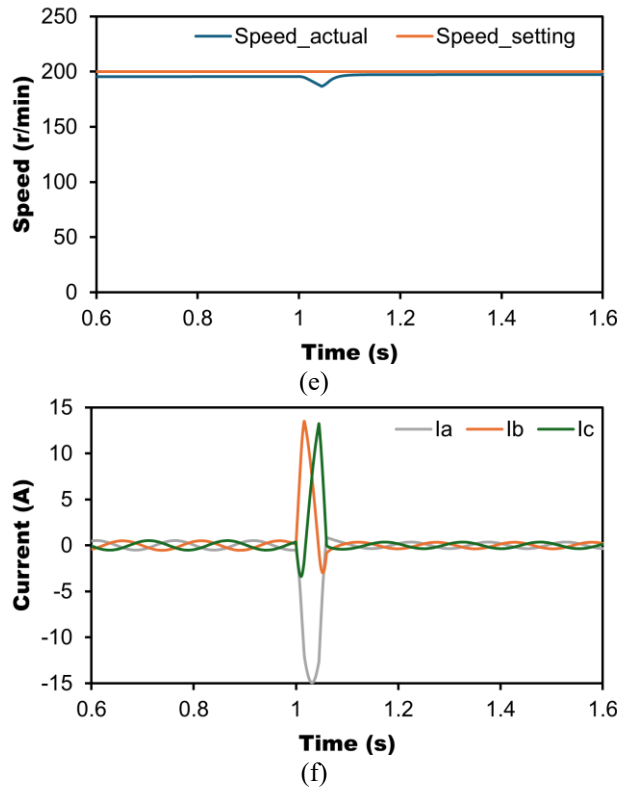
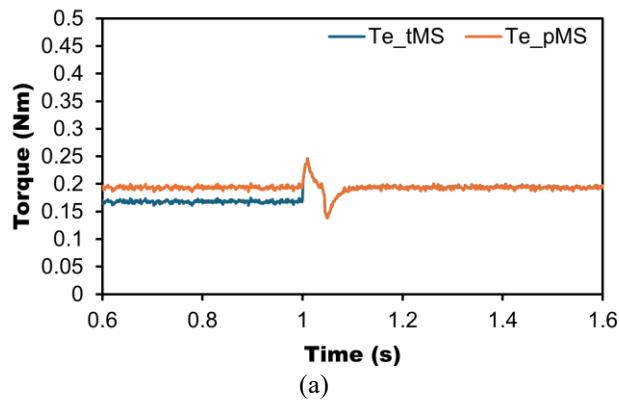
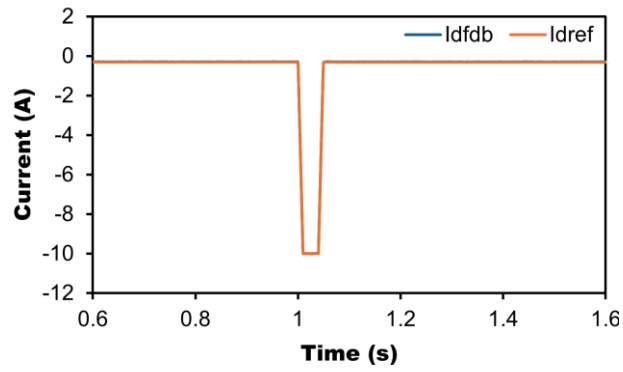


Fig. 6.4. Simulation results of remagnetization with 15 A magnetizing current pulse. (a) Calculated torque. (b) d -axis current. (c) q -axis current. (d) dq -axis voltages. (e) Speed. (f) Three-phase currents.

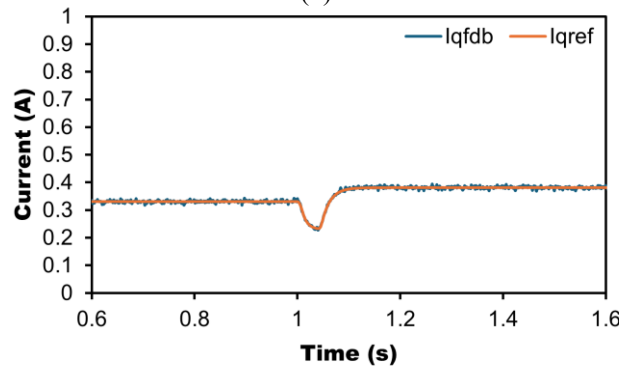
6.3.2 Demagnetization Simulation

The initial MS for demagnetization simulation is set as MR4. Then, the demagnetization is simulated from MR4 to MR2. The simulation results are shown in Fig. 6.5. When the torque under the target MS is smaller than the torque under the present MS, the demagnetization is needed. Based on the LUT, the MS is switched from MR4 to MR2 by injecting a -10 A demagnetizing current pulse.

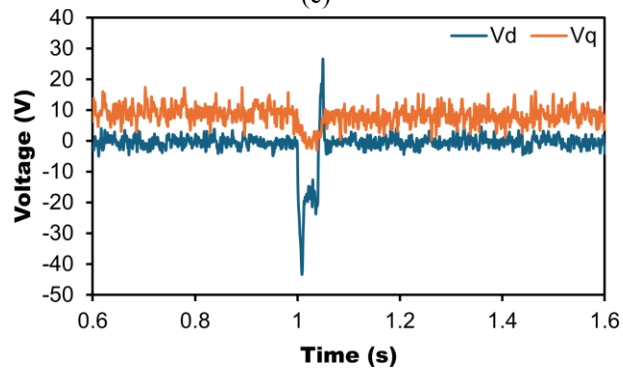




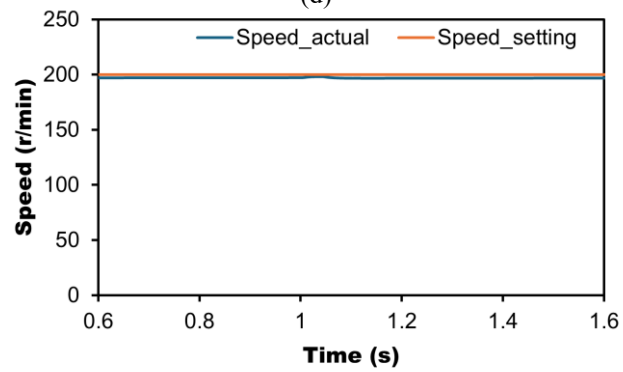
(b)



(c)



(d)



(e)

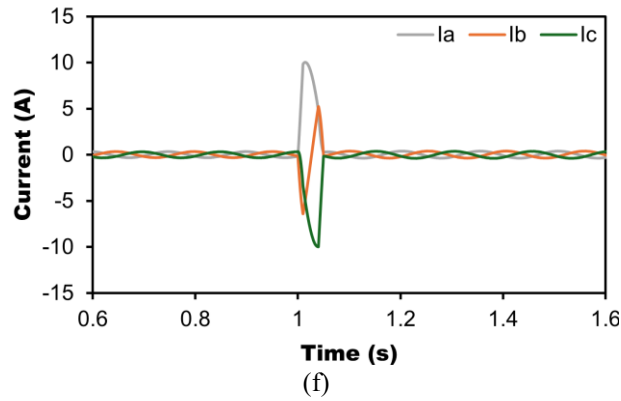
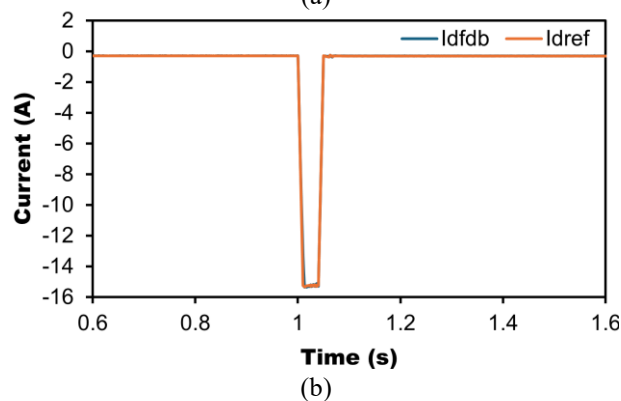
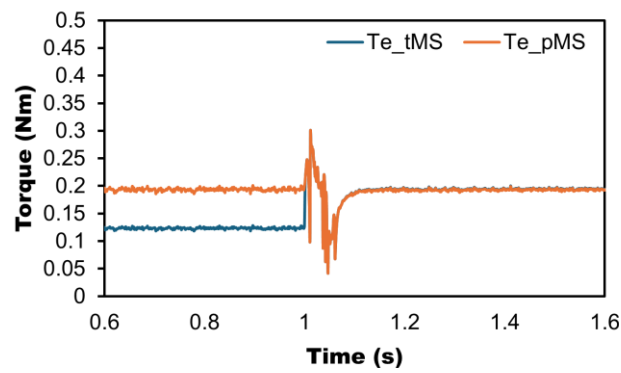
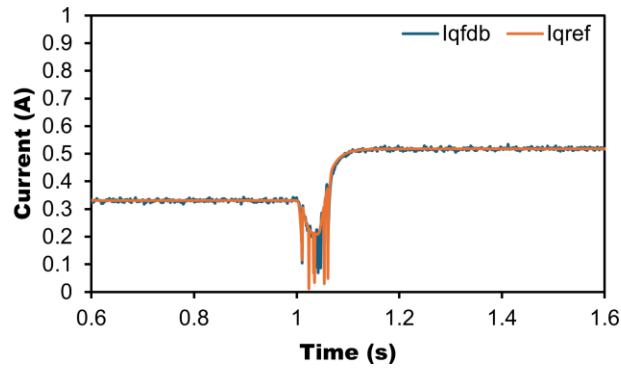


Fig. 6.5. Simulation results of demagnetization with -10 A magnetizing current pulse. (a) Calculated torque. (b) d -axis current. (c) q -axis current. (d) dq -axis voltages. (e) Speed. (f) Three-phase currents.

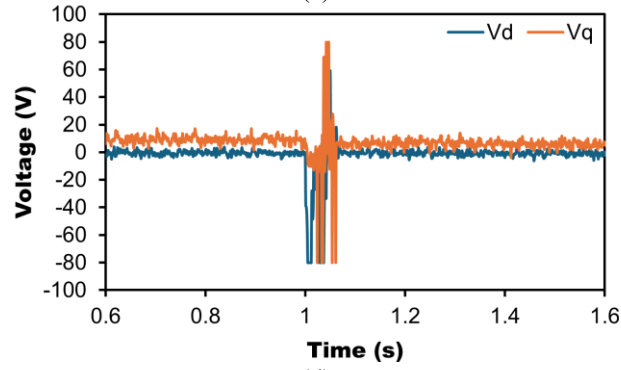
After the demagnetization, the torque under present MS keeps the same as the torque under target MS. The demagnetization is processed successfully.

To further test the proposed MS control method for demagnetization, a larger amplitude of magnetizing current pulse with -15 A to achieve demagnetization from MR4 to MR1 is simulated. The simulation results are presented in Fig. 6.6. Due to the injection of large amplitude of magnetizing current pulse, the demanded voltage increases, which is limited in Fig. 6.6(d). This causes the strikes in q -axis current and torque. Although the MS is manipulated successfully, the dynamic performance is not good.

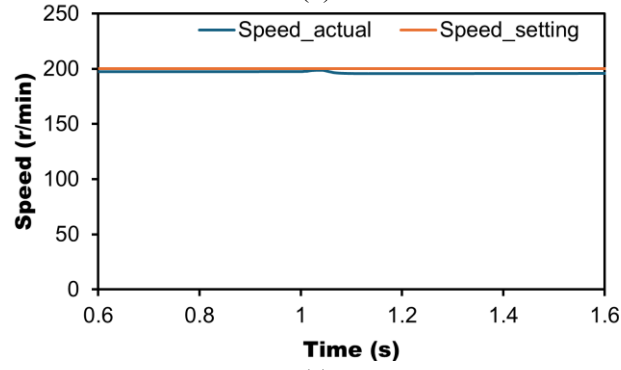




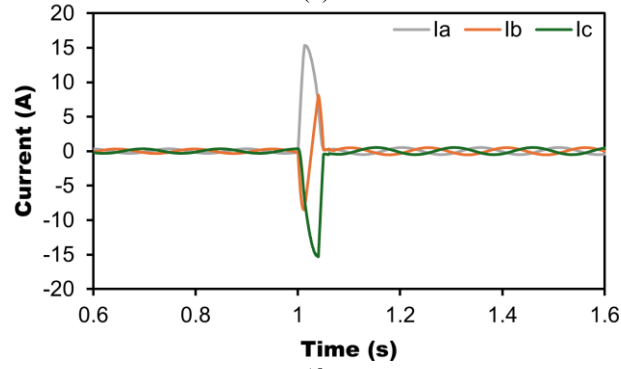
(c)



(d)



(e)



(f)

Fig. 6.6. Simulation results of demagnetization with -15 A magnetizing current pulse. (a) Calculated torque. (b) d -axis current. (c) q -axis current. (d) dq -axis voltages. (e) Speed. (f) Three-phase currents.

Through the simulation, the feasibility of the proposed MS control method is well validated.

6.4 Experimental Validation

The main parameters of the test are the same as Table 6.1.

6.4.1 Torque Calculation

First, the accuracy of the torque calculation is tested through a torque meter as shown in Fig. 6.7. The torque meter is connected between the investigated machine and the load machine. The torque display can show the torque value and transfer the value to the dSPACE to record.

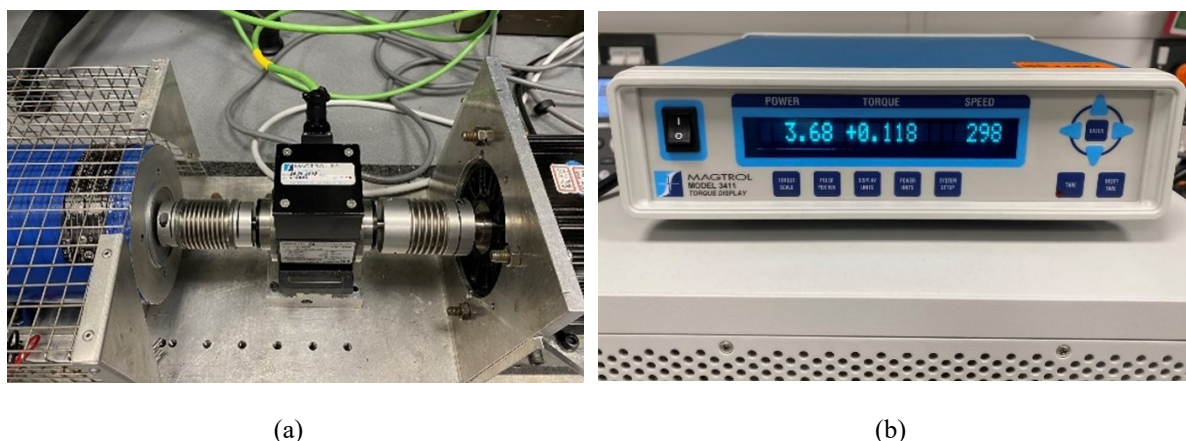
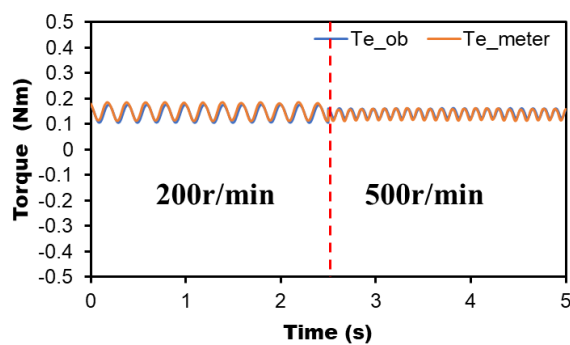


Fig. 6.7. Torque test equipment. (a) Torque meter. (b) Torque display.

The measured results of the torque calculation comparing with the torque meter reading under steady state are shown in Fig. 6.8. The calculated torque is consistent with the value from the torque meter very well. The steady-state fluctuations are caused by mechanical shafts not fully aligned, especially at low speeds. When the speed or the load increases, the steady fluctuations are reduced in Fig. 6.9(a) and Fig. 6.8(b). Besides, the dynamic performance of the torque calculation is tested as shown in Fig. 6.8(c), the calculated torque can follow the torque meter well. The accuracy of the calculated torque is acceptable for the proposed MS control method.



(a)

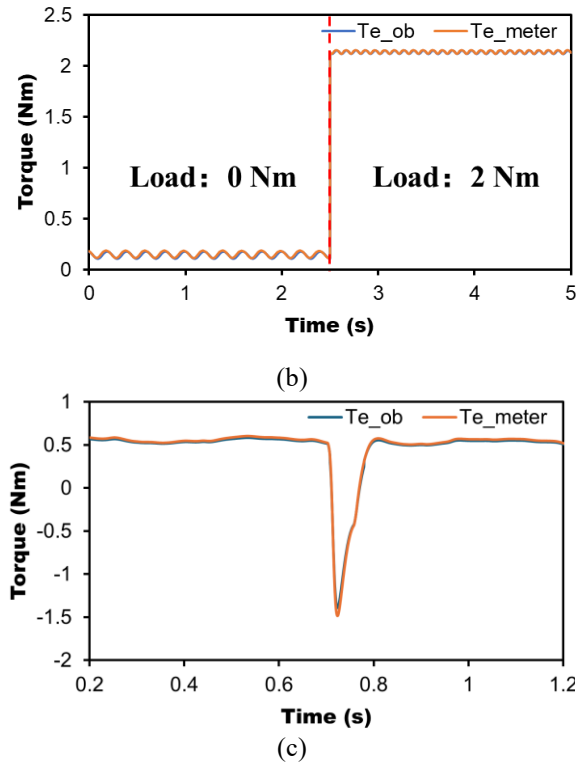
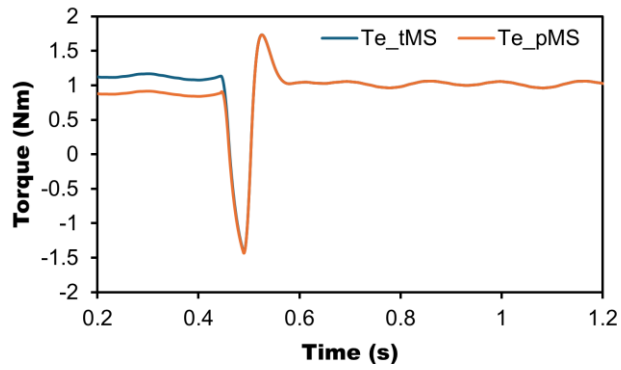


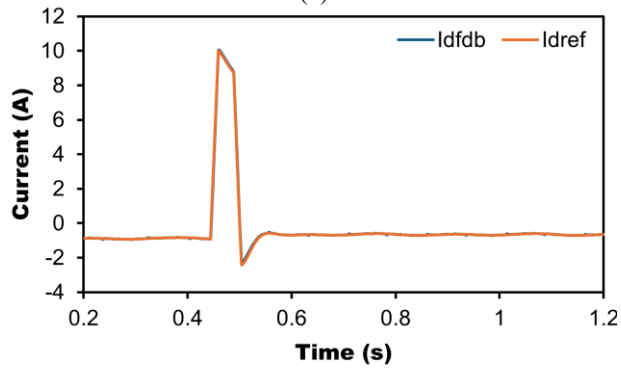
Fig. 6.8. Measured results of torque calculation accuracy. (a) Speed increasing. (b) Load increasing. (c) Dynamic performance.

6.4.2 Remagnetization Process

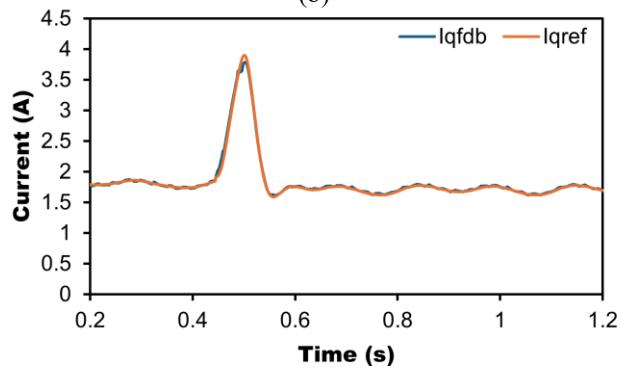
In the remagnetization experiment, the present MS is at MS_1 as shown in Table 6.1. The machine is operating at speed 200 r/min. The load is 0.8 Nm. The measured results are shown in Fig. 6.9. When a MS change command is entered into the control system, the torque calculation generates two torque components. If the torque under present MS T_{e_pms} is smaller than the torque under target MS T_{e_tms} and the torque deviation exceeds the threshold as shown in Fig. 6.9(a), remagnetization is processed. A positive magnetizing current pulse with amplitude of 10 A is added to the d -axis current as shown in Fig. 6.9(b). The magnetizing current pulse is a trapezoidal wave, with the 30ms amplitude duration. The dynamic performance of the q -axis current, the dq -axis voltages and the three-phase currents in the remagnetization process are shown in Fig. 6.9(c), Fig. 6.9(d), and Fig. 6.9(f), respectively. The position signal in Fig. 6.9(e) is also affected. After the remagnetization manipulation, the two torque waveforms coincide, the MS changes from MS_1 to MS_2 . The remagnetization process is completed.



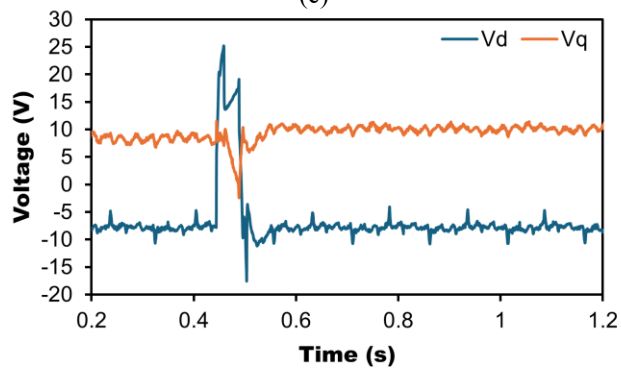
(a)



(b)



(c)



(d)

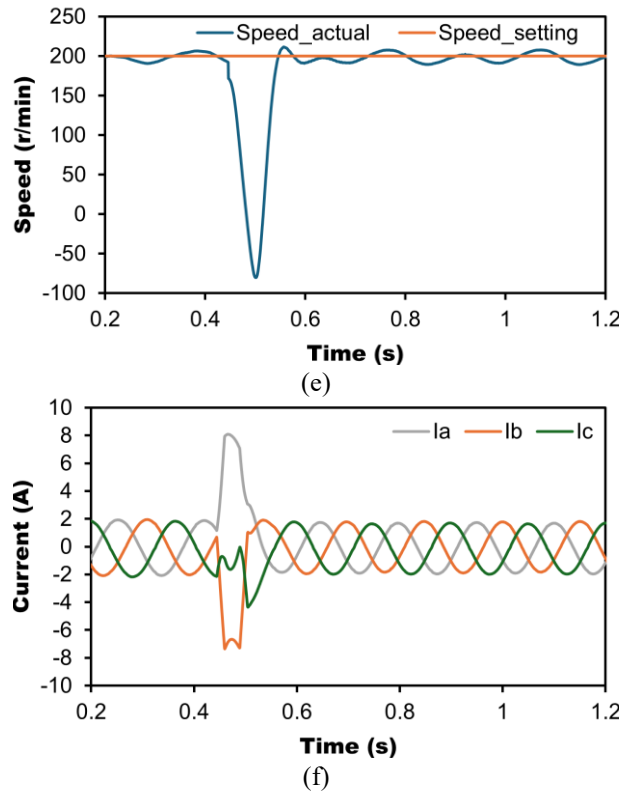
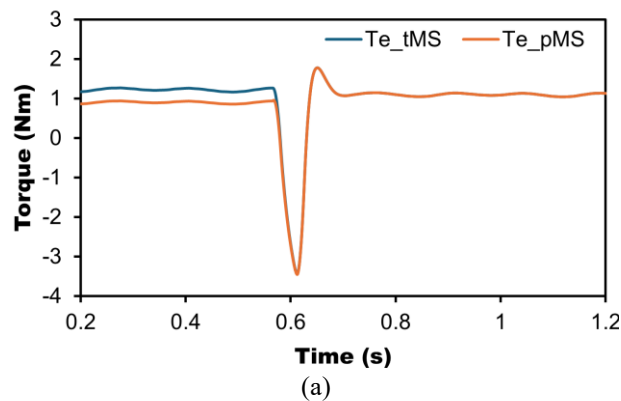
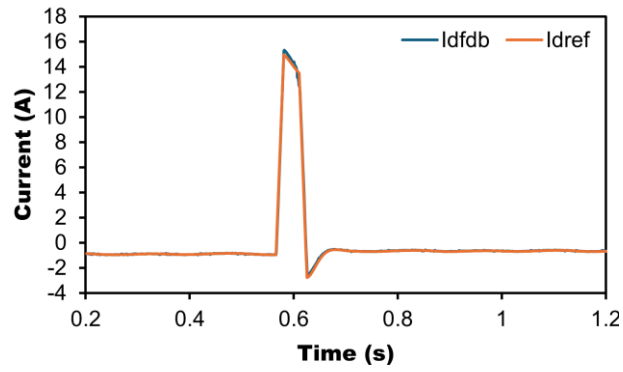


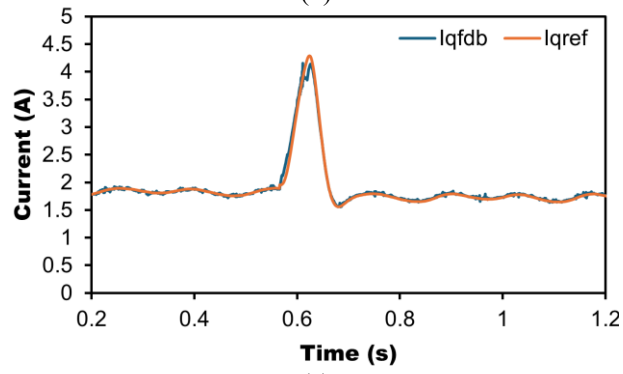
Fig. 6.9. Measured results of remagnetization with 10 A magnetizing current pulse. (a) Calculated torque. (b) d -axis current. (c) q -axis current. (d) dq -axis voltages. (e) Speed. (f) Three-phase currents.

To further validate the feasibility of the proposed MS control method, remagnetization from MR1 to MR3 is processed with 15 A magnetizing current pulse. The other experimental conditions are the same as the test with 10 A magnetizing current pulse. The measured results are presented in Fig. 6.10. The fluctuations increase in q -axis current, dq -axis voltages, and speed as shown in Fig. 6.10(c), Fig. 6.10(d), and Fig. 6.10(e), which is consistent with the simulation results.

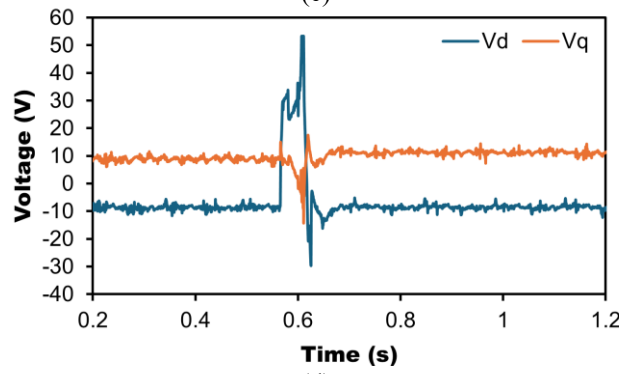




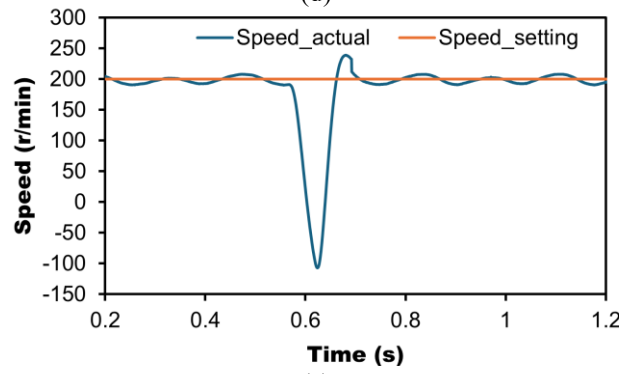
(b)



(c)



(d)



(e)

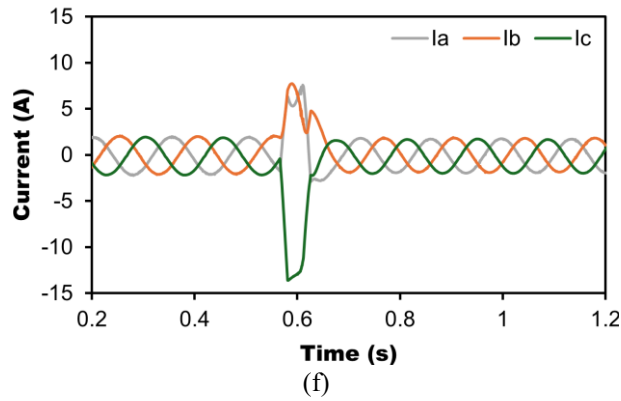
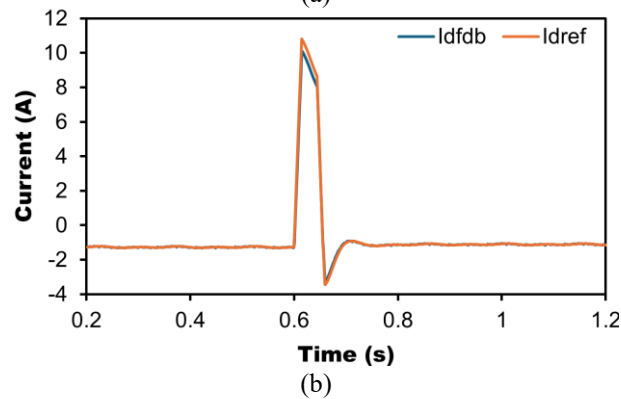
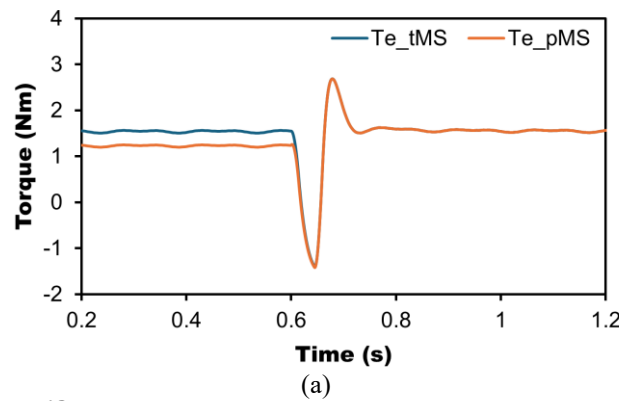
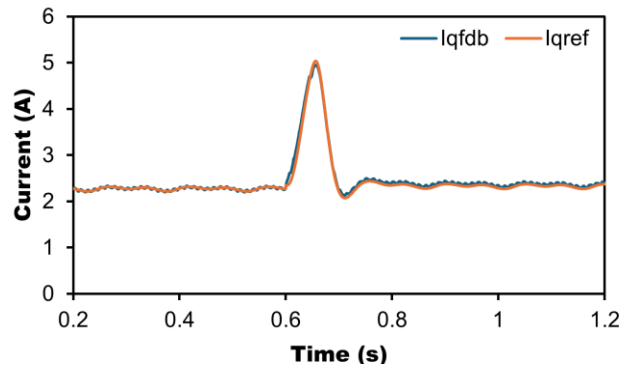


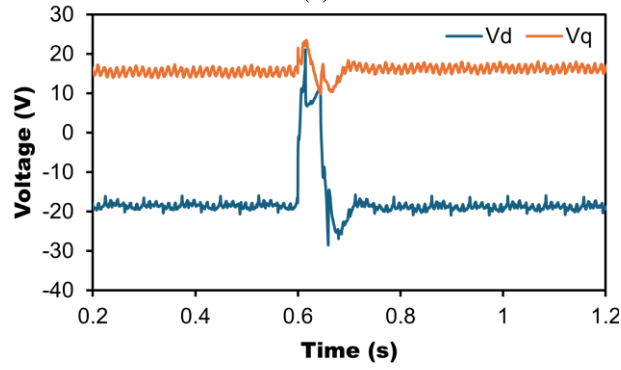
Fig. 6.10. Measured results of remagnetization with 15 A magnetizing current pulse. (a) Calculated torque. (b) d -axis current. (c) q -axis current. (d) dq -axis voltages. (e) Speed. (f) Three-phase currents.

Considering the effect of speed and load increasing on the magnetizing performance, the remagnetization from MR1 to MR2 is processed under 400 r/min with 1.5 Nm load. The measured results are presented in Fig. 6.11. The fluctuations caused by MS manipulation further increase. Since the torques under two MSs are the same after remagnetization, the MS is manipulated successfully.

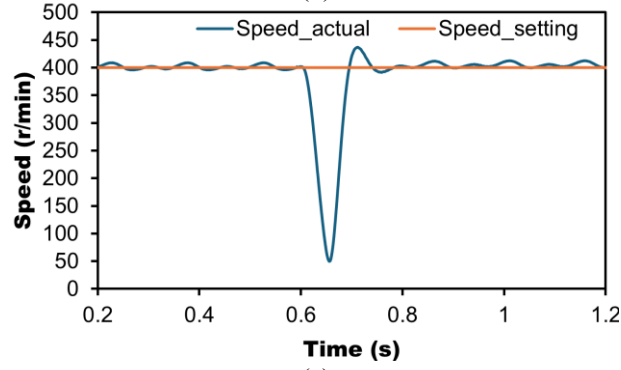




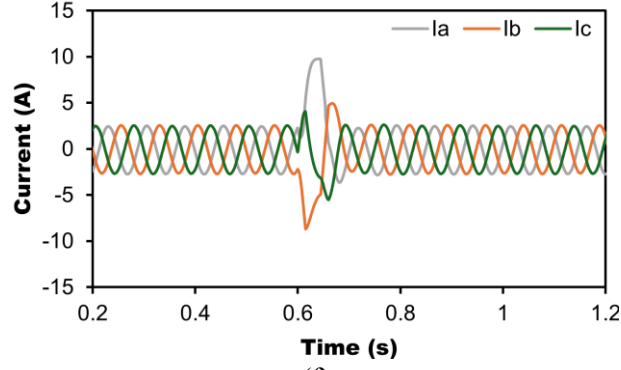
(c)



(d)



(e)



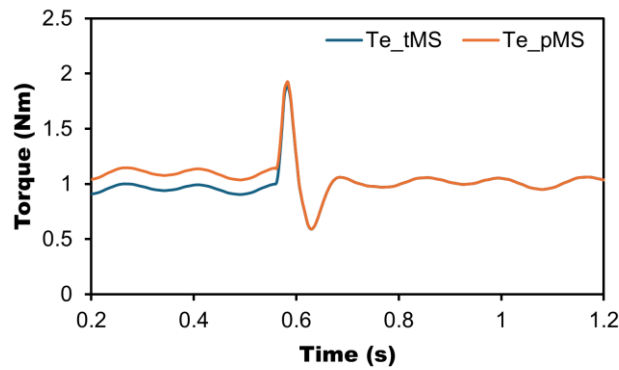
(f)

Fig. 6.11. Measured results of remagnetization with 10 A magnetizing current pulse under 1.5 Nm load. (a) Calculated torque. (b) d -axis current. (c) q -axis current. (d) dq -axis voltages. (e) Speed. (f) Three-phase currents.

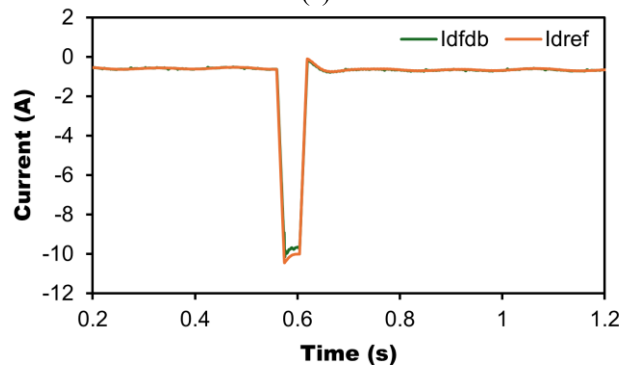
6.4.3 Demagnetization Process

In the demagnetization experiment, the present MS is at MS₄, and the speed of the machine is operating as the same as the remagnetization experiment. When received the MS change

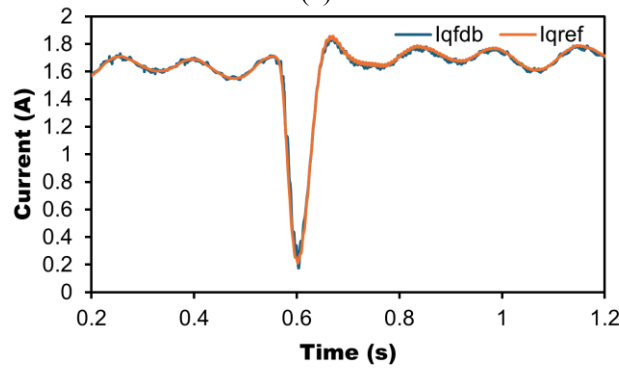
command, if the calculated torque under present MS T_{e_pms} is bigger than the calculated torque under target MS T_{e_tms} and the torque deviation exceeds the threshold as shown in Fig. 6.12(a), demagnetization is processed. A negative magnetizing current pulse with amplitude of 10 A is added to the d -axis current as shown in Fig. 6.12(b). After demagnetization manipulation, the two torque waveforms coincide, the MS changes from MS₄ to MS₂. The demagnetization process is completed. The dynamic performance of the related data is shown in Fig. 6.12. It can be observed that the fluctuations in torque and speed are significant during MS manipulation.



(a)



(b)



(c)

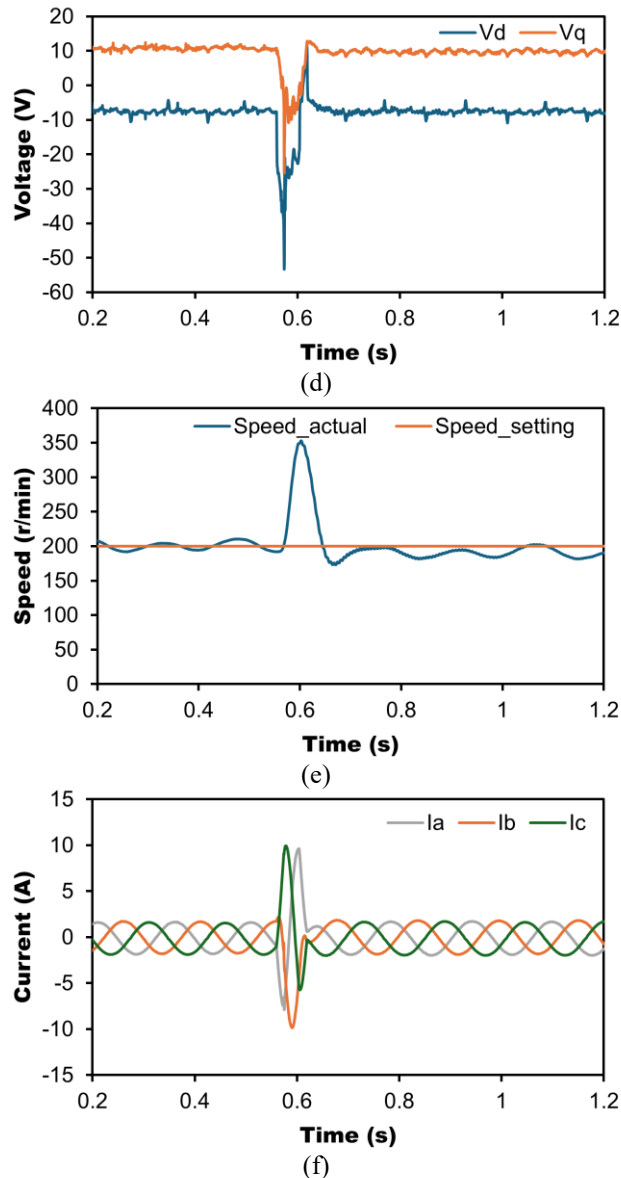
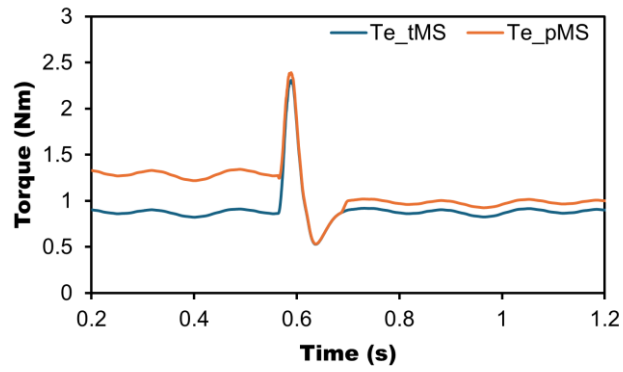
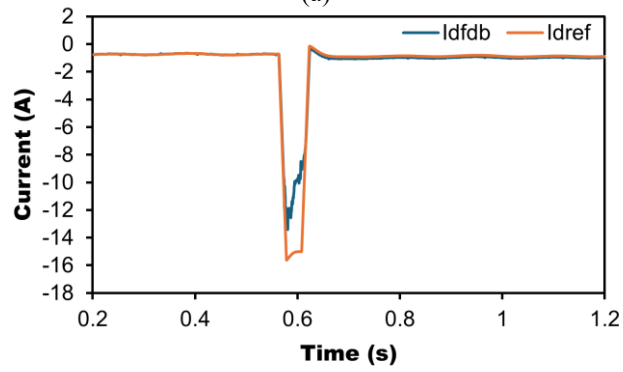


Fig. 6.12. Measured results of demagnetization with -10 A magnetizing current pulse. (a) Calculated torque. (b) d -axis current. (c) q -axis current. (d) dq -axis voltages. (e) Speed. (f) Three-phase currents.

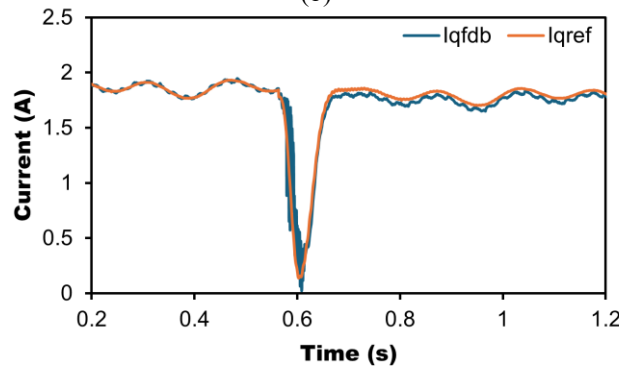
The same as the remagnetization experiments, the validation on demagnetization is tested from MR4 to MR1 with -15 A magnetizing current pulse. The measured results are presented in Fig. 6.13. Due to the voltage limitation in Fig. 6.13(d), the magnetizing current pulse does not reach to the demand value in Fig. 6.13(b). The MS is not processed to MR1, the torque after MS manipulation is not the same as the target value in Fig. 6.13(a). Besides, the fluctuations in q -axis current increase significantly.



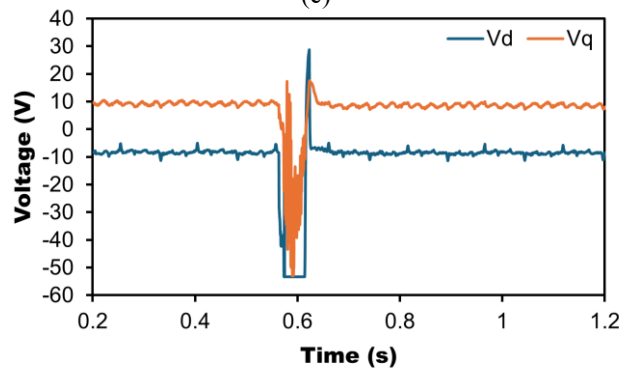
(a)



(b)



(c)



(d)

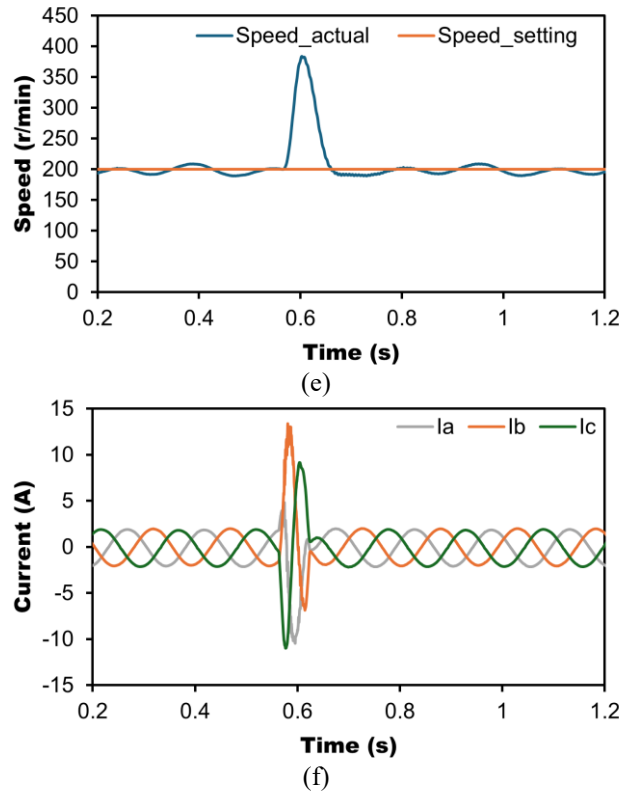
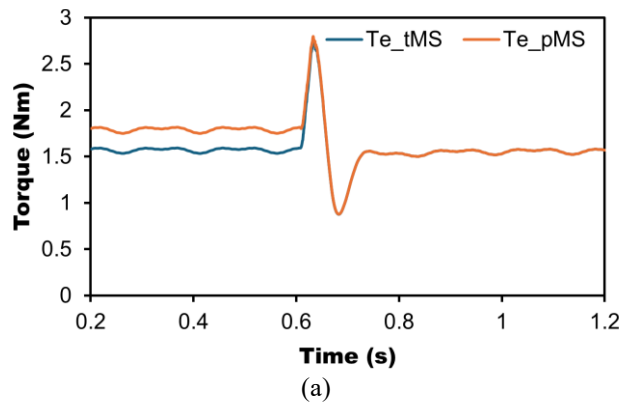
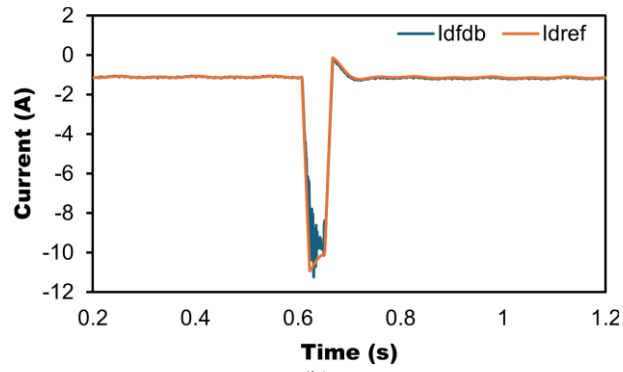


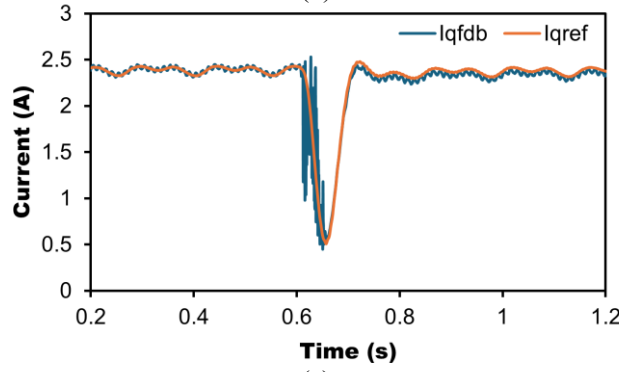
Fig. 6.13. Measured results of demagnetization with -15 A magnetizing current pulse. (a) Calculated torque. (b) d -axis current. (c) q -axis current. (d) dq -axis voltages. (e) Speed. (f) Three-phase currents.

Demagnetization is also tested with speed and load increasing. The test is under 400 r/min with 1.5 Nm load from MR4 to MR1. The measured results are presented in Fig. 6.14. The voltage limitation has a slight effect on the performance of MS manipulation in Fig. 6.14(d). Although there are small fluctuations, the magnetizing current pulse still reaches to the demand value in Fig. 6.14(b). After demagnetization, the torque is consistency with the target in Fig. 6.14(a). The MS is manipulated successfully.

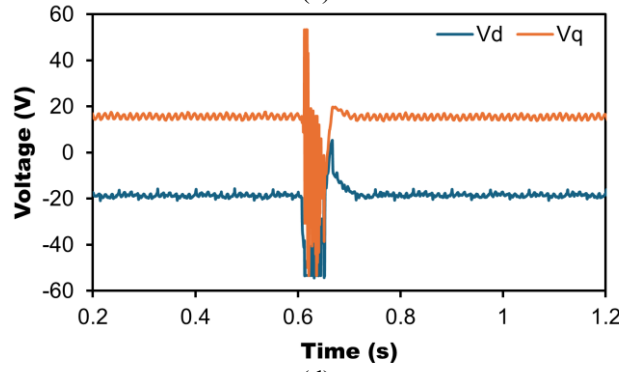




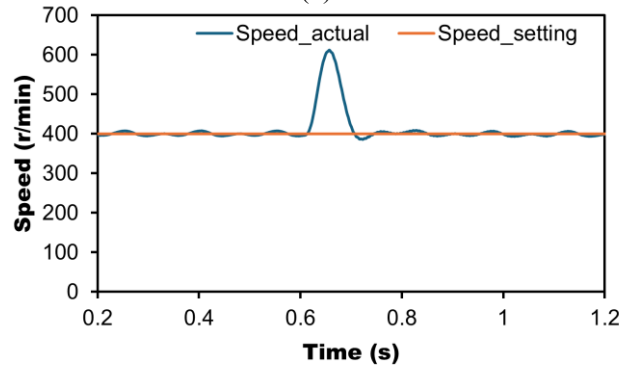
(b)



(c)



(d)



(e)

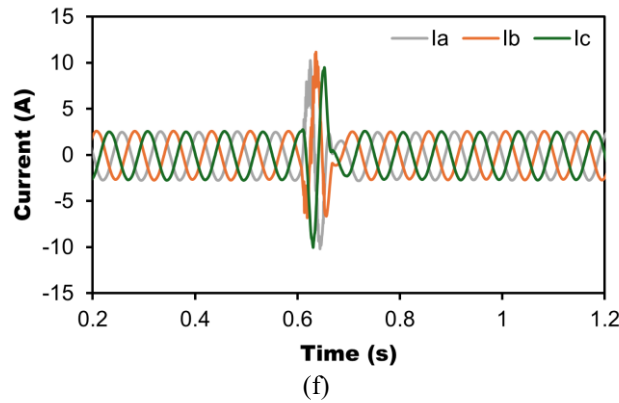


Fig. 6.14. Measured results of demagnetization with -10 A magnetizing current pulse under 1.5 Nm load. (a) Calculated torque. (b) d -axis current. (c) q -axis current. (d) dq -axis voltages. (e) Speed. (f) Three-phase currents.

Through the test with different magnetizing current pulses, different speeds, and different loads for both remagnetization and demagnetization, the feasibility of the proposed MS control method is well validated.

6.5 Conclusion

In this chapter, a novel MS control method by utilizing the torque deviation is proposed for VFMM to achieve the MS close-loop control. A look up table containing the information on the flux linkages, the dq -axis inductances, and the corresponding magnetizing current pulse under different MSs is built, A model-based torque calculation is adopted to estimate the steady state torque. The torque deviation between the present MS and the target MS is used to determine the type of MS manipulation: remagnetization, demagnetization, non-magnetization. The feasibility of the proposed MS control method is validated experimentally on a hybrid magnet memory machine system with different magnetizing current pulses, different speeds, and different loads for both remagnetization and demagnetization.

CHAPTER 7 GENERAL CONCLUSION AND FUTURE WORK

Since the concept of VFMM was proposed, more and more scholars have paid their attention on the related research. Due to adoption of LCF PMs and often combined with HCF PMs, the different arrangements of the PMs show significantly different performance for VFMM. More than 80% papers in the existing literature focused on the topologies of VFMMs. Basically, as a kind of PMSMs, the control methods applying for PMSMs are also suitable for VFMMs. The adjustable MS brings an extra freedom for the control of VFMMs. Therefore, the MS control is the crucial point for VFMM control. The research in this thesis mainly focuses on the MS manipulation methods and provides several novel solutions to improve the dynamic performance aiming to explore the applicability of VFMM in industry and daily life.

7.1 Summary of Research Work

The research work in this thesis can be summarized as follows:

1) Demagnetization timing control for HMMM. Based on the torque-speed curves of HMMM under different MSs as shown in Fig. 7.1, an optimal demagnetization grid is built, and this solution is also verified on remagnetization.

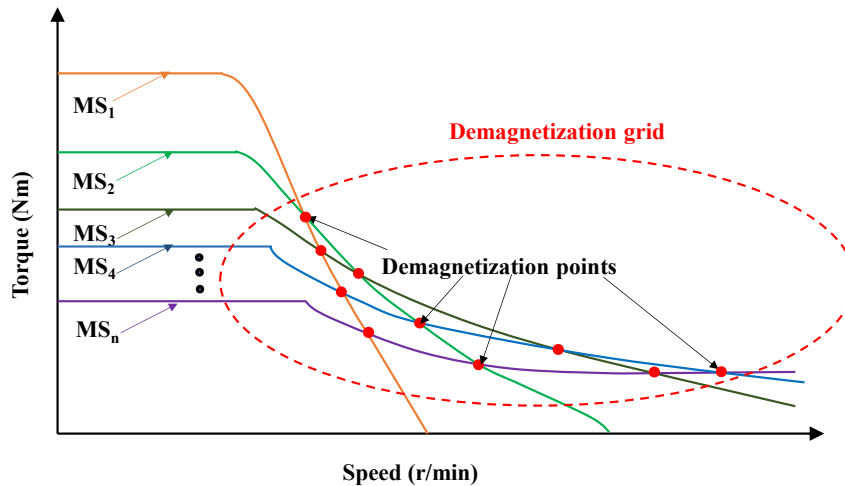


Fig. 7.1. Torque-speed curves of HMMM under different MSs.

2) Dual magnetizing current controller to mitigate speed fluctuation during MS manipulation. A q -axis current pulse is compensated when the d -axis magnetizing current pulse is injected to reduce the torque oscillations during MS control as shown in Fig. 7.2.

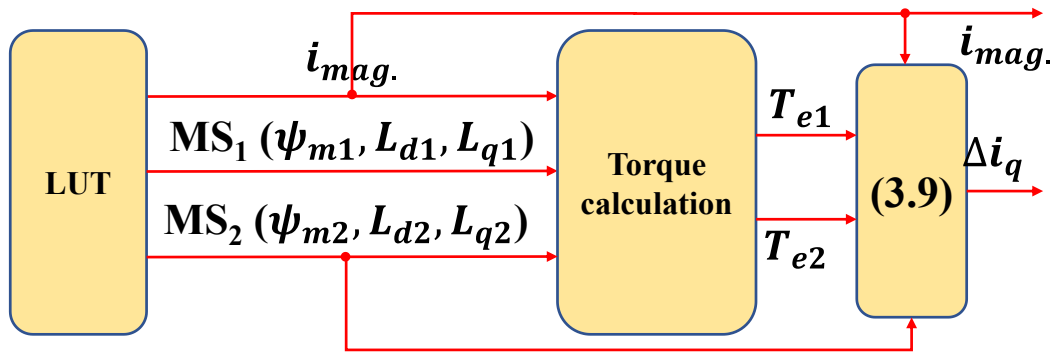


Fig. 7.2. Dual magnetizing current controller.

3) Novel MS control method based on modified voltage limitation. The circumscribed circle of the voltage vector hexagon is utilized as the modified voltage limitation and set as the boundary for MS manipulation as depicted in Fig. 7.3.

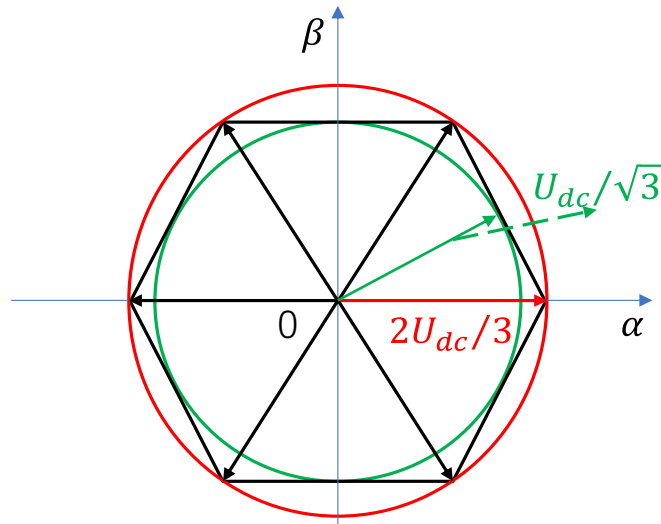


Fig. 7.3. Schematic diagram of space vector voltage limit circle.

4) Novel MS control method to eliminate UD issue of LCF PMs. The amplitude of demagnetization d -axis current pulse is used as the condition for the MS manipulation as presented in Fig. 7.4. Then, the amplitude of d -axis current is controlled within the amplitude of the demand demagnetization d -axis current pulse in the whole speed range.

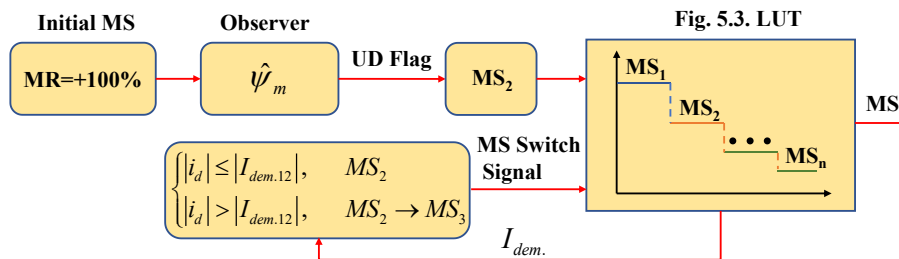


Fig. 7.4. Configuration of proposed MS controller.

5) A close-loop MS control method utilizing torque deviation. The torque deviation between the present MS and target MS is used to generate the MS switch signal, which will determine the type of MS manipulation as illustrated in Fig. 7.5.

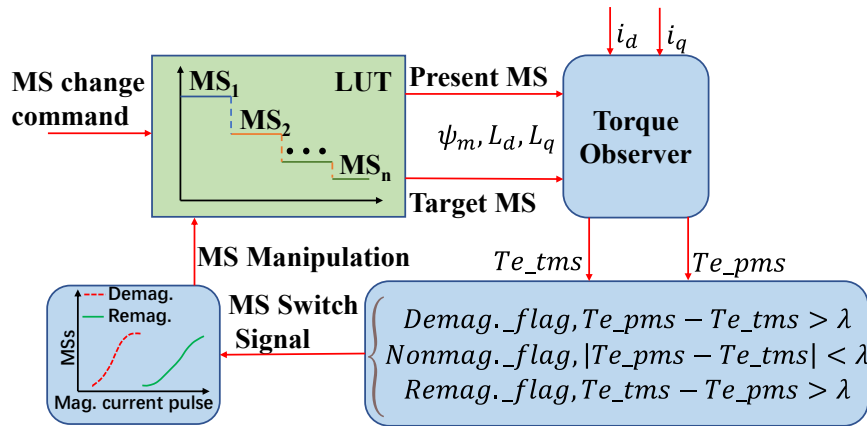


Fig. 7.5. Close-loop MS control method.

The summary of the work in this thesis is illustrated in Fig. 7.6. It is noted that all the proposed methods are verified experimentally on a HMMM drive system. All the topics are proposed and verified by simulations and experiments by myself.

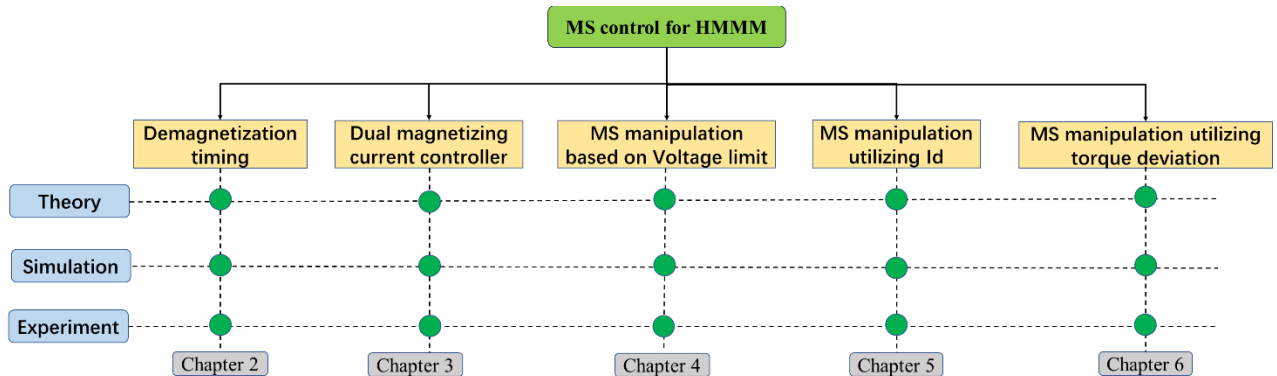


Fig. 7.6. Summary of work in this thesis.

7.2 Conclusion

7.2.1 Performance Improvement During MS Manipulation

In this thesis, to improve the performance during MS manipulation, the instant, number, and performance of demagnetization for HMMM are investigated firstly. Since the torques on the intersections of the torque-speed curves under different MSs are the same, demagnetization manipulation on the intersections can mitigate the fluctuation in speed caused by MS manipulation, which can be regarded as the best instant for demagnetization. Then, a

demagnetization grid is built based on these intersections. The measured results on the HMMM drive system show better performance on the proposed demagnetization grid, and dual demagnetization to achieve the final MS for the machine is optimal. The investigation is also processed on remagnetization tests.

When the fluctuation still affects the performance during MS manipulation or the MS manipulations are not processed on the proposed demagnetization grid, to further mitigate the speed fluctuation and improve the transient performance during MS manipulation, a novel dual magnetizing current controller is proposed. Since the torque oscillations caused by the d -axis magnetizing current pulse can be observed and calculated, a q -axis current pulse is injected at the same time as the d -axis magnetizing current pulse is injected to offset the torque oscillations. The transient performance experiments are validated on the HMMM control system, both for remagnetization and demagnetization. The measured results show that compared with the single magnetizing current method, the proposed dual magnetizing current method can significantly mitigate the speed fluctuation during MS manipulation and has much better transient performance.

7.2.2 Novel MS Control Methods

Three novel MS control methods are proposed in this thesis. Firstly, the circumcircle rather than the inscribed circle of the voltage vector hexagon is utilized as the voltage limitation. A novel MS control method based the modified voltage limitation is proposed. The maximum amplitude of the magnetizing current pulse under real-time operating conditions can be calculated, which is utilized as the boundary for MS manipulation. Within the boundary, the target MS can be achieved. When the MS is limited, the proposed MS control method also provides solutions to achieve the target MS by calculating the optimal operating speed. In this proposed method, the effect of the voltage limitation on the MS manipulation is considered.

Secondly, the demand demagnetization d -axis current pulse is used as the condition for MS manipulation. When the amplitude of negative d -axis current reaches at the amplitude of the demand demagnetization d -axis current, the MS manipulation is processed. Thus, the amplitude of d -axis current is controlled within the amplitude of the demand demagnetization d -axis current pulse in the whole speed range. Then, the flux weakening d -axis current will not cause the UD issue. The potential UD issue of LCF PM can be solved by this proposed MS control method for the investigated HMMM. Besides, a PM flux linkage estimation is adopted to monitor the UD issue, and VSI nonlinearity is compensated to improve the estimation

accuracy.

Then, to achieve the MS close-loop control, a novel MS control method by utilizing the torque deviation is proposed. On receiving the MS change command, the torque deviation between the present MS and the target MS can be calculated and used to generate the MS switch signal, which also determines the type of MS manipulation. The demand magnetizing current pulse will be injected into the control system according to the MS switch signal. Therefore, the MS close-loop control can be achieved.

The feasibilities of the proposed MS control methods are validated experimentally on the HMMM control system.

7.3 Future Work

7.3.1 Accurate MS Estimation

Accurate MS estimation can achieve the online MS control and improve the MS manipulation efficiency. Since the PM flux linkage is the main feature of MS in VFMMs, the research on MS estimation usually focuses on the PM flux linkage estimation in the existing literature. Only using PM flux linkage to represent the MS is not accurate, even not correct for some VFMMs. The BEMF of the investigated HMMM under different MSs is shown in Fig. 7.7. It can be observed that the BEMF is almost same from MR = 0% to MR = -100%, which means that the PM flux linkages rarely change. In this case, PM flux linkage cannot be used to indicate the MS.

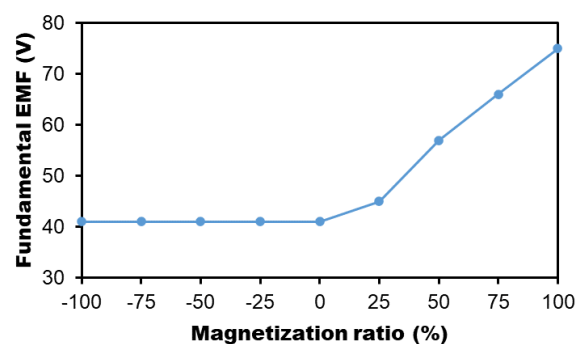


Fig. 7.7. BEMF fundamental magnitude against magnetization ratio of investigated HMMM.

Therefore, accurate MS estimation methods that can comprehensively reflect the information of MS are still highly desirable.

7.3.2 Effect of Load Changes on MS Control

In the existing literature, the MS control is usually verified on no load to ensure that the large magnetizing current pulse can be achieved. The capacity of MS control with load in the operation process has rarely been investigated. Besides, due to the MS manipulation process is instant, the operating state is usually considered as steady state, and the dynamic changes are ignored. Control methods considering the load changes to improve the dynamic performance are needed.

7.3.3 Oscillations in Three-phase Currents During MS Manipulation

As previous investigation, the magnetizing pulse should be at least 30 ms time duration to ensure the magnetizing capability. While in the industrial applications, the fault protections are generally at the ms level. When applied in high power industrial applications, the MS control methods of injecting magnetizing current pulses with large amplitude face more severe challenges. The significant disturbances in currents and voltages will bring harm to the inverter and the whole control system. The safety and reliability of the drive system are much more important in the industrial applications. Although the speed fluctuations can be mitigated by the research in this thesis, the oscillations in the three-phase currents brought by the magnetizing current pulses are difficult to solve, and the corresponding control methods remain underdeveloped, which will be an obstacle for the application of VFMM in industry and daily life.

7.3.4 Uncontrolled Generator Fault Prevention for VFMM

The Uncontrolled Generator Fault (UCGF) [ZHA17] [ZHU19] [JAH99] [GON20] [SOO05] [PEL11] that occurs at FW region is one of the most serious issues for PM machines, which could damage the machine drive system. When the negative d -axis current unintentionally disappears in FW region, the machine will keep rotating and work as a generator. As a result, the large BEMF will turn into a voltage source, which could be several times of the rated voltage. Then, the generated current will promptly charge the DC capacitor. If the generated energy cannot be consumed in time, it will damage the DC capacitor and the power electronic devices of the inverter, even the PM machines. It is stated that UCGF is usually caused by the damage of the position sensor or the gating signal removal of the inverter [ZHU19].

For VFMM, the MS demagnetization can reduce the PM flux linkage, this can decrease the BEMF, which will benefit for the UCGF prevention. In [LYU20b], a MS selection method is

proposed to prevent UCGF for VFMM. The voltage limitation is set as the condition of MS control. When the voltage reaches to the limitation, the MS manipulation is processed to reduce the voltage. But the voltage margin issue was ignored, since the MS manipulation also need enough voltage to process, especially for large amplitude of magnetizing current pulses. The control methods to prevent UCGF by utilizing MS manipulation are still needed to further investigate.

REFERENCES

- [ATH17] A. Athavale, K. Sasaki, B. S. Gagas, T. Kato, and R. D. Lorenz, “Variable flux permanent magnet synchronous machine (VF-PMSM) design methodologies to meet electric vehicle traction requirements with reduced losses,” *IEEE Trans. Ind. Appl.*, vol. 53, no. 5, pp. 4318–4326, Sep./Oct. 2017.
- [ATH18] A. Athavale, D. J. Erato, and R. D. Lorenz, “Enabling driving cycle loss reduction in variable flux PMSMs via closed-loop magnetization state control,” *IEEE Trans. on Ind. Appl.*, vol. 54, no. 4, pp. 3350-3359, July-Aug. 2018.
- [BAE03] B. H. Bae, N. Patel, S. Schulz, and S. K. Sul, “New field weakening technique for high saliency interior permanent magnet motor,” in *Conf. Rec. IEEE IAS Annu. Meeting*, 2003, pp. 898–905.
- [BED20] N. Bedetti, S. Calligaro and R. Petrella, “Analytical design and autotuning of adaptive flux-weakening voltage regulation loop in IPMSM drives with accurate torque regulation,” *IEEE Trans. on Ind. Appl.*, vol. 56, no. 1, pp. 301-313, Jan.-Feb. 2020.
- [BIN06] A. Binder, T. Schneider, and M. Klohr, “Fixation of buried and surface-mounted magnets in high-speed permanent-magnet synchronous machines,” *IEEE Trans. Ind. Appl.*, vol. 42, no. 4, pp. 1031–1037, Jul./Aug. 2006.
- [BOL14] S. Bolognani, S. Calligaro, and R. Petrella, “Adaptive flux-weakening controller for interior permanent magnet synchronous motor drives,” *IEEE Journal of Emerging and Selected Topics in Power Electronics*, vol. 2, no. 2, pp. 236-248, June 2014.
- [CHE05] Y. Chen, W. Pan, Y. Wang, R. Tang, and J. Wang, “Interior composite-rotor controllable-flux PMSM-memory motor,” in *Proc. Int. Conf. Elect. Mach. Syst.*, vol. 1, Sep. 2005, pp. 446–449.
- [CHE09] Y. Chen, L. Kong, and W. Zhong, “Finite element analysis of interior composite-rotor controllable flux permanent magnet synchronous machine,” in *Proc. Int. Conf. Elect. Mach. Syst.*, Nov. 2009, pp. 1-4.

- [CHE20] J. Chen, H. Fang, and R. Qu, "Online magnetization trajectory prediction and current control for a variable-flux permanent magnet machine," *IEEE Access*, vol. 8, pp. 41325-41334, 2020.
- [CHE22] Z. Chen, H. Lin, Y. Zhong, S. Lyu, and H. Yang, "A novel current control strategy for magnetization state manipulation of variable flux memory machine based on linear active disturbance rejection," *IEEE Trans. on Power Electron.*, vol. 37, no. 2, pp. 1962-1971, Feb. 2022.
- [FAN19] X. Fan, B. Zhang, R. Qu, D. Li, J. Li, and Y. Huo, "Comparative thermal analysis of IPMSMs with integral-slot distributed-winding (ISDW) and fractional-slot concentrated-winding (FSCW) for electric vehicle application," *IEEE Trans. Ind. Appl.*, vol. 55, no. 4, pp. 3577-3588, July/Aug. 2019.
- [FRE96] C. French and P. Acarnley, "Direct torque control of permanent magnet drives," *IEEE Trans. on Ind. Appl.*, vol. 32, no. 5, pp. 1080-1088, Sept.-Oct. 1996.
- [FUK15] T. Fukushige, N. Limsuwan, T. Kato, K. Akatsu, and R. D. Lorenz, "Efficiency contours and loss minimization over a driving cycle of a variable flux-intensifying machine," *IEEE Trans. Ind. Appl.*, vol. 51, no. 4, pp. 2984-2989, Jul. 2015.
- [GAG14] B. Gagas, T. Fukushige, T. Kato, and R. D. Lorenz, "Operating within dynamic voltage limits during magnetization state increases in variable flux PM synchronous machines," in *2014 IEEE Energy Conversion Congress and Exposition (ECCE)*, Pittsburgh, PA, 2014, pp. 5206-5213.
- [GAG16] B. S. Gagas, K. Sasaki, T. Fukushige, A. Athavale, T. Kato, and R. D. Lorenz, "Analysis of magnetizing trajectories for variable flux PM synchronous machines considering voltage, high-speed capability, torque ripple, and time duration," *IEEE Trans. on Ind. Appl.*, vol. 52, no. 5, pp. 4029-4038, Sept.-Oct. 2016.
- [GAG17] B. S. Gagas, K. Sasaki, A. Athavale, T. Kato, and R. D. Lorenz, "Magnet temperature effects on the useful properties of variable flux PM synchronous machines and a mitigating method for magnetization changes," *IEEE Trans. on Ind. Appl.*, vol. 53, no. 3, pp. 2189-2199, May-June 2017.

- [GAR98] A. Munoz-Garcia, T. A. Lipo, and D. W. Novotny, "A new induction motor V/f control method capable of high-performance regulation at low speeds," *IEEE Trans. on Ind. Appl.*, vol. 34, no. 4, pp. 813-821, July-Aug. 1998.
- [GE18] M. Ge, J. Li, R. Qu, Y. Lu, and J. Chen, "A synthetic frozen permeability method for torque separation in hybrid PM variable-flux machines," *IEEE Trans. on Applied Supercon.*, vol. 28, no. 3, pp. 1-5, April 2018.
- [GON09] Y. Gong, K. Chau, J. Jiang, C. Yu, and W. Li, "Analysis of doubly salient memory motors using Preisach theory," *IEEE Trans. Magn.*, vol. 45, no. 10, pp. 4679-4679, Oct. 2009.
- [GON20] C. Gong, Y. Hu, C. Gan, G. Chen, and A. Mohammed, "Modelling, analysis and attenuation of uncontrolled generation for IPMSM based electric vehicles in emergency," *IEEE Trans. Ind. Electron.*, vol. 67, no. 6, pp. 4453–4462, Jun. 2020.
- [GUL07] K. Gulez, A. A. Adam, and H. Pastaci, "A novel direct torque control algorithm for IPMSM with minimum harmonics and torque ripples," *IEEE/ASME Trans. on Mechatro.*, vol. 12, no. 2, pp. 223-227, April 2007.
- [HE21] T.R. He, Z. Q. Zhu, F. Xu, H. Bin, D. Wu, L. Gong, J. T. Chen, "Comparative study of 6-slot/2-pole high-speed permanent magnet motors with different winding configurations," *IEEE Trans. Ind. Appl.*, vol. 57, no. 6, pp. 5864-5875, Nov./Dec. 2021.
- [HE22] T. He, Z. Q. Zhu, F. Xu, Y. Wang, H. Bin, and L. Gong, "Electromagnetic performance analysis of 6-slot/2-pole high-speed permanent magnet motors with coil-pitch of two slot-pitches," *IEEE Trans. Energy Convers.*, vol. 37, no. 2, pp. 1335-1345, June 2022.
- [HON10] J. Hong, D. Hyun, S. B. Lee, J. Y. Yoo, and K. W. Lee, "Automated monitoring of magnet quality for permanent-magnet synchronous motors at standstill," *IEEE Trans. on Ind. Appl.*, vol. 46, no. 4, pp. 1397-1405, July-Aug. 2010.
- [HU20a] Y. Hu, J. Chen, R. Qu, B. Chen, Y. Xiao, and X. Li, "Closed-loop magnetization state control for a variable-flux memory machine," *IEEE Access*, vol. 8, pp. 146983–146993, 2020.

- [HU20b] Y. S. Hu, B. Chen, Y. Xiao, X. Li, Z. D. Zhang, J. F. Shi, and L. Y. Li, "Research and design on reducing the difficulty of magnetization of a hybrid permanent magnet memory motor," *IEEE Trans. on Energy Convers.*, vol. 35, no. 3, pp. 1421-1431, Sept. 2020.
- [HU21] Y. Hu, B. Chen, Y. Xiao, X. Li, J. Chen, and H. Fang, "Comprehensive control of a hybrid-magnet variable-flux memory machine for washing machine applications," in *2021 IEEE 4th International Electrical and Energy Conference (CIEEC)*, 2021, pp. 1-6.
- [HUA17a] H. Hua, Z. Q. Zhu, A. Pride, R. P. Deodhar, and T. Sasaki, "A novel variable flux memory machine with series hybrid magnets," *IEEE Trans. Ind. Appl.*, vol. 53, no. 5, pp. 4396-4405, Sept./Oct. 2017.
- [HUA17b] H. Hua, Z. Q. Zhu, A. Pride, R. P. Deodhar, and T. Sasaki, "Comparative study of variable flux memory machines with parallel and series hybrid magnets," in *Proc. Energy Convers. Congr. and Expo. (ECCE)*, 2017 IEEE, Cincinnati, U.S., 2017, pp. 1-8.
- [HUA19a] H. Hua, Z. Q. Zhu, A. Pride, R. Deodhar, and T. Sasaki, "Comparative study on variable flux memory machines with parallel or series hybrid magnets," *IEEE Trans. on Ind. Appl.*, vol. 55, no. 2, pp. 1408–1419, Mar. 2019.
- [HUA19b] H. Hua, Z. Q. Zhu, A. Pride, R. P. Deodhar, and T. Sasaki, "Comparison of end effect in series and parallel hybrid permanent-magnet variable-flux memory machines," *IEEE Trans. on Ind. Appl.*, vol. 55, no. 3, pp. 2529–2537, May 2019.
- [IBR15a] M. Ibrahim, L. Masisi, and P. Pillay, "Design of variable-flux permanent-magnet machines using alnico magnets," *IEEE Trans. Ind. Appl.*, vol. 51, no. 6, pp. 4482-4491, Nov./Dec. 2015.
- [IBR15b] M. Ibrahim, L. Masisi, and P. Pillay, "Design of variable flux permanent-magnet machine for reduced inverter rating," *IEEE Trans. Ind. Appl.*, vol. 51, no. 5, pp. 3666-3674, Sep./Oct. 2015.
- [ISH05] D. Ishak, Z. Q. Zhu, and D. Howe, "Eddy-current loss in the rotor magnets of permanent-magnet brushless machines having a fractional number of slots per

- pole,” *IEEE Trans. Magn.*, vol. 41, no. 9, pp. 2462-2469, Sept. 2005.
- [ITO13] J. I. Itoh, Y. Nakajima, and M. Kato, “Maximum torque per ampere control method for IPM synchronous motor based on V/f control,” in *2013 IEEE 10th International Conference on Power Electronics and Drive Systems (PEDS)*, Kitakyushu, Japan, 2013, pp. 1322-1327.
- [JAH84] T. M. Jahns, “Torque production in permanent magnet synchronous motor drives with rectangular current excitation,” *IEEE Trans. Ind. Appl.*, vol. IA-20, no. 4, pp. 803–813, 1984.
- [JAH86] T. M. Jahns, G. B. Kliman, and T. W. Neumann, “Interior permanent-magnet synchronous motors for adjustable-speed drives,” *IEEE Trans. on Ind. Appl.*, vol. IA-22, no. 4, pp. 738-747, July 1986.
- [JAH87] T. M. Jahns, “Flux-weakening regime operation of an interior permanent-magnet synchronous motor drive,” *IEEE Trans. on Ind. Appl.*, vol. IA-23, no. 4, pp. 681-689, July 1987.
- [JAH94] T. M. Jahns, “Motion control with permanent-magnet AC machines,” *Proceedings of the IEEE*, vol. 82, no. 8, pp. 1241-1252, Aug. 1994.
- [JAH99] T. M. Jahns and V. Caliskan, “Uncontrolled generator operation of interior PM synchronous machines following high-speed inverter shutdown,” *IEEE Trans. Ind. Appl.*, vol. 35, no. 6, pp. 1347–1357, Nov. 1999.
- [JAY19] R. Jayarajan, N. Fernando, and I. U. Nutkani, “A review on variable flux machine technology: topologies, control strategies and magnetic materials,” *IEEE Access*, vol. 7, pp. 70141-70156, 2019.
- [JIA15] L. Jian, Y. Gong, J. Wei, Y. Shi, Z. Shao, and T. W. Ching, “A novel claw pole memory machine for wide-speed-range applications,” *Journal of Applied Physics*, vol. 117, no. 17, 2015.
- [JIA22] J. Jiang and S. Niu, “A novel slot-PM-assisted hybrid magnet memory machine,” *IEEE Trans. Magn.*, vol. 58, no. 8, pp. 1-6, Aug. 2022.
- [JIA22a] Y. Jia, Z. Q. Zhu, J. H. Feng, S. Y. Guo, Y. F. Li, L. Hu, and H. Yang, “Investigation on the timing of demagnetization for variable flux memory motor,” in *2022 IEEE 5th International Electrical and Energy Conference*

(CIEEC), Nanjing, China, 2022, pp. 3473-3478.

- [JIA22b] Y. Jia, Z. Q. Zhu, Dawei Liang, J. H. Feng, S. Y. Guo, Y. F. Li, and L. Hu, "A novel magnetization state control method to eliminate the unintentional demagnetization of low-coercive force permanent magnet for a hybrid magnet memory motor," in *2022 International Conference on Electrical Machines (ICEM)*, Valencia, Spain, 2022, pp. 1096-1102.
- [JIA22c] Y. Jia, Z. Q. Zhu, L. Xu, J. H. Feng, S. Y. Guo, Y. F. Li, and L. Hu, "A novel magnetization state control method utilizing torque deviation for variable flux memory motor," *2022 25th International Conference on Electrical Machines and Systems (ICEMS)*, Chiang Mai, Thailand, 2022, pp. 1-5.
- [KAN95] Seog-Joo Kang and S. -K. Sul, "Direct torque control of brushless DC motor with nonideal trapezoidal back EMF," *IEEE Trans. on Power Electron.*, vol. 10, no. 6, pp. 796-802, Nov. 1995.
- [KAT14] T. Kato, N. Limsuwan, C. Yu, K. Akatsu, and R. D. Lorenz, "Rare earth reduction using a novel variable magnetomotive force flux-intensified IPM machine," *IEEE Trans. Ind. Appl.*, vol. 50, no. 3, pp. 1748-1756, May/Jun. 2014.
- [KIM06] Hag-Wone Kim, Myung-Joong Youn, Kwan-Yuhl Cho, and Hyun-Soo Kim, "Nonlinearity estimation and compensation of PWM VSI for PMSM under resistance and flux linkage uncertainty," *IEEE Trans. on Control Systems Technology*, vol. 14, no. 4, pp. 589-601, July 2006.
- [KIM97a] Sang-Hoon Kim and Seung-Ki Sul, "Voltage control strategy for maximum torque operation of an induction machine in the field-weakening region," *IEEE Trans. on Ind. Electron.*, vol. 44, no. 4, pp. 512-518, Aug. 1997.
- [KIM97b] Jang-Mok Kim and Seung-Ki Sul, "Speed control of interior permanent magnet synchronous motor drive for the flux weakening operation," *IEEE Trans. on Ind. Appl.*, vol. 33, no. 1, pp. 43-48, Jan.-Feb. 1997.
- [KUM87] T. Kume and T. Iwakane, "High-performance vector-controlled AC motor drives: applications and new technologies," *IEEE Trans. on Ind. Appl.*, vol. IA-23, no. 5, pp. 872-880, Sept. 1987.

- [KWO07] T. S. Kwon and S. K. Sul, "A novel flux weakening algorithm for surface mounted permanent magnet synchronous machines with infinite constant power speed ratio," in *Proc. Int. Conf. Electr. Mach. Syst.*, Oct. 8–11, 2007, pp. 440–445.
- [KWO08] T. S. Kwon, G. Y. Choi, M. S. Kwak, and S. K. Sul, "Novel flux weakening control of an IPMSM for quasi-six-step operation," *IEEE Trans. Ind. Appl.*, vol. 44, no. 6, pp. 1722–1731, Nov./Dec. 2008.
- [LEE08] J. H. Lee and J. P. Hong, "Permanent magnet demagnetization characteristic analysis of a variable flux memory motor using coupled Preisach modeling and FEM," *IEEE Trans. on Magnetics*, vol. 44, no. 6, pp. 1550–1553, Jun. 2008.
- [LEE20] K. Lee and Y. Han, "MTPA control strategy based on signal injection for V/f scalar-controlled surface permanent magnet synchronous machine drives," *IEEE Access*, vol. 8, pp. 96036-96044, 2020.
- [LI11a] W. Li, K. T. Chau, Y. Gong, J. Z. Jiang, and F. Li, "A new flux-mnemonic dual-magnet brushless machine," *IEEE Trans. Magn.*, vol. 47, no. 10, pp. 4223-4226, Oct. 2011.
- [LI11b] F. Li, K. T. Chau, and C. Liu, "Design of dual-magnet memory machines," in *Proc. Int. Conf. Elect. Mach. Syst.*, Aug. 2011, pp. 1-6.
- [LI14] F. Li, K. Chau, C. Liu, and C. Qiu, "New approach for pole-changing with dual-memory machine," *IEEE Trans. Appl. Supercond.*, vol. 24, no. 3, Jun. 2014.
- [LI21] Y. Li, H. Yang, and H. Lin, "A novel stator flux-concentrated hybrid permanent magnet memory machine," *IEEE Trans. Magn.*, vol. 57, no. 2, Feb. 2021.
- [LIU05] Y. Liu, Z. Q. Zhu, and D. Howe, "Direct torque control of brushless DC drives with reduced torque ripple," *IEEE Trans. Ind. Appl.*, vol. 41, no. 2, pp. 599–608, Mar./Apr. 2005
- [LIU08] H. C. Liu, H. Y. Lin, S. H. Fang, and X. L. Huang, "Investigation of permanent magnet shape on field-control parameters of variable flux memory motor with FEM," in *Proc. Conf. Rec. ICEF'08*, 2008, pp.335–339.

- [LIU09] H. Liu, H. Lin, S. Fang, and Z. Q. Zhu, “Permanent magnet demagnetization physics of a variable flux memory motor,” *IEEE Trans. on Magnetics*, vol. 45, no. 10, pp. 4736–4739, Oct. 2009.
- [LIU10] H. Liu, H. Lin, Z. Q. Zhu, M. Huang, and P. Jin, “Permanent magnet remagnetizing physics of a variable flux memory motor,” *IEEE Trans. on Magnetics*, vol. 46, no. 6, pp. 1679–1682, Jun. 2010.
- [LIU14c] K. Liu, and Z. Q. Zhu, “Online estimation of the rotor flux linkage and voltage-source inverter nonlinearity in permanent magnet synchronous machine drives,” *IEEE Trans. on Power Electronics*, vol. 29, no. 1, pp. 418-427, Jan. 2014.
- [LIU14d] K. Liu and Z. Q. Zhu, “Parameter estimation of PMSM for aiding PI regulator design of field-oriented control,” in *2014 17th International Conference on Electrical Machines and Systems (ICEMS)*, Hangzhou, China, 2014, pp. 2705-2711.
- [LIU14a] X. Liu, D. Wu, Z. Q. Zhu, A. Pride, R. P. Deodhar, and T. Sasaki, “Efficiency improvement of switched flux PM memory machine over interior PM machine for EV/HEV applications,” *IEEE Trans. Magn.*, vol. 50, no. 11, pp. 1106-1109, Nov. 2014.
- [LIU14b] C. Liu, K. Chau, and C. Qiu, “Design and analysis of a new magnetic-g geared memory machine,” *IEEE Trans. Appl. Supercond.*, vol. 24, no. 3, pp. 1-5, Jun. 2014.
- [LIU16] X. Liu, H. Chen, J. Zhao, and A. Belahcen, “Research on the performances and parameters of interior PMSM used for electric vehicles,” *IEEE Trans. Ind. Electron.*, vol. 63, no. 6, pp. 3533-3545, June 2016.
- [LIU19] Y. Liu, “Investigation of magnetic gearing effect in fractional slot and vernier permanent magnet synchronous machines,” *Ph.D. dissertation*, Dept. Electron. Elec. Eng., Univ. Sheffield, Sheffield, U.K., 2019.
- [LIU22] W. Liu, H. Yang, H. Lin, F. Peng, S. Lyu, and Y. Zhong, “A novel asymmetric-PM hybrid-magnetic-circuit variable flux memory machine for traction

applications,” *IEEE Trans. Veh. Technol.*, vol. 71, no. 5, pp. 4911-4921, May 2022.

- [LIU23] W. Liu, H. Yang, H. Lin, H. Zhan, W. Chen, D. Wu, and M. Yu, “Design tradeoff between saliency ratio and PM flux linkage in variable flux memory machines,” *IEEE Trans. on Energy Convers.*, vol. 38, no. 1, pp. 562-572, March 2023.
- [LYU19] S. Lyu, H. Yang, H. Lin, Z. Q. Zhu, H. Zheng, and Z. Pan, “Influence of design parameters on on-load demagnetization characteristics of switched flux hybrid magnet memory machine,” *IEEE Trans. on Magnetics*, vol. 55, no. 7, pp. 1–5, Jul. 2019.
- [LYU20a] S. Lyu, H. Yang, H. Lin, and Y. Ren, “A magnetization state initialization control scheme for variable flux memory machines without requiring position sensor information,” *IEEE Trans. on Transp. Electrification*, vol. 6, no. 3, pp. 1157–1166, Sep. 2020.
- [LYU20b] S. Lyu, H. Yang, and H. Lin, “Magnetization state selection method for uncontrolled generator fault prevention on variable flux memory machines,” *IEEE Trans. on Power Electron.*, vol. 35, no. 12, pp. 13270-13280, Dec. 2020.
- [LYU23] S. Lyu, H. Yang, H. Lin, H. Zhan, and Z. Chen, “Improved MTPA control for variable-flux memory machine with operating envelope prediction-based MS manipulation,” *IEEE Trans. on Power Electron.*, vol. 38, no. 3, pp. 3700-3710, March 2023.
- [MAC91] S. R. MacMinn and T. M. Jahns, “Control techniques for improved high-speed performance of interior PM synchronous motor drives,” *IEEE Trans. Ind. Appl.*, vol. 27, pp. 997-1004, Sep./Oct. 1991.
- [MAE14] S. Maekawa, K. Yuki, M. Matsushita, I. Nitta, Y. Hasegawa, T. Shiga, T. Hosoito, K. Nagai, and H. Kubota, “Study of the magnetization method suitable for fractional-slot concentrated-winding variable magnetomotive-force memory motor,” *IEEE Trans. on Power Electron.*, vol. 29, no. 9, pp. 4877–4887, Sep. 2014.
- [MAS15] L. Masisi, M. Ibrahim, and P. Pillay, “Control strategy of a variable flux machine using AlNiCo permanent magnets,” in *2015 IEEE Energy Convers.*

Congress and Expos. (ECCE), Montreal, QC, 2015, pp. 5249-5255.

- [MOR90] S. Morimoto, Y. Takeda, and T. Hirasa, "Expansion of operating limits for permanent magnet motor by current vector control considering inverter capacity," *IEEE Trans. Ind. Appl.*, vol. 26, no. 5, pp. 866–871, Sep./Oct. 1990.
- [MOR94] S. Morimoto, M. Sanada, and Y. Takeda, "Wide-speed operation of interior permanent magnet synchronous motors with high-performance current regulator," *IEEE Trans. on Ind. Appl.*, vol. 30, no. 4, pp. 920-926, July-Aug. 1994.
- [NOG05] T. Noguchi, Y. Takata, Y. Yamashita, Y. Komatsu, and S. Ibaraki, "220000 r/min 2kW PM motor drive for turbocharger," *IEEJ Trans. Ind. Appl.*, vol. 125, no. 9, pp. 854– 861, Sep. 2005.
- [OST01] V. Ostovic, "Memory motors-a new class of controllable flux PM machines for a true wide speed operation," *Conference Record of the 2001 IEEE Ind. Appl. Conf. 36th IAS Annual Meeting (Cat. No.01CH37248)*, Chicago, IL, USA, 2001, pp. 2577-2584 vol.4.
- [OST02] V. Ostovic, "Pole-changing permanent-magnet machines," *IEEE Trans. Ind. Appl.*, vol. 38, no. 6, pp. 1493-1499, Nov./Dec. 2002.
- [OST03] V. Ostovic, "Memory motors," *IEEE Ind. Appl. Magazine*, vol. 9, no. 1, pp. 52-61, Jan.-Feb. 2003.
- [OU21] J. Ou, Y. Liu, and M. Doppelbauer, "Comparison study of a surface-mounted PM rotor and an interior PM rotor made from amorphous metal of high-speed motors," *IEEE Trans. Ind. Electron.*, vol. 68, no. 10, pp. 9148-9159, Oct. 2021.
- [PEL11] G. Pellegrino, A. Vagati, and P. Guglielmi, "Design tradeoffs between constant power speed range, uncontrolled generator operation, and rated current of IPM motor drives," *IEEE Trans. Ind. Appl.*, vol. 47, no. 5, pp. 1995–2003, Sep. 2011.
- [PIL90] P. Pillay and R. Krishnan, "Control characteristics and speed controller design for a high performance permanent magnet synchronous motor drive," *IEEE Trans. on Power Electron.*, vol. 5, no. 2, pp. 151-159, April 1990.

- [QIA13] L. Qiao, F. Kong, X. Zhu, Y. Ge, and L. Quan, "Investigation on the dynamic performances of a doubly salient flux memory motor under on-line flux regulation for electric vehicles," in *2013 IEEE Vehicle Power and Propulsion Conference (VPPC)*, pp. 1–5, Oct. 2013.
- [QIA18] G. Qiao, Y. Liu, P. Zheng, J. Chen, S. Zhang, and M. Wang, "Analysis of magnetic properties of AlNiCo and methods of mitigating dynamic voltage limits in the combined-magnetic-pole memory motor," in *2018 21st International Conference on Electrical Machines and Systems (ICEMS)*, Jeju, 2018, pp. 1175-1180.
- [QIA19] G. Qiao, M. Wang, F. Liu, Y. Liu, P. Zheng, and Y. Sui, "Analysis of magnetic properties of AlNiCo and magnetization state estimation in variable-flux PMSMs," *IEEE Trans. on Magne.*, vol. 55, no. 7, pp. 1-6, July 2019.
- [QIA21] G. Qiao, M. Wang, F. Liu, Y. Liu, and P. Zheng, "Analysis of novel hybrid-PM variable-flux PMSMs with series–parallel magnetic circuits," *IEEE Trans. Magn.*, vol. 57, no. 2, Feb. 2021.
- [SAK09] K. Sakai, K. Yuki, Y. Hashiba, N. Takahashi, and K. Yasui, "Principle of the variable-magnetic-force memory motor," in *Proc. Int. Conf. Electr. Mach. Syst.*, Tokyo, Japan, 2009, pp. 1-6.
- [SAK11] K. Sakai, H. Hashimoto, and S. Kuramochi, "Principle of hybrid variable-magnetic-force motors," in *Proc. Int. Electr. Mach. Drives Conf. (IEMDC)*, Niagara Fall [67]s, ON, 2011, pp. 53-58.
- [SAK13] K. Sakai, N. Yuzawa, and H. Hashimoto, "Permanent magnet motors capable of pole changing and three-torque-production mode using magnetization," *IEEE Trans. Ind. Appl.*, vol. 2, no. 6, pp. 269–275, Jun. 2013.
- [SAK20] K. Sakai and S. Kataoka, "Variable-magnetization PM-motor yield widely variable flux due to small magnetizing current," in *Proc. Int. Conf. Elect. Mach.*, Dec. 2020, pp. 741-747.
- [SAK21] K. Sakai, K. Yoneda, and W. Suzuki, "Variable-magnetization interior permanent magnet motor yield widely variable flux due to small magnetizing

current and operating at high power over a wide speed range,” in *Proc. Energy Convers. Cognr. Expo.*, Oct. 2021, pp. 4205-4212.

- [SEK13] P. Sekerak, V. Hrabovcova, J. Pyrhonen, L. Kalamen, P. Rafajdus, and M. Onufer, “Comparison of synchronous motors with different permanent magnet and winding types,” *IEEE Trans. on Magnetics*, vol. 49, no. 3, pp. 1256-1263, March 2013.
- [SEN94] T. Senjyu, T. Shimabukuro, and K. Uezato, “Vector control of permanent magnet synchronous motors including stator iron loss,” in *Proceedings of 1994 IEEE International Conference on Industrial Technology - ICIT '94*, Guangzhou, China, 1994, pp. 1-5.
- [SIL91] K. F. da Silva, C. B. Jacobina, and A. M. N. Lima, “Vector control in synchronous machine drives,” in *Proceedings IECON '91: 1991 International Conference on Industrial Electronics, Control and Instrumentation*, Kobe, Japan, 1991, pp. 177-181 vol.1.
- [SNE85] B. Sneyers, D. W. Novotny, and T. A. Lipo. “Field weakening in buried permanent magnet AC motor drives,” *IEEE Trans. on Ind. Appl.*, vol. IA-21, no. 2, pp. 398-407, March 1985.
- [SON17] J. Song, J. H. Lee, D. Kim, Y. Kim, and S. Jung, “Analysis and modeling of concentrated winding variable flux memory motor using magnetic equivalent circuit method,” *IEEE Trans. on Magn.*, vol. 53, no. 6, pp. 1–4, Jun. 2017.
- [SON96] H. Song, J. M. Kim, and S. K. Sul, “A new robust SPMSM control to parameter variations in flux weakening region,” in *Proc. IEEE Ind. Electron. Soc. Annu. Conf.*, 1996, pp. 1193–1198.
- [SOO05] W. L. Soong, B. A. Welchko, and N. Ertugrul, “Uncontrolled generation in interior permanent-magnet machines,” *IEEE Trans. Ind. Appl.*, vol. 41, no. 4, pp. 945–954, Jul. 2005.
- [SOU22] F. D. de Sousa, A. Battiston, F. Meibody-Tabar, and S. Pierfederici, “Evaluation of Magnetic Behavior of a Single Pole Pair Fe-Cr-Co-Based Memory Motor Considering Standstill Magnetization,” *IEEE Trans. on Magn.*, vol. 58, no. 8, pp. 1-7, Aug. 2022.

- [SUN15] A. Sun, J. Li, R. Qu, J. Chen, and H. Lu, "Rotor design considerations for a variable-flux flux-intensifying interior permanent magnet machine with improved torque quality and reduced magnetization current," in *Proc. Energy Convers. Cognr. Expo.*, Sep. 2015, pp. 784-790.
- [SZA06] C. Szabo, I. I. Incze, and M. Imecs, "Voltage-hertz control of the synchronous machine with variable excitation," in *2006 IEEE International Conference on Automation, Quality and Testing, Robotics*, Cluj-Napoca, Romania, 2006, pp. 298-303.
- [TAK18] A. Takbash, and P. Pillay, "Magnetization and demagnetization energy estimation and torque characterization of a variable-flux machine," *IEEE Trans. on Energy Convers.*, vol. 33, no. 4, pp. 1837-1845, Dec. 2018.
- [TAN03] Lixin Tang, Limin Zhong, M. F. Rahman, and Yuwen Hu, "A novel direct torque control for interior permanent-magnet synchronous machine drive with low ripple in torque and flux-a speed-sensorless approach," *IEEE Trans. on Ind. Appl.*, vol. 39, no. 6, pp. 1748-1756, Nov.-Dec. 2003.
- [TSU21] R. Tsunata, M. Takemoto, S. Ogasawara, and K. Orikawa, "Variable flux memory motor employing double-layer delta-type PM arrangement and large flux barrier for traction applications," *IEEE Trans. Ind. Appl.*, vol. 57, no. 4, pp. 3545-3561, July/Aug. 2021.
- [WAN12] M. Wang, C. Tong, P. Zheng, L. Cheng, S. Zhang, G. Qiao, and Y. Sui, "Analysis of a novel hybrid-PM variable-flux machine using new magnet material CeFeB," *IEEE Trans. on Magn.*, vol. 55, no. 7, pp. 1-7, July 2019.
- [WAN15a] D. Wang, H. Lin, H. Yang, Y. Zhang, and X. Lu, "Design and analysis of a variable-flux pole-changing permanent magnet memory machine," *IEEE Trans. Magn.*, vol. 51, no. 11, Nov. 2015.
- [WAN15b] Q. Wang and S. Niu, "Electromagnetic design and analysis of a novel fault-tolerant flux-modulated memory machine," *Energies*, vol. 8, pp. 8069-8085, 2015.
- [WAN18] C. Wang, Z. Q. Zhu, and H. Zhan, "Adaptive voltage feedback controllers on the non-salient permanent magnet synchronous machine," in *2018 XIII*

International Conference on Electrical Machines (ICEM), Alexandroupoulos, Greece, 2018, pp. 1374-1380.

- [WAN19] M. Wang, C. Tong, P. Zheng, L. Cheng, S. Zhang, G. Qiao, and Yi Sui, “Analysis of a novel hybrid-PM variable-flux machine using new magnet material CeFeB,” *IEEE Trans. Magn.*, vol. 55, no. 7, Jul. 2019.
- [WU09] S. Wu, D. Reigosa, Y. Shibukawa, M. Leetmma, R. Lorenz, and Y. Li, “Interior permanent-magnet synchronous motor design for improving self-sensing performance at very low speed,” *IEEE Trans. Ind. Appl.*, vol. 45, no. 6, pp. 1939–1946, Nov./Dec. 2009.
- [WU14] D. Wu, Z. Q. Zhu, A. Pride, R. Deodhar, and T. Sasaki, “Cross coupling effect in hybrid magnet memory machine” in *Proc. 7th IET Int. Conf. Power Electron. Machin. Drives (PEMD)*, Manchester, UK. 2014.
- [WU14] D. Wu, Z. Q. Zhu, X. Liu, A. Pride, R. Deodhar, and T. Sasaki, “Cross coupling effect in hybrid magnet memory motor,” in *Proc. 7th IET Int. Conf. Power Electron., Mach. Drives (PEMD)*, Apr. 2014, pp. 1–6.
- [WU15] D. Wu, X. Liu, Z.Q. Zhu, A. Pride, R. Deodhar, and T. Sasaki, “Switched flux hybrid magnet memory motor,” *Proc. IET, Electric Power Applications, EPA*, vol.9, no.2, pp.160-170, Feb. 2015.
- [WU19] J. Wu, X. Zhu, L. Xu, L. Quan, D. Fan, and J. Yang, “Optimization design of a flux memory motor based on a new non-linear MC-DRN model,” *IET Electric Power Appl.*, vol. 13, no. 12, pp. 2035–2043, Oct. 2019.
- [XIE20a] Y. Xie, Z. Ning, and Z. Ma, “Comparative study on variable flux memory machines with different arrangements of permanent magnets,” *IEEE Access*, vol. 8, pp. 164304-164312, 2020.
- [XIE20b] Y. Xie, Z. Ning, Z. Ma, W. Cai, and J. Wei, “Design and research of novel variable flux memory motor with series hybrid magnets,” in *2020 23rd International Conference on Electrical Machines and Systems (ICEMS)*, Hamamatsu, Japan, 2020, pp. 2142-2147.
- [XU21] H. Xu, J. Li, J. Chen, Y. Lu, and M. Ge, “Analysis of a hybrid permanent magnet variable-flux machine for electric vehicle tractions considering

magnetizing and demagnetizing current,” *IEEE Trans. Ind. Appl.*, vol. 57, no. 6, pp. 5983-5992, Nov./Dec. 2021.

- [YAN14a] H. Yang, H. Lin, J. Dong, J. Yan, Y. Huang, and S. Fang, “Analysis of a novel switched-flux memory motor employing a time-divisional magnetization strategy,” *IEEE Trans. Magn.*, vol. 50, no. 2, pp. 849-852, Feb. 2014.
- [YAN14b] H. Yang, H. Lin, S. Fang, Z. Q. Zhu, and Y. Huang, “Flux-regulatable characteristics analysis of a novel switched-flux surface-mounted PM memory machine,” *IEEE Trans. Magn.*, vol. 50, no. 11, pp. 1-4, Nov. 2014.
- [YAN14c] H. Yang, H. Lin, Z. Q. Zhu, S. Fang, and Y. Huang, “Novel flux-regulatable dual-magnet vernier memory machines for electric vehicle propulsion,” *IEEE Trans. Appl. Supercond.*, vol. 24, no. 5, pp. 1-5, Oct. 2014.
- [YAN16d] H. Yang, Z. Q. Zhu, H. Lin, Y. Zhang, S. Fang, Y. Huang, and N. Feng, “Performance improvement of partitioned stator switched flux memory machines with triple-magnet configuration,” *IEEE Trans. on Magnetics*, vol. 52, no. 7, pp. 1–4, Jul. 2016.
- [YAN16f] H. Yang Z. Q. Zhu, H. Lin, D. Wu, H. Hua, S. Fang, and Y. Huang, “Novel high-performance switched flux hybrid magnet memory machines with reduced rare-earth magnets,” *IEEE Trans. on Ind. Appl.*, vol. 52, no. 5, pp. 3901–3915, Sep. 2016.
- [YAN16a] H. Yang, H. Lin, S. Fang, Y. Huang, and Z. Q. Zhu, “A novel stator-consequent-pole memory machine,” in *Proc. Energy Convers. Cognr. Expo.*, Sep. 2016, pp. 1-8.
- [YAN16b] H. Yang, H. Lin, Z. Q. Zhu, K. Guo, D. Wang, S. Fang, and Y. Huang, “Flux-concentrated external-rotor switched flux memory machines for direct-drive applications,” *IEEE Trans. Appl. Supercond.*, vol. 26, no. 7, pp. 1-6, Oct. 2016.
- [YAN16c] H. Yang, H. Lin, Z. Q. Zhu, D. Wang, S. Fang, Y. Huang, “A variable-flux hybrid-PM switched-flux memory machine for EV/HEV applications,” *IEEE Trans. Ind. Appl.*, vol. 52, no. 3, pp. 2203-2214, May/June. 2016.
- [YAN16d] H. Yang, Z. Q. Zhu, H. Lin, D. Wu, H. Hua, S. Fang, and Y. Huang, “Novel high-performance switched flux hybrid magnet memory machines with

- reduced rare-earth magnets,” *IEEE Trans. Ind. Appl.*, vol. 52, no. 5, pp. 3901-3915, Sep./Oct. 2016.
- [YAN16e] H. Yang, Z. Q. Zhu, H. Lin, H. Zhan, H. Hua, E. Zhuang, S. Fang, and Y. Huang, “Hybrid-excited switched-flux hybrid magnet memory machines,” *IEEE Trans. Magn.*, vol. 52, no. 6, pp. 1-15, Jun. 2016.
- [YAN16f] H. Yang, Z. Q. Zhu, H. Lin, Y. Zhang, S. Fang, Y. Huang, and N. Feng, “Performance improvement of partitioned stator switched flux memory machines with triple-magnet configuration,” *IEEE Trans. Magn.*, vol. 52, no. 7, pp. 1–4, Jul. 2016.
- [YAN16g] H. Yang, H. Lin, E. Zhuang, S. Fang, and Y. Huang, “Investigation of design methodology for non-rare-earth variable-flux switched-flux memory machines,” *IET Electr. Power Appl.*, vol. 10, no. 8, pp. 744-756, Feb. 2016.
- [YAN16h] H. Yang, H. Lin, Z. Q. Zhu, S. Fang, and Y. Huang, “A dual consequent-pole vernier memory machine,” *Energies*, vol. 9, no. 134, pp. 1-15, 2016.
- [YAN17a] H. Yang, Z. Q. Zhu, H. Lin, K. Guo, S. Fang, and Y. Huang, “Analysis of on-load magnetization characteristics in a novel partitioned stator hybrid magnet memory machine,” *IEEE Trans. on Magn.*, vol. 53, no. 6, pp. 1–4, Jun. 2017.
- [YAN17b] H. Yang, Z. Q. Zhu, H. Lin, K. Guo, Y. Guo, S. Fang, and Y. Huang, “Analysis of on-load magnetization characteristics in a novel partitioned stator hybrid magnet memory machine,” *IEEE Trans. Magn.*, vol. 53, no. 6, Jun. 2017.
- [YAN17c] H. Yang, H. Lin; Z. Q. Zhu, and S. Lyu, “Novel variable reluctance hybrid magnet memory machines,” in *Proc. Int. Conf. Elect. Mach. Syst.*, Aug. 2017, pp. 1-6.
- [YAN17d] H. Yang, H. Lin, Z. Q. Zhu, H. Wang, S. Fang, and Y. Huang, “A novel flux-reversal hybrid magnet memory machine,” in *Proc. Energy Convers. Cognr. Expo.*, Oct. 2017, pp. 1-8.
- [YAN18] G. Yang, M. Lin, N. Li, G. Tan, and B. Zhang, “Flux-weakening control combined with magnetization state manipulation of hybrid permanent magnet axial field flux-switching memory machine,” *IEEE Trans. on Energy Convers.*, vol. 33, no. 4, pp. 2210–2219, Dec. 2018.

- [YAN18a] H. Yang, Z. Q. Zhu, H. Lin, and S. Lyu, "Comparative study of hybrid PM memory machines having single- and dual-stator configurations," *IEEE Trans. on Ind. Electron.*, vol. 65, no. 11, pp. 9168–9178, Nov. 2018.
- [YAN18c] H. Yang, H. Lin, Z. Q. Zhu, S. Lyu, and H. Wang, "A novel dual-layer PM variable flux hybrid memory machine," in *Proc. Energy Convers. Congr. Expo.*, 2018, pp. 262-268.
- [YAN18b] H. Yang, H. Lin, and Z. Q. Zhu, "Recent advances in variable flux memory machines for traction applications: A review," *CES Trans. on Electric Machines and Systems*, vol. 2, no. 1, pp. 34–50, Mar. 2018.
- [YAN18f] H. Yang, H. Lin, Y. Li, H. Wang, S. Fang, and Y. Huang, "Analytical modeling of switched flux memory machine," *IEEE Trans. on Magn.*, vol. 54, no. 3, pp. 1–5, Mar. 2018.
- [YAN18d] H. Yang, Z. Q. Zhu, H. Lin, S. Fang, Y. Huang, and Z. Xu, "Novel dual-stator switched-flux memory machines with hybrid magnets," *IEEE Trans. Ind. Appl.*, vol. 54, no. 3, pp. 2129-2140, May/Jun. 2018.
- [YAN18e] H. Yang, Z. Q. Zhu, H. Lin, S. Fang, and Y. Huang, "Synthesis of hybrid magnet memory machines having separate stators for traction applications," *IEEE Trans. Veh. Technol.*, vol. 67, no. 1, pp. 183-195, Jan. 2018.
- [YAN18g] H. Yang, H. Lin, Z. Q. Zhu, S. Lyu, and K. Wang, "A novel dual-sided PM variable flux memory machine," *IEEE Trans. Magn.*, vol. 54, no. 11, Nov. 2018.
- [YAN19a] G. Yang, M. Lin, N. Li, and L. Hao, "Magnetization state regulation characteristic study of series hybrid permanent magnet axial field flux-switching memory machine," *IEEE Trans. on Applied Supercond.*, vol. 29, no. 2, pp. 1–6, Mar. 2019.
- [YAN19d] H. Yang, H. Zheng, Z. Q. Zhu, H. Lin, S. Lyu, and Z. Pan, "Comparative study of partitioned stator memory machines with series and parallel hybrid PM configurations," *IEEE Trans. on Magnetics*, vol. 55, no. 7, pp. 1-8, July 2019.
- [YAN19b] H. Yang, S. Lyu, H. Lin, Z. Q. Zhu, F. Peng, E. Zhuang, S. Fang, and Y. Huang, "Stepwise magnetization control strategy for DC-magnetized memory

- machine,” *IEEE Trans. on Ind. Electron.*, vol. 66, no. 6, pp. 4273–4285, Jun. 2019.
- [YAN19c] H. Yang, H. Zheng, H. Lin, Z. Q. Zhu, and S. Lyu, “A novel variable flux dual-layer hybrid magnet memory machine with bypass airspace barriers,” in *2019 IEEE Inter. Electric Machines & Drives Conf. (IEMDC)*, 2019, pp. 2259-2264.
- [YAN20] H. Yang, S. Lyu, H. Lin, Z. Zhu, H. Zheng, and T. Wang, “A novel hybrid-magnetic-circuit variable flux memory machine,” *IEEE Trans. on Ind. Electron.*, vol. 67, no. 7, pp. 5258–5268, Jul. 2020.
- [YAN21] H. Yang, H. Zheng, H. Lin, Z. Q. Zhu, W. Fu, W. Liu, J. Lei, and S. Lyu, “Investigation of hybrid-magnet-circuit variable flux memory machines with different hybrid magnet configurations,” *IEEE Trans. Ind. Appl.*, vol. 57, no. 1, pp. 340-351, Jan./Feb. 2021.
- [YAN22] H. Yang, W. Liu, H. Zheng, H. Lin, Z. Q. Zhu, F. Peng, Y. Li, S. Lyu, and X. Huang, “A novel delta-type hybrid-magnetic-circuit variable flux memory machine for electrified vehicle applications,” *IEEE Trans. Transpor. Electrifi.*, vol. 8, no. 3, pp. 3512-3523, Sept. 2022.
- [YU11a] C. Yu and K. Chau, “Dual-mode operation of DC-excited memory motors under flux regulation,” *IEEE Trans. Ind. Appl.*, vol. 47, no. 5, pp. 2031-2041, Sep./Oct. 2011.
- [YU11b] C. Yu and K. T. Chau, “Design, analysis, and control of DC-excited memory motors,” *IEEE Trans. on Energy Convers.*, vol. 26, no. 2, pp. 479–489, Jun. 2011.
- [YU14] C. Yu, T. Fukushige, N. Limsuwan, T. Kato, D. D. Reigosa, and R. D. Lorenz, “Variable-flux machine torque estimation and pulsating torque mitigation during magnetization state manipulation,” *IEEE Trans. on Ind. Appl.*, vol. 50, no. 5, pp. 3414-3422, Sept.-Oct. 2014.
- [YU15] C. Yu, S. Niu, S. L. Ho, W. Fu, and L. Li, “Hysteresis modeling in transient analysis of electric motors with AlNiCo magnets,” *IEEE Trans. Magn.*, vol. 51, no. 3, pp. 1-4, Mar. 2015.
- [ZHA17] Y. Zhang and T. M. Jahns, “Uncontrolled generator operation of PM

synchronous machine drive with current-source inverter using normally on switches,” *IEEE Trans. Ind. Appl.*, vol. 53, no. 1, pp. 203–211, Jan. 2017.

- [ZHA18] S. Zhang, P. Zheng, T. M. Jahns, L. Cheng, M. Wang, and Y. Sui, “A novel variable-flux permanent-magnet synchronous machine with quasi-series magnet configuration and passive flux barrier,” *IEEE Trans. on Magnetics*, vol. 54, no. 11, pp. 1-5, Nov. 2018.
- [ZHA21] S. Zhang, P. Zheng, Y. Liu, M. Wang, G. Qiao, and F. Liu, “A high-torque-density variable-flux memory machine utilizing novel (Ce, Nd)-Fe-B magnets,” *IEEE Trans. Magn.*, vol. 57, no. 2, pp. 1-6, Feb. 2021.
- [ZHE19] Y. Zheng, L. J. Wu, Y. Fang, X. Huang, and Q. Lu, “A hybrid interior permanent magnet variable flux memory machine using two-part rotor,” *IEEE Trans. Magn.*, vol. 55, no. 7, pp. 1-8, Jul. 2019.
- [ZHO16] Y. Zhou, Y. Chen, and J. Shen, “Analysis and improvement of a hybrid permanent-magnet memory motor,” *IEEE Trans. on Energy Convers.*, vol. 31, no. 3, pp. 915-923, Sept. 2016.
- [ZHO22a] Y. Zhong, H. Lin, Z. Chen, S. Lyu, and H. Yang, “Online-parameter-estimation-based control strategy combining MTPA and flux-weakening for variable flux memory machines,” *IEEE Trans. on Power Electron.*, vol. 37, no. 4, pp. 4080-4090, April 2022.
- [ZHO22b] Y. Zhong, H. Lin, J. Wang, R. Tu, H. Yang, S. Lyu, and X. Liu, “Variable time magnetization current trajectory control method for variable flux memory machines,” *IEEE Trans. on Transpor. Electrifi.*, vol. 8, no. 3, pp. 3100-3110, Sept. 2022.
- [ZHO23a] Y. Zhong, H. Lin, J. Wang, and H. Yang, “Improved adaptive sliding-mode observer-based position sensorless control for variable flux memory machines,” *IEEE Trans. on Power Electron.*, vol. 38, no. 5, pp. 6395-6406, May 2023.
- [ZHO23b] Y. Zhong, H. Lin, J. Wang, R. Tu, H. Yang, S. Lyu, and X. Liu, “Variable time magnetization current trajectory control method for variable flux memory machines,” *IEEE Trans. on Transp. Electrifi.*, vol. 8, no. 3, pp. 3100-3110, Sept.

2022.

- [ZHO24] Y. Zhong, H. Lin, J. Wang, W. Liu, and H. Yang, “Q-axis current reverse control of variable flux memory machines with high salient ratio during magnetization process for speed fluctuation reduction,” *IEEE Trans. on Ind. Electron.* vol. 71, no. 1, pp. 226-236, Jan. 2024.
- [ZHO23c] Y. Zhong, H. Lin, J. Wang, Z. Chen, and H. Yang, “Speed fluctuation mitigation control for variable flux memory machine during magnetization state manipulations,” *IEEE Trans. on Ind. Electron.*, vol. 70, no. 1, pp. 222-232, Jan. 2023.
- [ZHO97] L. Zhong, M. F. Rahman, Y. W. Hu, and K. W. Lim, “Analysis of direct torque control in permanent magnet synchronous motor drives,” *IEEE Trans. Power Electron.*, vol. 12, no. 3, pp. 528–536, May 1997.
- [ZHU00] Z. Q. Zhu, Y. S. Chen, and D. Howe, “Online optimal flux-weakening control of permanent-magnet brushless AC drives,” *IEEE Trans. on Ind. Appl.*, vol. 36, no. 6, pp. 1661-1668, Nov.-Dec. 2000.
- [ZHU06] Z. Q. Zhu, Y. Liu, and D. Howe, “Minimizing the influence of cogging torque on vibration of PM brushless machines by direct torque control,” *IEEE Trans. on Magnetics*, vol. 42, no. 10, pp. 3512-3514, Oct. 2006.
- [ZHU07] Z. Q. Zhu and D. Howe, “Electrical machines and drives for electric, hybrid, and fuel cell vehicles,” *Proceedings of the IEEE*, vol. 95, no. 4, pp. 746 - 765, 2007.
- [ZHU11] X. Zhu, L. Quan, D. Chen, M. Cheng, W. Hua, and X. Sun, “Electromagnetic performance analysis of a new stator-permanent-magnet doubly salient flux memory motor using a piecewise-linear hysteresis model,” *IEEE Trans. on Magn.*, vol. 47, no. 5, pp. 1106–1109, May 2011.
- [ZHU17] Z. Q. Zhu, H. Hua, A. Pride, R. Deodhar, and T. Sasaki, “Analysis and reduction of unipolar leakage flux in series hybrid permanent-magnet variable flux memory machines,” *IEEE Trans. Magn.*, vol. 53, no. 11, pp. 1-4, Nov. 2017.
- [ZHU19] Z. Q. Zhu, N. Pothi, P. L. Xu, and Y. Ren, “Uncontrolled generator fault

protection of novel hybrid-excited doubly salient synchronous machines with field excitation current control,” *IEEE Trans. Ind. Appl.*, vol. 55, no. 4, pp. 3598–3606, Jul. 2019.

[ZHU21] Z. Q. Zhu, D. Liang, and K. Liu, “Online parameter estimation for permanent magnet synchronous machines: an overview,” *IEEE Access*, vol. 9, pp. 59059–59084, 2021.

APPENDIX A TOPOLOGY OF INVESTIGATED HMMM

The topology of the investigated HMMM with airspace barriers [YAN19c] is shown in Fig. A.1. It has 21 stator slots and 4 rotor poles, and uses AlNiCo as the LCF PM and NdFeB as the HCF PM. The HCF and LCF magnets are geometrically separated within one PM rotor pole, forming a dual layer structure. The radially magnetized LCF PMs are located nearby the airgap, which can be demagnetized easily, and the circumferentially magnetized HCF PMs are placed on the two sides of the LCF magnet. This series structure arrangement of hybrid PMs can combine the advantages of high torque capability of HCF PMs and wide flux regulation merit of LCF PMs and prevent the unintentional demagnetization risk of the LCF PMs. Besides, the airspace barriers and adjacent iron bridges are designed at the d -axis position, which can effectively reduce the oversized inverter power rating and required fully demagnetizing current pulse level. Due to the presence of the upper-side iron bridge and airspace barrier, a short-circuiting path for the HCF PM magnetic fields will occur at the flux-weakened state. As shown in Fig. A.1, there is no extra magnetizing coils in the HMMM. The magnetizing current pulse is injected into the d -axis armature current to achieve MS manipulation.

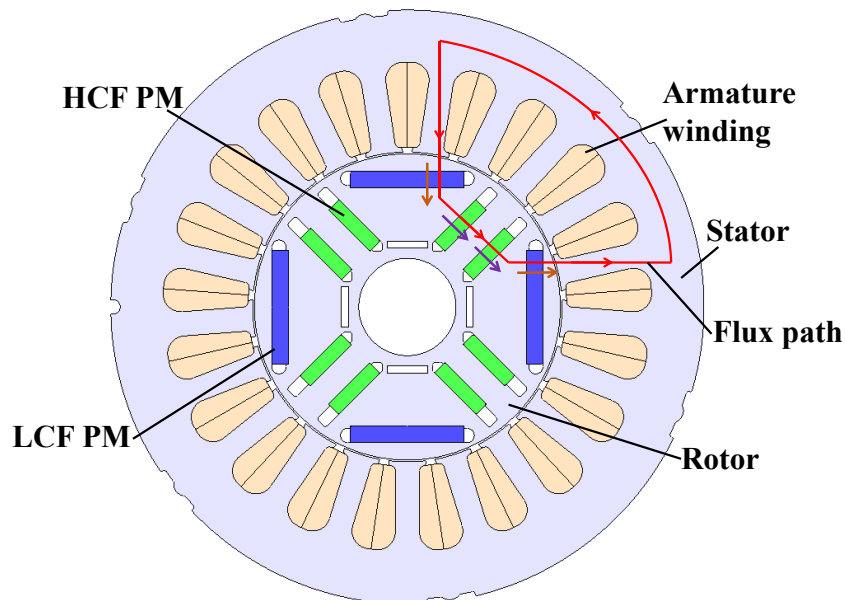


Fig. A.1. Topology of investigated HMMM.

The main parameters of the investigated HMMM prototype are listed in Table A.1.

Table A.1. Main parameters of investigated HMMM prototype.

Item	Symbol	Value
Rated power	P	1100W
Rated current (RMS)	I_m	7.5A
Rated speed	n	1500 r/min
Number of pole pairs	p	2
Phase resistance	R	1.9 Ω
HCF PM grade	-	N35SH
LCF PM grade	-	AlNiCo 9
HCF PM coercivity	-	915 kA/m
LCF PM coercivity	-	112 kA/m
HCF PM remanence	-	1.2T
LCF PM remanence	-	1.0T
Steel grade	-	35CS440

As above mentioned, the LCF PMs and HCF PMs are made of AlNiCo and NdFeB, respectively. Their B-H curves are depicted in Fig. A.2. For LCF PMs, the hysteresis curve of AlNiCo can allow its operating points to move flexibly.

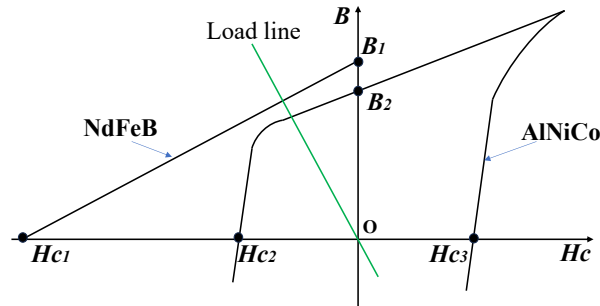
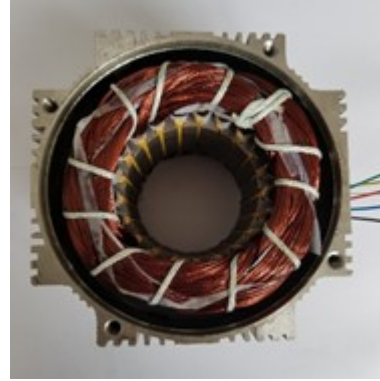


Fig. A.2. BH curves for NdFeB and AlNiCo (B: Flux density, Hc: magnetic field strength).

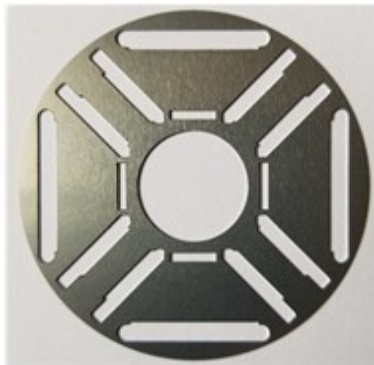
The stator part, rotor part and photos of the HMMM are shown in Fig. A.3.



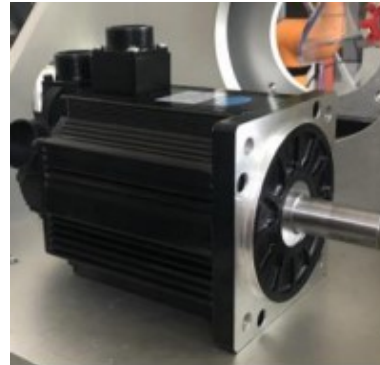
(a)



(b)



(c)



(d)

Fig. A.3. Photos of HMMM. (a) Stator. (b) Stator with armature windings. (c) Rotor laminations. (d) Appearance.

APPENDIX B MATHEMATICAL MODEL FOR VFMM

The PM flux linkage of VFMM is not a constant but a variable parameter relating with d -axis magnetizing current pulse. Therefore, the dq -axis mathematical model considering the process of remagnetization and demagnetization of LCF PMs is (referred to as dynamic mathematical model):

$$\begin{cases} u_d = Ri_d + L_d \frac{di_d}{dt} + \frac{d\psi_m(i_{mag.})}{dt} - \omega L_q i_q \\ u_q = Ri_q + L_q \frac{di_q}{dt} + \omega L_d i_d + \omega \psi_m(i_{mag.}) \end{cases} \quad (\text{B.1})$$

where R is the winding resistance, u_d and u_q are the dq -axis voltages, ω is the electrical angular speed, i_d and i_q are the dq -axis stator currents, L_d and L_q are the dq -axis inductances (for a non-salient-pole VFMM, $L_d = L_q$), $\psi_m(i_{mag.})$ is the PM flux linkage, which is adjusted by a d -axis magnetizing current pulse, $i_{mag.}$ is the d -axis magnetizing current pulse.

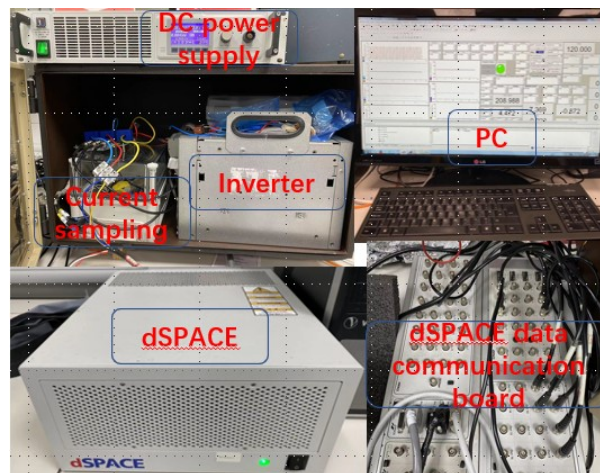
The torque equation of VFMM considering MS change is:

$$T_e = 1.5p[\psi_m(i_{mag.})i_q + (L_d - L_q)i_d i_q] \quad (\text{B.2})$$

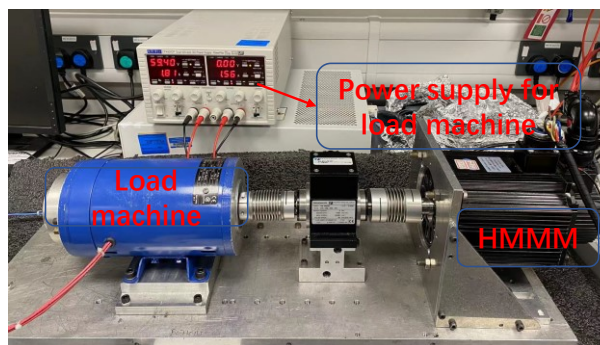
where p is the pole pair number of VFMM.

APPENDIX C TEST PLATFORM FOR EXPERIMENTAL VALIDATION

The test platform for the investigated HMMM is shown in Fig. C.1. It consists of a PC, a three-phase IGBT inverter, a dSPACE, a self-made current sampling board, a load machine, the investigated machine, and several DC power supplies. The PC is used to compile the control algorithm and monitor the real-time data generated by the dSPACE, in which both the PWM frequency and sampling frequency are 10 kHz. The three-phase IGBT inverter is a Semikron unit, and its type is SEMiX 71GD12E4s. The PWM signal is processed in the inverter. The PWM signal and the real-time data are translated by the dSPACE data communication board. The current sampling board connects the investigated machine and the inverter. The servo machine is utilized as the load for the experiments.



(a)



(b)

Fig. C.1. Experiment platform for investigated HMMM. (a) Experiment and control equipment. (b) Prototype and test rig.